# Oxygen Dynamics in Amorphous Silicon Suboxide Resistive Switches

Manveer Singh Munde

*Department of Physics & Astronomy*,

*University College London*,

Doctoral thesis submitted for the fulfilment of the requirements for the degree of Doctor of Philosophy (Ph.D.) of University College London

I, *Manveer Singh Munde*, confirm that the work presented in this thesis is my own. Where information has been derived from other sources, I confirm that this has been indicated in the thesis.

Manveer Singh Munde, June 2017

# Abstract

This thesis aims to improve our understanding of intrinsic resistive switching behaviour in silicon suboxides using transmission electron microscopy characterisation and density functional theory modelling. The main new results of this thesis can be summarised as follows.

In sputter-deposited silicon suboxides, oxide-wide structural reorganisation occurs during electrical stressing. This is a result of large-scale oxygen dynamics, which can result in oxygen outmigration from the oxide and electrode deformation.

The fabrication of sputter-deposited silicon suboxides greatly influences device performance. Firstly, growing the oxide layer on a rougher substrate surface promotes lower electroforming voltages and greater device endurance. This is consistent with enhanced columnar microstructure in the oxide. Secondly, thin oxide layers ($< 5$ nm) will lead to electrode migration into the oxide layer as a result of high electric fields. This will limit the thickness of the oxide layer needed for intrinsic switching behaviour.

The formation of oxygen vacancy dimers and trimers is energetically favourable at some sites in amorphous silicon dioxide, with maximum binding energies of 0.13 eV and 0.18 eV, respectively. However, neutral oxygen vacancies are immobile under room temperature operating conditions and diffuse with a mean adiabatic barrier height of 4.6 eV.

In amorphous silicon dioxide, double electron trapping is energetically feasible at oxygen vacancies at Fermi energies above 6.4 eV. This greatly improves vacancy mobility; however, vacancy diffusion competes with thermal ionisation of the electrons into the conduction band. Oxygen vacancies also compete with intrinsic sites for electron trapping. This results in an inefficient diffusion process, which cannot explain the formation of a silicon-rich conductive path.

These results will help guide the optimisation of future silicon suboxide-based resistive random access memory and provide new insights into the role of oxygen vacancies during the electrical stressing of silicon oxides.

# Acknowledgements

This project was an international and interdisciplinary collaboration, which would not be possible without the involvement of a number of entities. Firstly, I would like to thank my supervisors Professor Alexander Shluger and Professor Tony Kenyon and their research groups for continued support and insightful discussions at University College London (UCL). In particular, I would like to thank David Gao and Al-Moatsem El-Sayed who acted as mentors for the theoretical calculations presented in this thesis, and Adnan Mehonic, Mark Buckwell, Luca Montesi, and Wing Ng, who fabricated, prepared, and sent the samples studied in this thesis for TEM characterisation in Singapore. I would also like to thank collaborations with the University of Southampton and Sematech for sample fabrication, and a collaboration with Forschungszentrum Jülich where I was first introduced to TEM characterisation courtesy of Martial Duchamp, Vadim Migunov, and Amir Tavabi.

Equally, I would like to thank Michel Bosman who supervised me for two years during my time at the Institute of Materials Research and Engineering (IMRE) in Singapore, and provided me with training and a wealth of expertise in TEM techniques. In addition, I thank Hui Ru Tan, June Ong Lay Ting, Siew Lang Teo, and Hui Kim Hui for the preparation of TEM samples and SEM imaging at IMRE using the FIB. I am also in debt to Cheah Wei Li at the Institute of High Power Computing (IHPC), who provided constant support for my theoretical calculations in Singapore. Furthermore, I would like to mention the support of Professor Kin Leong Pey and his research group at the Singapore University of Technology and Design (SUTD), which provided me with additional opportunities to discuss my work and carry out experiments, and gave me a real sense of belonging to the research group. In particular, I would like to mention Sen Mei and Alok Ranjan, who assisted with electrical probing measurements at SUTD. Furthermore, I am thankful for a collaboration with the National University of Singapore for providing access to the Jeol JEM-ARM200F TEM.

Finally, I would like to thank the UK Doctoral Training Centre for Molecular Modelling & Materials Science and ESPRC for funding during my time at UCL, A*STAR for funding through the A*STAR Research Attachment Programme (ARAP) in Singapore, and the

UK Materials Chemistry Consortium for providing countless hours of simulation via the ARCHER UK National Supercomputing Service. I would also like to mention the HR team at IMRE who made possible an additional month of funding, which provided a number of very exciting results in this thesis.

# List of Publications

The following publications and pending publications are derived from the work in this thesis:

1. Mehonic, Adnan, Mark Buckwell, Luca Montesi, Manveer Singh Munde, David Gao, Stephen Hudziak, Richard J. Chater et al. "Silica: Nanoscale Transformations in Metastable, Amorphous, Silicon-Rich Silica." Advanced Materials 28, no. 34 (2016): 7549.

2. Munde, Manveer S., David Z. Gao, Alexander L. Shluger, "Diffusion and Aggregation of Oxygen Vacancies in Amorphous Silica." Accepted in Journal of Physics: Condensed Matter.

3. Mehonic, Adnan, Manveer. S. Munde, Wing Ng, Mark Buckwell, Luca Montesi, Michel Bosman, Alexander L. Shluger, and Anthony J. Kenyon. "Intrinsic Resistance Switching in Amorphous Silicon Oxide for High Performance SiOx ReRAM Devices." Accepted in Microelectronic Engineering.

4. Munde, Manveer S., Adnan Mehonic, Wing Ng, Mark Buckwell, Luca Montesi, Michel Bosman, Alexander L. Shluger, and Anthony J. Kenyon. "Intrinsic Resistance Switching in Amorphous Silicon Suboxides: The Role of Columnar Microstructure." Submitted to Scientific Reports.

*To my parents, family, and friends,old and new...*

# Contents


**1 Abbreviations** **16**

**2 Introduction and Thesis Objective** **18**

**3 Literature Review** **23**

3.1 Introduction . . . . . . . . . . 23

3.2 ReRAM Types and Examples from Literature . . . . . . . . . . 23

3.2.1 Electrochemical Metallisation Memory (ECM) . . . . . . . . . . 23

3.2.2 Valence Change Memory (VCM) . . . . . . . . . . 26

3.2.3 Thermochemical Memory (TCM) . . . . . . . . . . 28

3.3 Resistive Switching in Amorphous Silicon Oxides . . . . . . . . . . 29

3.3.1 Amorphous Silicon Dioxide . . . . . . . . . . 29

3.3.2 Amorphous Silicon Suboxide . . . . . . . . . . 30

3.4 The Structure of Silicon Suboxides and the Existence of Oxygen Vacancy Defects . . . . . . . . . . 32

3.5 The Structure of Amorphous Silica and Oxygen Vacancies . . . . . . . . . . 34

3.6 Electron Trapping at Oxygen Vacancies and Intrinsic Sites in Amorphous Silica . . . . . . . . . . 37

3.7 Oxygen Migration in Silicon Oxides . . . . . . . . . . 38

3.8 Examples of Theoretical Studies on Vacancy Interaction . . . . . . . . . . 41

3.9 Discussion and Summary . . . . . . . . . . 43

**4 Transmission Electron Microscopy Characterisation** **46**

4.1 Introduction . . . . . . . . . . 46

4.2 A Brief Summary of the Layout of a TEM . . . . . . . . . . 46

4.3 TEM Sample Preparation using a Focused Ion Beam (FIB) . . . . . . . . . . 50

4.4 Factors Affecting Image Quality . . . . . . . . . . 51

4.5 TEM and STEM . . . . . . . . . . 52

4.6 Energy Dispersive X-ray Spectroscopy (EDX) and Electron Energy-Loss Spectroscopy (EELS) . . . . . . . . . . 54

4.7 The Energy-Loss Spectrum . . . . . . . . . . . . . . . . . . . . . . . . . . . 56
4.8 Electron Tomography . . . . . . . . . . . . . . . . . . . . . . . . . . . . . 60

**5 Fabrication and Electrical Behaviour of *MIM* Structures to be Characterised Using TEM 62**

5.1 Introduction . . . . . . . . . . . . . . . . . . . . . . . . . . . . . . . . . 62
5.2 Fabrication . . . . . . . . . . . . . . . . . . . . . . . . . . . . . . . . . . 62
5.2.1 Sample Fabrication Using the Reactive Sputtering Technique . . . 62
5.2.2 Device 1 . . . . . . . . . . . . . . . . . . . . . . . . . . . . . . . 65
5.2.3 Device 2 . . . . . . . . . . . . . . . . . . . . . . . . . . . . . . . 66
5.2.4 Device 3 . . . . . . . . . . . . . . . . . . . . . . . . . . . . . . . 67
5.2.5 Device 4 . . . . . . . . . . . . . . . . . . . . . . . . . . . . . . . 71
5.3 Electroforming . . . . . . . . . . . . . . . . . . . . . . . . . . . . . . . . 73
5.3.1 Device 1 . . . . . . . . . . . . . . . . . . . . . . . . . . . . . . . 75
5.3.2 Device 2 . . . . . . . . . . . . . . . . . . . . . . . . . . . . . . . 76
5.3.3 Device 3 . . . . . . . . . . . . . . . . . . . . . . . . . . . . . . . 76
5.3.4 Device 4 . . . . . . . . . . . . . . . . . . . . . . . . . . . . . . . 79
5.4 Discussion and Summary . . . . . . . . . . . . . . . . . . . . . . . . . . 79

**6 Nanoscale Oxygen Dynamics in Electrically Stressed *MIM* Structures with an a-SiO$_x$ Insulating Layer 82**

6.1 Introduction . . . . . . . . . . . . . . . . . . . . . . . . . . . . . . . . . 82
6.2 Methodology . . . . . . . . . . . . . . . . . . . . . . . . . . . . . . . . . 83
6.3 Results . . . . . . . . . . . . . . . . . . . . . . . . . . . . . . . . . . . . 85
6.3.1 Device 1 . . . . . . . . . . . . . . . . . . . . . . . . . . . . . . . 85
6.3.2 Device 2 . . . . . . . . . . . . . . . . . . . . . . . . . . . . . . . 94
6.3.3 Device 3 . . . . . . . . . . . . . . . . . . . . . . . . . . . . . . . 100
6.4 Discussion and Summary . . . . . . . . . . . . . . . . . . . . . . . . . . 109

**7 Observation of Electrode Migration in *MIM* devices with Thin a-SiO$_x$ Insulating Layers 112**

7.1 Introduction . . . . . . . . . . . . . . . . . . . . . . . . . . . . . . . . . 112

7.2 Methodology . . . . . . . . . . . . . . . . . . . . . . . . . . . . . . . . . . 113
7.3 Results . . . . . . . . . . . . . . . . . . . . . . . . . . . . . . . . . . . . . . . 114
7.4 Discussion and Summary . . . . . . . . . . . . . . . . . . . . . . . . . . . . 120

**8 Density Functional Theory 122**

8.1 Introduction . . . . . . . . . . . . . . . . . . . . . . . . . . . . . . . . . . . 122
8.2 The Kohn-Sham Equations . . . . . . . . . . . . . . . . . . . . . . . . . . . 123
8.3 Solving the Kohn-Sham Equations . . . . . . . . . . . . . . . . . . . . . . 125
8.4 The CP2K Software for Density Functional Theory Calculations . . . . . . 127
8.5 The PBE0-TC-LRC Hybrid Functional and The Auxiliary Density Matrix Method (ADMM) . . . . . . . . . . . . . . . . . . . . . . . . . . . . . . . . . 129
8.6 The Calculation of Minimum Energy Paths (MEP) using the Nudged Elastic Band Method (NEB) . . . . . . . . . . . . . . . . . . . . . . . 130
8.7 Corrections for Supercells with a Net Charge . . . . . . . . . . . . . . . . . 132

**9 The Diffusion and Aggregation of Neutral Oxygen Vacancies in Amorphous Silica 134**

9.1 Introduction . . . . . . . . . . . . . . . . . . . . . . . . . . . . . . . . . . . 134
9.2 Methodology . . . . . . . . . . . . . . . . . . . . . . . . . . . . . . . . . . 134
9.3 Results . . . . . . . . . . . . . . . . . . . . . . . . . . . . . . . . . . . . . . . 141
9.3.1 Correlation Between Vacancy Formation Energy and Pristine Cell Geometry . . . . . . . . . . . . . . . . . . . . . . . . . . . . . . . . . 141
9.3.2 Exploring the Aggregation of Oxygen Vacancies in Amorphous Silica 146
9.3.3 Exploring the Migration of Neutral Oxygen Vacancies in Amorphous Silica . . . . . . . . . . . . . . . . . . . . . . . . . . . . . . . . . . . 149
9.4 Discussion and Summary . . . . . . . . . . . . . . . . . . . . . . . . . . . . 151

**10 Exploring Electron Trapping at Oxygen Vacancies 153**

10.1 Introduction . . . . . . . . . . . . . . . . . . . . . . . . . . . . . . . . . . . 153
10.2 Methodology . . . . . . . . . . . . . . . . . . . . . . . . . . . . . . . . . . 153
10.3 Results . . . . . . . . . . . . . . . . . . . . . . . . . . . . . . . . . . . . . . . 156
10.3.1 Competition for Electrons between O Vacancies and Intrinsic Traps 156
10.3.2 Electron Trapping at O Vacancies . . . . . . . . . . . . . . . . . . . 157

10.3.3 The Migration of Negatively Charged Oxygen Vacancies . . . . . . 161
10.4 Discussion and Summary . . . . . . . . . . . . . . . . . . . . . . . . . . . . . 164

**11 Conclusion and Further Work** **166**

**12 Bibliography** **170**

# List of Figures and Tables


**3.1** Schematic illustrating conductive filament formation in an ECM cell. . . . . . . . . . . . . . . 24

**3.2** Illustration of the I-V curve for switching an ECM cell. . . . . . . . . . . . . . . . . . . . . . . . . . . . . 25

**3.3** Schematic illustrating conductive path formation in a VCM cell. . . . . . . . . . . . . . . . . . . . 26

**3.4** Illustration of the I-V curve for switching a VCM cell. . . . . . . . . . . . . . . . . . . . . . . . . . . . . . 27

**3.5** Illustration of the I-V curve for switching a TCM cell. . . . . . . . . . . . . . . . . . . . . . . . . . . . . . 29

**3.6** Illustration of tetrahedral units making up the continuous random network associated with the random bonding model of a-SiO$_x$. . . . . . . . . . . . . . . . . . . . . . . . . . . . . . . . . . . . . . . . . . . 34

**3.7** Molecular orbitals for electrons trapped in a-SiO$_2$. . . . . . . . . . . . . . . . . . . . . . . . . . . . . . . . 39

**3.8** Illustration of an oxygen double bridge interstitial in a-SiO$_2$. . . . . . . . . . . . . . . . . . . . . . . 41

**3.9** A schematic summarising the processes believed to occur in amorphous silicon oxides during electrical stressing. . . . . . . . . . . . . . . . . . . . . . . . . . . . . . . . . . . . . . . . . . . . . . . . . . . . . . 45

**4.1** Simplified schematic of a TEM. . . . . . . . . . . . . . . . . . . . . . . . . . . . . . . . . . . . . . . . . . . . . . . . . 47

**4.2** SEM images showing the main stages of FIB sample preparation. . . . . . . . . . . . . . . . . 51

**4.3** Schematic illustrating the origin of spherical aberrations in electron lenses. . . . . . . . 52

**4.4** Schematic illustrating the difference between bright and dark field detectors in STEM mode. . . . . . . . . . . . . . . . . . . . . . . . . . . . . . . . . . . . . . . . . . . . . . . . . . . . . . . . . . . . . . . . . . . . . 53

**4.5** Simplified schematic of a Gatan Imaging Filter (GIF). . . . . . . . . . . . . . . . . . . . . . . . . . . . 55

**4.6** Schematic illustrating the difference in positioning of EDX and EELS detectors in a TEM. . . . . . . . . . . . . . . . . . . . . . . . . . . . . . . . . . . . . . . . . . . . . . . . . . . . . . . . . . . . . . . . . . . . . . 56

**4.7** EELS spectrum taken from a-SiO$_2$. . . . . . . . . . . . . . . . . . . . . . . . . . . . . . . . . . . . . . . . . . . . 58

**4.8** Background extraction followed by multiple scattering deconvolution of the *O-K* edge in a-SiO$_2$. . . . . . . . . . . . . . . . . . . . . . . . . . . . . . . . . . . . . . . . . . . . . . . . . . . . . . . . . . . . . . . . 59

**4.9** Schematic illustrating the Fourier slice theorem. . . . . . . . . . . . . . . . . . . . . . . . . . . . . . . . . 60

**5.1** Illustration of the reactive sputtering technique used to fabricate a-SiO$_x$ thin film layers. . . . . . . . . . . . . . . . . . . . . . . . . . . . . . . . . . . . . . . . . . . . . . . . . . . . . . . . . . . . . . . . . . . . . . . . 63

**5.2** BF STEM image of an FIB-prepared cross-section from device 1. . . . . . . . . . . . . . . . . 66

**5.3** BF STEM image of an FIB-prepared cross-section from device 2. . . . . . . . . . . . . . . . . 67

**5.4** BF STEM image of an FIB-prepared cross-section from device 3. . . . . . . . . . . . . . . . . 68

**5.5** BF STEM image of an FIB-prepared cross-section from device 3, with enhanced con-

trast in the Au and Mo layers. . . . 69
**5.6** STEM images showing columnar growth in the a-SiO$_x$ layer from device 3. . . . 70
**5.7** AFM topography maps taken on the surface of the a-SiO$_x$ layer from device 3. . . . 71
**5.8** BF STEM image of an FIB-prepared cross-section from device 4. . . . 72
**5.9** Schematic illustrating electron transport processes across the insulating layer in an *MIM* structure. . . . 74
**5.10** Typical electroforming curve for device 1. . . . 75
**5.11** Electroforming curve for device 2. . . . 76
**5.12** Typical electroforming curve for device 3 for a negatively biased Au electrode. . . 77
**5.13** Demonstration of the endurance of device 3 during resistive switching when a negative bias is applied to the Au electrode for electroforming. . . . 78
**5.14** Electroforming curve for device 3 for a positively biased Au electrode. . . . 78
**5.15** Electroforming curve for device 4. . . . 79

**6.1** EELS spectrum images from unstressed and electroformed cross-sections from device 1 . . . . 88
**6.2** Comparison of ELNES at *Si*-$L_{2,3}$ edge from device 1. . . . 89
**6.3** Line profile taken along the oxide layer of the electroformed cross-section from device 1. . . . 89
**6.4** SEM top view image of an electroformed contact from device 1. . . . 90
**6.5** Void stuctures present between the top electrode and oxide layer from device 1. . 91
**6.6** Tomographic reconstructions of Figure 6.5(a)1 and (a)2. . . . 92
**6.7** Tomographic reconstructions of Figure 6.5(b)1 and (b)2. . . . 93
**6.8** EELS spectrum images from unstressed and stressed cross-sections from device 2. . . . 96
**6.9** Comparison of ELNES at *Si*-$L_{2,3}$ edge from device 2. . . . 97
**6.10** Line profile taken along the oxide layer of the stressed cross-section from device 2. . . . 97
**6.11** Larger EELS spectrum images from unstressed and stressed cross-sections from device 2. . . . 98
**6.12** Line profiles taken from bottom electrode to top electrode in device 2. . . . 99
**6.13** Comparison of ELNES in oxide, interface, and TiN layers from device 2. . . . 99
**6.14** EELS spectrum images from unstressed and stressed cross-sections from device

3. . . . 102
**6.15** Comparison of ELNES at *Si*-$L_{2,3}$ edge from device 3. . . . 103
**6.16** Line profile taken along the oxide layer of the negatively electroformed cross-section from device 3. . . . 103
**6.17** SEM top view images of stressed contacts from device 3. . . . 106
**6.18** SEM image of an FIB-prepared cross-section from the magnified region in Figure 6.17(a). . . . 107
**6.19** EELS spectrum images taken under interfacial voids in stressed cross-sections from device 3. . . . 108

**7.1** BF STEM image of an FIB-prepared cross-section from device 4. . . . 114
**7.2** HAADF images of unstressed and stressed cross-sections from device 4. . . . 115
**7.3** High-resolution EELS point spectra taken in the oxide layer at features A and B from Figure 7.2. . . . 116
**7.4** EELS spectrum image taken from the stressed cross-section from device 4. . . . 118
**7.5** Magnified BF STEM and HAADF images of the breakdown site in Figure 7.4. . . . 119

**9.1** 216 atom a-$SiO_2$ structure produced using classical molecular dynamics. . . . 136
**9.2** Radial distribution functions for Si-O, O-O, and Si-Si distances for the a-$SiO_2$ geometries used in this study. . . . 136
**9.3** Histograms showing distributions of O-Si-O angles, Si-O-Si angles, and rings from across the studied a-$SiO_2$ geometries. . . . 137
**9.4** Histogram comparing the Si-Si bond lengths at O vacancies using the even ring sampling in this study to a previous study. . . . 138
**9.5** Illustration of an oxygen vacancy site. . . . 139
**9.6** Vacancy formation energy plotted against Si-Si bond lengths at O vacancy sites after network relaxation. . . . 142
**9.7** Si-Si bond lengths at neutral O vacancy sites after network relaxation plotted against the position of the LUMO with respect to the valence band maximum (VBM). . . . 142
**9.8** Vacancy formation energy plotted against total tetrahedral volume $V_{tot}$. . . . 144
**9.9** Si-Si bond length after network relaxation plotted against total tetrahedral volume $V_{tot}$. . . . 145
**9.10** A histogram showing the predicted Si-Si bond lengths across 5 cells using the rela-

tionship from Figure 9.6. . . . . . . . . . . . . . . . . . . . . . . . . . . . . . . . . . . . . . . . . . . . . . . . . . . . . 146
**9.11** Scatter plot of formation energy of a di-vacancy or tri-vacancy aggregate per vacancy plotted against the mean formation energy of the very same vacancies when present individually. . . . . . . . . . . . . . . . . . . . . . . . . . . . . . . . . . . . . . . . . . . . . . . . . . . . . 148
**9.12** Final geometric configurations of tri-vacancy clusters. . . . . . . . . . . . . . . . . . . . . . . . . . 148
**9.13** Schematic showing the HOMO during the diffusion of neutral oxygen vacancies to adjacent sites. . . . . . . . . . . . . . . . . . . . . . . . . . . . . . . . . . . . . . . . . . . . . . . . . . . . . . . . . 150

**10.1** Schematic illustrating the difference between optical and thermal ionisation energies using potential energy surfaces. . . . . . . . . . . . . . . . . . . . . . . . . . . . . . . . . . . . . . . . . . . 154
**10.2** HOMO in and a-$SiO_2$ cell illustrating competition for electrons between oxygen vacancies and intrinsic electron traps. . . . . . . . . . . . . . . . . . . . . . . . . . . . . . . . . . . . . . . . . . . . . 156
**10.3** Scatter plot with the Si-Si bond length of the studied vacancies plotted against the position of the lowest unoccupied molecular orbital (LUMO) of the 215 atom cell in which the vacancy is situated. . . . . . . . . . . . . . . . . . . . . . . . . . . . . . . . . . . . . . . . . . . . . . . . . . . . . 157
**10.4** Formation energies of neutral, single negative, and double negatively charged oxygen vacancies as a function of Fermi energy. . . . . . . . . . . . . . . . . . . . . . . . . . . . . . . . . . . . . . . . 158
**10.5** Histograms summarising the charge transition levels for vacancies with $q$=-1 and -2. 159
**10.6** Charge transition levels for $q$=-1 as a function of Si-Si bond length at the neutral vacancy. . . . . . . . . . . . . . . . . . . . . . . . . . . . . . . . . . . . . . . . . . . . . . . . . . . . . . . . . . . . . . . . . 159
**10.7** Optical and thermal ionisation energies as a function of Si-Si bond length at the neutral vacancy. . . . . . . . . . . . . . . . . . . . . . . . . . . . . . . . . . . . . . . . . . . . . . . . . . . . . . . . . . . . . 160
**10.8** Schematic showing the HOMO during the diffusion of negatively charged oxygen vacancies to adjacent sites. . . . . . . . . . . . . . . . . . . . . . . . . . . . . . . . . . . . . . . . . . . . . . . . . . . . . 162
**10.9** Images from an a-$SiO_2$ cell for the rare case where double electron trapping at a vacancy facilitated the formation of a nearby vacancy. . . . . . . . . . . . . . . . . . . . . . . . . . . . . . . 165

**Table 1** Table summarising dependences of current density on electric field and temperature for various electron transport processes in insulators. . . . . . . . . . . . . . . . . . . . . . . . . . . 73
**Table 2** Table summarising main characteristics of the studied *MIM* stacks. . . . . . . . . . . 80

# 1 Abbreviations

The following list of abbreviations will be a useful reference throughout this thesis:

AES = Auger Electron Microscopy
AFM = Atomic Force Microscopy

CBM = Conduction Band Minimum
CMOS = Complementary Metal-Oxide-Semiconductor

DFT = Density Functional Theory

ECM = Electrochemical Memory
EELS = Electron Energy-Loss Spectroscopy

FFT = Fast Fourier Transform
FIB = Focused Ion Beam
FNE = Fowler-Nordheim Tunnelling

GGA = Generalised Gradient Approximation
GTO = Gaussian Type Orbital

HAADF = High-Angle Annular Dark Field
HF = Hartree-Fock
HOMO = Highest Occupied Molecular Orbital
HRTEM = High-Resolution Transmission Electron Microscopy

IMRE = Institute of Materials Research and Engineering (in Singapore)

LUMO = Lowest Unoccupied Molecular Orbital

MD = Molecular Dynamics
MIM = Metal-Insulator-Metal

NEB = Nudged Elastic Band

PECVD = Plasma-Enhanced Chemical Vapour Deposition

PFE = Poole-Frenkel Emission

ReRAM = Resistive Random Access Memory

RGA = Residual Gas Analysis

SAD = Selected Area Diffraction

SEM = Scanning Electron Microscopy

SIMS = Secondary Ion Mass Spectroscopy

STEM = Scanning Transmission Electron Microscopy

STM = Scanning Tunnelling Microscopy

SUTD = Singapore University of Technology and Design

TAT = Trap-Assisted Tunnelling

TCM = Thermochemical Memory

TEM = Transmission Electron Microscopy

UCL = University College London

VBM = Valence Band Maximum

VCM = Valence Change Memory

XAS = X-ray Absorption Spectrocopy

XPS = X-ray Photoelectron Spectroscopy

# 2 Introduction and Thesis Objective

Amorphous silicon suboxide (a-$SiO_x$) was once considered a negative consequence of attempting to fabricate pure amorphous silicon dioxide (a-$SiO_2$). Research had primarily focused on fabricating high quality a-$SiO_2$ in order to eliminate reliability issues for its use as a gate dielectric in complementary metal-oxide-semiconductor (CMOS) devices. However, pioneering work in the 1980s [DiMaria 1984] highlighted the possible use of a-$SiO_x$ in opto-electronic applications through the observation of electroluminescence. This newly observed property was attributed to small silicon nanoclusters embedded into the oxide matrix and later studies greatly enhanced the potential for future application not only for electroluminescence, but also for photovoltaic solar cells [Conibeer 2008][Khriachtchev 2012].

Shortly before the commencement of my project, Mehonic et al. [Mehonic 2012A] were studying previously observed electroluminescence behaviour in Er-doped a-$SiO_x$ at University College London (UCL) [Kenyon 1994]. This study aimed to develop a silicon-oxide based light-emitting diode (LED). However, by controlling the electrical bias applied across an Er-doped a-$SiO_x$ film in a metal-insulator metal (*MIM*) stack, it was found that device resistance could be altered between an initial high resistance state and a low resistance state. The device was capable of maintaining its resistance state when the electrical bias was removed. Similar behaviour had also been observed in different *MIM* stacks and has since developed into a highly anticipated research field looking to find an alternative type of non-volatile memory to current Flash memories. This is a result of increasing reliability problems associated with the continuous downscaling of Flash [Ielmini 2009]. The new approach makes use of high and low resistance states as a basis for memory storage and has been termed 'resistive random access memory' (ReRAM). Devices capable of outperforming current Flash memories in many areas such as programming speed, endurance, and scalability have already been found [Waser 2012] and appear to offer a promising alternative. However, if commercially viable, an a-$SiO_x$ insulating layer has a number of advantages over competing materials: a-$SiO_x$ is cheaply produced from an abundant resource, and easily integrated with existing silicon-based fabrication technology.

Additional studies were carried by Mehonic et al. in order to further understand the characteristics of such devices [Mehonic 2012A][Mehonic 2012B]. These studies suggest that the observed resistive switching behaviour is intrinsic to the a-SiO$_x$ insulating layer [Mehonic 2012A]. However, the mechanism by which resistive switching occurs in a-SiO$_x$-based ReRAM devices remains controversial. Previous studies have suggested the formation of a silicon-rich conductive path resulting from oxygen vacancy accumulation at some local site within the oxide layer. Proposed mechanisms include the aggregation of diffusing oxygen vacancies [Yao 2010][Mehonic 2012A] and the creation of additional vacancies [Yao 2010][Wang 2013] during electrical stressing. Defects within the devices have been proposed as either possible aggregation sites for migrating oxygen vacancies [Yao 2010][Mehonic 2012], or centers for additional vacancy production [Yao 2010][Yao 2012][Mehonic 2016][Gao 2016].

My project resulted from the need to further understand structural change in the a-SiO$_x$ layer during electrical stressing. An interdisciplinary collaboration was formed between experimental and theoretical research groups within UCL and the Agency for Science Technology and Research (A*STAR) in Singapore. In 2013, I was drawn to this project because it offered me the opportunity to gain an insight into theoretical and experimental materials characterisation methods in an international context. At UCL, funding provided by The Centre for Doctoral Training in Molecular Modelling and Materials Science (M3S CDT) allowed me to develop an understanding of materials modelling using density functional theory (DFT). In addition, during my time at A*STAR, the A*STAR Research Attachment Programme (ARAP) provided me with training for the use of transmission electron microscopy (TEM) for materials characterisation. In this thesis, I make use of both of these characterisation tools to gain a deeper insight into intrinsic resistive switching behaviour in a-SiO$_x$ and fulfil the following thesis objective:

**Thesis Objective**: For *MIM* stacks with a sputter-deposited a-SiO$_x$ insulating layer, what are the structural changes associated with resistive switching behaviour intrinsic to the a-SiO$_x$ layer, and how does the structure of the *MIM* stack affect device performance?

Following this introduction, chapter 3 is a literature review beginning with an overview of different types of ReRAM devices and then focusing on silicon oxide-based devices. Previous studies regarding the structure of a-SiO$_x$ are then discussed and suggest that

the sputtering fabrication of a-$SiO_x$ films used in this study could imply an approximately homogenous distribution of oxygen vacancies. This motivates a deeper discussion on the structure of a-$SiO_2$ and the nature of oxygen vacancies and oxygen transport in a-$SiO_2$.

Chapter 4 provides the reader with a background on TEM operation and the TEM characterisation tools available throughout the duration of this project. The fabrication of the *MIM* stacks to be studied is discussed together with its impact on their end stucture in chapter 5. The associated electrical characteristics of the *MIM* stacks are also briefly discussed. Scanning transmission electron microscopy (STEM) analysis suggests that sputter-deposition of a-$SiO_x$ onto a rougher electrode substrate promotes more desirable switching behaviour, and is consistent with enhanced columnar microstructure in the oxide layer. Although fabrication and electrical characterisation are not the principal objectives of this thesis, chapter 5 provides essential background and perspective for understanding the TEM studies in the following sections.

In chapter 6, STEM, electron energy-loss spectroscopy (EELS), and electron tomography analysis of electrically stressed *MIM* stacks reveals oxygen dynamics on an oxide-wide scale. Large-scale oxygen dynamics is shown to result in oxygen outmigration from the oxide layer and the resulting deformation of the electrodes. In addition, EELS data suggests the potential build-up and transport of oxygen along intercolumnar boundaries. A far thinner oxide layer is analysed in chapter 7 through the use of an aberration-corrected TEM and reveals undesirable electrode migration as a result of the high electric fields. This suggests a limit to device scaling.

In chapter 8, the basic concepts of DFT are introduced followed by an emphasis on the aspects of the method used in this thesis. These methods are used in chapter 9 to tackle the question of whether neutral oxygen vacancies may diffuse and aggregate to form a conductive path. Favourable sites for vacancy aggregation in a-$SiO_2$ are revealed by optimising the geometries of vacancies and vacancy dimers and trimers. However, barriers for vacancy migration calculated using the climbing-image nudged elastic band method (CI-NEB) are found to be too high for diffusion to occur under room temperature operating conditions. In addition, previously unreported trends between the structure of oxygen vacancies and the geometry at different sites in the pristine a-$SiO_2$ network are

revealed.

The effect of electron trapping at oxygen vacancies is studied in chapter 10. Under electrical stressing conditions, vacancies are shown to be capable of trapping up to two electrons, which enhances their mobility. However, the resulting barriers for diffusion suggest that charged vacancy diffusion would be inefficient as a result of the thermal ionisation of the trapped electrons. In addition, vacancies are found to compete with intrinsic electron traps present in a-$SiO_2$, suggesting a dependence on both types of trap in trap-assisted tunnelling, which has been shown to occur in the low resistance state [Mehonic 2012A][Mehonic 2012B]. The migration and aggregation of oxygen vacancies is ruled out as an effective mechanism for conductive path formation and an alternative mechanism is suggested. Finally, in chapter 11, this thesis is concluded and possible directions for future investigation are discussed.

The main new results of this thesis can be summarised as follows:

- In sputter-deposited silicon suboxides, oxide-wide structural reorganisation occurs during electrical stressing. This is a result of large-scale oxygen dynamics, which can result in oxygen outmigration from the oxide and electrode deformation. This is contrary to the relatively inert behaviour expected from insulating materials.

- The fabrication of sputter-deposited silicon suboxides greatly influences device performance. Firstly, growing the oxide layer on a rougher substrate surface promotes lower electroforming voltages and greater device endurance. This is consistent with enhanced columnar microstructure in the oxide, and EELS data indicates that inter-columnar boundaries could play an important role in oxygen transport. Secondly, thin oxide layers (< 5 nm) will lead to electrode migration into the oxide layer as a result of high electric fields. This will limit the thickness of the oxide layer needed for intrinsic switching behaviour.

- The formation of oxygen vacancy dimers and trimers is energetically favourable at some sites in amorphous silicon dioxide, with maximum binding energies of 0.13 eV and 0.18 eV, respectively. However, neutral oxygen vacancies are immobile under room temperature operating conditions and diffuse with a mean adiabatic barrier height of 4.6 eV.

- In amorphous silicon dioxide, single and double electron trapping is energetically feasible at oxygen vacancies at Fermi energies above 6.2 and 6.4 eV, respectively. This greatly improves vacancy mobility, with average adiabatic barrier heights of 2.7 eV and 2.0 eV, respectively. However, diffusion competes with thermal ionisation of the electrons into the conduction band. Oxygen vacancies also compete with intrinsic sites for electron trapping. This results in an inefficient diffusion process, which cannot explain the formation of a silicon-rich conductive path and suggests an alternative mechanism for oxygen vacancy accumulation.

# 3 Literature Review

## 3.1 Introduction

A large body of work has been published on resistive switching. This chapter will begin with an explanation of different types of ReRAM devices with references to examples from literature. This will be followed by a more comprehensive review of switching studies of amorphous silicon oxides, the subject of this thesis. Experimental evidence for the structure of a-$SiO_x$ will then be summarised, resulting in the motivation to theoretically study the behaviour of the oxygen vacancy in a-$SiO_2$. The next review section focuses on literature regarding the structure of a-$SiO_2$ and the characteristics of oxygen vacancies. Following this, electron trapping at oxygen vacancies is discussed since electrical stressing will result in electron injection into the oxide layer. This is followed by a section dedicated to oxygen migration in silicon oxides since this would be required for both the aggregation of oxygen vacancies and additional vacancy production. Finally, the accumulation of oxygen vacancies will lead to inter-vacancy interaction. Though no first principles studies have been carried out on this topic for silicon oxides, a number of crystalline materials have been studied. The final review section concentrates on these investigations. The reader is referred to chapters 4 and 8 for a description of TEM and DFT techniques.

## 3.2 ReRAM Types and Examples from Literature

### 3.2.1 Electrochemical Metallisation Memory (ECM)

An electrochemical metallisation memory (ECM) cell consists of active metal (*M'*) and inert metal (*M"*) electrodes with an insulating layer (*I*) between them [Waser 2012]. The insulating layer (*I*) must be capable of conducting cations from the active electrode. By applying a positive voltage to the active electrode, metal atoms at the boundary between *M'* and *I* become oxidised to form $M'^{n+}$ cations. The cations are then conducted through the insulator under the influence of the electric field and reduced back to *M'* atoms at

the boundary between *I* and *M”*. This results in the growth of a conductive filament of *M’* beginning at *M”* and eventually making contact with *M’* when the cell is in the low resistance ’set’ state. This coincides with a large and sudden decrease in resistance. The profile of the filament is expected to be conical, becoming thinner towards the direction of the active electrode. A current compliance is used during the set process to limit further changes as a result of Joule heating when contact is made. Figure 3.1 illustrates filament formation.

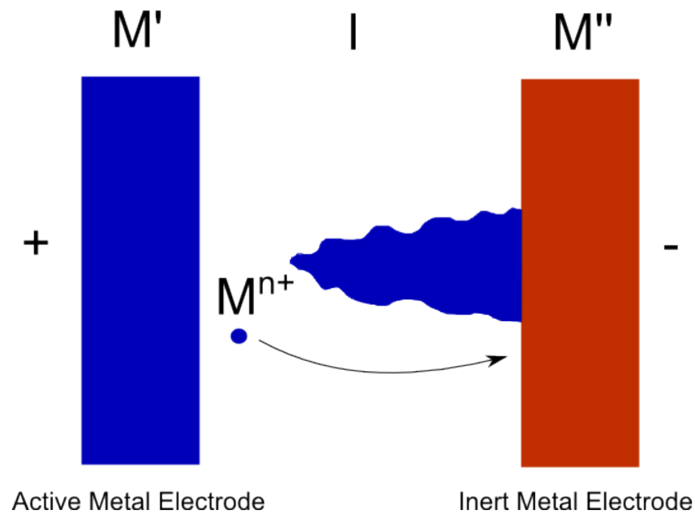


Figure 3.1: Conductive filament formation in an ECM cell. *M’* ions are oxidised at the active metal electrode and reduced at the inert metal electrode. This results in a conical filament growing thinner towards the active metal electrode.

A return to the high resistance ’reset’ state is achieved by applying a negative voltage to the active electrode. Since a positive voltage must be applied to set an ECM cell and a negative voltage is required to reset the cell, ECM cells are said to exhibit ’bipolar’ switching behaviour. Current compliance is removed during the reset process since Joule heating is believed to play an important role [Waser 2012]. Figure 3.2 illustrates the expected switching behaviour. In order to first set a cell, a higher initial voltage is required. This process is termed ’electroforming’. Because cations must travel through the insulating layer, it is been proposed that during electroforming, defects such as grain boundaries facilitate cation diffusion and the formation of the initial conductive filament. And since after electroforming lower voltages are required to set the cell, it is thought that during subsequent switching cycles only a small region of the filament is ruptured [Waser 2012].

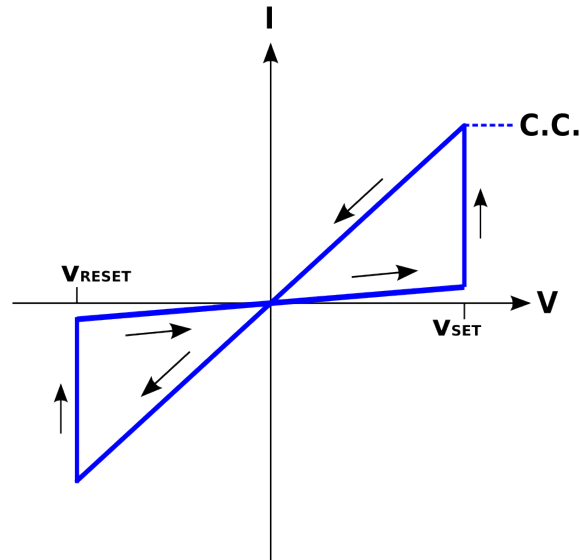


Figure 3.2: An illustration of the I-V curve for switching an ECM cell. A positive voltage with a current compliance (indicated by the dashed line) is applied to the active electrode for setting and a negative voltage is applied for resetting.

Xu et al. [Xu 2010] carried out *in situ* TEM switching experiments on a Ag/$AgS_2$/W structure, where the W electrode acted as the tip used for electrically stressing the device. A positive voltage was applied to the Ag electrode and in the set state a crystalline structure was observed to grow from the W electrode. Energy dispersive X-ray spectroscopy (EDX) and selected area diffraction (SAD) analysis revealed a greater ratio of Ag to S in the crystalline region and the existence of diffraction spots corresponding to the argentite phase ($Ag_2S$) and Ag. A model was proposed whereby $Ag^+$ ions migrate towards the W electrode where they are reduced, resulting in the formation of a mixed $Ag_2S$/Ag conductive filament. Similarly, Fujii et al. [Fujii 2011] carried out *in situ* switching studies on a Pt-Ir/Cu-GeS/Pt-Ir structure. One Pt-Ir tip was used as a substrate while the other was used to apply electrical stress. The growth of a crystalline region was again observed to begin at the negatively charged electrode with EDX and SAD revealing the presence of a conductive filament composed of Cu. The devices studied by Yang et al. [Yang 2012] consisted of Ag and Pt active and inert electrodes. Three insultating layers were studied: $SiO_2$, $Al_2O_3$, and amorphous silicon (a-Si). For $SiO_2$ and $Al_2O_3$, *ex situ* studies using SAD revealed the growth of an Ag conductive filament beginning at the inert electrode. However, the filament was thickest at the active electrode and thinnest at the inert electrode, exhibiting a 'dentritic' growth towards the active electrode. This behaviour was attributed to the low cation mobility of the insulating layers relative to the chalcogenide-based insu-

lating layers studied by Xu et al. and Fujii et al., and would result in the reduction of the $Ag^+$ ions preferably occuring at the end of the existing filament. In the a-Si device, the conductive filament was seen to grow beginning from the active electrode and this was confirmed by *in situ* studies. The authors suggested that an even lower cation mobility would allow electrons to tunnel across the insulating layer to reduce the $Ag^+$ ions nearby the Ag electrode.

### 3.2.2 Valence Change Memory (VCM)

A valence change memory (VCM) cell consists of an active electrode (*M'*) with ideally a low oxygen affinity, an ohmic electrode with ideally a high oxygen affinity (*M"*), and a mixed ionic-electronic conducting (MIEC) insulating layer (*I*) [Waser 2012]. Assuming an oxide-based insulating layer and electron conduction, the set state is obtained by applying a negative voltage to the active electrode. The formation of the resulting low resistance conductive path is a result of oxygen vacancy accumulation in the insulating layer driven by the electric field. $O^{2-}$ ions have been suggested to migrate towards the ohmic electrode, enhanced by its high oxygen affinity. The field driven migration of oxygen vacancies has also been suggested [Waser 2012]. A current compliance is again used during the set process to limit further changes as a result of Joule heating when the low resistance state is obtained. Figure 3.3 illustrates the set process using $O^{2-}$ ions.

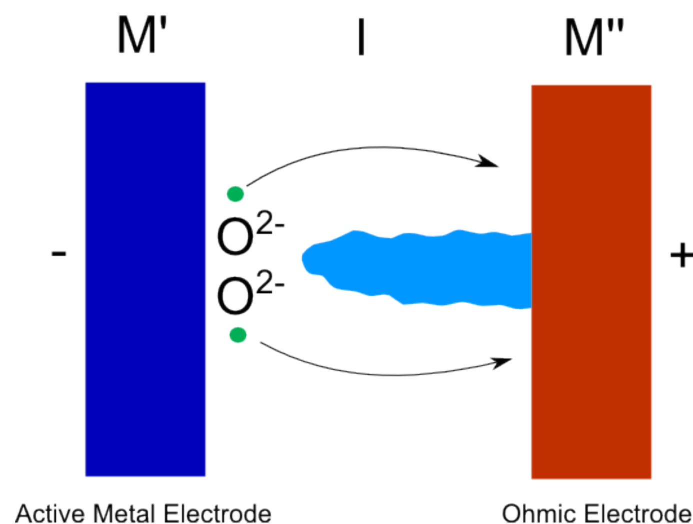


Figure 3.3: Conductive path formation in a VCM cell. Field driven oxygen vacancy formation leads to the formation of a conductive path.

To reset the cell, a positive voltage must be applied to the active electrode, causing a break in the conductive path. This is believed to lead to the field-driven return of oxygen to the active electrode end of the path, enhanced by the low oxygen affinity of the active electrode. As a result, VCM cells also exhibit bipolar switching behaviour. Figure 3.4 illustrates the switching process.

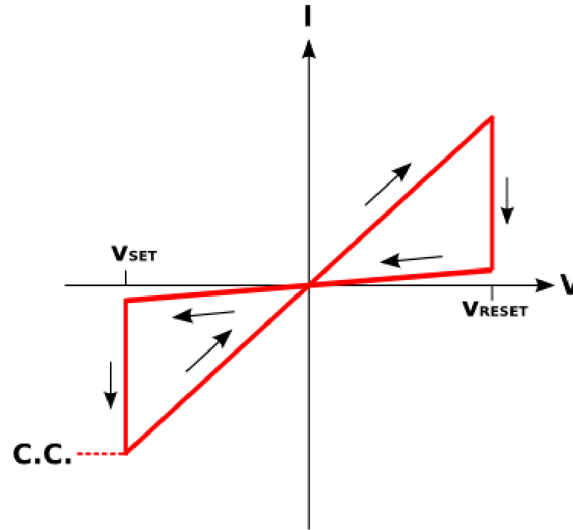


Figure 3.4: An illustration of the I-V curve for switching a VCM cell. A negative voltage is applied to the active electrode for setting and a positive voltage for resetting.

Lee et al. first reported a device exhibiting endurances of over $10^{12}$ cycles [Lee 2011]. Later *in situ* TEM studies were carried out by Park et al. on a slightly modified version of the device [Park 2013]. The insulating layer consisted of three different oxide layers with Pt active and ohmic electrodes. An a-$SiO_2$ layer was placed in contact with the active electrode followed by an amorphous $Ta_2O_{5-x}$/$TaO_{2-x}$ bi-layer. After electroforming *in situ*, high-angle annular dark field (HAADF) images were taken of a filament-like structure observed in the a-$SiO_2$ layer. This showed the apparent presence of tantalum oxide clusters in the layer, which were assumed to originate from the electroforming process. After several switching cycles, electron energy-loss spectra (EELS) in the a-$SiO_2$ layer revealed a lower oxygen concentration during the set state, indicating conduction through metallic phases of Ta. Depth profiling using Auger electron spectroscopy (AES) showed that the lower region of the $TaO_{2-x}$ layer had an increased oxygen content in the set state and this was confirmed using EDX. The authors proposed that the formation of oxygen vacancies in the upper part of the $TaO_{2-x}$ layer would cause the diffusion of the vacancies into the $Ta_2O_{5-x}$ layer, eventually resulting in a complete conductive bridge

across the cell. The importance of oxygen vacancies was also observed during *in situ* studies by Yang et al. [Yang 2014A] in a device consisting of a titanate-based insulating bi-layer and Pt and Ag electrodes. A notable variation in the EELS *O-K* edge during switching at the Pt interface revealed changes in local stoichiometry. Jeong et al. studied electroforming in a Pt/$TiO_2$/Pt device [Jeong 2008]. Compositional analysis using time of flight secondary ion mass spectroscopy (ToF-SIMS) revealed the presence of areas of enhanced oxygen concentration not present in an unstressed device. Depth profiles revealed that on electroforming, oxygen had migrated into the electrodes. In addition, through the use of atomic force microscopy (AFM), deformation on the surface of the $TiO_2$ was measured on the application of a negative voltage at the AFM tip, with conductivity increasing at the deformed region. It was suggested that this is caused by oxygen gas migrating towards the electrode.

### 3.2.3 Thermochemical Memory (TCM)

In a thermochemical memory (TCM) cell, the switching process is thought to be similar to that of a VCM with thermal effects as well as the electric field playing an important role in the switching process. Such devices exhibit unipolar behaviour: the set and reset states are achieved using the same voltage polarity. A set voltage is applied with a current compliance, and a reset voltage of the same polarity is then applied with the current compliance removed, leading to a thermally driven reset. Figure 3.5 illustrates the switching process.

*In situ* switching experiments were carried out by Chen et al. on a Pt/ZnO/Pt structure [Chen 2013]. TEM imaging revealed conductive filament growth beginning from the anode and exhibiting a 'dendritic' growth towards the cathode, with a corresponding resistance decrease on connection with the cathode. This type of growth was attributed to the presence of a stronger electric field between the growing filament's tip and the positively biased electrode. SAD revealed the structure of metallic Zn present in the filament with EELS scans indicating a higher oxygen concentration near the anode in the set state. In another study, Celano et al. [Celano 2015] used a diamond conductive atomic force microscopy (c-AFM) tip to act as a scalpel on an electrically stressed sample of

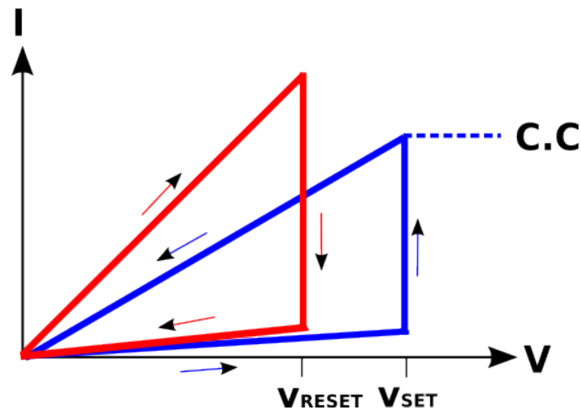


Figure 3.5: An illustration of the I-V curve for switching a TCM cell. A positive voltage with a current compliance (indicated by the dashed line) is applied to the active electrode for setting and a positive voltage without current compliance is applied for resetting.

non-stoichiometric hafnium oxide ($HfO_x$). Though a destructive technique, this allowed the use of three-dimensional tomography mapping of a conductive filament. The filament was found to be conical in shape with a width between 10-40 $nm^2$. A study by Russo et al. [Russo 2007] focused on the nature of the thermally driven reset in Au/NiO/Si structures. By measuring the I-V characteristics of a device in the set state, and assuming a cylindrical conductive filament, a critical temperature of ≈550 K was inferred at the moment of reset. An electro-thermal model was used to model the evolution of the conductive filament. The filament diameter was observed to decrease most rapidly at the hottest region in the filament and would in turn lead to current constriction causing self-enhanced filament rupture.

## 3.3 Resistive Switching in Amorphous Silicon Oxides

### 3.3.1 Amorphous Silicon Dioxide

Resistive switching-like behaviour was first reported for silicon oxides as far back as the late 1960s [Lamb 1967]. The mention of switching as a memory storage application are more recent. For example, Schindler et al. [Schindler 2007] reported a device consisting of Cu and W top and bottom electrodes and a Cu-doped a-$SiO_2$ insulating layer. SEM images of set devices revealed what appeared to be the increased presence of Cu in the insulating layer in the set state. Based on this finding, the authors proposed the field

driven migration of Cu ions into and out of the insulating layer as a switching mechanism. An atomistic descripition of this ECM-like behaviour was provided in a study by Onfrio et al. [Onfrio 2015] in which ab-initio molecular dynamics was used to model switching at an atomistic level in a Cu/$SiO_2$/Cu cell. After electroforming, it was found that Cu atoms at the positively charged active electrode become oxidised and dissolve into the a-$SiO_2$ layer. During the electroforming process, metastable, single-atom conductive bridges were observed to be constantly forming and breaking. The true stable filament was found to be larger and formed from aggregates of Cu ions being reduced at the inert electrode. These aggregates were seen to form 50 per cent of the time when Cu atoms dissolved into the insulating layer. On the other hand, resistive switching based on oxygen vacancy accumulation has not been reported for amorphous silicon dioxide. However, vacancy accumulation is believed to be responsible for long-term dielectric breakdown leading to device failure. The origin of this process was explored by Li et al. [Li 2008]. A protrusion of silicon into the oxide layer termed a 'dielectric breakdown-induced epitaxy' (DBIE) was observed at the breakdown site [Pey 2002]. EELS scans carried out above the DBIE revealed signs of a decrease in the number of Si-$O_4$ sites at the *Si*-$L_{2,3}$ edge. This was complemented by a decrease in intensity and lowering of onset of the *O-K* Edge. The physical process responsible for these observations may share a similar mechanism with the resistive switching observed in a-$SiO_x$.

### 3.3.2 Amorphous Silicon Suboxide

The observation of resistive switching in a silicon-rich silica (a-$SiO_x$) layer has been reported by Yao et al. [Yao 2010], Mehonic et al. [Mehonic 2012A], Chang et al. [Chang 2012], Wang et al. [Wang 2013], and Wang et al. [Wang 2014], where the devices used by Mehonic et al. [Mehonic 2012A] are the subject of further study in this thesis. In the first four cases, the switching is concluded to be intrinsic to the oxide layer, while in the final case, nanoporous a-$SiO_x$ is used with ion migration from the positively biased electrode thought to play a role during the electroforming process. In the case of Yao et al. [Yao 2010], similar switching properties were measured for different electrode materials. In addition to confirming this, Mehonic et al. measured semiconductor-like resistance-temperature behaviour in the set state. Furthermore, Mehonic et al. and Chang et al.

[Chang 2012] reported that switching behaviour appeared to be independent of electrical contact size, suggesting the formation of a single conductive path. High-resolution TEM (HRTEM) imaging by Yao et al. [Yao 2010] revealed the presence of small crystalline nanoclusters aligned parallel to the direction of current flow, with lattice spacing matching that of silicon. This lead the authors to conclude that either oxygen vacancy aggregation or additional vacancy production during switching results in a conductive path formed from silicon nanoclusters. Later *in situ* switching studies [Yao 2012] revealed that after electroforming, nanoclusters approximately 3 nm in diameter appeared to form a conductive path. These clusters were observed to shrink in the reset state. Mehonic et al. carried out atomic force microscopy (AFM) and scanning tunnelling microscopy on the surface of the a-SiO$_x$ layer. This revealed dome-like features on the surface with a high conductivity at their edges. Since the a-SiO$_x$ was formed using sputtering, it was suggested that the structure of the layer may be columnar [Thornton 1986][McCann 2011], and that these structures could potentially act as nuclei for oxygen vacancy aggregation. Furthermore, by recording current-field characteristics through impedance spectroscopy for partial-set and set states, current was shown to best fit to a trap-assisted tunnelling model in the low resistance state. In contrast to Yao et al. and Mehonic et al., Wang et al. [Wang 2013] proposed a percolation model whereby field driven effects would lead to the breaking of Si-O bonds, leaving a path of Si dangling bonds along which electron conduction could occur. This was due to much lower programming voltages than those observed by Yao et al. and Mehonic et al. Additionally, Wang et al. observed a change in surface structure of the top Pt electrode when a positive voltage was applied. This was attributed to the release of oxygen gas from the a-SiO$_x$ towards the Pt layer through S-O bond breaking. A similar process had been observed in a Pt/TiO$_2$/Pt device [Jeong 2013]. The devices reported by Yao et al and Chang et al. only functioned under vacuum conditons, while the other two devices functioned at room temperature and pressure, with Wang et al. reporting poor performance in a vacuum. Furthermore, the devices reported by Mehonic et al. were capable of exhibiting bipolar switching behaviour, whereas only unipolar switching behaviour was reported for the remaining devices. It therefore appears that all four devices, although exhibiting switching intrinsic to the a-SiO$_x$ layer, may exhibit slightly different switching mechanisms. This may have been a product of fabrication conditions. The device used by Yao et al. made use of an a-SiO$_x$ layer formed by thermal oxidation resulting in an $x$ value of between 1.9 and 2. In contrast, Mehonic et al. used

the sputtering method (see chapter 5), resulting in a final $x$ value ≈1.3 and Wang et al. used plasma-enhanced chemical vapour deposition (PECVD) to obtain a final $x$ value of ≈0.73. The oxide layers prepared by Chang et al. were also sputter-deposited. Although no values for stoichiometry were reported by Chang et al., the presented switching data suggested that devices with a greater oxygen content exhibited more reliable switching behaviour. Furthermore, devices with increasingly thin oxide layers were found to be less reliable.

## 3.4 The Structure of Silicon Suboxides and the Existence of Oxygen Vacancy Defects

The structure of silicon suboxides is not clearly defined. Although a number of studies have been carried out, experimental evidence has most commonly been interpreted to support two different structural models: the 'random mixture' [Brady 1954] and 'random bonding' [Philipp 1972] models (RMM and RBM). The random mixture model proposes regions of pure Si and $SiO_2$, separated by small interfacial boundaries. In contrast, the random bonding model suggests a continuous random network of tetrahedral units of $SiSi_4$, $SiSi_3O$, $SiSi_2O_2$, $SiSiO_3$, and $SiO_4$, where Si is the centre of the unit in each case. These units are illustrated in Figure 3.6. Fewer studies have suggested alternative models, such as a S-O ring structure suggested by Yasaitis et al. [Yasaitis 1972], or the 'interface clusters model' suggested by Hohl et al. [Hohl 2003], which proposes that a significant number of atomic sites are situated in interfacial regions between sub-nm Si and $SiO_2$ inclusions. This model can be viewed as an intermediate model between the RBM and RMM, with the interfacial regions having a structure similar to the RBM, and the Si and $SiO_2$ inclusions resembling the RMM.

A number of different experimental methods have been used in order to characterise silicon suboxide samples, which have themselves been prepared using various techniques. The earliest attempts to characterise the structure of silicon suboxides made use of radial distribution functions (RDF) obtained from the analysis of diffraction patterns. The RDF gives the probability of finding a particle B at a specific distance from a reference particle A. Thus the RDF obtained for a sample of silicon suboxide can be compared to reference

distributions from Si and $SiO_2$ for structural analysis. Brady et al. [Brady 1959] used X-ray diffraction to obtain RDFs for commercially produced SiO, which is typically produced by heating mixtures of Si and $SiO_2$ [Temkin 1975]. The resulting analysis concluded with a match for the RMM. This was consistent with additional X-ray diffraction analysis of RDFs performed by Temkin et al. [Temkin 1975]. Coleman et al. [Coleman 1967] used electron diffraction to obtain RDFs of oxide films prepared using the glow discharge and evaporation techniques and also suggested a RMM film structure. However, Philipp et al. [Philipp 1972] proposed the RBM structure on the basis of optical reflectance and absorption spectra. This study also accounted for $SiO_{1.5}$ samples in addition to SiO. Later methods for structural characterisation made increasing use of spectroscopic fingerprints to identify different bonding environments across a range of stoichiometries. For example, Johanessen et al. carried out Auger electron spectroscopy (AES) analysis and suggested a RMM structure for evaporated oxide films [Johanessen 1975]. In addition, a later study by Forty et al. [Forty 1986] made use of X-ray photoelectron spectroscopy (XPS) and X-ray absorption spectroscopy (XAS) analysis and again reported a good fit to the RMM for samples fabricated using the electron beam evaporation technique. In contrast, Greaves et al. [Greaves 1986] used XAS analysis on oxide films produced using the glow discharge technique and favoured the RBM. More recently, a study of commercially produced SiO by Schulmeister et al. [Schulmeister 2003] used EELS fingerprints combined with energy filtered imaging and concluded with a RMM structure. In comparison, for sputtered SiO films, measurement by Sasaki et al. [Sasaki 2013] suggested a RBM structure using evidence from infrared absorption and Raman spectra. This is supported by evidence for random bonding in sputtered films provided by Zhang et al. [Zhang 2010] using a combination of Raman and XPS spectroscopy. However, Zhang et al. noted a degree of inhomogenity within the samples, with a greater likelihood of larger Si inclusions with decreasing oxygen content.

These studies suggest structural differences in oxide films prepared using the commercial, evaporation, glow discharge, and sputtering techniques. It should also be noted that use of annealing after fabrication has also been shown to result in structural reorganisation and the formation of Si nanoclusters with a resulting structure akin to the RMM [Hohl 2003][Yurtsever 2006]. This may partly explain why heating-based methods used to produce oxide films by evaporation and commercial oxides consistently favour

the RMM. For the glow discharge and sputtering methods, these studies also suggest that specific deposition conditions may play an additional role as indicated by the varying conclusions reached by Coleman et al. [Coleman 1967] and Greaves et al. [Greaves 1986], and Sasaki et al. [Sasaki 2013] and Zhang et al. [Zhang 2010]. Since the devices to be studied further were fabricated using the sputtering technique [Mehonic 2012A], this could suggest a structure more consistent with the RBM [Zhang 2010][Sasaki 2013]. Further evidence for this is provided by the TEM studies in chapter 6. For the a-SiO$_x$ layers studied in this investigation, $x \gtrapprox$1.3 (see chapter 5). This implies a network rich in oxygen vacancy defects with an approximately homogenous distribution. However, direct evidence for the structure of such defects is difficult to obtain due to the length scales involved. As a result, computational methods have been used extensively in order to characterise the nature of oxygen vacancies.

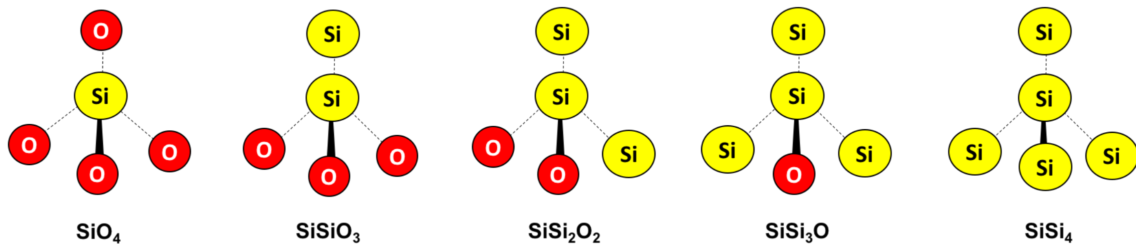


Figure 3.6: Tetrahedral units making up the continuous random network associated with the random bonding model of a-SiO$_x$.

## 3.5 The Structure of Amorphous Silica and Oxygen Vacancies

Theoretical studies on oxygen vacancy defects concentrate on a-SiO$_2$. These studies are likely to give an indication of the behaviour of vacancies in the sputtered a-SiO$_x$ used in this thesis since it can be treated as vacancy-rich a-SiO$_2$ in the context of the RBM. Zachariesen [Zachariesen 1932] first proposed a structure for a-SiO$_2$ glass consisting of a continuous random network (CRN) of SiO$_4$ tetrahedra. Later studies used X-ray diffraction experiments to obtain radial distribution functions (RDF), which provided strong evidence for this model [Mozzi 1969][Warren 1992]. Mozzi et al. obtained a distribution of nearest neighbour Si-O bond lengths in a-SiO$_2$ centered around an average

of 1.62 Å. This can be compared to a value of 1.61 Å in crystalline $\alpha$-quartz [Wyckoff 1963]. In addition, the Si-O-Si angle in a-$SiO_2$ was found to be distributed around 109$^\circ$, the same value as in $\alpha$-quartz [Wyckoff 1963].

The consistency in average bond lengths and angles represents a short-range order in amorphous materials. Examining the structure of a CRN of amorphous silica on a multi-tetrahedral scale leads to the postulated existence of ring structures, which represent a medium-range order. The King's criterion [King 1967] defines rings in terms of nodes and nearest neigbours. In the case of $SiO_2$, Si atoms are selected as nodes, and two of their neighbouring O atoms are defined as nearest neighbours. A ring is then defined as the shortest path along the CRN between the two nearest neigbour O atoms of the Si node. A shortest path containing $N_{mr}$ Si nodes defines an $N_{mr}$-member ring. Models of a-$SiO_2$ have reported rings containing as low as 2 and as many as 10 Si nodes [Rino 1993][Vollmayr 1996]. Crystalline compounds do not exhibit a distribution in ring sizes, and smaller rings with 3 and 4 nodes in particular are believed to result in unique properties observed in a-$SiO_2$. Calculations on 3- and 4-member rings in a-$SiO_2$ have yielded relatively high strain energies [Uchino 2000][Hamann 1997]. This has in turn has been used to explain the optical absorption at 7.9 eV in the vacuum ultraviolet region [Hosono 2001] and two sharp features in the Raman spectrum of a-$SiO_2$ at 495 and 606 cm$^{-1}$ [Pasquarello 1998]. More recently, ring structures have been atomically resolved in 2-dimensional sheets of a-$SiO_2$ using STEM [Huang 2012]. In this study a range of ring sizes were observed from 3-member rings to 10-member rings; however, the distribution of rings was not in agreement with theoretical predictions. This highlights one key difference between experiment and theoretical models.

In order to study the behaviour of oxygen vacancies, computational methods are required which can accurately simulate the structure of a-$SiO_2$. A popular approach used for the DFT simulations in this thesis [El-Sayed 2015A] involves the use of classical molecular dynamics to melt and rapidly quench a sample of crystalline silica [Sarnthein 1995][Vollmayr 1996][Donaldio 2001][Tamura 2004][Anderson 2011][El-Sayed 2015A]. RDFs, angular distributions, and densities are then obtained for these simulated samples and have been shown to adequately reproduce experimental measurements. In order to directly characterise the structure of the oxygen vacancy in a-$SiO_2$, first principles cal-

culations have been used extensively through the use of the embedded cluster method using Hartree-Fock calculations [Mukhodpadhyay 2004][Mukhopadhyay 2005][Sushko 2005] and density functional theory calculations with LDA [Martin-Samos 2004] and hybrid functionals [El-Sayed 2015A]. In all cases, upon network relaxation after the removal of an O atom, Si-Si bonds form at the vacancy site with corresponding bond length distributions ranging from 2.2 to 2.8 Å. For reference, a value of 2.36 Å has been reported for $\alpha$-quartz by Sulimov et al. [Sulimov 2002]. The effect of network relaxation upon the oxygen deficient structure shows a relatively long-range shift in geometry up to 10 Å from the defect site [Mukhopadhyay 2005]. Using the HF method, the formation of the vacancy has been found to introduce a doubly occupied deep defect state in the band gap distributed over a range of approximately 1.5 eV and peaked around 2 eV from the valence band maximum [Mukhopadhyay 2005]. This can be compared with the PBE0-TC-LRC hybrid functional [Guidon 2009], where the band gap state is distributed over approximately 1.0 eV around an average of 0.81 eV from valence band maximum (VBM) [El-Sayed 2015A]. Similarly, distributions in formation energies vary between studies as a result of differences in calculation methods. For example, Mukhopadhyay et al. reported values peaked between 4.2 and 4.4 eV [Mukhopadhyay 2005], which can be compared to a mean of 5.4 eV calculated by Martin-Samos et al. Differences within the HF and DFT implementations of the calculations could play an important role in determining these differences. Also, the embedded cluster method allows the full accomodation of network relaxation when compared to the constrained cell used by Martin-Samos et al. [Mukhodpadhyay 2004]. As an additional comparison, Anderson et al. [Anderson 2011] produced O vacancies prior to initiating a melt and quench procedure and reported a mean formation energy of 4.4 eV. Conversely, in other studies oxygen atoms have been removed from a pristine cell after melting and quenching. Anderson et al. noted that this alternative method for producing vacancies more favourably accounts for network relaxation. Local atomic-level stress fluctuations have been used to explain the range of formation energy values by Martin-Samos et al. [Martin-Samos 2004]. For comparison to experiment, optical absorption spectra were calculated by Mukhopadhyay et al. [Mukhopadhyay 2005] and peaked at a value of 8.5 eV. Mukhopadhyay et al. noted a dependence of the calculated values on Si-Si bond length, with longer Si-Si bonds corresponding to lower energy absorptions. It was suggested that the discrepancy between the peak absorption value and experimental measurements may be a result of sample

preparation affecting the distribution of Si-Si bonds.

It is generally accepted that the optical absorption band at 7.6 eV referred to as ODC(I) (ODC=oxygen deficient centre) is associated with an Si-Si bond or 'relaxed' oxygen vacancy structure [Pacchioni 1997][Skuja 1998]. A more controversial assignment is the photoluminescence band in the range 4.3-4.4 eV referred to as ODC(II), with evidence provided for an oxygen vacancy model and a 2-coordinated silicon model [Skuja 1998]. In addition, cathodoluminescence studies have associated the Si-Si bond with the blue cathodoluminescence band in the range 2-2.4 eV. Positively charged oxygen vacancies will not be discussed in detail in this literature review; however, it is worth mentioning that the electron paramagnetic resonance signals referred to as the E'$_1$ centre (in $\alpha$-quartz) and the E'$_\gamma$ centre (in a-$SiO_2$) are widely accepted to be associated with positively charged oxygen vacancies [Pantelides 2008]. Calculations of EPR parameters of the 'puckered' configuration for the positively charged oxygen vacancy proposed by Rudra et al. in 1987 showed excellent agreement with experimental measurements for the E'$_1$ centre [Rudra 1987]. This was later supported by calculations carried out by Boero et al. [Boero 1997], which also suggested the puckered configuration as a model for the E'$_\gamma$ centre.

## 3.6 Electron Trapping at Oxygen Vacancies and Intrinsic Sites in Amorphous Silica

In the context of ReRAM, electrically stressing an *MIM* stack facilitates electron injection into the oxide layer. Many prior studies have suggested electron injection as an important mechanism contributing to dielectric breakdown [DiMaria 1989][DiMaria 1993][Dumin 1995][Degraeve 1999][Bersuker 2008]. For an Si electrode, hot electron injection has been suggested to generate electron-hole pairs through impact ionisation [DiMaria 1993], or release hydrogen molecules at the oxide-anode interface, which can form electron traps at the cathode [DiMaria 1989]. In contrast, for metallic electrodes, Bersuker et al. proposed that electron trapping at oxygen vacancies contributes to additional trap generation [Bersuker 2008]. Kimmel et al. explored the injection of an electron into cells with four different oxygen vacancy configurations in a-$SiO_2$ using a DFT implementation

of the embedded cluster method with the B3LYP hybrid functional [Becke 1993]. This resulted in localisation at an antibonding orbital situated between the two silicon atoms at the vacancy site. The corresponding molecular orbital is shown in Figure 3.7(Left). Before electron injection, four unoccupied states were reported to be located between 0.5 and 1.6 eV from the CBM. On relaxation of the system after the introduction of a single electron, the occupied states were distributed between 2.0 and 3.3 eV below the CBM. This coincided with the increase of Si-Si bond length by approximately 0.2 Å. A more recent investigation using the PBE0-TC LRC hybrid functional [El-Sayed 2015A] noted similar changes, with the newly occupied defect level positioned between 1.8 to 3.5 eV below the CBM.

In addition, El-Sayed also identified intrinsic electron-trapping sites in non-defective a-$SiO_2$ located 3.2 eV below the CBM on average, with a narrow distribution of 0.1 eV [El-Sayed 2013][El-Sayed 2014]. The electron was observed to localise on precursor Si-O-Si angles above approximately 132$^\circ$ with the corresponding molecular orbital shown in Figure 3.7. The concentration of these traps was estimated to be $\approx 10^{19}$ cm$^{-3}$. Due to a high predicted concentration, intrinsic traps were correlated with trap states associated with the SiC/$SiO_2$ interface [Pintilie 2010]. The interface trap states were measured to be located $\approx$ 2.8 eV below the a-$SiO_2$ CBM by Afanas'ev et al. [Afanas'ev 1997] through the use of photon-stimulated electron tunnelling (PST). Furthermore, later calculations of optical absoption spectra associated with intrinsic electron traps were consistent with an experimental absorption peak at 3.7 eV [El-Sayed 2015B]. For the silicon-rich oxides used in this study, there will also be an appreciable concentration of oxygen vacancies. An overlap in the distributions of oxygen vacancy traps and intrinsic electron traps may indicate competition for electrons injected into the system.

## 3.7 Oxygen Migration in Silicon Oxides

A number of experimental and theoretical studies have been carried out on the mechanism by which oxygen is likely to migrate through $SiO_2$. Studies focus on three possible mechanisms: (i)$O_2$ molecule diffusion; (ii)the diffusion of oxygen vacancies through the

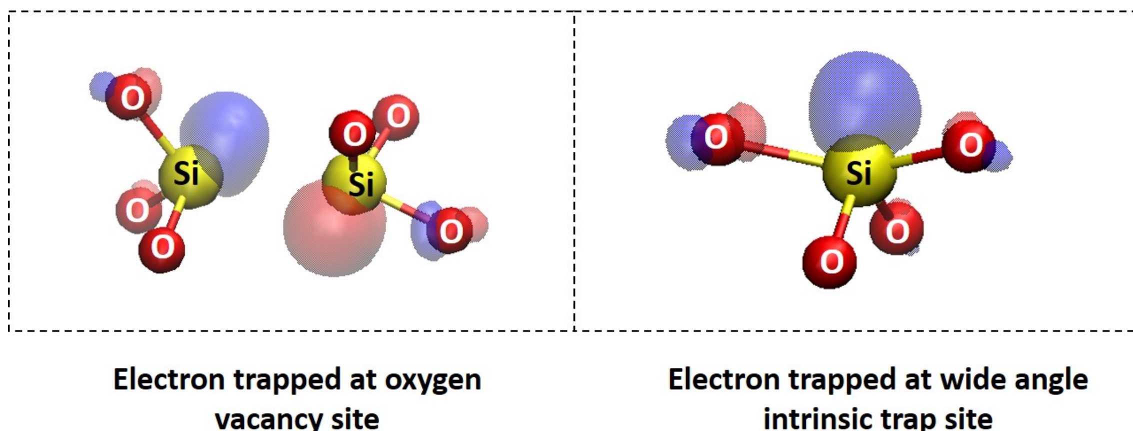


Figure 3.7: Molecular orbitals of electron traps in amorphous silica. Positive and negative isosurfaces are shown in blue and red respectively.

$SiO_2$ network; and (iii)the migration of oxygen atoms which are incorporated into the $SiO_2$ network. Experimental studies consist of permeation experiments for mechanism (i) and the tracking of isotopes of oxygen for mechanisms (ii) and (iii) to calculate activation energies for diffusion as defined in Arrhenius' equation (see section 8.6). Relatively fewer studies on crystalline $SiO_2$ have been carried out, with measurements relating to mechanism (iii) yielding activation energies of 2.0 eV and 2.4 eV for $\alpha$-quartz [Lamkin 1992]. In contrast, a number of investigations have been conducted to determine the nature of oxygen migration in a-$SiO_2$. Studies on mechanism (i) have resulted in activation energies ranging from 1.2 eV to 1.4 eV, while those for (ii) yielded 4.7 eV. Finally, for mechanism (iii), energies ranging from 0.9 eV to 1.3 eV were obtained [Lamkin 1992]. The similarity between (i) and (iii) may indicate related mechanisms. There is no clear experimental evidence of mechanism (iii) being a definite and distinct possibility to (i).

A number of theoretical investigations into mechanism (i) in $SiO_2$ have focused on crystalline $SiO_2$. In all cases triplet $O_2$ is favoured as the diffusive species. By considering a possible diffusion pathway, Orellana et al. [Orellana 2001] obtained a barrier for diffusion of approximately 0.6 eV using the PBE functional [Perdew 1996]. Further investigation using PBE by Akiyama et al. [Akiyama 2005] suggested an even lower diffusion barrier of approximately 0.2 eV. A study of a-$SiO_2$ using the generalized gradient approximation (GGA) was carried out by Bakos et al. [Bakos 2002] and assumed the diffusion of triplet state $O_2$. Barriers for diffusion between 0.6 eV and 1.5 eV were calculated in good agreement with experiment. These values were consistent with second study using the PW91

functional [Perdew 1992] carried out by Bongiorno et al. [Bongiorno 2002], where an average barrier for diffusion of 1.1 eV was obtained. Modlin et al. [Modlin 1985] studied the effect of an electric field upon the oxidation of Si and concluded with no correlation between reversing field polarity and oxidation rate. Energetic arguments were also referred to which were later confirmed through DFT calculations carried out by Stoneham et al. [Stoneham 2001]. In this second study, interstitial calculations using the PW91 functional were carried out for neutral and negatively charged O atoms and molecules. It was found that neutral molecular $O_2$ is the most energetically stable as an interstitial. Song et al. [Song 2001] concentrated on mechanism (ii) in $\alpha$-quartz. Vacancy diffusion barriers were calculated using PW91 [Perdew 1991] and yielded a barrier height of 4.1 eV for a neutral oxygen vacancy, which is consistent with experiments [Lamkin 1992]. This was reduced to 1.8 eV for a positively charged vacancy and 1.7 eV for an excited neutral vacancy in the triplet state. No such studies have been carried out for a-$SiO_2$.

DFT calculations on $\alpha$-quartz were carried out by Hamann [Hamann 1998] using the PBE functional and focused on mechanism (iii). The migration of O via peroxy linkages in the bonding network yielded a barrier height of 1.3 eV. A separate study was conducted by Hoshino et al. [Hoshino 2003] on $\alpha$-quartz and $\beta$-cristobalite using the more favourable B3LYP hybrid functional. Calculations on peroxy linkages similar to those conducted by Hamann [Hamann 1998] produced an identical result of 1.3 eV for $\beta$-cristobalite and 1.6 eV for $\alpha$-quartz. Jin et al. [Jin 2001] performed calculations on $\alpha$-quartz using the PBE functional. In addition to confirming the peroxy linkage as the most stable configuration for a single O atom interstitial, the effects of additional positive and negative charges were considered. In the +1 and +2 charge states, the peroxy linkage was again shown to be the most stable. However, in the -1 and -2 charge states the oxygen double bridge configuration was revealed to be more stable. Geometrically this structure resembled a 2-member ring consisting of two Si atoms bridged by two O atoms as illustrated in Figure 3.8. The double bridge configuration was found to diffuse with a barrier height of 0.11 eV to 0.27 eV. A later investigation by Mehonic et al. [Mehonic 2016] used the PBE0-TC-LRC hybrid functional to confirm the presence of the oxygen double bridge in a-$SiO_2$ as a stable structure, with a charge of -2 and a barrier for diffusion of approximately 0.20 eV. It was proposed that electron injection from the electrodes during electrical stressing may allow the generation of such states. Since the present study is also concerned with

the effects of electrical stressing, the diffusion of oxygen as a double bridge interstitial is the most energetically feasible of the studied processes in a-$SiO_2$.

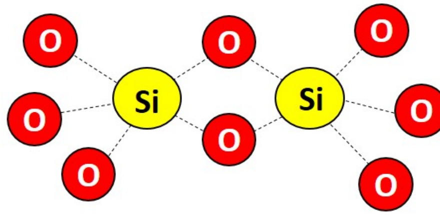


Figure 3.8: Illustration of an oxygen double bridge interstitial in a-$SiO_2$. Using 2 additional electrons, an O atom can form an additional bond between two Si atoms.

## 3.8 Examples of Theoretical Studies on Vacancy Interaction

Many studies on vacancy interaction consider the thermodynamics of vacancy accumulation. Magyare-Kope et al. [Magyari-Köpe 2012] used first principles calculations to study the effect of ordering oxygen vacancies in $TiO_2$ and NiO, with an application in resistive switching devices. In a $TiO_2$ supercell, it was found that 8 ordered vacancies repeated periodically along the [001] direction yielded the most energetically favourable arrangement for a conductive path. Oxygen atoms were then sequentially replaced from adjacent sites into the vacancies, with the authors concluding that two atoms were enough to result in the reset state. Similar conclusions were drawn for a NiO supercell. Furthermore, directional and site-dependent oxygen vacancy clustering has also been predicted theoretically in $SrTiO_3$ [Cuong 2007] and $BaZrO_3$ [Alay-e-Abbas 2016]. An additional study by Grau-Crespo et al. [Grau-Crespo 2009] also accounted for statistical considerations. This study explored the likelihood of hydrogen vacancy aggregation in $MgH_2$, a material often used as a hydrogen storage material. The storage mechanism results from a phase change between the ionically bonded $MgH_2$ crystal, and metallic Mg with $H_2$ interstitials. The latter phase resulted in hydrogen vacancies. Grau-Crespo et al. [Grau-Crespo 2009] modelled monovacancies, di-vacancies, and tri-vacancies using a grand canonical ensemble ($\mu$VT), with a $MgH_2$ solid in equilibrium with $H_2$ gas. The use of the grand canonical ensemble was attributed to the need for a feasible cell size in the limit of small vacancy concentrations. Probabilities of separated and clustered vacancies (up to and including tri-vacancies) were calculated under varying environmental conditions.

It was found that under conditions of practical interest for $H_2$ storage, the small concentration of vacancies suppressed aggregation. This contrasted with first principles calculations, which indicated that vacancy clusters are in fact energetically favourable when compared with separated monovacancies. In this case, energetics were outweighed by statistical probability. Ganduglia-Pirovano et al. [Ganduglia-Pirovano 2015] performed first principles calculations on surface and sub-surface oxygen vacancy pairs for $CeO_2$ and $VO_3$ structures, also accounting for statistical probability. O vacancy pairs for $CeO_2$ were shown to be consistently repulsive, with the formation energy per vacancy increasing when vacancies were brought together. This agreed with STM measurements in which vacancies were not observed to aggregate. In contrast, for $VO_3$ it was found that aggregation is favoured at high enough vacancy concentrations but is direction-specific. This was again confirmed by STM imaging.

Several studies have also considered the kinetics of vacancy aggregation. Kuzovkov et al. [Kuzovkov 2001] proposed a semiempirical model for oxygen vacancies in crystalline MgO. The aim of the study was to develop a model for experimentally observed nanocavities within the material, which are thought to be formed from oxygen vacancy aggregation. Such cavities had only been observed after approximately 10 minutes for vacancy concentrations of higher than approximately $10^{18}$ $cm^3$. Aggregation would begin to occur only when the activation energy for diffusion, experimentally estimated to be $\sim$3.4 eV, was surpassed. This was found to be at a temperature of approximately 1500 K. An attraction of 0.035 eV between vacancies was found to agree best with experiment. Carrasco et al. [Carrasco 2004] studied the diffusion of and interactions between O vacancies in a series of metal oxides including MgO, CaO, $\alpha$-$Al_2O_3$ and ZnO. Diffusion barriers for the ionically bonded compounds (MgO, CaO, $\alpha$-$Al_2O_3$) were found to be relatively higher, with a barrier height decreasing with greater Madelung potential in the order MgO, CaO, $\alpha$-$Al_2O_3$. Interactions between vacancies situated a short distance from one another were compared to isolated vacancy cases. An energy gain was reported for the ionic compounds suggesting attraction between vacancies. In contrast, the aggregation of O vacancies in ZnO was found to be energetically unfavourable. In a separate study, Carrasco et al. [Carrasco 2006] compared vacancy diffusion along surface sites to diffusion in the bulk, and diffusion from the surface to the bulk for MgO, CaO and BaO. In all cases, barriers for diffusion were lowest for diffusion along the surface. For MgO,

surface diffusion towards step edge sites was found to be particularly favourable and was correlated with STM measurements. Bradley et al. [Bradley 2015A] modelled clusters of 2, 3, and 4 oxygen vacancies in crystalline $HfO_2$. This study aimed to test vacancy aggregation as a switching mechanism for $HfO_2$ insulating layer-based ReRAM devices. Calculations showed that there is an energy gain in aggregating vacancies compared to the infinite separation case, with binding energy varying with cluster size and shape. Although neutral vacancy aggregation was shown to energetically feasible, based on the work of Kuzovkov et al. [Kuzovkov 2001], it was concluded the aggregation of neutral vacancies would not be a suitable mechanism for conductive path formation under practical conditions. This was attributed to a vacancy diffusion barrier of 2.4 eV, requiring a temperature on the order of 1000 K. Such temperatures would result in the breaking up of vacancy aggregates. An additional study by Bradley et al. explored the injection of electrons into cells containing oxygen vacancy sites. At some sites, the trapping of two electrons at the vacancy resulted in the formation of a Frenkel defect pair consisting of a neutral di-vacancy site and an $O^{2-}$ interstitial ion. This supported a mechanism of cluster growth from pre-existing vacancy sites [Bradley 2015B]. The presented studies indicate that vacancy aggregation is clearly a viable phenomenon in some oxides; however, this is a material and morphology dependent process.

## 3.9 Discussion and Summary

The devices studied in the current investigation originate from the study performed by Mehonic et al. [Mehonic 2012A]. This suggests resistive switching intrinsic to the oxide layer, and the establishment of a silicon-rich conductive path through oxygen vacancy accumulation, which is facilitated by exisiting defects. AFM and STM measurements indicated a columnar structure within the oxide layer with the suggestion that the edges of columns could act as the defects in question due to their high conductivity. TEM studies will be valuable for identifying and chemically characterising the suggested defect sites as well as the conductive path itself through different techniques such as STEM, EELS, and EDX. Such studies are presented in chapters 5, 6, and 7.

A mechanism for the formation of accumulations of oxygen vacancies has not been es-

tablished. As explored for $HfO_2$ by Bradley et al. [Bradley 2015A][Bradley 2015B], this could be due to the aggregation of existing oxygen vacancies or additional vacancy production. In the latter case, under electron injection conditions, the formation of the oxygen double bridge interstitial allows the migration of oxygen atoms away from defect sites at a relatively low energy cost, as suggested by Mehonic et al. [Mehonic 2016]. In the low resistance state, Mehonic et al. found a trap-assisted tunnelling model to best fit the current characteristics [Mehonic 2012A]. As discussed in section 3.6, oxygen vacancies and intrinsic sites can act as potential electron traps and could play an important role in this process. More recently, it has been shown that intrinsic electron traps can accomodate up to two electrons, and in some cases this results in the formation of a vacancy and oxygen double bridge interstitial [Gao 2016]. This mechanism is comparable to the mechanism proposed by Bradley et al. [Bradley 2015B], where oxygen vacancies could act as electron traps to generate oxygen interstitials. However, further study is required for electron trapping at oxygen vacancies in a-$SiO_2$ to understand their role in similar mechanisms. Figure 3.9 summarises the processes believed to occur in amorphous silicon oxides during electrical stressing as discussed in this review chapter. In chapters 9 and 10, the aggregation and diffusion of oxygen vacancies and electron trapping at oxygen vacancies are studied in further detail.

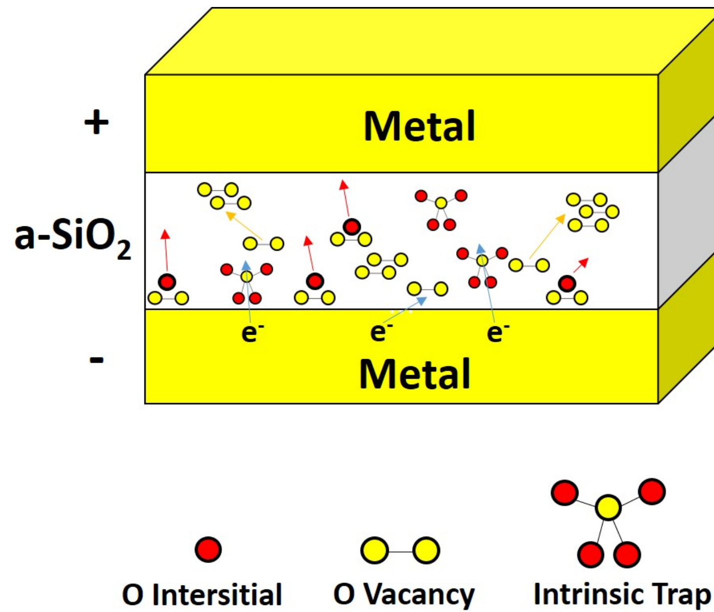


Figure 3.9: A schematic summarising the processes believe to occur in amorphous silicon oxides during electrical stressing as discussed in this review chapter. Prior studies have suggested the diffusion and aggregation of oxygen vacancies [Yao 2010][Mehonic 2012A] and the formation of additional oxygen vacancies and interstitials [Yao 2012][Mehonic 2016][Gao 2016] as mechanisms for oxygen vacancy accumulation. Oxygen vacancies and intrinsic sites in a-$SiO_2$ can trap electrons. Such traps may play an important role in the trap-assisted tunnelling process measured in the low resistance state during resistive switching in amorphous silicon suboxides [Mehonic 2012A].

# 4 Transmission Electron Microscopy Characterisation

## 4.1 Introduction

A transmission electron microscope (TEM) can be used for the imaging and characterisation of materials at sub-nanometer resolution. A beam of high speed electrons is transmitted through a thin sample, with some electrons interacting with the material in the process. The outgoing electrons are then collected and implemented in image formation and spectral analysis. This idea was first conceived by Knoll and Ruska in 1932 [Knoll 1932] and has since developed into one of the most effective and versatile tools for materials analysis. Modern TEMs come equipped with a number of detectors besides a standard imaging camera. For example, an additional X-ray detector allows energy dispersive X-ray spectroscopy (EDX) analysis, and an additional specialised electron detector allows the acquisition of electron energy-loss spectra (EELS) and energy-filtered images. Scanning transmission electron microscopy (STEM) involves the use of an electron beam which converges at the plane of the sample as opposed to the typical parallel beam used in a TEM. Imaging in this mode has, for example, the benefit of local chemical structure analysis through spectroscopy. Nowadays many TEMs are capable of switching between both of these imaging modes. It should be noted that all TEMs also possess a diffraction mode in addition to an imaging mode. This allows the accurate measurement of crystallographic information. The following section aims to briefly outline the main parts and principles of operation of a modern TEM. This will be followed by an overview of the benefits and limitations of the analytical techniques described above.

## 4.2 A Brief Summary of the Layout of a TEM

A TEM can be divided into three principle sections beginning from the electron source, usually located at the top of the vacuum column [Williams 2009A]: the illumination system; the stage; and the imaging system. Figure 4.1 represents a simplified schematic of a TEM in imaging mode.

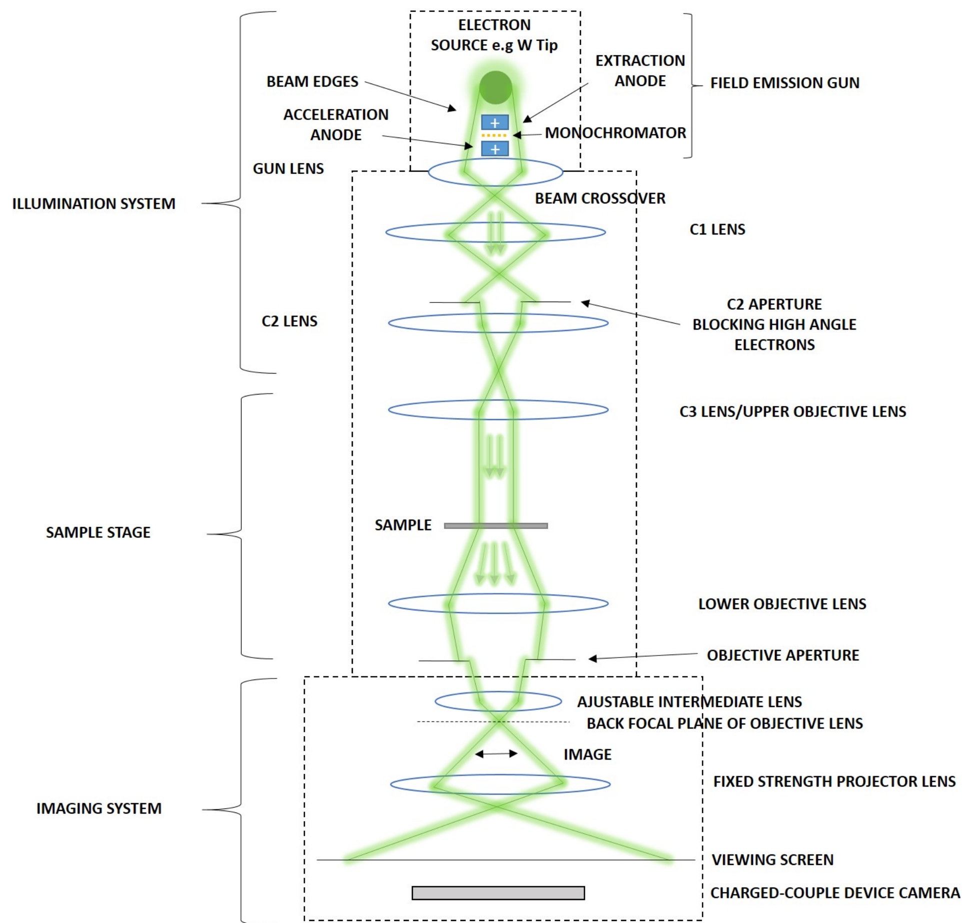


Figure 4.1: A simplified schematic of a TEM in imaging mode. For STEM, the beam is made to converge at the plane of the sample. It should be noted that the imaging system is also simplified and that modern TEMs make use of a greater number of lenses for finer control of the electron beam.

The illumination system consists of the electron source (often termed an 'electron gun') followed by a series of 'condenser lenses' and 'apertures'. These are used to manipulate the electron beam's orientation and current so that it falls either parallel (for TEM) or convergent (for STEM) onto the sample. This investigation will make use of TEMs equipped with a Schottky field emission gun (FEG) or a 'cold' FEG [Williams 2009B]. A Schottky FEG is standard for the majority of TEMs and makes use of heating in addition to an electric field to obtain a combination of thermionic and field emission. A fine tungsten (W) tip is subjected to an electric field and simultaneously heated to extract electrons. Below the tip, two anodes are positioned one after the other. The initial anode acts to extract the electrons, while the latter accelerates the electrons up to the required voltage, which will range from 80 keV to 200 keV throughout this investigation. Cold FEGs

are less common and exclusively make use of field emission. After their emission and acceleration up to the required voltage, the electrons are focused by the gun lens before entering the main TEM column [Williams 2009B]. Two additional condenser lenses, referred to as the C1 and C2 lenses, form the remainder of the illumination system. A TEM makes use of round magnetic lenses, which focus the electron beam through the use of the Lorentz force. The lenses consist of a central 'polepiece' wrapped in a copper coil. The polepiece is made of a magnetically soft material such as soft iron with a hole or 'bore' drilled through the middle. By running a current through the copper coil, the induced magnetic field deflects the electron beam as it passes through the bore. This focusing action on the electron beam allows the strength of the lenses to be changed simply by varying the lens currents. At specific focal planes, apertures can be inserted into the path of electrons. An aperture consists of a circular hole in a rod made of a heavy metal, typically platinum (Pt) or molybdenum (Mo), to partially block the electron beam. Apertures play a number of important roles within a TEM. For example, within the system of condenser lenses they are used to control image and spectral resolution by altering beam intensity [Williams 2009C]. Rarer TEMs have an electron monochromator located near the electron source to minimise the variation in emitted electron wave frequencies and obtain enhanced resolution (see section 4.4). A TEM used within this investigation has a Wien-type monochromator fitted. Such monochromators consist of perpendicular electric and magnetic fields, which can be used to disperse and filter electrons moving at particular velocities (and hence frequencies) by passing them through a selection slit.

The stage firstly consists of the sample holder on which the sample is fixed and allows it to be tilted and moved up, down, left, and right. This has a number of important functions. For example, it allows the sample to be orientated appropriately. In this investigation, the orientation of the sample will be important since each layer of an *MIM* structure must be clearly visible. In addition, during instances where the sample isn't needed (e.g. parts of the alignment procedure), it can be moved out of the beams path to prevent unnecessary damage. The sample is immersed in the strong magnetic field of the objective lens, which most commonly consists of upper and lower pole pieces (see Figure 4.1). Elastic and inelastic scattering of the electrons during interaction with the sample leads to the modulation of the phases and amplitudes of the electrons. This in turn leads to constructive and destructive interference of the electrons and results in contrast varia-

tions in the image. The objective lens forms the final image, which will subsequently be magnified by the imaging system. The objective aperture is particularly important and directly plays a role in determining image resolution and contrast in TEM mode. By preventing electrons at high angles of incidence from contributing to the image, spherical aberrations can be minimised, which improves image resolution (see section 4.4). However, a small aperture wil also cut out high frequency information from an image, which may lead to reduced image resolution. Conversely, TEM image contrast is enhanced by a smaller aperture. All of these effects need to be considered for selecting the optimum-sized aperture. Imaging in STEM mode does not make use of an objective aperture (see section 4.5).

The imaging system firstly consists of an additional set of lenses making up the magnification system of the TEM. These lenses are not used in STEM mode where magnification is instead controlled by scanning probe dimensions. To switch between imaging mode and diffraction mode, the imaging plane of the objective lens (for imaging) or the back focal plane of the objective lens (for diffraction) must play the role of the object for the imaging system of lenses. This is achieved by adjusting the strength of the intermediate lens (see Figure 4.1) [Williams 2009A]. 'Camera length' can be described as the distance of a diffraction pattern from the recording plane [Williams 2009A]. By varying camera length using the illumination system, the diffraction pattern can firstly be magnified so that any features are more discernible. Secondly, in STEM mode, camera length influences image contrast and controls the solid angle by which the electrons that are scattered from the sample fall upon the EELS detector (see section 4.4). A longer camera length gives the greater image contrast and a smaller solid scattering angle relative to fixed detectors. This results in less electrons being collected during EELS acquisition and degrades the signal-to-noise ratio in the EELS spectrum. This may in turn affect the spatial resolution of the spectrum. The imaging system consists of many different types of detector for image formation. For system alignment, it is common to make use of a fluorescent viewing screen positioned below the imaging system. A common fluorescent coating material is doped Zinc Sulphide (ZnS). The viewing screens can be lifted away from the beam path to allow digital image recording. Modern TEMs most often use 'Charged Couple Device' (CCD) camera detectors. CCD detectors consist of an array of 'pixels' in the form of individual, electrically isolated capacitors. Electrons from the trans-

mitted beam fall upon a scintillator, this produces photons, which are guided to the pixels positioned below the scintillator using a fibre-optic light guide. This generates a stored charge in each pixel proportional to light (and therefore image) intensity. The capacitors are subsequently read-out row-by-row and column-by-column to generate images or spectra [Williams 2009D]. By reading out several pixels at once, acquisition times can be improved. This process is termed ’binning’. However, binning comes with the danger of saturating the read-out. The resulting reduction in intensity will in turn lower image resolution. Before the final image is viewed, additional processing is required in the form of ’dark’ and ’gain’ current corrections. Dark current originates from current generated in the pixels when no photons are generated; this must be subtracted from the final image. Gain current originates from the difference in output current and input intensity for each pixel. For example, due to slight differences in fabrication, the output current can vary from pixel to pixel for a particular input light intensity. Gain current corrections remove these variations. In STEM mode, a CCD is not used for imaging (see section 4.5).

## 4.3 TEM Sample Preparation using a Focused Ion Beam (FIB)

A variety of methods are available for the preparation of electron-transparent TEM samples. Examples include grinding and crushing, electropolishing, and ion milling [Williams 2009G]. However, in this investigation, a focused ion beam (FIB) will be used for sample preparation. This method offers excellent thickness control and allows precise site-specificity. An FIB unit uses a gallium (Ga) ion beam together with an electron beam, the latter of which is used to view sample preparation using Scanning Electron Microscopy (SEM). The region of interest is firstly identified at the sample surface using the SEM electron beam. The specific area to be cut then has a layer of platinum (Pt) deposited over it in order to protect the sample region during the following milling process. The ion beam is then used to mill downwards into the sample surface to form two trenches on either side of the deposited Pt. After further ion thinning, the sample is lifted out by attaching it to a probe and after to a supporting grid. Pt is commonly used as the ’welding’ material for making these attachments, and in this investigation Cu supporting grids are used. The sample is finally thinned at low ion energies (as low as 2 eV) until most of the surface layers damaged by the initial thinning are removed. Figure 4.2 shows SEM

images taken during sample preparation using a FIB.

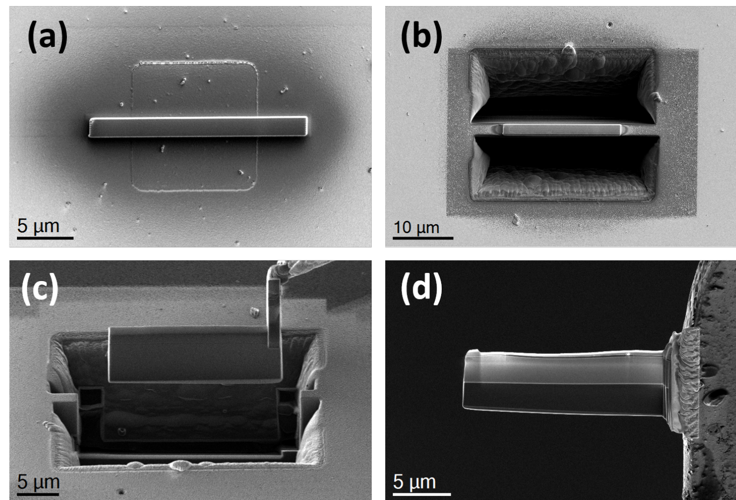


Figure 4.2: SEM images showing the main stages of FIB sample preparation. These images are provided courtesy of Siew Lang Teo at IMRE. **(a)** A strip of Pt is deposited across an electrode pad used for electrical stressing. **(b)** A Ga ion beam is used to mill downwards either side of the deposted Pt. **(c)** The sample is lifted out by welding to a probe with Pt. **(d)** The sample after attaching to a Cu grid and low ion energy thinning.

## 4.4 Factors Affecting Image Quality

Theoretically, although image resolution should be defined by the electron wavelength following the Rayleigh criterion, round magnetic lenses lead to unwanted resolution deterioration. The main problems encountered are analogous to those encountered with optical microscopes: spherical aberrations; chromatic aberrations; and astigmatism. Spherical aberrations are a result of a stronger focusing effect for electrons entering a lens further from the optical axis. As illustrated in Figure 4.3, this causes the image to be focused at several different points along the optical axis instead of at a single point. Spherical aberrations can be minimised in a number of ways. The most basic procedure is the use of a limiting aperture to remove electrons, which are further away from the optical axis. However, this leads to a reduction in intensity and image resolution. Modern aberration correctors use additional multipole lenses to compensate for spherical aberrations.

Chromatic aberrations originate from electrons of slightly varying wavelength being emitted from the electron source, which leads to stronger focusing for shorter wavelength

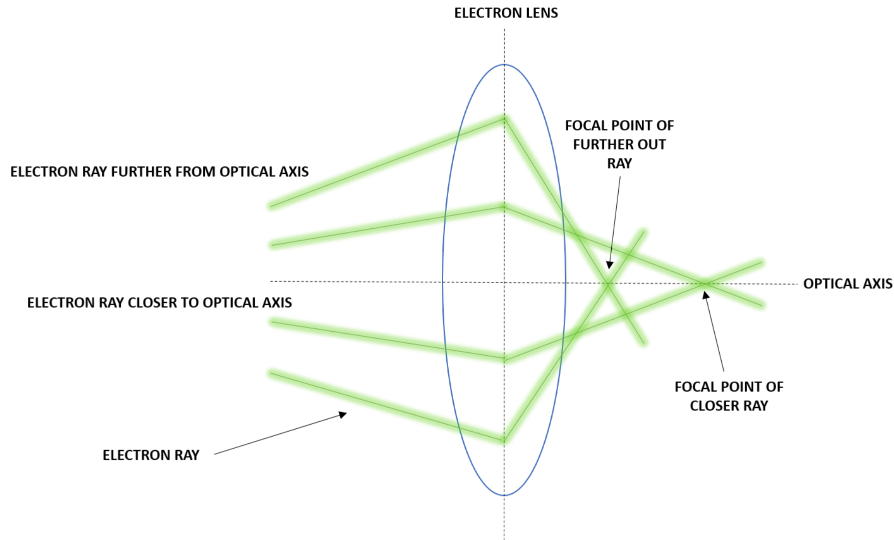


Figure 4.3: A schematic showing the origin of spherical aberrations in electron lenses. Electron rays further from the optical axis are focused closer to the lens.

electrons. Hence the end result is similar to spherical aberrations. The effect of chromatic aberrations on image quality is only noticeable after spherical aberration correction. Once the latter is corrected, the use of a good quality electron source combined with a monochromator can minimise such effects. Shortening electron wavelength (and therefore increasing speed) through the use of a higher acceleration voltage is an additional option. However, due to inelastic scattering within the sample itself, chromatic aberrations cannot be completelely avoided and it is important to use as thin a TEM sample as possible to minimise scattering events. A thickness of less than 100 nm is preferable. Astigmatism is a result of the non-uniformity of the electromagnetic field of an electron lens and leads to image distortions. It is the only factor of the three which can be completely corrected. This is achieved by the addition of independent compensating electromagnetic coils within the lenses known as 'stigmators'.

## 4.5 TEM and STEM

As mentioned earlier, TEM images are formed from a parallel or mildly converged electron beam, whereas STEM images make use of a beam which converges strongly to form a probe. The small probe used in STEM makes detailed local elemental analysis possible during spectral acquistion. In addition, by collecting electrons which have scattered

elastically from atomic nuclei, element sensitive 'Z-contrast' images can be acquired [Pennycook 1991]. Heavier elements have a more strongly positively charged nucleus (and hence a high atomic number Z), which leads to higher scattering angles than for lighter elements. In order to detect these electrons and form an image, a STEM makes use of an annular shaped scintillator detector as opposed to a CCD camera. Elastically scattered electrons falling into the ring-shaped detector generate photons, which in turn are collected by a photomultiplier. Often Z-contrast imaging may be referred to as 'high-angle annular dark field' (HAADF) imaging due to the use of a ring-shaped detector. In such images, heavier elements appear brighter while the vacuum appears dark. These images are therefore referred to as 'dark field' (DF) images. STEMs can also be used to detect electrons which have not been scattered. Images formed from such electrons are referred to as 'bright field' (BF) images. In this case, lighter elements appear brighter. These images are formed by collecting electrons with a disk-shaped scintillator detector which is placed on the optical axis. Figure 4.4 shows a schematic which illustrates the difference between bright and dark field detectors.

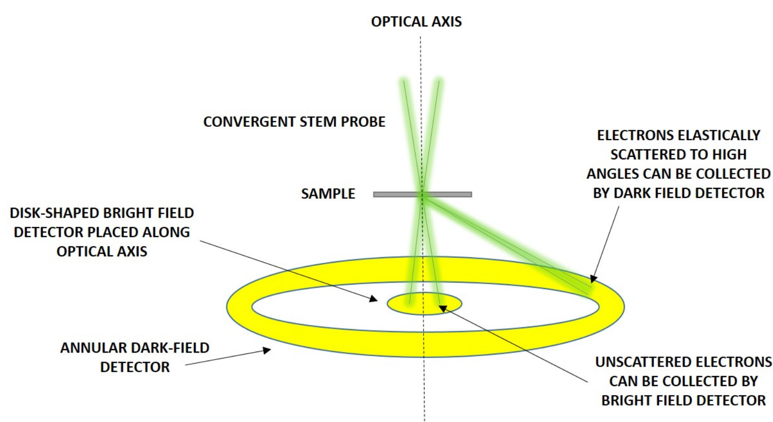


Figure 4.4: Schematic illustrating the difference between bright and dark field detectors in STEM mode. It should be noted that the magnification system lies between the sample and detectors.

While a TEM image can be taken with a parallel camera readout, a STEM image requires the probe to scan over the entire imaging region and requires a serial readout. As a result of the usually slower image acquisition, effects such as drift are more likely to distort STEM images. The STEM operator must therefore ensure the stability of the sample during image acquisition. An additional setback of STEM is the need for a thoroughly cleaned sample. A concentrated electron beam tends to more strongly attract

contamination from hydrocarbons to the sample region being probed. This leads to poor image acquisition due to electrons being blocked out. Inorganic samples can be cleaned by exposing them to oxygen plasma before inserting into the TEM. In this investigation a gas mixture composed of 75% Ar and 25% O is utilised to produce oxygen plasma for sample cleaning. However, organic samples such as polymers are easily damaged by plasma cleaning and must be inserted into the TEM without exposure to oxygen plasma. In STEM, this results in contamination being drawn towards the STEM probe. This effect is strengthened by the need for serial image acquisition. To summarise, although STEM is capable of providing a greater depth of information, sample stability and preparation are essential.

## 4.6 Energy Dispersive X-ray Spectroscopy (EDX) and Electron Energy-Loss Spectroscopy (EELS)

Elastically scattered electrons typically scatter between 1$^\circ$ (17.45 mrad) to 10$^\circ$(174.53 mrad), whereas inelastically scattered electrons rarely surpass 1$^\circ$[Williams 2009F]. While Z-contrast STEM imaging makes use of elastically scattered electrons, EDX and EELS make use of the inelastically scattered electrons. EDX and EELS are often referred to as 'core' spectroscopies. This refers to the mechanism by which energy is lost. Incoming electrons interact with and excite atomic core electrons and are consequently scattered by losing some of their kinetic energy. Upon transmission through the sample, the resulting energy losses are analysed with EELS. The excited core electron may then de-excite and emit an X-ray in the process. These X-rays are then collected during EDX. In this respect, both EDX and EELS are related techniques. While EDX typically gives higher signals for heavier elements, EELS tends to give higher signals for lighter elements. This is a result of detector design and sample interaction. The EDX detector used in this investigation is cooled using liquid nitrogen and is located above the sample. It is isolated from the stage section of the TEM by a 'window' composed of a thin beryllium (Be) sheet. X-rays passing into the detector must pass through the window. However, X-rays emitted for elements below Na (Z = 11) are absorbed by the window, which reduces signal strength. More advanced detection systems may make use of an 'ultrathin' window or even a windowless detector to avoid this problem. X-rays passing through the window

fall on to a p- and n-doped Si semiconductor detector and generate electron-hole pairs. These pairs can be separated by applying a reverse bias across the p-n junction and the electrons can be detected [Williams 2009G]. An EELS detector makes use of a small aperture below the sample to collect electrons scattered by the sample. As a result, electrons that are inelastically scattered to high angles (and therefore by heavier elements) give a weaker signal. For the Gatan Imaging Filter (GIF) used to collect EELS spectra in this investigation, electrons pass through the aperture into a 'drift tube' immersed in the field of a magnetic prism. The trajectories of electrons which have lost more energy are more strongly perturbed by the Lorentz force due to their smaller velocities. This allows electrons with different energy losses to be dispersed into a spectrum. A selection slit at the end of the drift tube allows the possibility of filtered imaging. The selection slit is followed by a series of lenses forming an imaging system. Within this imaging system, the dispersed beam of electrons is further refined and the EELS spectrum is recorded using a CCD [Williams 2009G]. EELS can offer more in-depth information than EDX. For example, examination of the fine structure of EELS spectra can provide information about local coordination and bonding structure. These characteristics of EELS spectra will be further expanded upon in the following section. Figure 4.5 is a simplified schematic of a GIF and Figure 4.6 shows the typical positioning of EDX and EELS detectors in a TEM.

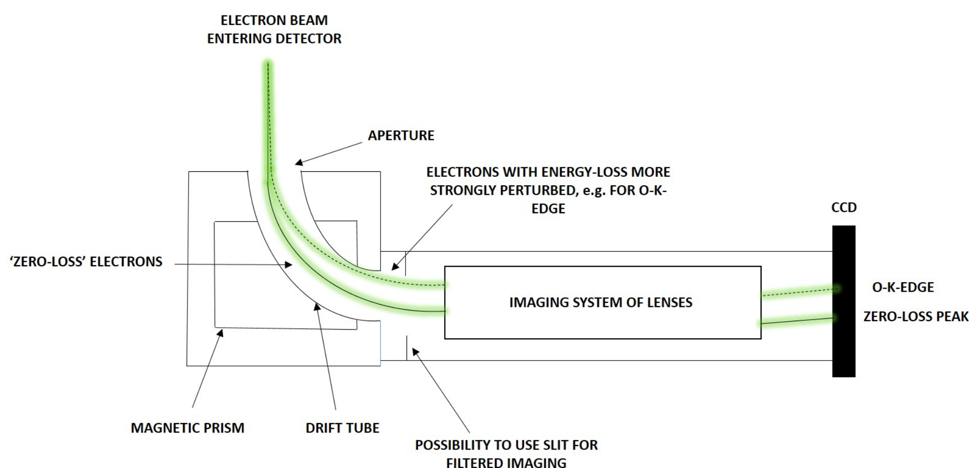


Figure 4.5: Simplified schematic of a Gatan Imaging Filter (GIF).

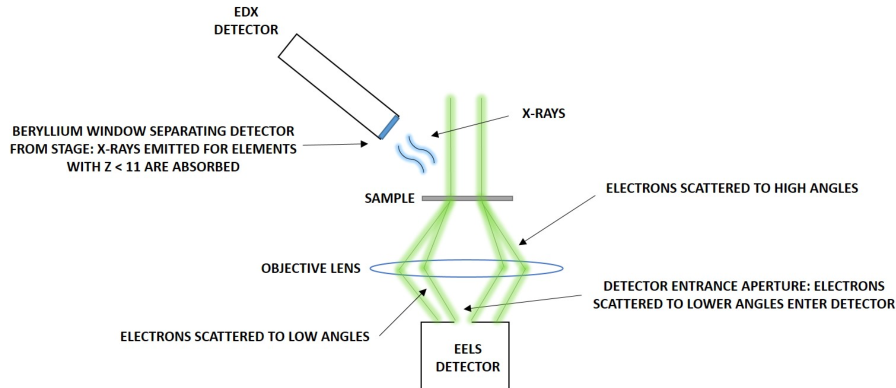


Figure 4.6: Schematic illustrating the difference in positioning of EDX and EELS detectors in a TEM.

## 4.7 The Energy-Loss Spectrum

The spectrum obtained from EELS measurements contains a vast store of information. Examples of derivable information include but are not limited to local thickness, composition, and local bonding structure. The 1-100 eV region of a spectrum is generally referred to as the low-loss region [Egerton 1996A]. Beginning from the zero-loss peak centred at 0 eV, this region contains a number of additional broad peaks referred to as plasmon peaks. Such peaks are products of collective excitations of outer-shell valence electrons as opposed to core electrons. Occasionally additional fine structure may be found to be superimposed onto plasmon peaks. Such structures correspond to interband transitions of single electrons within the valence band. Above 100 eV, core-loss spectra are encountered [Egerton 1996B]. Core-loss spectra are characterised by 'edges', which refers to a signal increase at an energy corresponding to the excitation of a core electron to the conduction band. Edges can be interpreted as a representation of the specimen's local unoccupied electron density of states. Onset can be sudden, with an initial rapid rise in a short energy interval followed by gradual decay. Such edges are referred to as 'hydrogenic'. Other edges may rise more slowly and have a more rounded appearance. Such edges are termed 'minor' edges. Edges at higher energies produce a weaker intensity signal since higher energy losses are less probable. Edges are classed as either *K*, *L*, *M*, or *N* edges, which refer to excitations from atomic shells with principal quantum numbers 1, 2 ,3, and 4 respectively. For *L*, *M*, and N edges, an additional subscript is used corresponding to the total angular momentum quantum number (e.g. $Si$-$L_2$ edge). Fine

structure is visible after edge onset, which is termed the 'Energy-Loss Near Edge Spectrum' or ELNES. It was found that such a structure is unique for different compounds, allowing the use of fingerprinting to determine local bonding structure. This can often be extrapolated to determine potential bonding structure in unknown compounds. Beyond 50 eV from edge onset, an extended fine structure referred to as 'extended energy-loss fine structure' or EXELFS is encountered [Egerton 1996C]. Fourier analysis of this fine structure allows the derivation of a local radial distribution function (RDF) and hence the determination of any short-range order. In this investigation, Si and O oxygen edges will play a particularly important role. Both elements produce hydrogenic edges with the *Si*-$L_{2,3}$ edge observable at around 100 eV and the *O-K* edge onset starting at around 532 eV.

After recording an EELS spectrum, the appropriate data must be correctly isolated for accurate quantitative analysis. For example, the *O-K* edge at 532 eV will be preceded by a number of plasmon peaks and edges depending upon the composition and thickness of the material. These lower-energy excitations will form a background before the onset of the *O-K* edge. This background must be subtracted to isolate the oxygen signal before further processing. Background subtraction is most commonly performed by modelling the background according to a power law of the form $f(E) = aE^{-k}$. Usually an energy window just preceding edge onset is selected in order to determine the constants $a$ and $k$, with the assumption that the modelled background within the energy window extends to higher energies. A further complication is the multiple scattering of electrons. A fast electron may interact with more than one electron within a material, which leads to increased signal intensities at particular energies. This interaction could be in the form of additional core-loss excitation or plasmons. This signal increase must be deconvolved from the spectra before quantitative analysis. Figure 4.7 shows the sum of three EELS spectra taken from amorphous silicon dioxide in an energy range which includes the *O-K* edge. For the following examples, the Digital Micrograph© software has been used for data processing.

Figure 4.8 shows Figure 4.7 with background subtracted and the multiple scattering contribution deconvolved. The thinner the sample, the less the contribution. The multiple scattering contribution can be deconvolved through use of two different Fourier trans-

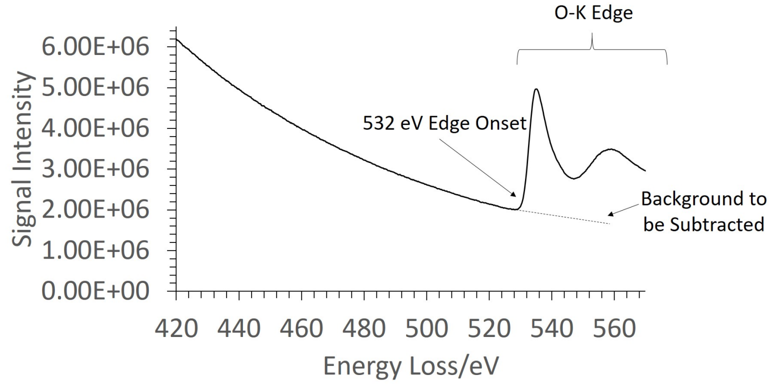


Figure 4.7: EELS spectrum taken from amorphous silicon dioxide. The onset of the *O-K* edge is visible at around 532 eV and is followed by additional fine structure. Preceding the edge is a background originating from lower-energy excitations.

form methods. In Figure 4.8, the Fourier-Ratio method has been employed [Egerton 1996D]. This procedure involves dividing the Fourier transform of the core-loss region (>100 eV), by that of the low-loss region (up to 100 eV). The Fourier transform of the multiple scattering corrected spectrum, $s(\nu)$, is then given by

$$s(\nu) = I_0 \frac{i^{coreloss}(\nu)}{i^{lowloss}(\nu)}, \tag{1}$$

where $I_0$ is the zero-loss intensity, $i^{coreloss}(\nu)$ is the Fourier transform of core-loss region, $i^{lowloss}(\nu)$ is the Fourier transform of the low-loss region, and $\nu$ is the Fourier frequency. As a result of this procedure, an additional modification is required for $s(\nu)$ in order to reduce noise amplification before performing a reverse Fourier transform. An alternative method to obtaining $s(\nu)$ is the Fourier-Log method [Egerton 1996E]. In this case,

$$s(\nu) = I_0 ln[\frac{j(\nu)}{z(\nu)}], \tag{2}$$

where $j(\nu)$ is the Fourier transform of the entire EELS spectrum, and $z(\nu)$ is the Fourier transform of the zero-loss component. An additional modification is again required to remove noise amplification. In order to perform Fourier-Log deconvolution, an entire EELS spectrum is required (from the zero-loss peak to beyond the edge of interest) and can be achieved through the use of a coarse energy dispersion setting or by splicing

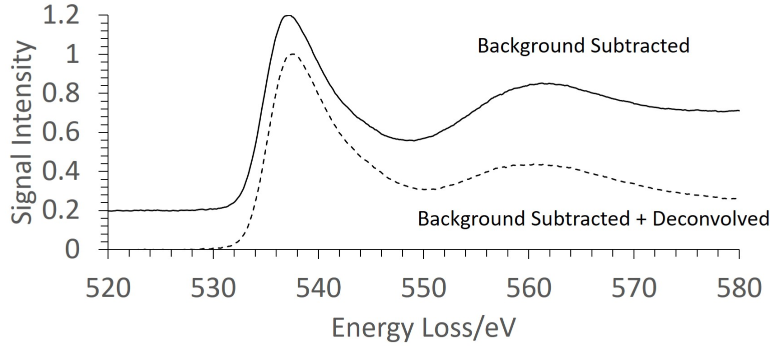


Figure 4.8: Background extraction followed by multiple scattering deconvolution of the *O-K* edge in amorphous silicon dioxide. The background subtracted peak has been shifted upwards for clarity. After deconvolution, the most notable differences are the changes in peak height ratios. It should be noted that signal intensity has been normalised.

together separately recorded spectra. This procedure allows the removal of multiple scattering effects before subtracting pre-edge background. As a result, any pre-edge effects resulting from lower energy core-loss edges can be removed. This allows a more accurate background subtraction. However, in many cases the entire EELS spectrum will not be recorded. For example, data for a particular element may be of interest, and more detailed measurements of the corresponding core-loss edge would require a finer energy dispersion setting. In this case, an EELS spectrum of the low-loss region can be recorded separately and used to apply Fourier-Ratio deconvolution. In cases with no significant pre-edge modification, this is a more rapid procedure with a negligible trade-off in accuracy.

The most simple procedure for an estimation of sample thickness is the Log-Ratio method [Egerton 1996G]. For a sample of thickness, $t$, and a mean free path for inelastic scattering, $\lambda$,

$$\frac{t}{\lambda} = ln(\frac{J_t}{Z_0}), \tag{3}$$

where $J_t$ is the area under the entire EELS spectrum, and $Z_0$ is the area under the zero-loss component. Absolute thickness can subsequently be estimated by using an appropriate approximation for $\lambda$ [Egerton 1996G].

## 4.8 Electron Tomography

Tomography aims to reconstruct a three-dimensional body by using a set of two-dimensional projections. A mathematical foundation for reconstruction is provided by the Fourier slice theorem, which is illlustrated in Figure 4.9. The Fourier slice theorem has its origins in the Radon transform [Radon 1986] and its relationship with the Fourier Transform [Bracewell 1956]. The Radon transform is geometrically equivalent to a two-dimensional projection of a three-dimensional object [Midgley 2003], and its Fourier transform is equivalent to a plane passing through the origin in the object's Fourier space. Therefore, by obtaining enough projections, a three-dimensional object can be reconstructed through the use of the inverse Fourier transform. This is often referred to as 'back-projection'. However, due to a finer sampling of low-frequency data (see Figure 4.9), direct back-projection leads to a 'blurry' reconstruction. In the Fourier transform approach this can be resolved by 'weighted' back-projection [Crowther 1970][Midgley 2003] methods to improve the sampling distribution in frequency space.

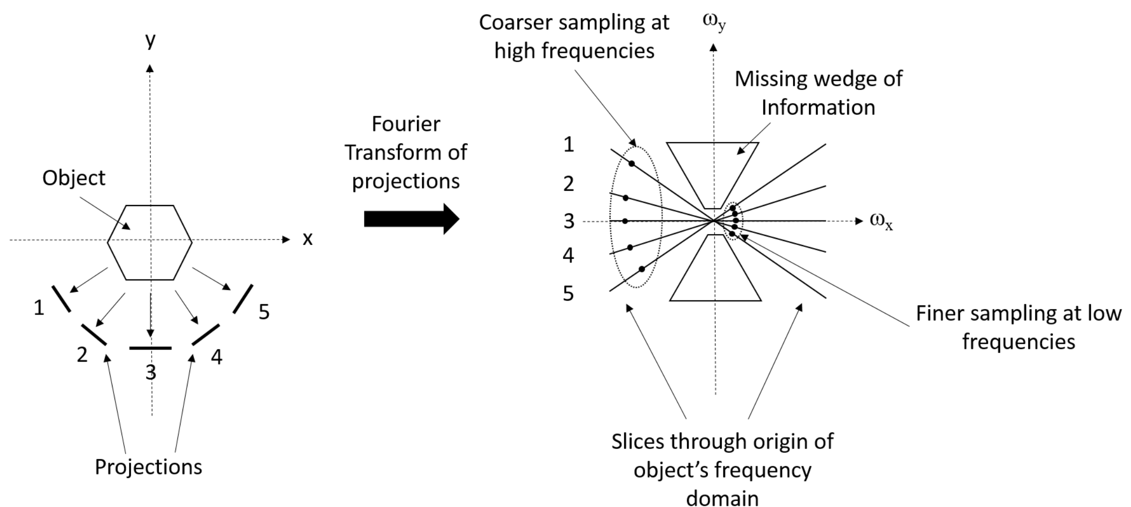


Figure 4.9: Schematic illustrating the Fourier slice theorem. Images 1 to 5 provide three-dimensional information from the object in a two-dimensional projection. Fourier transforms of these projections represent planes passing through the origin of the object's frequency space. In electron tomography, projections are usually taken at angular increments. Sampling is higher for low frequencies, and a restricted angular range of images results in a 'missing wedge' of information in frequency space.

Iterative methods provide an alternative to the reconstruction problem and do not require the use of Fourier transforms. They aim to discretise the problem through a set of linear

equations, which can be represented in the form $Sx = p$. The $p$ vector represents the various projections, which are equivalent to a set of line integrals along the line of site. The 'projection requirement' for tomographic reconstruction states that the recorded signal must be some monotonic function of a physical property of the object [Midgley 2003]. For example, in the case of HAADF imaging this signal is proportional to local atomic number. The line integrals represented by a projection therefore integrate over this property of the object along the line of site. $x$ represents a three-dimensional discretisation of this property and $S$ is a matrix whose coefficients describe the contribution of $x$ to each projection.

During electron tomography, images are taken at regular angular intervals with respect to the object, typically 1-2$^\circ$ [Midgley 2009]. In many cases projections cannot be acquired for a full range of angles. This leads to the 'missing wedge' of information illustrated in Figure 4.9. This can be problematic for back-projection based methods whereas iterative methods are capable of minimising the resulting errors [Midgley 2003]. However, this comes at an increased computational cost. A minimum tilt range between 75-80$^\circ$ has been shown to minimise any artefacts of reconstruction [Kawase 2007][Midgley 2009]. In this thesis, the iterative Simultaneous Iterative Reconstruction Technique (SIRT) is used [Gilbert 1972] due to a limit on angle and the availability of adequate computational resources.

The use of HAADF STEM as opposed to TEM to acquire a tilt series has a number of advantages. The parallel TEM beam provides a coherent beam of electrons, which is diffracted in preferred directions when interacting with crystalline regions of a sample. This leads to diffraction contrast. In addition, a coherent beam of electrons will diffract around small bodies in a material and leads to phase contrast through the observation of Fresnel fringes. These effects are a result of non-monotonic effects and violate the projection requirement. In contrast, a HAADF image from a converged STEM beam is almost completely incoherent and its intensity is proportional to the local atomic number in HAADF images [Pennycook 1991][Midgley 2003][Midgley 2009].

# 5 Fabrication and Electrical Behaviour of *MIM* Structures to be Characterised Using TEM

## 5.1 Introduction

In this thesis, a total of four *MIM* stacks were characterised using TEM, which will be referred to as devices 1, 2, 3, and 4, respectively. In this chapter, firstly the fabrication and structure of the samples to be studied will be discussed. Secondly, in chapters 6 and 7, the effects of electrical stressing on the *MIM* structures are analysed using STEM and EELS. In this chapter, the electrical characteristics of the of each *MIM* stack will be briefly discussed. Finally, the characteristics of devices 1 to 4 will be summarised for future reference in the following chapters.

It should be emphasised that sample fabrication and electrical characterisation are not the principle objectives of this thesis. However, this chapter provides an essential background to the results discussed in chapters 6 and 7 and will be a useful reference. In addition, it should be noted that sample fabrication was carried out by third parties at the University of Southampton (devices 1 and 2), University College London (device 3, courtesy of Adnan Mehonic and Wing Ng), and Sematech (device 4). Furthermore, the electrical stressing of devices 1, 3, and 4 was carried out by third parties at UCL (courtesy of Mark Buckwell and Luca Montesi), while device 2 was stressed at SUTD (courtesy of Mei Sen). Finally, the AFM measurements briefly discussed in this chapter are provided courtesy of Mark Buckwell at UCL. All TEM measurements and DFT calculations presented from Chapters 5 to 9 represent my contribution to this collaborative effort.

## 5.2 Fabrication

### 5.2.1 Sample Fabrication Using the Reactive Sputtering Technique

For the a-$SiO_x$ insulating layers used in this study, the 'reactive sputtering' technique was used in their fabrication. In this technique, fabrication takes place within a vacuum

chamber with the presence of an inert 'working gas' (typically Ar) and oxygen gas. A silicon 'target' is placed opposite a substrate material. By applying a high enough voltage across the chamber, a glow discharge (plasma) is formed and the resulting Ar ions are accelerated towards the Si target. This causes some material to eject towards the substrate. During this process, the ejected silicon reacts with oxygen in the chamber and is deposited as a-$SiO_x$ onto the substrate. Altering the flow of oxygen into the vacuum chamber will have a direct effect on the end stoichiometry. As will be discussed later, the structure of the resulting film is strongly dependent upon the substrate temperature, the working gas pressure, and the applied voltage. The reactive sputtering process is illustrated in Figure 5.1.

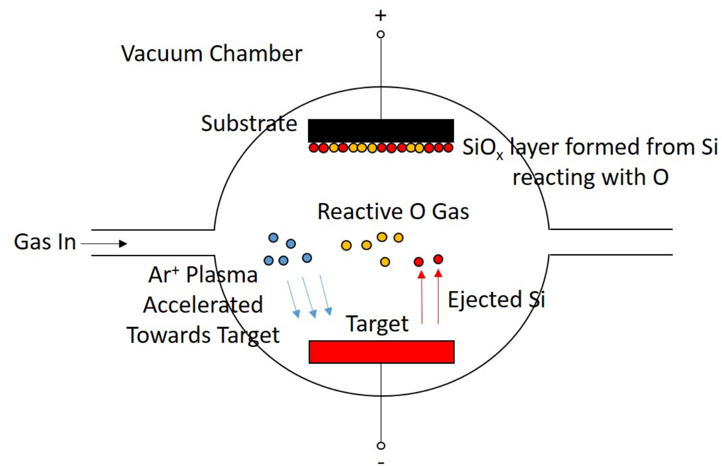


Figure 5.1: An illustration of the reactive sputtering technique used to fabricate a-$SiO_x$ insulating layers. Ions from an Ar plasma are accelerated towards an Si target. The Si is ejected and reacts with O in the vacuum chamber. This results in the deposition of a-$SiO_x$ onto the target.

The reactive sputtering method belongs to a set of thin film preparation methods collectively termed 'physical vapour deposition' (PVD). PVD is characterised by three key steps which take place in a vacuum environment. Firstly, the desired material is vaporised from a source material through the use of high temperatures or plasma. The ejected material is then transported through the vacuum towards a substrate material. Finally, upon reaching the substrate, the material condenses onto its surface. Whereas reactive sputtering makes use of oxygen gas within the vacuum chamber, 'co-sputtering' offers an alternative fabrication method for a-$SiO_x$. In this technique, instead of the use of oxygen gas, two solid Si and $SiO_2$ targets are used. It should be noted that electrode layers in

the *MIM* structures in this study were also fabricated using sputtering methods, except in the case of device 3 (see later), where the top electrode layers were deposited using the electron beam evaporation technique. The following implications for the end structure of the oxide layer are therefore also applicable to the sputtered electrode materials.

At low substrate temperatures, it has been noted that sputtered materials exhibit a columnar type growth, which consists of columnar grain structures separated by intercolumnar boundaries, which are less densely packed with atoms [Thornton 1986][McCann 2011]. This columnar microstructure is enhanced by the roughness of the substrate surface since particles arriving at the surface tend to aggregate at high points on the surface. This effect is termed 'atomic shadowing' and results in more continuous intercolumnar boundaries. The nature of this columnar growth can be controlled by substrate temperature, the working gas pressure, and the acceleration voltage.

Thin film growth by sputtering can be divided in to three principal stages [Thornton 1986]. The first stage involves the transport of the target material towards the substrate. Secondly, the target material is adsorbed onto the surface. Once adsorbed, surface diffusion can occur, followed by eventual incorporation into the growing layer. Depending on the circumstances, the adsorbed particle may additionally be revaporised from the substrate surface. Finally, assuming that the particle is incorporated into the thin film layer, bulk diffusion may occur. The working gas pressure plays an important role in the transport step, whereas substrate temperature and acceleration voltage play a critical role after adsorption. By increasing the working gas pressure within the vacuum chamber, the probability of vaporised particles colliding with the gaseous plasma during the transport stage is increased. As a result, particles approach the substrate surface more frequently at oblique angles, which in turn enhances the effects of atomic shadowing and columnar growth [Thornton 1986]. Conversely, a high temperature substrate surface promotes greater adatom mobility, which inhibits columnar growth [Thornton 1986]. Additionally, an increased acceleration voltage will lead to ions more strongly impacting the target with the consequence of more energetic vaporised particles. These particles will in turn impact the growing film surface with greater energy, which promotes recrystallisation and inhibits columnar growth [Thornton 1986]. This bombardment of the growing film surface also increases the probability of material resputtering and has been observed to result in

more planar film surfaces [Thornton 1986].

The ’zone model’ originally proposed in 1969 [Movchan 1969] attempted to characterise the result of substrate temperature in a more systematic way for sputtered metals. This model divided the resulting microstructure of the thin film into three ’zones’. Zone 1 applies when $\frac{T}{T_m} < 0.3$, where $T$ is substrate temperature, and $T_m$ is the melting point of the target material. Structures belonging to zone 1 consist of tall vertical columns separated by intercolumnar boundaries. Zone 2 is defined for $0.3 < \frac{T}{T_m} < 0.5$ and structures in this zone consist of columnar grain structures stacked upon one another into larger vertical columns separated by intercolumnar boundaries. Finally, zone 3 is defined for $\frac{T}{T_m} > 0.5$ and consists of even grain stuctures with size increasing with bulk activation energies for diffusion. In 1974, this model was extended to account for working gas pressure [Thornton 1974], with higher pressures favouring zone 1 type growth. Models of this type are a useful guide during sample fabrication. A zone 1 type structure with more continuous intercolumnar boundaries could facilitate resistive switching applications in two possible ways. Firstly, as proposed by Mehonic et al. [Mehonic 2012A], vacancies could more rapidly aggregate along a pre-defined intercolumnar boundary leading to conductive path formation. Alternatively, in the case of O interstitial diffusion [Jin 2001][Mehonic 2016], more continuous intercolumnar boundaries could provide a lower resistance diffusion path across the oxide layer. This could again result in conductive paths forming more rapidly and in turn benefit device operating speeds and electroforming/switching voltages. Furthermore, in the case of O interstitial diffusion, lower operating voltages could lead to slower oxide degredation during subsequent device cycling, and greater device endurance.

### 5.2.2 Device 1

Device 1 was a symmetric *MIM* structure consisting of TiN top and bottom electrodes, with fabrication aiming to achieve an a-$SiO_x$ stoichiometry with $x \approx 1.3$. Figure 5.2 shows a BF STEM image of an FIB-prepared cross-section from device 1. The top and bottom TiN layers are approximately 85 nm and 80 nm thick, respectively, while the $SiO_x$ is close to 35 nm in thickness.

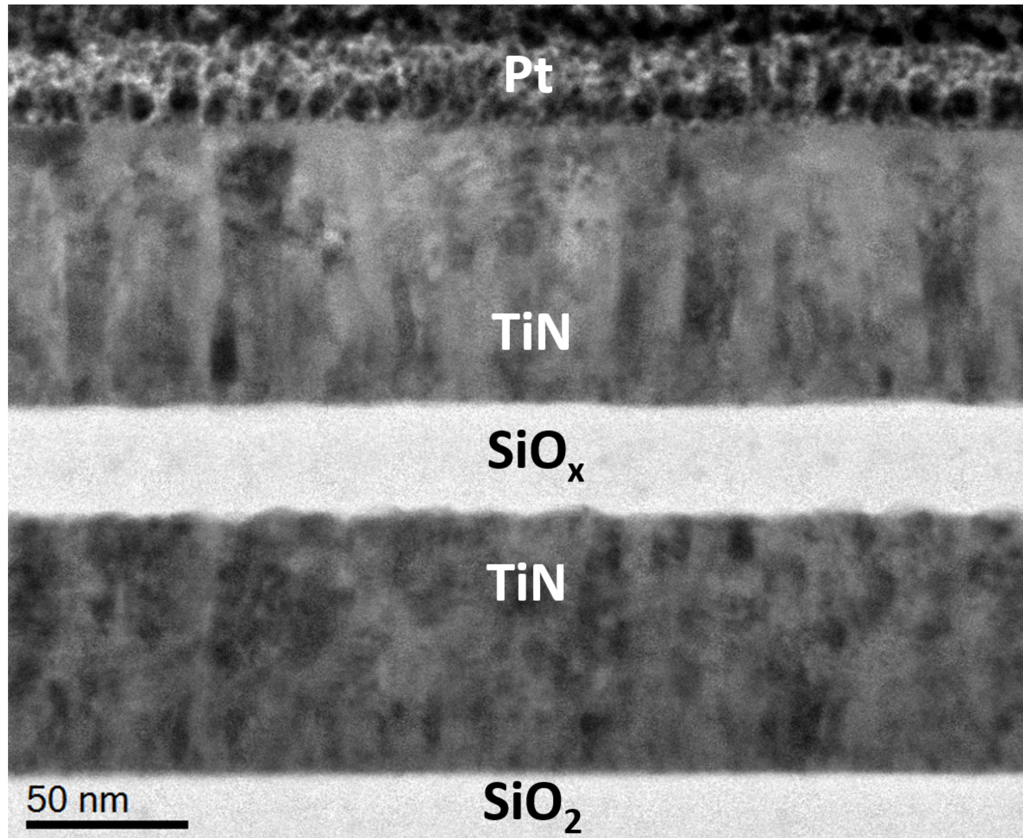


Figure 5.2: BF STEM image of an FIB-prepared cross-section from device 1. The TiN top and bottom electrodes are approximately 85 nm and 80 nm thick, respectively, and are separated by a $SiO_x$ layer close to 35 nm in thickness. Sputtering was carried out onto a $SiO_2$ substrate, while the top Pt layer is needed for FIB sample preparation.

For all devices except device 4, sputtering was carried out onto an a-$SiO_2$ substrate, while the top Pt layer is needed for FIB sample preparation for use in a TEM. Columnar microstructure can be observed in the TiN electrode layer, particularly in the top TiN electrode layer. In addition, the bottom TiN interface is comparatively rougher. Atomic shadowing effects may therefore enhance the possibility of columnar growth within the a-$SiO_x$ layer, although there is no obvious columnar microstructure visible in Figure 5.2.

### 5.2.3 Device 2

Device 2 had the same *MIM* composition as device 1. However, the top and bottom TiN electrodes were approximately 10 nm and 15 nm thick, respectively, with an a-$SiO_x$ layer approximately 35 nm in thickness and $x \approx 1.3$. The corresponding FIB-prepared

cross-section is shown in Figure 5.3.

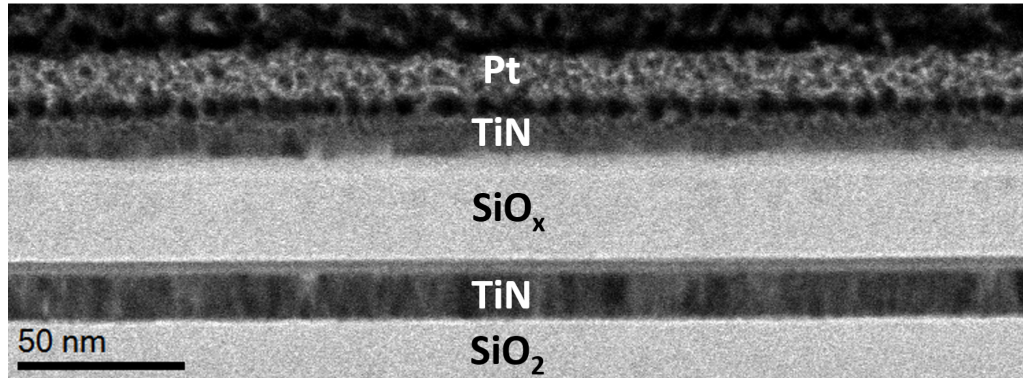


Figure 5.3: BF STEM image of an FIB-prepared cross-section from device 2. The TiN top and bottom electrodes are approximately 10 nm and 15 nm thick, respectively, and are separated by a $SiO_x$ layer approximately 35 nm in thickness. An sub-5 nm thick interfacial layer can be observed at the bottom electrode. EELS scans indicated an ELNES comparable with silicon dioxide and titanium monoxide. Sputtering was carried out using an $SiO_2$ substrate, while the top Pt layer is needed for FIB sample preparation.

Columnar microstructure is again visible within the TiN layers. However, the oxide-electrode interfaces are comparatively planar when compared to device 1. The more planar interface may indicate inhibited columnar growth in the oxide layer [Thornton 1986]. An interfacial layer with a sub-5 nm thickness is also visible between the bottom TiN electrode and the oxide layer. EELS analysis (presented in more detail in chapter 6) revealed ELNES fingerprints comparable with titanium monoxide and silicon dioxide. During fabrication, differences in processing conditions appear to have resulted in enhanced oxidation at the bottom interface. The mechanism by which this occured is unclear.

### 5.2.4 Device 3

Device 3 differed in the choice of electrode layers. The top electrode consisted of a Au layer above a thin Ti wetting layer, while Mo was used for the bottom electrode. The associated FIB-prepared cross-section is shown in Figure 5.4. The Au and Ti top electrodes are approximately 115 nm and 5 nm thick, respectively, while the bottom Mo electrode is close to 280 nm in thickness. Although the presence of the Ti layer is not obvious, its existence and thickness was confirmed using EELS spectrum imaging (see chapter 6). The a-$SiO_x$ layer is similar in thickness to devices 1 and 2 at approximately

35 nm. EELS point scans revealed an ELNES fingerprint close to that of silicon dioxide within the a-SiO$_x$ layer with $x \approx 2$ (see chapter 6).

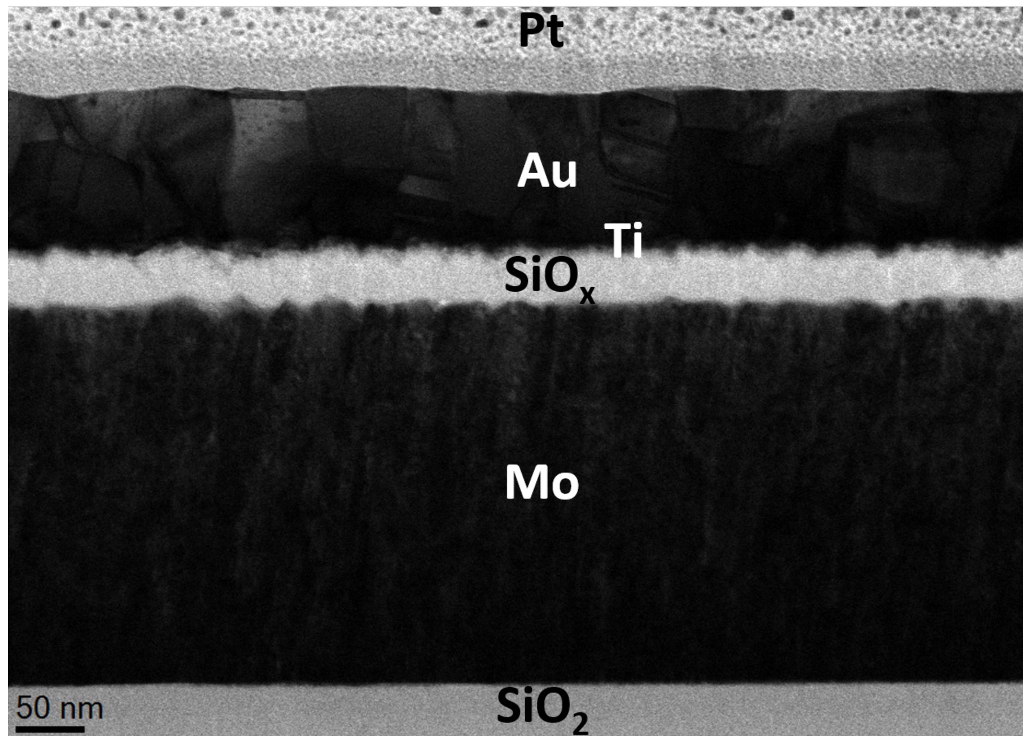


Figure 5.4: BF STEM image of an FIB-prepared cross-section from device 3. The top electrode consists of Au and Ti layers approximately 115 nm and 5 nm thick, respectively, and are separated by an SiO$_x$ layer around 35 nm in thickness. The presence of the Ti layer is not obvious, its existence and thickness was confirmed using EELS spectrum imaging. The bottom Mo electrode has a thickness of approximately 280 nm. Sputtering was carried out onto a SiO$_2$ substrate, while the top Pt layer is needed for FIB sample preparation.

The relatively large differences in atomic mass between Au, Mo, Si, and O, gives more detail in the a-SiO$_x$ layer at the expense of contrast in the Au and Mo layers in Figure 5.4. The bottom interface in device 3 is rougher (RMS roughness = 1.10 nm) in comparison to device 1 [Thornton 1986]. Figure 5.5 shows greater contrast in the Au and Mo layers in which columnar microstructure is evident. An additional granular structure is visible in the Au layer where the grains appear to be stacked upon one another to form columns. This structure is comparable to a zone 2 type structure [Movchan 1969], whereas the Mo layer better fits the description of a zone 1 type structure.

A closer inspection of the oxide layer in Figure 5.4 reveals faint and relatively bright

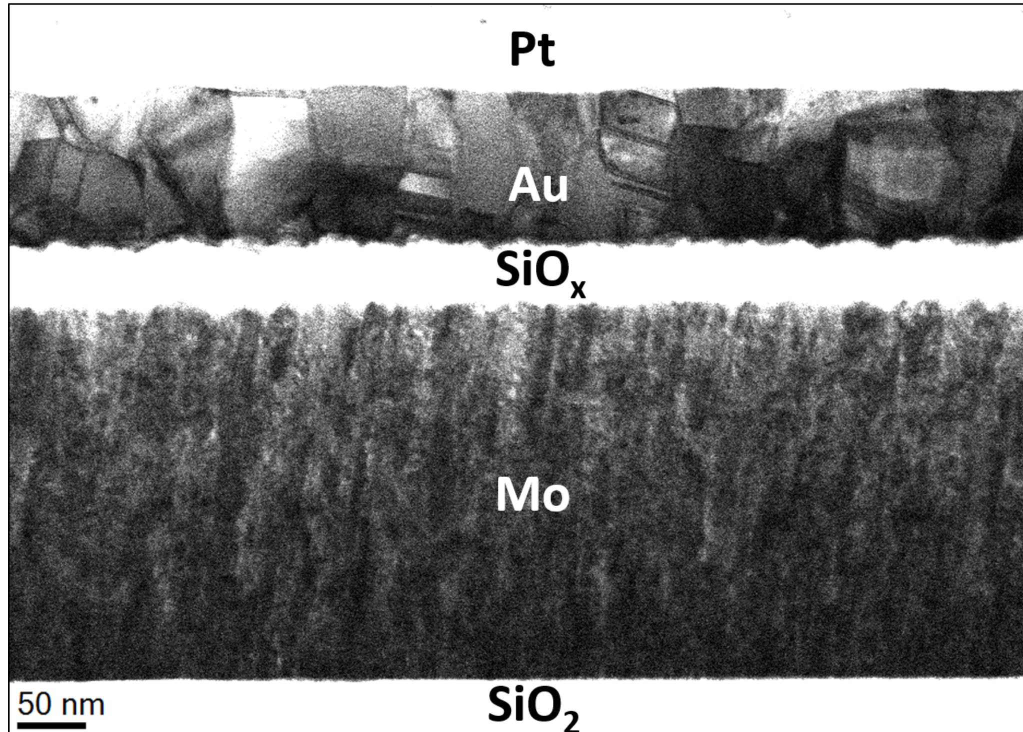


Figure 5.5: BF STEM image of an FIB-prepared cross-section from device 3, with enhanced contrast in the Au and Mo layers. Columnar microstructure is visible in these layers. Additionally, granular structure can be observed in the Au layer in which the grains appear to be stacked upon one another to form columns.

vertical streaks. In order to investigate this further, images with greater magnification were taken in additional regions of the cross-section. Figure 5.6 shows BF STEM and HAADF images in one such region. At features A and B in Figure 5.6(a), columnar microstructure in the Mo layer can be observed to extend into and across the oxide layer in which bright vertical streaks are visible. A constrast-enhanced BF STEM image is shown in (b). The bright streaks in the oxide layer in (b) correspond to the dark streaks in the HAADF image in (c). Lower brightness in the HAADF image indicates regions of low average atomic number [Pennycook 1991] and suggests the presence intercolumnar boundaries separating columns of a-SiO$_x$ that are roughly 20 nm in width. This can be compared with AFM topography maps taken on the surface of the oxide layer as shown in Figure 5.7. Bump-like features are observed on the surface, which are also approximately 20 nm in diameter. This is consistent with the columnar microstructure observed in the oxide layer in Figure 5.6.

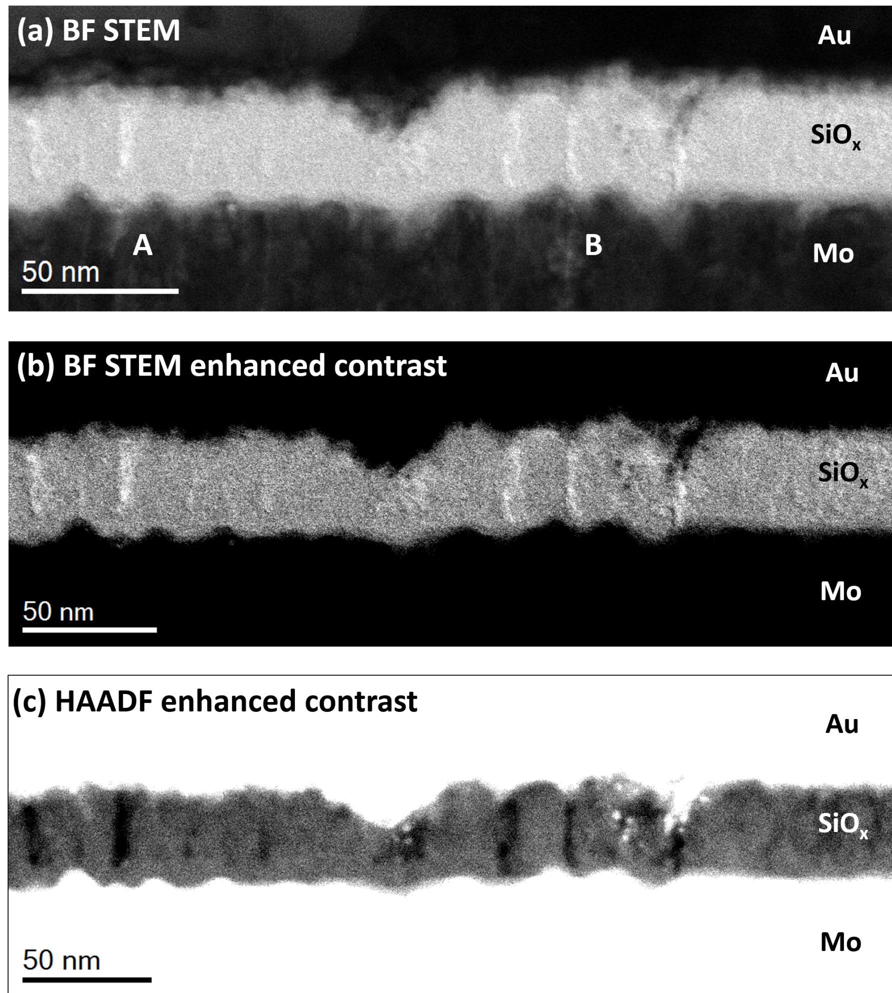


Figure 5.6: **(a)** BF STEM image of an FIB-prepared cross-section from device 3. Features A and B in Figure 5.6(a) suggest that columnar microstructure in the Mo layer extends into the oxide layer where bright vertical streaks can be observed. **(b)** Contrast-enhanced BF STEM image showing identical region to (a). Bright vertical streaks are visible in the oxide layer, which may indicate intercolumnar boundaries between columns of $SiO_x$. **(c)** Contrast-enhanced HAADF image showing identical region to (a). Dark vertical streaks are visible in the $SiO_x$ in the same regions as the bright vertical streaks in (b) and correspond to regions of low average atomic number [Pennycook 1991].

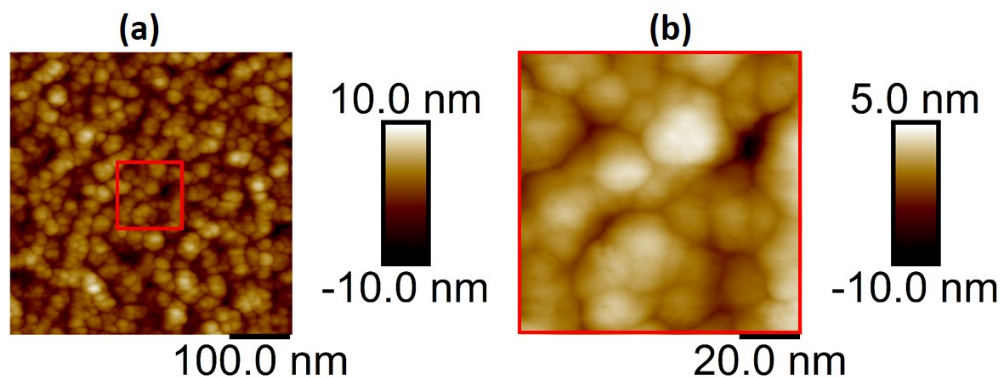


Figure 5.7: AFM topography maps taken on the surface of the a-SiO$_x$ layer in device 3 provided courtesy of Mark Buckwell at UCL. Bump-like features are observed on the surface, which are approximately 20 nm in diameter. **(b)** is a magnified topography map of the red enclosed region in **(a)**.

### 5.2.5 Device 4

Device 4 differed significantly in the thickness of the oxide layer. A top TiN electrode approximately 8 nm thick was sputtered onto an a-SiO$_x$ layer close to 5 nm in thickness. The bottom electrode consisted of Ru and TiN layers approximately 30 nm and 20 nm thick, respectively. The corresponding FIB-prepared cross-section is shown in Figure 5.8. Another unique aspect of device 4 visible from Figure 5.8 is that *MIM* sites were located along the bottom of trench structures separated by SiN spacers. For the trench structure studied here, the area at the bottom of the trench is approximately 200 nm$^2$. Since the top TiN was deposited by sputtering, it can be seen that the TiN layer becomes thicker away from the bottom of the trench. This illustrates the preferred deposition of vaporised particles onto high points on the substrate surface during sputtering. Like device 3, EELS point scans (see chapter 6) revealed an ELNES fingerprint close to that of silicon dioxide in the a-SiO$_x$ with $x \approx 2$.

Columnar microstructure is visible in the TiN and Ru electrode layers but the electrode interfaces are more planar when compared to devices 1 and 3 and may suggest inhibited columnar growth in the a-SiO$_x$ layer [Thornton 1986]. However, the thinner oxide layer may exhibit lower switching voltages due to a greater electric field strength. At the centre

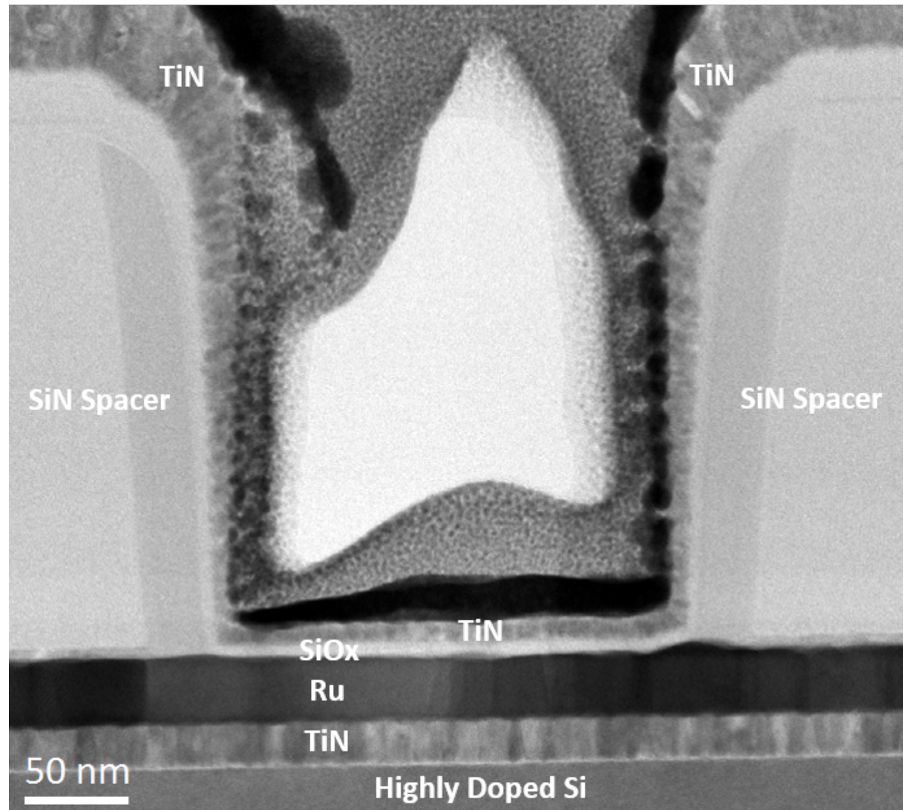


Figure 5.8: BF STEM image of an FIB-prepared cross-section from device 4. The top electrode consists of a TiN layer approximately 8 nm thick and is situated above a $SiO_x$ layer close to 5 nm in thickness. The bottom electrode consists of Ru and TiN electrodes approximately 30 nm and 20 nm in thickness. The *MIM* site is located along the bottom of a trench structure with an area of approximately 200 $nm^2$. The top TiN layer can be observed to become thicker away from the bottom of the trench as a result of the preferred deposition of vaporised particles onto high points on the substrate surface during sputtering [Thornton 1986]. The Pt and Au layers are a result of FIB sample preparation.

of the a-$SiO_x$ layer, towards the bottom interface, a small protrusion of Ru appears to be present. The oxide layer appears to be thinner in this region, and such a site may be particularly favourable site for conductive path formation.

| Transport Type | Dependence |
|---|---|
| Schottky Emission | $J \propto T^2 exp(A\frac{\sqrt{E}}{T} - B)$ |
| Direct Tunnelling | $J \propto exp(-A\epsilon_r t_{ox,eq})$ |
| Fowler-Nordheim Tunnelling | $J \propto E^2 exp(\frac{-A}{E})$ |
| Poole-Frenkel Emission | $J \propto E exp(A\frac{\sqrt{E}}{T} - B)$ |
| Trap-Assisted Tunnelling | $J \propto exp(\frac{-A}{E})$ |

Table 1: Table summarising dependences of current density (J) on electric field (E) and temperature (T) for various electron transport processes in insulators [Lim 2015]. For direct tunnelling, $\epsilon_r$ is the relative dielectric constant, and $t_{ox,eq}$ is the equivalent thickness of the insulating layer. $A$ and $B$ are constants.

## 5.3 Electroforming

During the electroforming process in an *MIM* stack, electron transport across the insulating layer can take place through a number of mechanisms. At high enough temperatures, electrons at the cathode can gain enough energy to overcome the Schottky barrier and enter the insulator's conduction band ('Schottky emission'). For oxides thinner than 3 nm, 'direct tunnelling' across to the anode may also become significant [Lim 2015]. In contrast, a strong enough electric field in thicker oxides can also permit significant 'Fowler-Nordheim' tunnelling into the conduction band from the cathode. As discussed in chapter 3, intrinsic electron traps [El-Sayed 2013A] as well as oxygen vacancies [Kimmel 2009] can form electron trapping sites in silicon oxides. Electrons approaching from the cathode may also tunnel into such traps. These electrons can be transported across the insulator through thermal excitations and through tunnelling into additional traps. 'Poole-Frenkel emission (PFE)' is characterised by repeated thermal excitation from traps into the conduction band followed by electron capture at additional electron traps. In contrast, 'trap-assisted tunnelling' (TAT) is a result of tunnelling between electron traps across the insulting layer into the anode. The discussed processes are illustrated in Figure 5.9 and their dependences on electric field and temperature are summarised in Table 1

Changes in I-V behaviour during electroforming and between the set and reset states in ReRAM devices indicate a change in the contribution from various electron transport

processes. Fitting I-V data to models for different transport processes can give an idea of which processes are involved. For resistive switching in a-SiO$_x$ at room temperature and pressure as studied in this thesis, an analysis of conduction mechanisms was presented by Mehonic et al. [Mehonic 2012A][Mehonic 2012B]. The studied devices were capable of bipolar and unipolar switching behaviour. In the high resistance state, a good fit for FNT and TAT was found [Mehonic 2012A]. In contrast, during bipolar switching a good fit was found only for TAT in the low resistance state. Furthermore, in the unipolar low resistance state, both Ohmic and TAT were a good match to the I-V characteristics. TAT between Si nanoinculsions in the oxide matrix was therefore suggested as a conduction mechanism in the low resistance state [Mehonic 2012A][Mehonic 2012B]. In the following I-V curves, the top electrode was positively biased, except in the case of device 3 where the Au electrode was both positively biased and negatively biased.

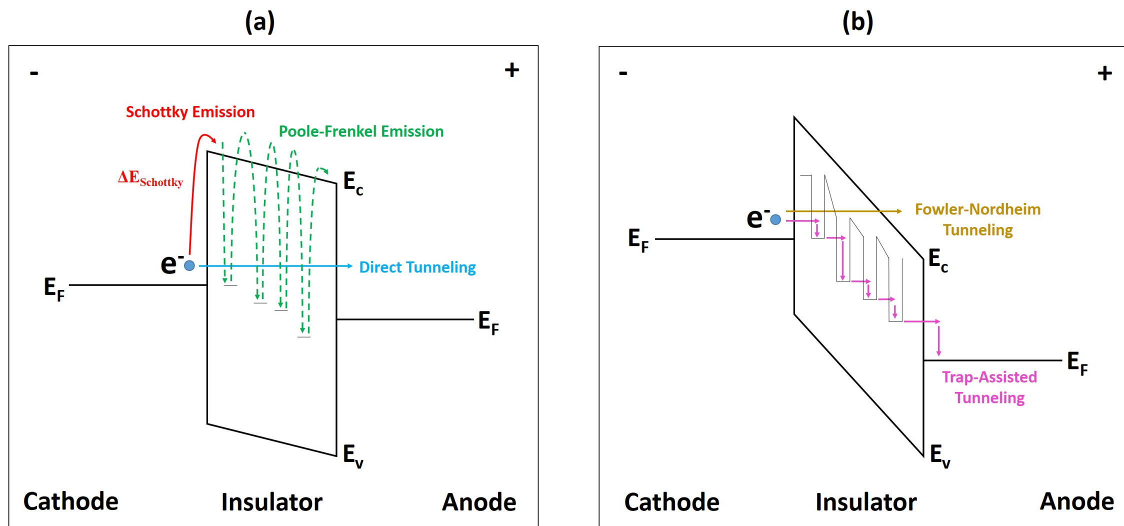


Figure 5.9: Schematic illustrating electron transport processes across the insulating layer in an *MIM* structure. **(a)** Schottky emission: electrons overcome the Schottky barrier $\Delta E_{Schottky}$ to enter the insulator's conduction band $E_c$; direct tunnelling: for thin insulating layers, significant one-step tunnelling across the insulating layer can occur; Poole-Frenkel emission: trapped electrons can be repeatedly thermally excited into the conduction band of the insulating layer. **(b)** Fowler-Nordheim tunnelling: a high enough electric field promotes significant tunnelling into the conduction band of the insulating layer; trap-assisted tunnelling: electrons tunnel across the insulating layer through electron traps.

### 5.3.1 Device 1

Device 1 exhibited unipolar switching behaviour and a typical electroforming voltage of approximately 6 V, with an endurance on the order of $10^2$ switching cycles [Mehonic 2015][Mehonic 2016]. This switching behaviour was observed to be independent of electrical contact size, suggesting the formation of a single conductive path. An example electroforming curve for device 1 is shown in Figure 5.10. Switching to the low resistance state is observed at approximately 5 V with a current compliance of 3 mA, which corresponds to an approximate electric field strength of 1.4 MV $cm^{-1}$. This can be compared to a much larger electric field strength of ≈10 MV $cm^{-1}$ typically required for hard breakdown in silicon dioxide films of a similar thickness [Osburn 1972]. Beginning from 0 V, an upwards slope of relatively constant curvature and decreasing gradient is observed until 3 V. Above 3 V, relatively large jumps in current are observed until the low resistance state is obtained. The rapid changes in current above 3 V are perhaps indications of the growth of Si nanoinclusions and the onset of more dominant TAT as suggested by Mehonic et al. [Mehonic 2012B].

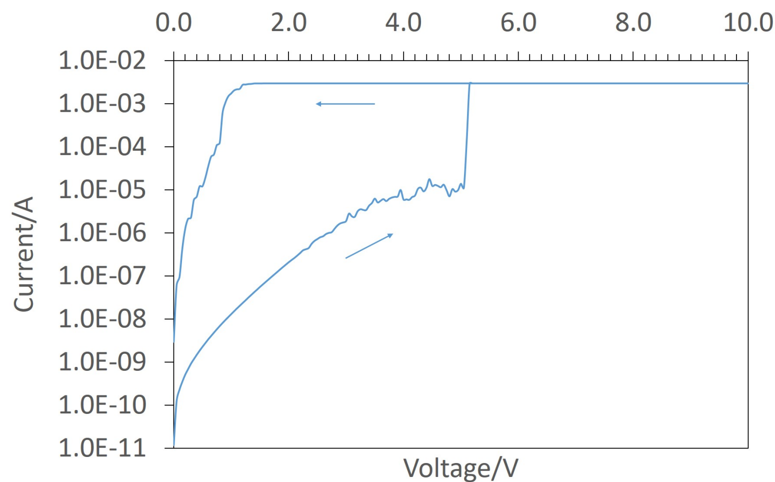


Figure 5.10: Typical electroforming curve for device 1 provided courtesy of Mark Buckwell at UCL. Switching to the low resistance state is observed at approximately 5 V with current compliance of 3 mA. When current compliance is reached, the voltage is held at approximately 1.2 V.

### 5.3.2 Device 2

Device 2 exhibited no resistive switching behaviour. The I-V curve for the FIB cross-section from device 2 is shown in Figure 5.11, where it can be seen that breakdown occurs at approximately 18 V with a current compliance of 100 $\mu$A. This corresponds to an approximate electric field strength of 5.1 MV cm$^{-1}$, which is more than three times the value for device 1. The I-V curve can be split into three regions marked (a), (b), and (c), respectively, with different gradients. This suggests changes in the electron transport regime during electrical stressing and indicates a deviation from the conduction mechanism observed in device 1. Region (a) is characterised by a relatively small gradient, whereas in region (b), the I-V curve exhibits a constant curvature and decreasing gradient, which is comparable to device 1. In region (c), a more linear slope is again observed.

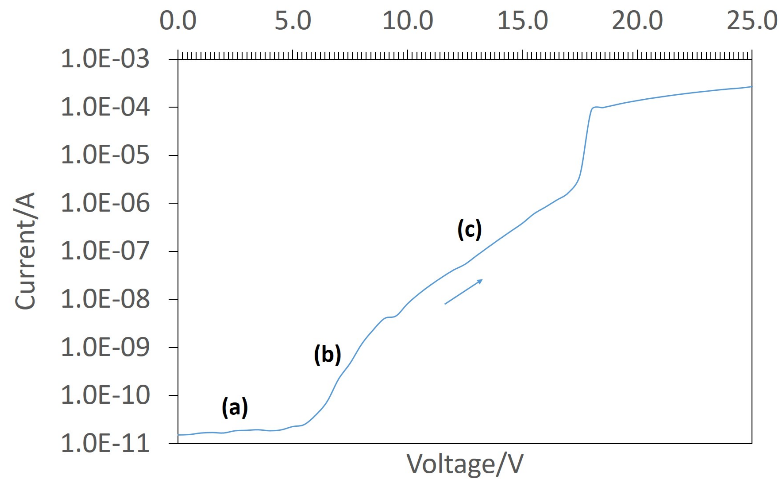


Figure 5.11: I-V curve for the FIB cross-section from device 2. Breakdown occurs at approximately 18 V with a current compliance of 100 $\mu$A.

The poor switching behaviour could be related to the flatter interfaces, which may indicate inhibited columnar growth in the oxide layer [Thornton 1986]. This is also likely to be strongly influenced by the oxygen-rich interfacial layer at the bottom electrode.

### 5.3.3 Device 3

Device 3 only exhibited resistive switching behaviour when the top Au electrode was negatively biased. Such devices exhibited bipolar switching behaviour with a typical electro-

forming voltage of approximately -4 V and an endurance on the order of $10^7$ switching cycles. This is the lowest electroforming voltage and the greatest endurance of all of the studied devices and could be a result of rougher oxide-electrode interfaces and enhanced columnar microstructure. This switching behaviour was observed to be independent of electrical contact size, again suggesting the formation of a single conductive path. An example electroforming curve is shown in Figure 5.13. The low resistance state is obtained at approximately -2.6 V with a 1 mA current compliance. This corresponds to an approximate electric field strength of 0.7 MV cm$^{-1}$. Rapid jumps in current are observed beginning at around -1 V, which is similar to the behaviour of device 1 after 3 V. The behaviour of the current above -1 V may again indicate the growth of Si nanoinclusions and the onset of more dominant TAT as suggested by Mehonic et al. [Mehonic 2012A]. Figure 5.13 demonstrates the endurance of these devices, showing $10^7$ switching cycles, with the high and low resistance states separated by about one order of magnitude.

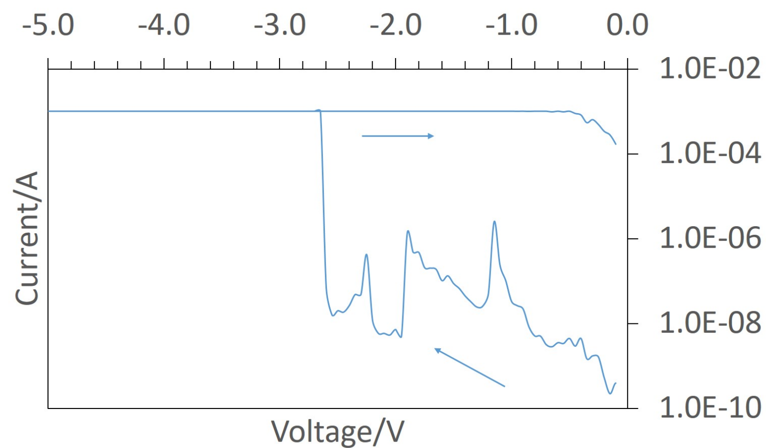


Figure 5.12: Typical electroforming curve for device 3 for a negatively biased Au electrode provided courtesy of Adnan Mehonic at UCL. Switching to the low resistance state is observed at approximately -2.6 V with a current compliance 1 mA. When current compliance is reached, the voltage is held at close to 0.4 V.

When the Au electrode was positively biased, no resistive switching behaviour was observed. The I-V curve for the FIB cross-section from the positively biased device is shown in Figure 5.14. The current compliance of 50 $\mu$A is reached at approximately 15 V, which corresponds to an approximate electric field strength of 4.3 MV cm$^{-1}$. Until 3 V, a relatively constant curvature is observed, with gradient decreasing with increased voltage. Above approximately 3 V, rapid jumps in current can be observed until current compliance is reached. It should be noted that no abrupt change in current is seen in

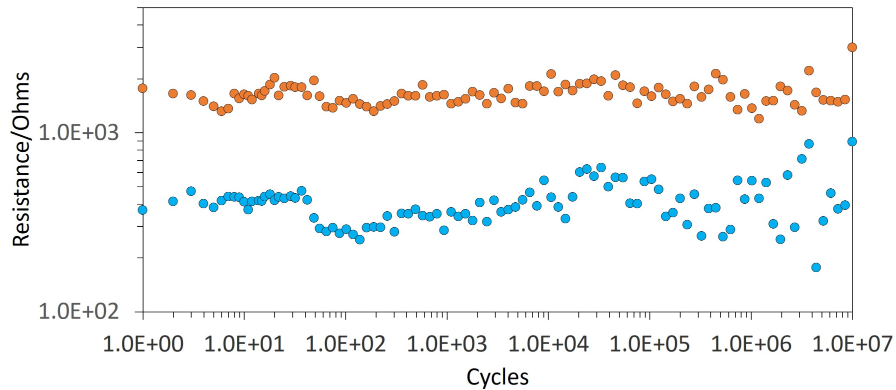


Figure 5.13: Demonstration of the endurance of device 3 when cycled between high (orange) and low (blue) resistance states when a negative bias is applied to the Au electrode. Approximately $10^7$ switching cycles are recorded. This data is provided courtesy of Adnan Mehonic at UCL.

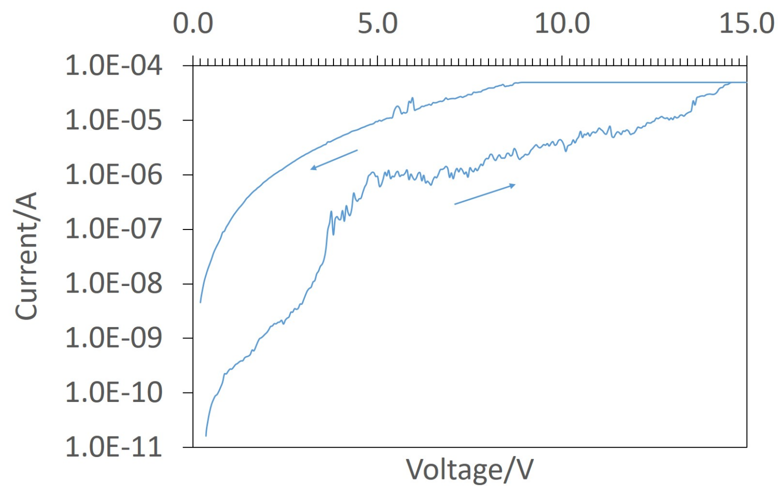


Figure 5.14: I-V curve for device 3 associated with the positively biased cross-section provided courtesy of Adnan Mehonic at UCL. The current compliance of 50 $\mu$A is reached at approximately 15 V. When current compliance is reached, the voltage is held at approximately 9 V.

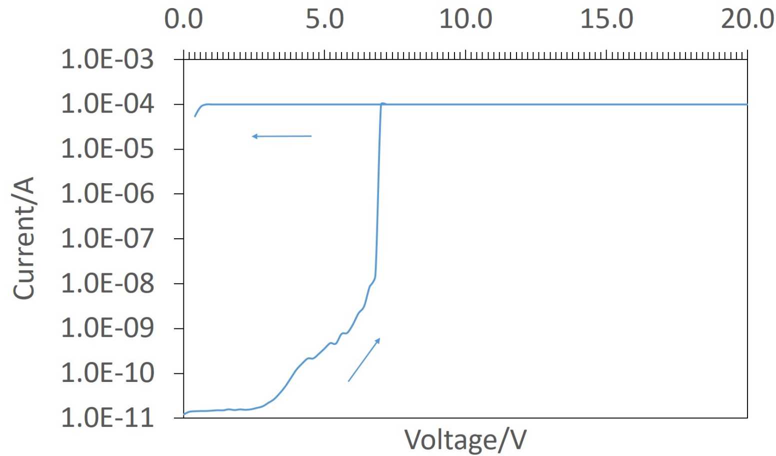


Figure 5.15: I-V curve for the FIB cross-section from device 4 provided courtesy of Luca Montesi at UCL. Breakdown occurs at approximately 7 V with a current compliance of 100 $\mu$A. When current compliance is reached, the voltage is held at close to 0.6 V.

the studied device, although this was observed in some of the positively biased devices. The differences in behaviour of device 3 under positive and negative biasing may be a result of the asymmetry in its *MIM* structure. This will be discussed further in chapter 6.

### 5.3.4 Device 4

Device 4 exhibited no resistive switching behaviour. The I-V curve for the FIB cross-section from device 4 is shown in Figure 5.15, where it can be seen that breakdown occurs at approximately 7 V with a current compliance of 100 $\mu$A. This corresponds to an approximate electric field strength of 14 MV cm$^{-1}$ and far exceeds devices 1 to 3. However, previous studies suggest that thinner oxide layers require stronger electric fields for breakdown to occur [Osburn 1972]. Initially, the I-V curve has a relatively constant slope similar to region (a) for device 2. Above approximately 2.5 V, a relatively constant curvature is observed with decreasing gradient until breakdown occurs.

## 5.4 Discussion and Summary

The characteristics of devices 1 to 4 are summarised in Table 2 and will be a useful reference in the following chapters.

|  | Structure | Thickness/nm | Stoichiometry $x$ | Electric Field for Electroforming/Breakdown/MV cm$^{-1}$ |
|---|---|---|---|---|
| Device 1 | TiN/SiO$_x$/TiN | 85/35/80 | 1.3 | 1.4 (2.9) |
| Device 2 | TiN/SiO$_x$/TiN | 15/35/10 | 1.3 | 5.1 |
| Device 3 Negative Bias | Au/Ti/SiO$_x$/Mo | 115/5/35/280 | 2 | 0.7 (2.6) |
| Device 3 Positive Bias | Au/Ti/SiO$_x$/Mo | 115/5/35/280 | 2 | 4.3 |
| Device 4 | TiN/SiO$_x$/Ru/TiN | 8/5/30/20 | 2 | 14 |

Table 2: Table summarising main characteristics of the *MIM* stacks studied in this thesis. For all devices, the displayed electric field strengths for electroforming/breakdown correspond to the I-V curves shown in section 5.3, and the values in the brackets for device 1 and device 3(negative bias) show the maximum recorded electroforming field strengths. Only these devices displayed resistive switching behaviour, with the latter exhibiting the lowest electroforming voltages and the greatest endurance. Device 3 also has the most rough interfaces out of all of the devices, followed by device 1. In contrast, devices 2 and 4 have relatively flat interfaces. 'Positive Bias' and 'Negative Bias' refer to the top Au electrode in device 3.

The presented analysis of device structure and electrical behaviour appears to reveal some notable patterns in the studied devices. Firstly, device 3 (negative bias) was found to exhibit the lowest electroforming voltages and greatest endurance, followed by device 1. Both devices were observed to have rough oxide-electrode interfaces, with device 3 having the roughest interface. Furthermore, columnar microstructure was clearly visible in the oxide layer for device 3. This is consistent with enhanced columnar growth on substrates with rougher surfaces during sputtering, which results in more continuous intercolumnar boundaries [Thornton 1986]. Both devices also exhibit comparable electroforming behaviour before reaching the low resistance state. In contrast, devices 2 and 4 possessed relatively flat interfaces, which indicate inhibited columnar growth in the oxide layer [Thornton 1986]. All non-switching devices (devices 2, 3 (positive bias), 4) also exhibited contrasting I-V behaviour to devices 1 and 3, with characteristically high electric fields above 4 MV cm$^{-1}$ for breakdown. Meanwhile for devices 1 and 3 (negative bias), electroforming typically occurs at electric fields below 2 MV cm$^{-1}$. Finally, it should be noted that in devices 1, 2 and 3(negative form), the thickness of the oxide layer is similar and relatively inert electrode materials have been chosen, which are unlikely to result in metallic ion migration and the formation of a metallic filament. Additionally, previous studies on a-SiO$_x$ have concluded in resistive switching behaviour being intrinsic to the oxide layer (see Section 3.2.2). This indicates that the differences in electrical behaviour of devices 1, 2, and 3(negative form) are strongly dependent on the differences in the oxide layer. The most obvious difference in the oxide layer is increased electrode-oxide interface roughness, resulting in the enhanced columnar microstructure in device 3. This suggests that increasing interface roughness, which results in enhanced columnar microstructure, promotes lower electroforming voltages and improved device endurance.

# 6 Nanoscale Oxygen Dynamics in Electrically Stressed *MIM* Structures with an a-SiO$_x$ Insulating Layer

## 6.1 Introduction

Literature regarding hard and soft breakdown in silicon oxides has often focused on the location and analysis of a local breakdown site. However, the sizes of the electrical contacts used in devices 1, 2, and 3, made the identification of such sites difficult for analysis in a TEM. Furthermore, a collaborative conductive AFM tomography study on device 1 suggested that these sites may be far greater in extent than the thickness of a TEM sample prepared using an FIB, reaching an approximate diameter of 900 nm [Buckwell 2015]. However, Buckwell et al. used a tungsten probe in direct contact with the a-SiO$_x$ layer in order to form a breakdown path. Stressing voltages of 20 V were used, which are far greater than the typical 6 V required when electroforming using a top TiN contact [Buckwell 2015][Mehonic 2016]. A high voltage was deliberately applied in order to form a large conductive path and overcome the oxygen-rich surface layer since the surface was exposed to the atmosphere. The AFM probe was then used to locate a conductive spot on the surface of the a-SiO$_x$ and etch away the layer. Despite the difficulty in locating a conductive path for analysis in a TEM, the following *ex situ* studies on electrically stressed device cross-sections revealed structural changes in the oxide layer far greater in extent than previously believed. The following experimental data formed part of a large collaborative effort [Buckwell 2015][Mehonic 2015][Montesi 2016][Mehonic 2016] to understand structural change in *MIM* stacks with an a-SiO$_x$ insulating layer under electrical stressing conditions. In this chapter, the effects of electrical stressing on devices 1, 2, and 3, are studied using STEM imaging, STEM tomography, and EELS analysis. Following a description of the methods used, each device will be discussed in turn. The reader is referred to Table 2 in section 5.4 for a summary of the structure and electrical behaviour of devices 1 to 3. It should be emphasised that the electrically stressed devices in this chapter have been either electroformed or have exhibited hard breakdown, and no further switching has been attempted. FIB sample preparation was carried out by Hui Ru Tan (device 1), June Ong Lay Ting (device 2), and Siew Lang Teo (device 3)

at IMRE.

## 6.2 Methodology

TEM sample cross-sections were prepared and the following scanning electron microscopy (SEM) images were acquired using an FEI Helios Nanolab 600 FIB. Details of this procedure are given in section 3.2. STEM imaging was carried out and EELS spectra were acquired at 80 keV using an FEI Titan (S)TEM, as this high tension value was found to produce minimal beam damage to the studied cross-sections during spectrum acquisition. Higher resolution, aberration-corrected images were taken at 200 keV using a JEOL JEM-ARM200F TEM. EELS spectra were acquired using a Gatan Imaging Filter (GIF) with a 14.4 mrad convergence semi-angle. For device 1, a collection semi-angle of 25 mrad was recorded, whereas for the remaining devices a semi-angle of 30 mrad was recorded. All data processing was carried out using the Digital Micrograph© software. For devices 1 and 2, a power law background was found to best fit the EELS spectra, while for device 3 a first degree log polynomial provided a more suitable background fit. All of the displayed spectra have been deconvolved using the Fourier-Ratio method (see section 3.6).

For device 1, the core-loss spectrum image for the unstressed cross-section was acquired using an acquisition time of 200 ms per spectrum, while for the electroformed cross-section 400 ms per spectrum was used. The difference in acquisition time was a result of obtaining the maximum signal-to-noise ratio without saturating the GIF. Low-loss spectrum images were acquired for 200 ms per spectrum for both cross-sections. Two sets of spectrum maps were acquired for device 2 from unstressed and stressed cross-sections. Firstly, a pair of higher resolution core-loss maps were acquired at 200 ms per spectrum, and the corresponding low-loss maps at 100 ms per spectrum. Secondly, a pair of lower resolution maps were acquired at 100 ms and 50 ms per spectrum for core-loss and low-loss maps respectively. For device 3, all core-loss maps were acquired at 100 ms per spectrum, while low-loss maps were acquired at 20 ms per spectrum. Relative mass density maps in the oxide layer were obtained by combining Si and O elemental maps with the corresponding relative thickness map [Thomas 2013][Lakoubovskii 2008]

(also see section 3.6). The relative mass density map, $\rho$, can be calculated from the following formula:

$$\rho \propto \sqrt[0.7]{\frac{\sum_i I_{elementalMap_i}}{I_{thicknessMap}}}, \tag{4}$$

where $I_{elementalMap_i}$ is the background-corrected and multiple scattering deconvolved intensity map of the element $i$, and $I_{thicknessMap}$ is the relative thickness map. It was assumed that the compatibility of this method with a-$SiO_2$ extends to a-$SiO_x$. All of the displayed EELS spectra, EELS spectrum images, and relative density maps have been normalised using the highest recorded count. As a result, only relative differences in counts are comparable within the maps.

STEM HAADF tomography was carried out at 80 keV using a Fischione analytical tomography holder (2021). Tilting increments of 2$^{\circ}$ were used in all cases. Reconstruction was carried out using the SIRT algorithm as implemented in the Inspect 3D© software with 50 iterations and the resulting tomograms were processed using the Amira© software. It should be noted that the presented tomograms are displayed in greyscale and represent 3-dimensional HAADF images, with regions of high intensity corresponding to regions of high atomic number [Pennycook 1991]. The corresponding isosurfaces represent intervals within the intensity range, with intervals located at the lowest intensities corresponding to regions of low atomic number.

## 6.3 Results

### 6.3.1 Device 1

Figure 6.1 shows BF STEM images of regions in unstressed and electroformed FIB-prepared cross-sections from device 1. The contrast between bright and dark regions within the oxide layer is greater for the electroformed cross-section, which suggests a greater degree of inhomogeneity in the oxide matrix when compared to the unstressed cross-section. An EELS spectrum image was taken within the red enclosed region in the BF STEM images together with a HAADF image. The HAADF images also indicate a degree of inhomogenity within the unstressed cross-section; however, the corresponding Si and O coreloss maps show a clear enhancement of this inhomogeneity after electroforming. The relative mass density maps suggest that regions of high Si counts are more dense. Figure 6.2 shows a plot of the *Si-L*$_{2,3}$ edge for spectra summed from regions of high and low Si counts in the Si maps for the electroformed cross-section. An averaged sum from the unstressed cross-section is also shown for reference. The *Si-L*$_{2,3}$ edge shows an increase in the relative height of the shoulder A as compared to peak B for high Si count regions, with a difference in heights of approximately 0.27. This can be compared to a difference of approximately 0.34 in the low Si count regions. Peak B was previously observed to indicate the number of Si-$O_4$ bonding environments [Batson 1993], and suggests that at high Si count regions the relative O content is lower.

A closer examination of the electroformed Si map and relative mass density maps appears to show a periodic repetition in high intensity signal along the width of the cross-section. Figure 6.3(a) shows a line profile taken from left to right of the Si, O, and relative mass density maps, and integrated across the thickness of the oxide layer. Peaks in Si intensity are seen approximately every 10 nm and indicate periodic changes in density along the a-Si$O_x$ layer. Peaks in Si signal coincide with troughs in the O signal, and regions of high O signal can be observed to coincide with regions of low relative mass density. Figure 6.3(b) confirms the apparent negative correlation between Si and O counts along the width of the cross-section. These structures could be related to columnar growth in the oxide layer as a result of the use of sputtering in its preparation [Thornton 1986]. The enhancement in contrast in the electroformed cross-section

could suggest the build-up of O at less densely packed intercolumnar boundaries, since regions of high Si counts are associated with regions of low density.

Figure 6.4 shows a scanning electron microscope (SEM) top view image taken from an electroformed top TiN contact on device 1 and reveals dome-like deformations on the surface. These observations are consistent with AFM measurements [Mehonic 2015][Mehonic 2016] and were a common feature of electroformed devices. Such deformations have previously been attributed to the build up of gaseous oxygen under the top electrode in $TiO_2$ and $SiO_x$ [Jeong 2008][Wang 2013]. Figure 6.5(a) and (b) show cross-sectional HAADF images in the unstressed and electroformed cross-sections of device 1. In each case, a dark protrusion into the top TiN electrode from the oxide layer can be seen. This is particularly visible in Figure 6.5(b)2, where the protrusion is darker than the oxide layer and suggests the presence of an interfacial void. These structures have corresponding deformations on the surface of the TiN electrode, which are enhanced in the electroformed cross-section, and are consistent with the deformations in Figure 6.4. Features C and D in Figure 6.5(b)1 and (b)2 indicate that the TiN layer has been subjected to physical stress, which is not visible in the unstressed cross-section. Figure 6.5(c) shows an aberration-corrected BF STEM image of feature C in Figure 6.5(b)1, where the edge of a TiN crystallite is cleary visible on the left. These observations could suggest the dislocation of a column of TiN. Furthermore, a high-resolution EELS points scan shown in Figure 6.5(d) and taken at feature E in Figure 6.5(b)2 reveals the presence of O with no corresponding Si signal. Only Ti and N signals were detected, suggesting oxidation of the TiN layer. This could indicate an upwards migration of O towards the positively biased electrode during electrical stressing. Also shown for comparison is the corresponding signal at the *O-K* edge in the TiN layer of the unstressed cross-section. Finally, feature F in Figure 6.5(b)2 shows a grey, globular structure present within the a-$SiO_x$ and similar features are present elsewhere. Such features revealed a faint TiN signal under high-resolution EELS point scans, and no signal was detected using the spectrum image acquisition parameters. Tomographic reconstruction revealed that these features are in fact present on the surface of the TEM cross-section and suggest the re-deposition of TiN during ion beam milling for FIB preparation. Regions of re-deposition were only visible in devices 1 and 2. As a result, sites for EELS spectrum imaging were selected with care in order to avoid such regions. This would suggest that TiN is particularly susceptible to

re-deposition during FIB milling. Lower ion milling energies were used in order to prevent this effect; however, this was only partially successful.

In order to gain a deeper understanding of the possible void structures, STEM tomographic reconstructions of Figure 6.5(a) and (b) were analysed. Figure 6.6 shows 3D reconstructions for Figure 6.5(a)1 and (a)2. In both cases, the interval from the lowest isosurface values (corresponding to regions of lowest atomic number [Pennycook 1991]) reveals that the structures are open at one end of the cross-section and closed at the other end of the cross-section, and are indeed voids. This would suggest that they form part of a larger defect, perhaps small dome-like formations similar to those observed in Figure 6.4. Figure 6.7 shows 3D reconstructions of Figure 6.5(b)1 and (b)2. The dislocation of the TiN column is visible through the thickness of the electroformed cross-section in Figure 6.5(b)1, and strong plastic deformation is visible in the top TiN layer in Figure 6.5(b)2. In a collaborative study, *in situ* electrical stressing was carried out using a SIMS in residual gas analysis (RGA) mode. As a result of electrical stressing, O molecules originating from the positively biased top TiN contact were detected [Mehonic 2016]. Together with presented observations, this suggests potential outmigration of oxygen from the oxide layer and *MIM* structure, which results in plastic deformation of the positively biased top TiN electrode. Oxygen collecting at interfacial void structures between electrodes in unstressed devices may result in pressures high enough to push up a column of TiN. This may in turn result from columnar microstructure in the TiN electrode through sputtering deposition [Thornton 1986].

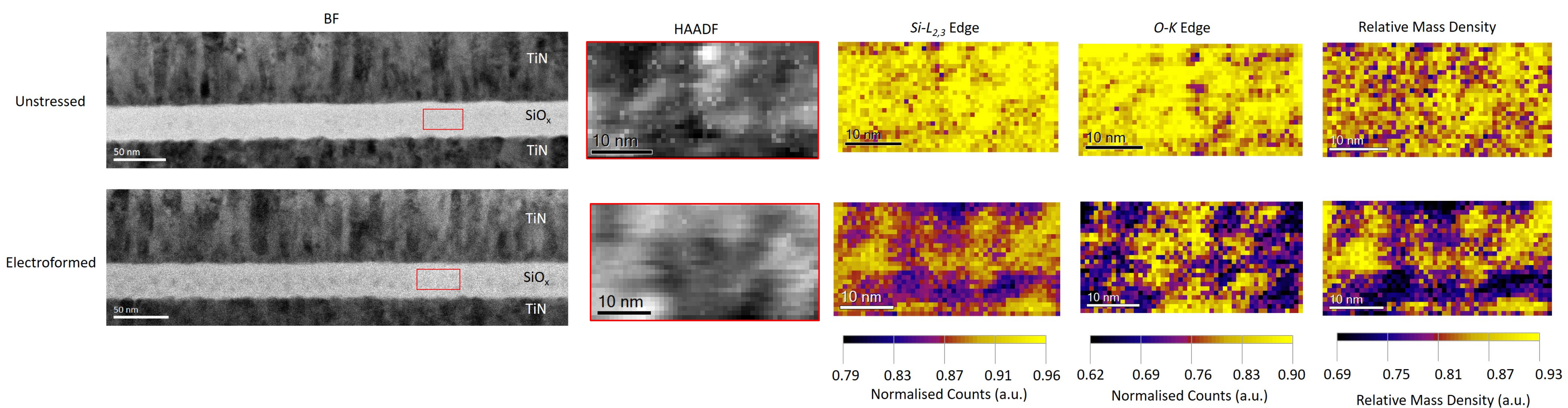


Figure 6.1: From device 1, EELS spectrum images have been taken within the red enclosed region shown in the BF STEM images and the corresponding normalised relative mass density maps have been derived. An increased degree of inhomogeneity is apparent from the BF STEM images in the electroformed cross-section. The HAADF images indicate that this is also the case for the unstressed cross-section. However, the elemental maps indicate a clear enhancement of inhomogeneity after electrical stressing, with silicon-rich regions corresponding to higher relative mass density.

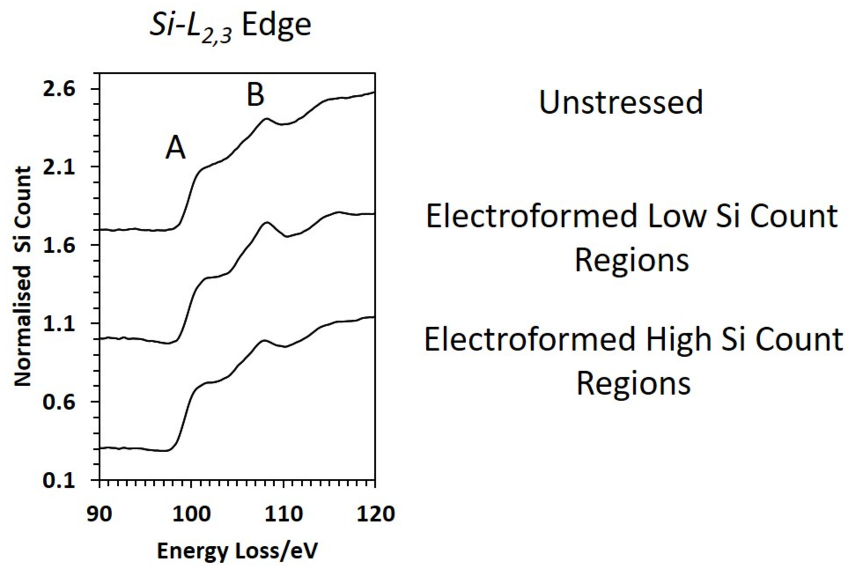


Figure 6.2: Plot showing the *Si-L*$_{2,3}$ edge, with summed spectra taken from the high and low Si count regions in the Si maps, respectively, for the electroformed cross-section from Figure 6.1. An averaged spectrum from the unstressed cross-section is also shown for reference. The increase in height of the shoulder at A relative to peak B (B-A≈0.27) in the high Si count regions as compared to the low Si count regions (B-A≈0.34) indicates a reduction in Si-$O_4$ bonding environments [Batson 2003].

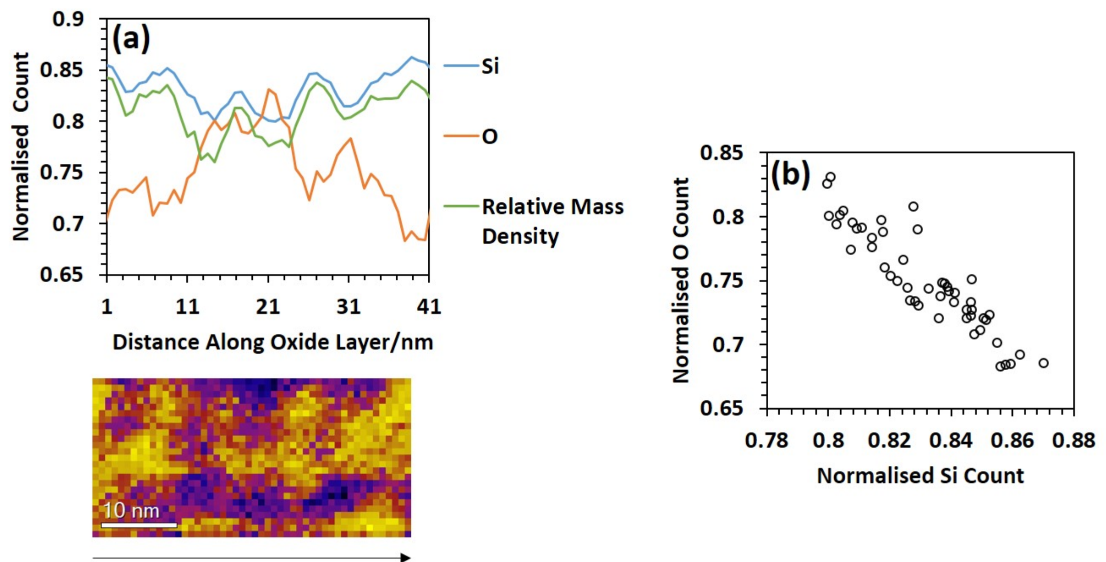


Figure 6.3: **(a)** Line profile taken along the a-Si$O_x$ layer from left to right, and integrated across the thickness of the layer for the electroformed Si map, O map, and relative mass density map in Figure 6.1. Peaks in Si intensity appear periodically with intervals of approximately 10 nm. Peaks in the Si and relative mass density maps coincide with troughs in the O map. **(b)** Plot of normalised O count against normalised Si count in (a): a negative correlation can be observed.

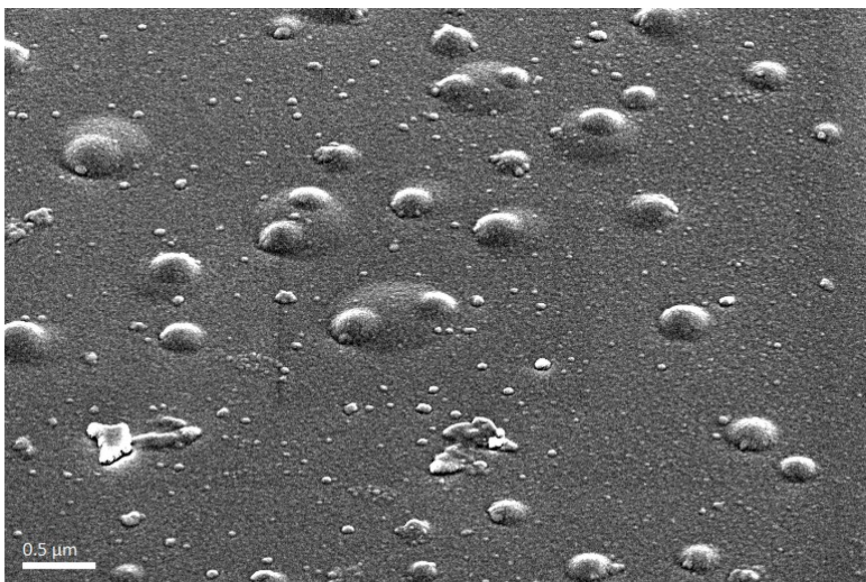


Figure 6.4: An SEM top view image of an electroformed contact from device 1 reveals the presence of dome-like deformations on the surface of the top TiN electrode. This image is provided courtesy of Hui Kim Hui at IMRE.

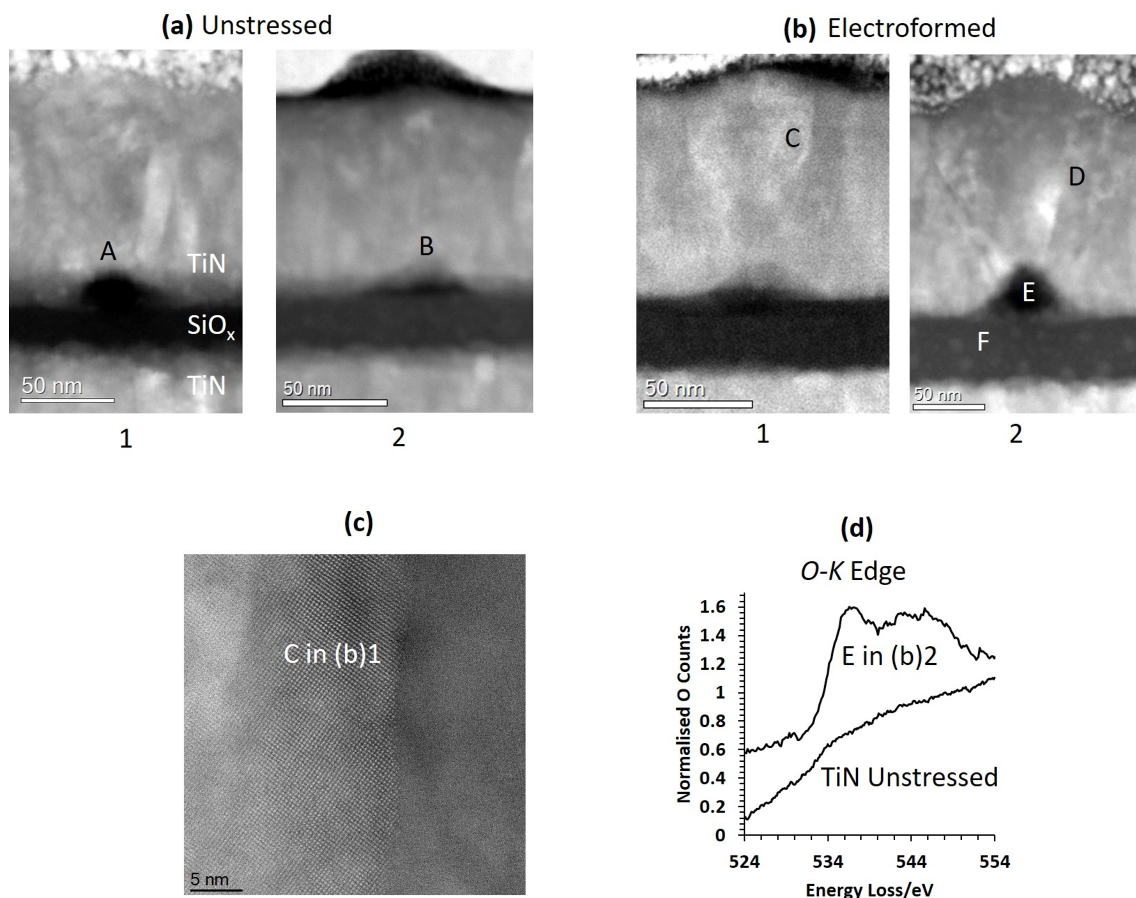


Figure 6.5: **(a)**HAADF images of dark protrusions into the top TiN electrode layer from the oxide layer in the unstressed cross-section of device 1. These structures are approximately 50 nm in width and coincide with slight deformations on the surface of the TiN layer above. **(b)** HAADF images of dark protrusions into top TiN electrode layer from the oxide layer in the electroformed cross-section of device 1. In this case, these structures can clearly be correlated with deformation of the surface of the TiN layer, with signs of physical stress in the TiN layer at features C and D in (b)1 and (b)2. The darker contrast in the protrusion in (b)2 suggests the presence of an interfacial void. Feature F in (b)2 shows a globular structure in the oxide layer. This was a result of re-deposition of the TiN layer onto the surface of the TEM cross-section in some regions during FIB preparation. **(c)** A higher resolution image at feature C in (b)1 reveals the edge of a columnar crystallite in the TiN layer. **(d)** EELS point scans at feature E in (b)2 revealed the presence of O with no detectable Si signal. However, Ti and N signals were detected, suggesting oxidation of the top TiN electrode. Also shown is the signal from the *O-K* edge in the TiN layer of the unstressed cross-section for comparison.

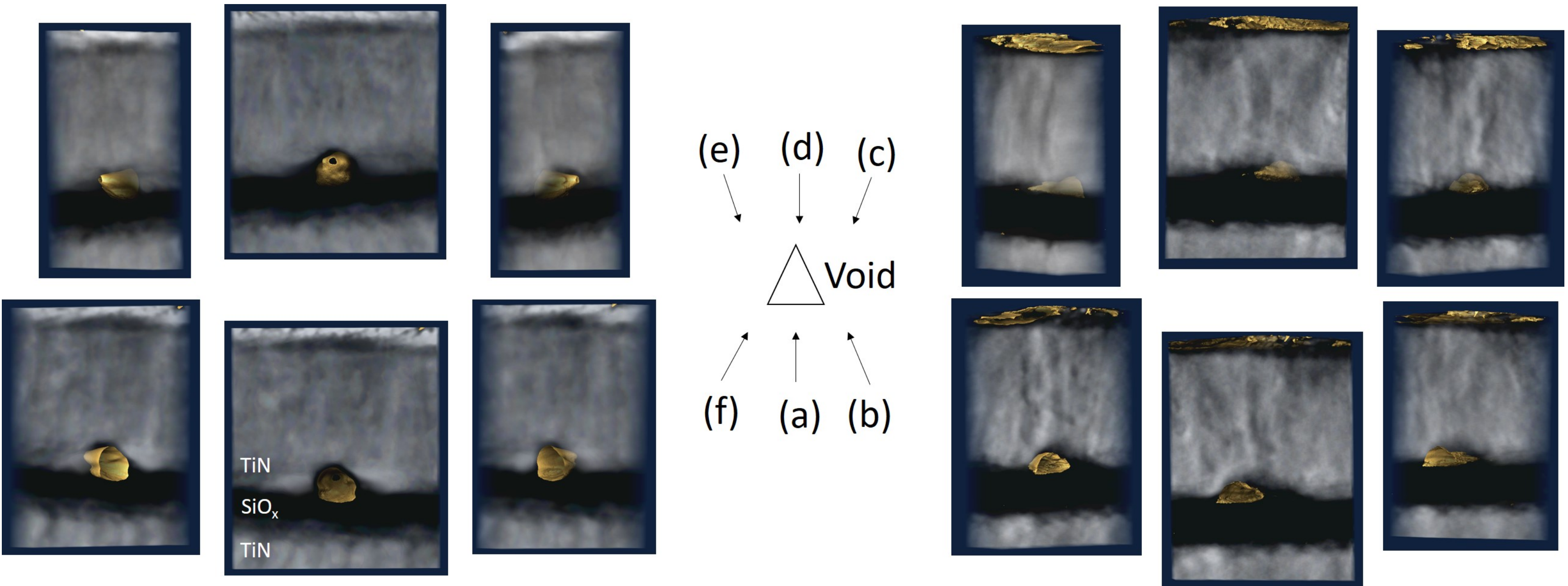


Figure 6.6: Tomographic reconstructions of Figure 6.5(a)1 and (a)2. Images (a)-(f) correspond to different viewing angles, where (a) is taken to be the front of the cross-section. A greyscale colour scheme has been implemented so that lighter regions correspond to greater atomic number. In addition, a gold feature is shown which corresponds to an interval from the lowest isosurface values. Part of isosurface is located at features A and B from Figure 6.5(a)1 and (a)2, indicating that they are indeed voids. In both cases, the feature is open at one end of the cross-section and closed at the other side of the cross-section. In 2, some of the isosurface is also visible in the Pt layer and can be attributed to small air bubbles within the Pt deposition layer needed for FIB sample preparation.

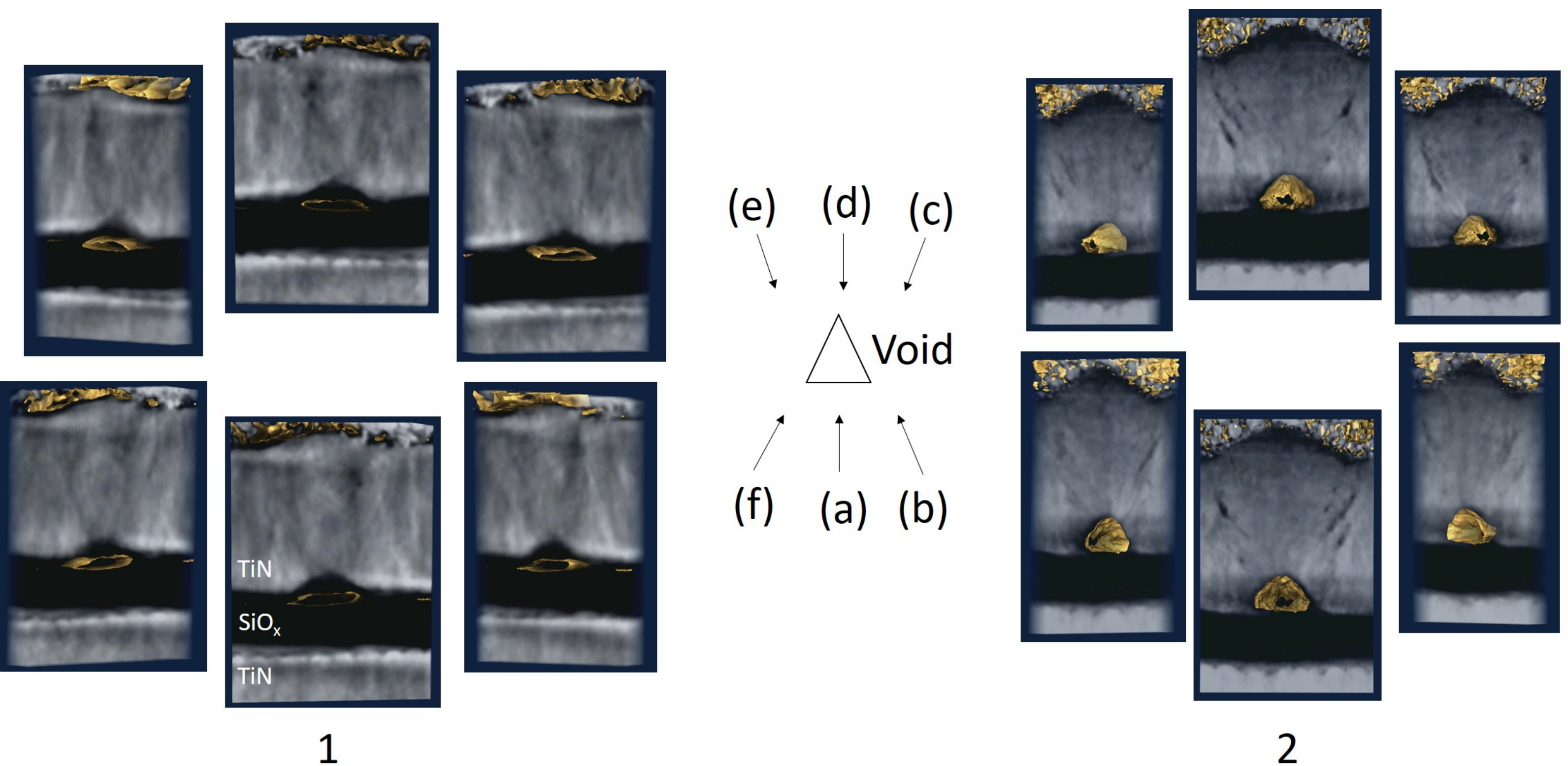


Figure 6.7: Tomographic reconstructions of Figure 6.5(b)1 and (b)2. Images (a)-(f) are correspond to different viewing angles, where (a) is taken to be the front of the cross-section. A greyscale colour scheme has been implemented so that lighter regions correspond to greater atomic number. In addition, a gold feature which corresponds to an interval from the lowest isosurface values indicates the presence of void structures between the top electrode and oxide layer. In 1, the void is present through the thickness of the cross-section, while for 2 the void is open at one end of the cross-section and closed at the other end of the cross-section. In 1, the edges of a column of TiN are visible above the void, whereas strong plastic deformation is visible in the TiN layer in 2. Part of the isosurface is also visible in the Pt layer and can be attributed to small air bubbles within the Pt deposition layer needed for FIB sample preparation.

### 6.3.2 Device 2

Figure 6.8 shows BF STEM images of regions in unstressed and stressed FIB-prepared cross-sections from device 2. Greater inhomogeneity in the oxide layer is observed in the BF STEM and HAADF images of the stressed cross-section and is confirmed by the Si and O elemental maps, for which the scatter plots below the elemental maps reveal an enhancement in inhomogeneity in the stressed cross-section. Figure 6.9 shows a plot of the $Si\text{-}L_{2,3}$ edge for spectra summed from regions of high and low Si counts in the Si maps for the stressed cross-section. An averaged sum from the unstressed cross-section is again shown for reference. The relative differences in height between peaks A and B in Figure 6.9 are greater in device 2 when compared to device 1. In the high Si count regions, the difference in height between B and A is approximately 0.24, as compared to 0.44 in the low Si count regions. This could be explained by the greater electric field strength for breakdown of 5.1 MV $cm^{-1}$ required for device 2, compared to 1.4 MV $cm^{-1}$ for electroforming in device 1 (see Table 2). However, greater inhomogeneity is apparent in the unstressed cross-section of device 2 to begin with.

Further examination of the stressed Si map and relative mass density map again indicates a periodic nature in signal intensity along the width of the cross-section. Figure 6.10(a) shows a line profile taken from left to right of the stressed Si, O, and relative mass density maps, and integrated across the thickness of the oxide layer. Peaks in Si intensity are seen approximately every 10 nm and indicate periodic changes in density along the a-$SiO_x$ layer. Figure 6.10(b) also confirms the apparent negative correlation between Si and O counts along the width of the cross-section. A columnar microstructure in the stressed Si map and relative mass density map is more obvious in device 2 when compared to the electroformed cross-section from device 1. High O signal clearly coincides with regions of low relative mass density, again suggesting the build-up of oxygen at intercolumnar boundaries. Figure 6.8 also suggests the increased presence of O at the top interface relative to the bulk for the stressed cross-section. An O line profile from bottom to top and integrated along the width of the oxide layer is presented in Figure 6.12(Left). The profile in the unstressed cross-section is notably more uniform, whereas a far greater number of counts were recorded relative to the bulk for the stressed cross-section. In order to further investigate this and the observed oxide restructuring ef-

fects on a larger scale, an additional pair of EELS spectrum images were taken over a larger area at the cost of reduced resolution. The spectrum images in Figure 6.11 are approximately 100 nm in length as opposed to 40 nm from Figure 6.8. Inhomogeneity visible in the unstressed cross-section is again shown to be greatly enhanced through electrical stressing. The O line profile shown in Figure 6.12(Right) is in agreement with the higher resolution O map, and shows an increase in O signal at the top interface relative to the bulk. This suggests a net migration of O towards the positively biased electrode as observed in device 1 [Mehonic 2016].

An interfacial layer with a sub-5nm thickness is visible at the bottom TiN electrode in the BF STEM of the unstressed cross-section in Figure 6.11. In order to understand the structure of this layer, a series of high-resolution EELS points scans were taken in the oxide, the interfacial layer, and the bottom TiN electrode layer, to identify changes in chemical composition and bonding environments. These spectra are presented in Figure 6.13. A notable change is visible at the Si-$L_{2,3}$ edge when moving from the insulating layer to the interface, where the shoulder at A is greatly reduced in height and peak B is greatly enhanced. These ELNES indicate the increased presence of Si-$O_4$ bonding environments at the interface, with a stoichiometry closer to that of silicon dioxide [Batson 1993]. Peaks C and D present in the *Ti-*$L_{2,3}$ edge and the *O-K* edge may also suggest the presence of Ti-O bonds at the interface. A shoulder can be seen to develop to the left of peak C, whereas the extra peak D is visible to the left of the peak at 540 eV. Peaks C and D have been previously observed for the TiO phase [Stoyanov 2007]. This oxide layer at the interface could hinder the formation of a conductive path at low voltages and may instead lead to hard breakdown at higher voltages.

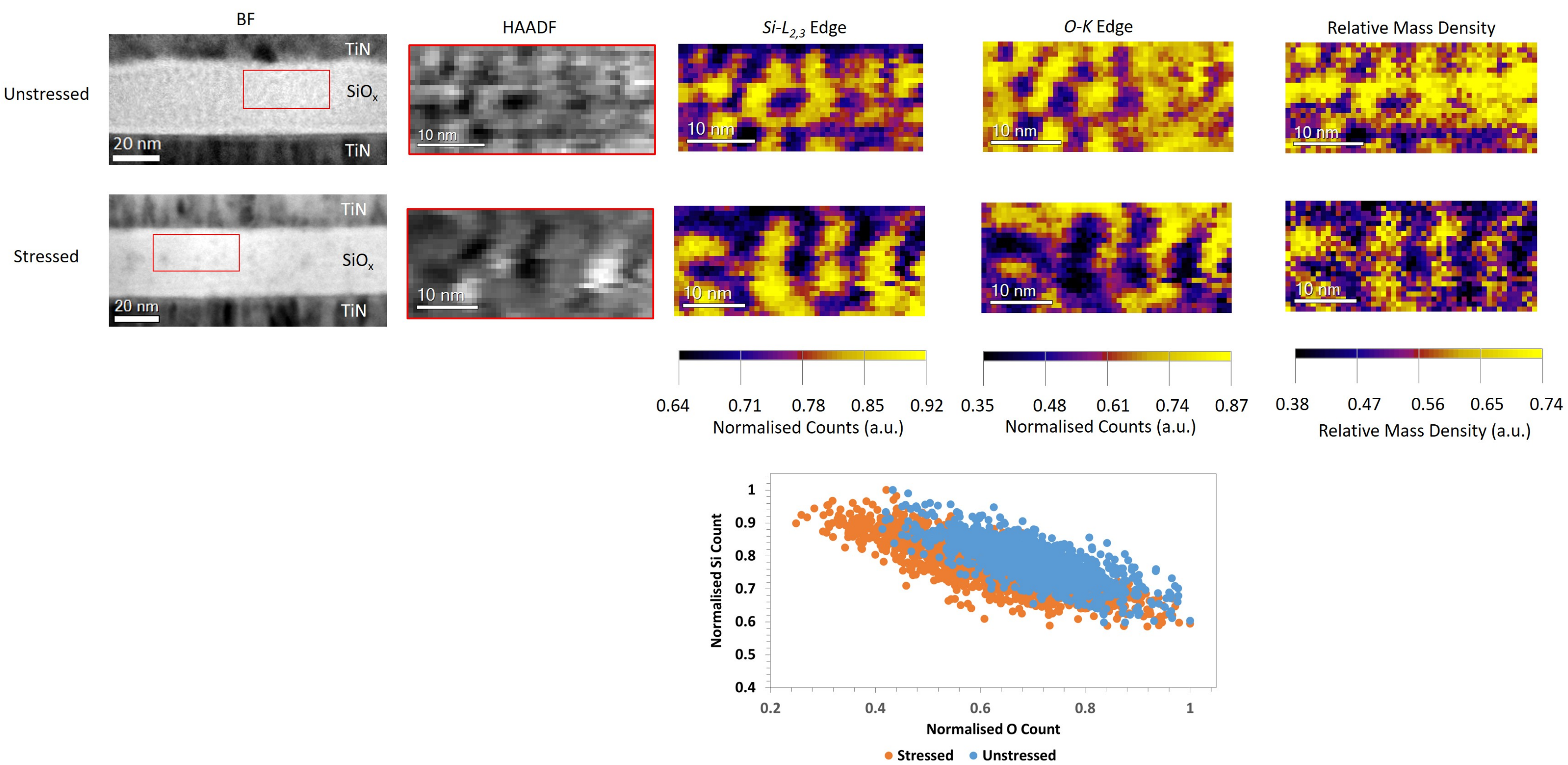


Figure 6.8: From device 2, EELS spectrum images have been taken within the red enclosed region shown in the BF STEM images and the corresponding normalised relative mass density maps have been derived. An increased degree of inhomogeneity is apparent from the BF STEM and HAADF images in the stressed cross-section. The scatter plots below the elemental maps indicate a clear enhancement of inhomogeneity after electrical stressing, with silicon-rich regions corresponding to higher relative mass density.

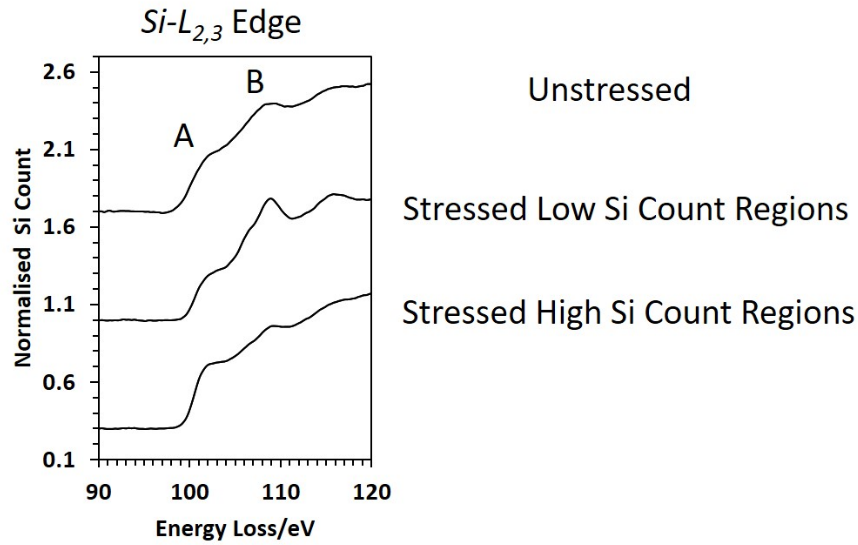


Figure 6.9: Plot showing the $Si$-$L_{2,3}$ edge, with summed spectra taken from the high and low Si count regions in the Si maps for the stressed cross-section from Figure 6.8. An averaged spectrum from the unstressed cross-section is also shown for reference. The increase in height of the shoulder at A relative to peak B (B-A≈0.24) in the high Si count regions as compared to the low Si count regions (B-A≈0.44) indicates a reduction in Si-$O_4$ bonding environments [Batson 2003].

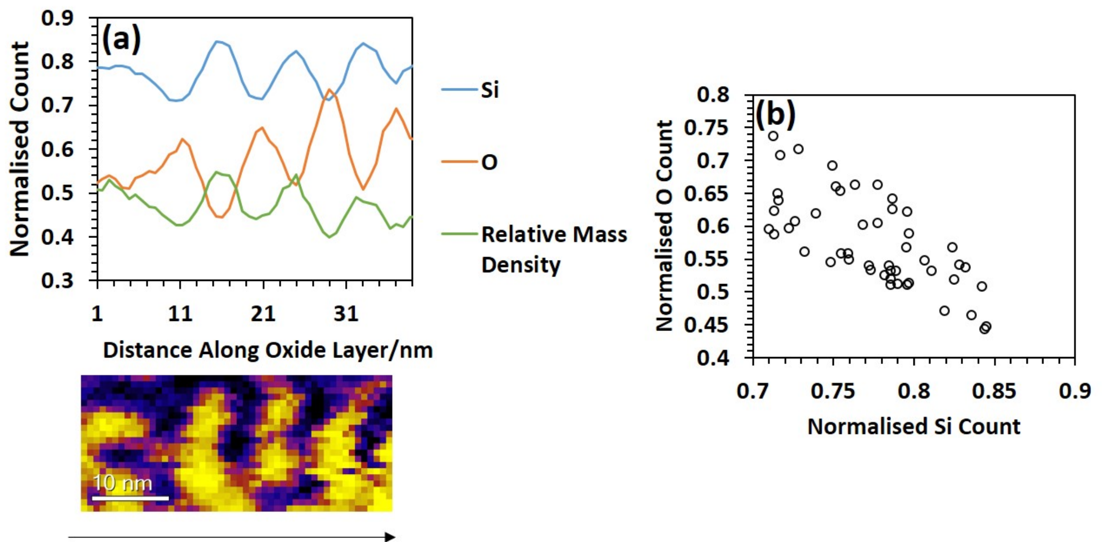


Figure 6.10: **(a)** Line profile taken along the a-$SiO_x$ layer from left to right, and integrated across the thickness of the layer for the stressed Si map, O map, and relative mass density map in Figure 6.8. Peaks in Si intensity appear periodically with intervals of approximately 10 nm. Peaks in the stressed Si map and relative mass density map coincide with troughs in the O map. **(b)** Plot of normalised O count against normalised Si count in (a): a negative correlation can be observed.

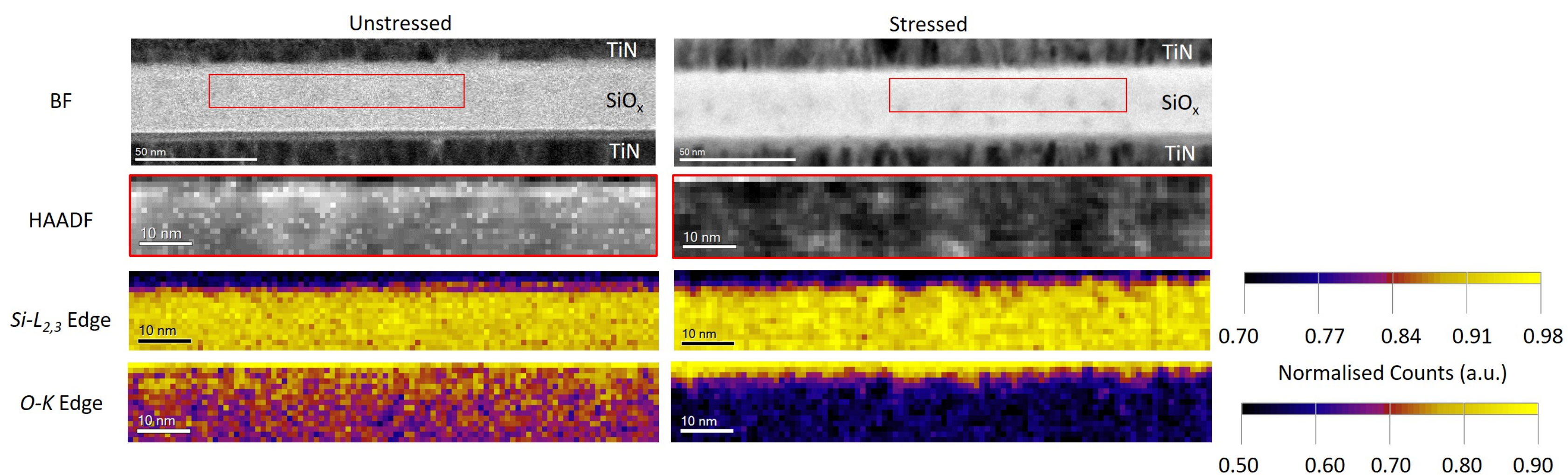


Figure 6.11: From device 2, EELS spectrum images have been taken within the red enclosed region shown in the BF STEM images. An increased degree of inhomogeneity is apparent from the BF STEM and HAADF images in the stressed cross-section. The elemental maps indicate a clear enhancement of inhomogeneity after electrical stressing. The O count near the top interface is higher relative to the bulk in the stressed cross-section.

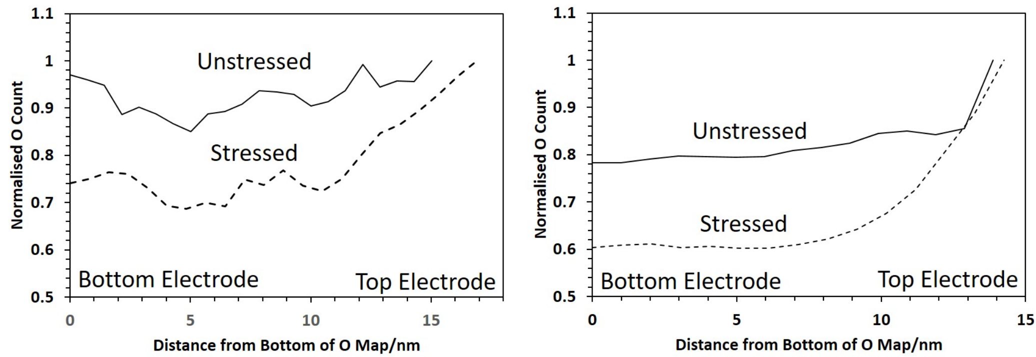


Figure 6.12: O line profile taken from bottom to top and integrated along the width of the oxide layer from Figure 6.8(Bottom) and Figure 6.11(Right). In both cases, a higher O count is recorded at the top electrode relative to the bulk in the stressed cross-section. This could suggest a net upward migration of O towards the positively biased electrode.

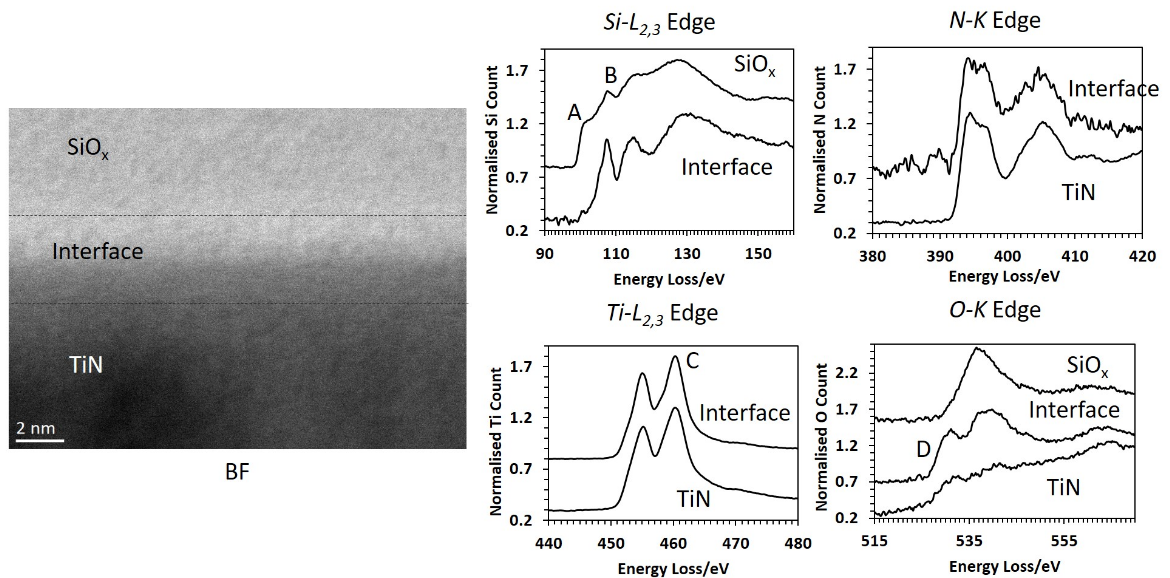


Figure 6.13: High-resolution EELS point scans comparing chemical composition at the oxide layer, the interface, and the TiN electrode shown in the BF STEM image on the left. The changes observed at the shoulder A and peak B suggest an increased presence of Si-$O_4$ bonding environments at the interface, with the ELNES more closely resembling that of $SiO_2$ [Batson 2003]. Peaks C and D also suggest the existence of Ti-O bonds and are comparable with the ELNES for TiO [Stoyanov 2007].

### 6.3.3 Device 3

BF STEM images of unstressed, positively biased, and negatively electroformed cross-sections for device 3 are shown in Figure 6.14. Relative to the lower stoichiometry devices ($x \approx 1.3$), variations within the oxide layer as a result of electrical stressing are less apparent and may be a result of device 3's higher O content. A small region of relatively high intensity is visible at feature B in the centre of the BF STEM image of the negatively electroformed cross-section, and its vertical structure could indicate the presence of an intercolumnar void. A more faint vertical streak is also visible at feature A in the centre of the unstressed cross-section. The corresponding HAADF images obtained with the elemental maps also show no notable change within the oxide layer; however, the EELS maps clearly reveal greater inhomogeneity in Si and O signals in the stressed devices. In addition, the top Ti electrode layer is clearly visible in the Ti elemental maps with an approximate 5 nm thickness. Figure 6.15 shows a plot of the *Si*-$L_{2,3}$ edge for summed spectra taken from the high and low Si count regions in the Si maps for the positive and negatively biased cross-sections from Figure 6.14. An averaged spectrum from the unstressed cross-section is also shown for reference, which resembles the ELNES of $SiO_2$ [Muller 1999]. In the positively biased cross-section, peak A is relatively greater in height than peak B in the low Si count regions, whereas in the high Si count regions the situation is reversed. This is consistent with the change in Si-$O_4$ bonding environments from devices 1 and 2. A similar but smaller change in the height of peak A can be observed in the negatively electroformed cross-section as indicated by the greater homogeneity in the corresponding EELS elemental maps. This could be explained by the lower electric field strength of 0.7 MV cm$^{-1}$ required for electroforming during negative biasing, compared to 4.3 MV cm$^{-1}$ for breakdown in the positively biased cross-section (see Table 2). In addition, the height of peak A in the unstressed cross-section is greater than the height of peak A in both of the stressed cross-sections and appears to suggest an overall reduction in O content in the insulating layer. In the positively biased cross-section in Figure 6.14, a relatively higher O count is visible close to the top electrode, and could suggest the migration of oxygen towards the positive biased Au electrode in agreement with devices 1 and 2. In contrast, the Si map for the negatively electroformed cross-section in Figure 6.14 reveals a consistently stronger Si signal along the top half

of the insulating layer, and may suggest O migration towards the bottom electrode. However, this is not clear from the corresponding O map, although smaller regions of low O count can be seen near the top electrode. This is likely to be a result of the much smaller differences in relative intensity within the negatively electroformed cross-section, together with a comparatively weaker signal at the *O-K* edge.

A closer inspection of the Si map for the negatively electroformed cross-section in Figure 6.14 suggests that from left to right, the Si signal can be divided into four columnar regions, roughly 20 nm in diameter, with relatively low Si counts in the regions between them. These regions are indicated by the numbers 1 to 4 on the Si map. Figure 6.16(a) shows a line profile taken from left to right of the Si and O maps and integrated across the thickness of the oxide layer. The corresponding regions 2-4 in Figure 6.14 appear to be separated by troughs in the line profile at approximately 70 nm and 110 nm. The trough between regions 2 and 3 corresponds to feature B from the BF STEM image of the negatively electroformed cross-section in Figure 6.14. The noisier O profile suggests an additional trough between regions 1 and 2 at approximately 30 nm, although this is not clear in the Si profile. In contrast to devices 1 and 2, Figure 6.16(b) indicates a weakly positive correlation between Si and O counts along the width of the sample. Regions 1 to 4 can perhaps be related to the columnar structures observed elsewhere in device 3 as shown in Figure 5.6 in chapter 5. The width of these regions is roughly 20 nm or greater; comparatively larger than the approximate 10 nm for devices 1 and 2 indicated in the stressed cross-sections in Figure 6.1 and Figure 6.8. If columns have a larger width in device 3, then intercolumnar boundaries will be less common. This may lead to a slower segregation of silicon and oxygen and could, together with an electric field strength for electroforming of 0.7 MV $cm^{-1}$, explain why an anticorrelation is not observed in Figure 6.16(b)

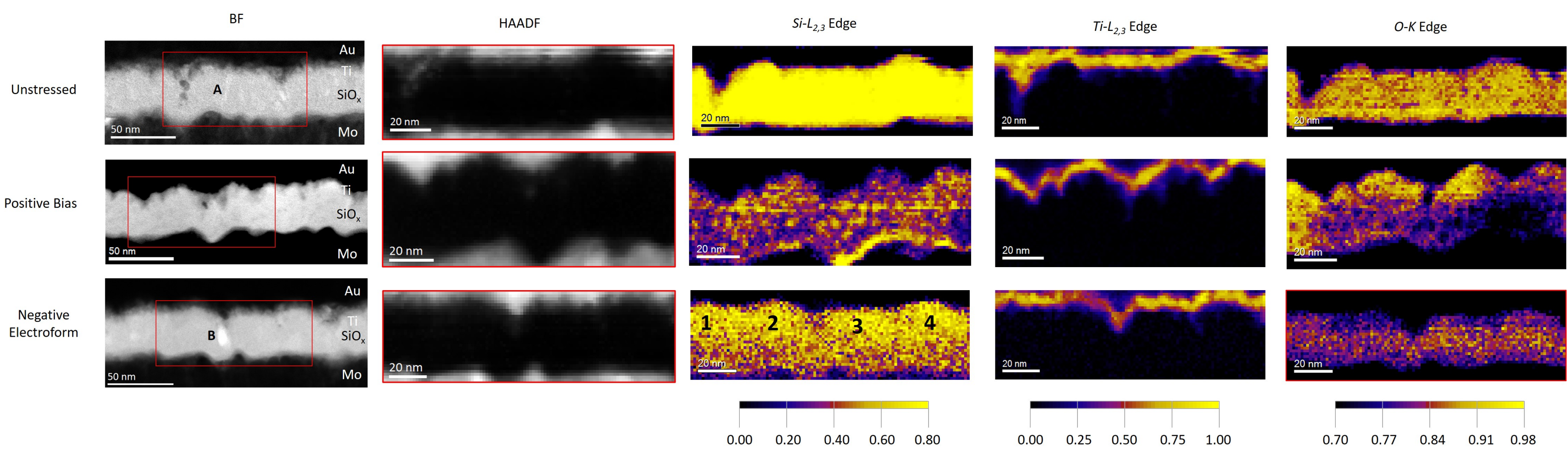


Figure 6.14: From device 3, EELS spectrum images have been taken within the red enclosed region shown in the BF STEM images. Relative to devices 1 and 2, changes as a result of electrical stressing are not obvious from the images taken within the oxide layer. However, the elemental maps indicate a clear enhancement of inhomogeneity after electrical stressing. Features A and B in the BF STEM images are bright vertical streaks within the oxide layer, which could indicate the presence of intercolumnar boundaries as a result of the sputtering preparation method [Thornton 1986]. The labels 1 to 4 on the Si map of the negatively electroformed cross-section highlight that the oxide layer appears to be divided into columnar regions roughly 20 nm in diameter.

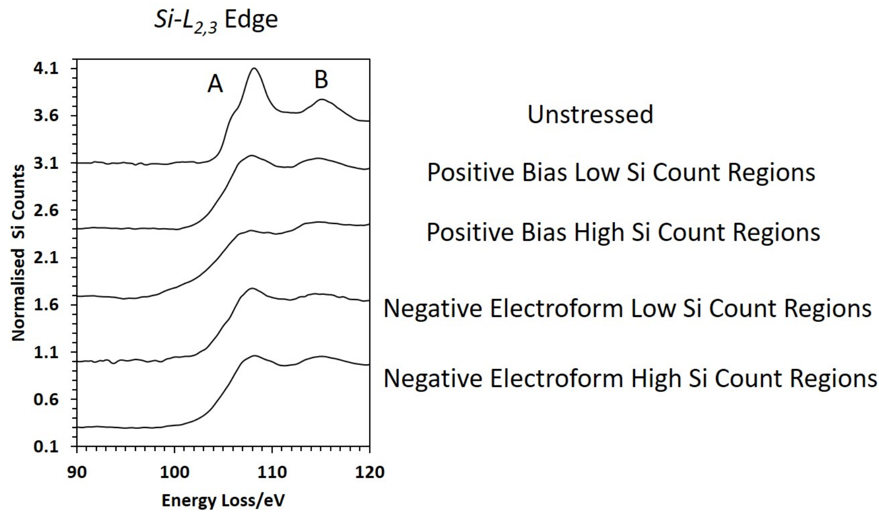


Figure 6.15: Plot showing the $Si$-$L_{2,3}$ edge, with summed spectra taken from the high and low Si count regions in the Si maps for the stressed cross-sections from Figure 6.14. An averaged spectrum from the unstressed cross-section is also shown for reference. A reduction in the height of peak A corresponds to a reduction in S-$O_4$ bonding environments [Batson 1993]. In the positively biased cross-section, peak A is greater in height than peak B in the low Si count regions, whereas the opposite is true in the high Si count regions. A similar but smaller change is visible for the negatively electroformed cross-section. When compared to the unstressed cross-section, peak A is consistently lower for both of the stressed cross-sections, suggesting a net reduction in O content within the insulating layer.

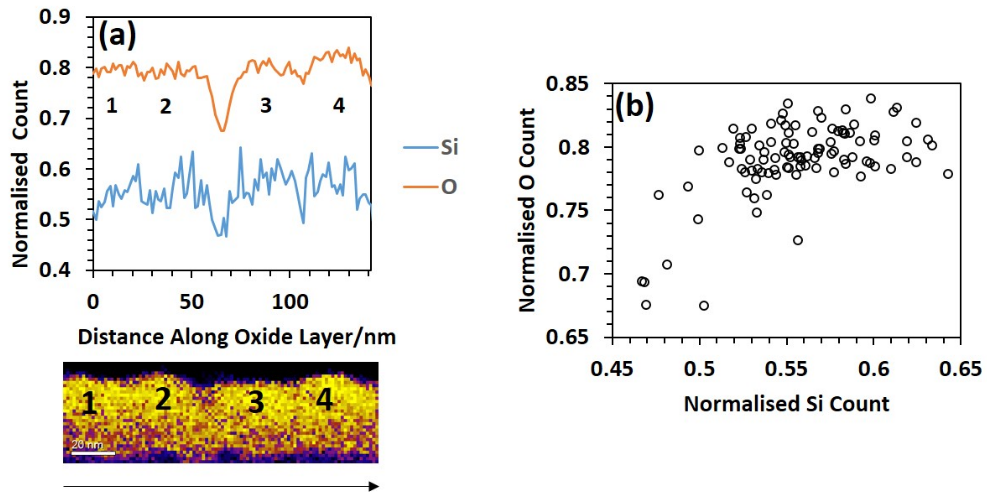


Figure 6.16: **(a)** Line profile taken along the a-$SiO_x$ layer from left to right, and integrated across the thickness of the layer for the negatively electroformed Si and O maps in Figure 6.14. The corresponding regions 2-4 in Figure 6.14 appear to be separated by troughs in the line profile at approximately 70 nm and 110 nm. The noisier O profile suggests an additional trough between regions 1 and 2 at approximately 30 nm although this is not clear from the Si profile. **(b)** Plot of normalised O count against normalised Si count: a weakly positive correlation can be observed.

The SEM images of the stressed contacts on device 3 shown in Figure 6.17 also reveal changes to the surface of the top electrode. For the positively biased cross-section in Figure 6.17(a), the top contact appears to have peeled off and cracked during electrical stressing. An FIB cross-section was prepared at the magnified region in Figure 6.17(a), and the corresponding SEM image is shown in Figure 6.18. A crack can be observed to propagate across the *MIM* stack at the center of the image. Furthermore, for the negatively electroformed cross-section in Figure 6.17(b), small crater-like formations are visible on the Au electrode. BF STEM images of void structures observed in the FIB-prepared cross-sections of device 3 are presented in Figure 6.19. A bright white region can be seen between the Ti and Au layers as a result of positive and negative biasing, which suggests the presence of an interfacial void. However, a greater degree of deformation is evident in the negatively electroformed cross-section. In the BF STEM image of the positively biased cross-section, features A and B highlight relatively brighter vertical streaks across the thickness of the oxide layer. These correspond to dark vertical streaks in the HAADF image in Figure 6.19(a)(ii) and could suggest the presence of intercolumnar boundaries. Features A and B can be seen to correspond to a region of relatively weak O signal in the O EELS map. O may more easily travel along intercolumnar boundaries towards the Au electrode, resulting in the observed region of weak O signal. For the positively biased cross-section, the void region takes the form of two dome structures on either side of features A and B. The dashed lines in Figure 6.19(a)(i) above the dome structures run along two boundaries of a large columnar Au grain situated above the void. The mismatch between these boundaries and the boundaries at features A and B may be responsible for a build up in pressure and the formation of the void, which is relieved when O can travel along intercolumnar boundaries in the Au electrode. Feature C indicates a bright vertical streak present in the negatively electroformed cross-section, which corresponds to a region of relatively weak signal in the Si and O elemental maps. Also, higher Si counts are present in the top half of the insulating layer in the negatively electroformed cross-section, whereas higher O counts are present in the bottom half of the insulating layer. This may again indicate oxygen migration towards the positively biased electrode and would be consistent with devices 1 and 2. The HAADF image in Figure 6.19(b) is taken above the void for the negatively electroformed cross-section and shows clear signs of physical stress in the Au layer above. This is comparable to the physical stress observed in the top TiN electrode in Figure 6.5 for

device 1. In Figure 6.19(c), a high-resolution EELS point scan at the edge of the Ti layer below the void reveals a strong signal at the *O-K* edge with no corresponding Si signal, and could indicate the oxidation of the Ti layer. The Ti maps in Figure 6.19 also show a notable change in the distribution of Ti. From an initial thickness close to 5 nm (see Figure 6.14), in the positive and negatively biased cross-sections the Ti layer extends up to 20 nm and 10 nm, respectively. Figure 6.19(d) shows the distribution of Ti in the oxide layer in the unstressed cross-section from Figure 6.14, and the positive and negatively biased cross-sections in Figure 6.19. A weak Ti signal is detected at features A and B for the positively biased cross-section. This may suggest the migration of Ti cations towards the negatively biased electrode, facilitated by the presence of intercolumnar boundaries. However, the unstressed cross-section suggests that such sites could also be a product of fabrication. This is not seen in the negatively biased cross-section. Instead, the signal at the *O-K* edge in (c) suggests oxidation of the Ti layer. If the O migration towards the positively biased electrode is assumed, the mechanism by which the deformation of the Au electrode may occur in the negatively electroformed cross-section is unclear. However, it should be noted that deformation as a result of electrical stressing has been reported previously at a negatively biased electrode [Jeong 2008] (see section 3.2).

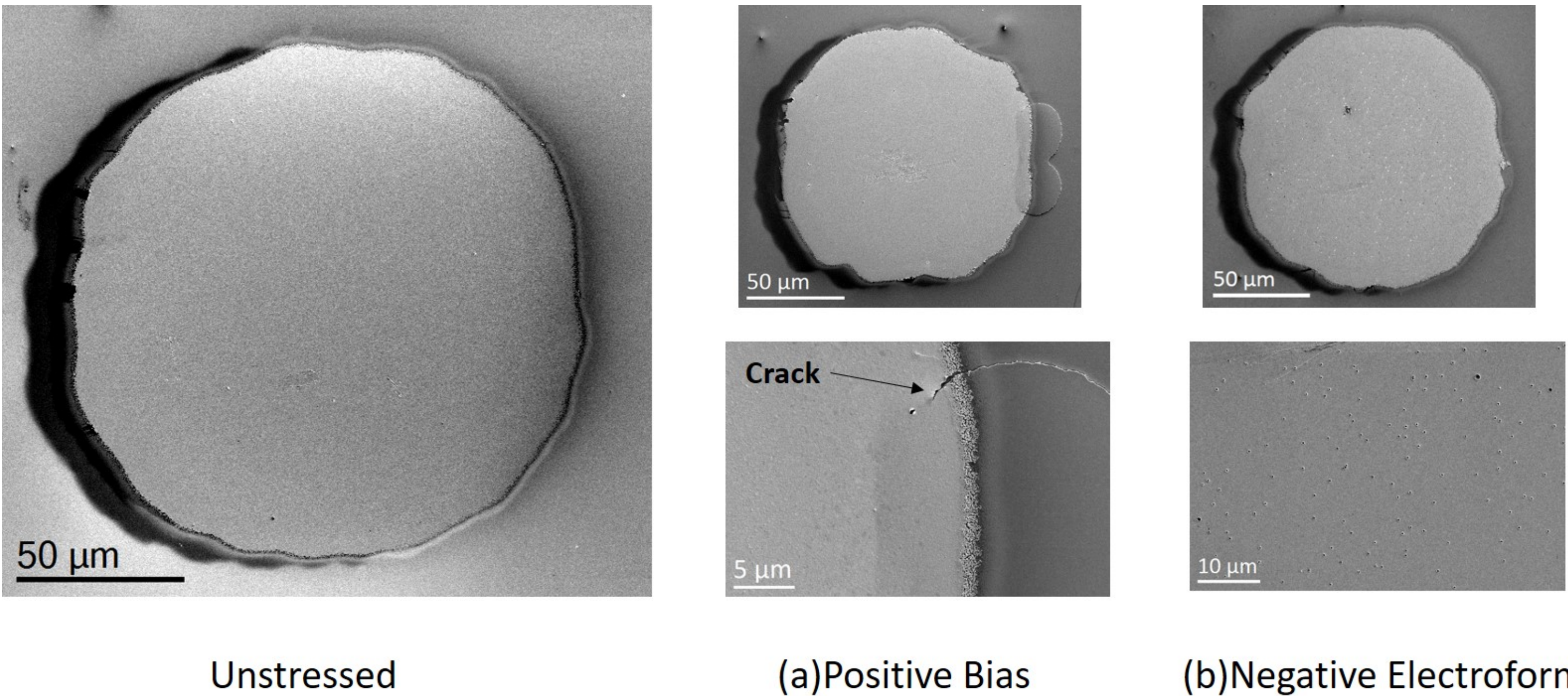


Figure 6.17: SEM top view images of unstressed and stressed contacts on device 3, where the corresponding images below the stressed contacts are taken at greater magnification. These images are provided courtesy of Siew Lang Teo at IMRE. **(a)** The positively biased contact appears to have peeled off and cracked during electrical stressing. **(b)** Crater-like formations are visible on the negatively electroformed cross-section.

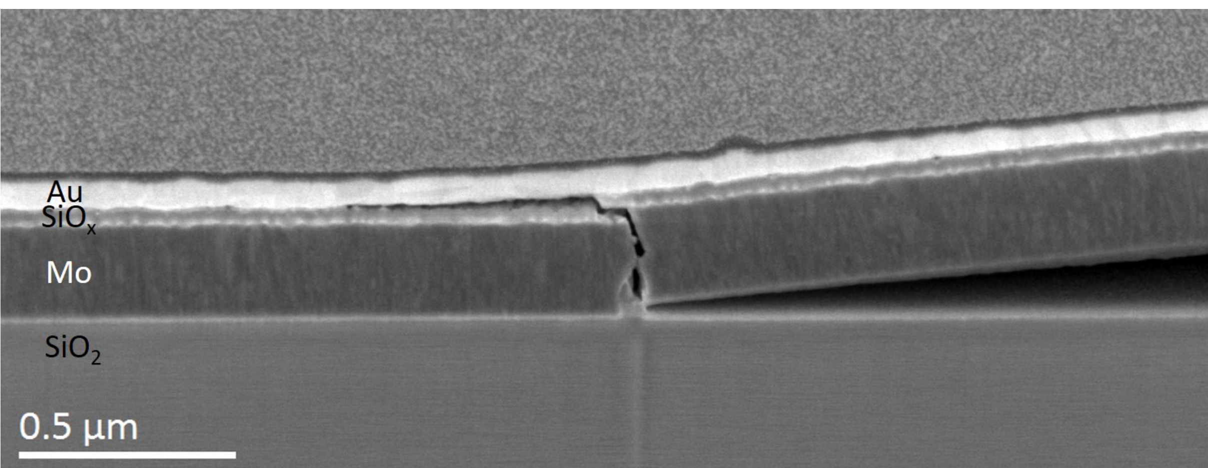


Figure 6.18: An SEM image of an FIB cross-section prepared at the magnified region in Figure 6.17(a). This image is provided courtesy of Siew Lang Teo at IMRE. A crack can be observed to propagate across the *MIM* stack at the center of the image.

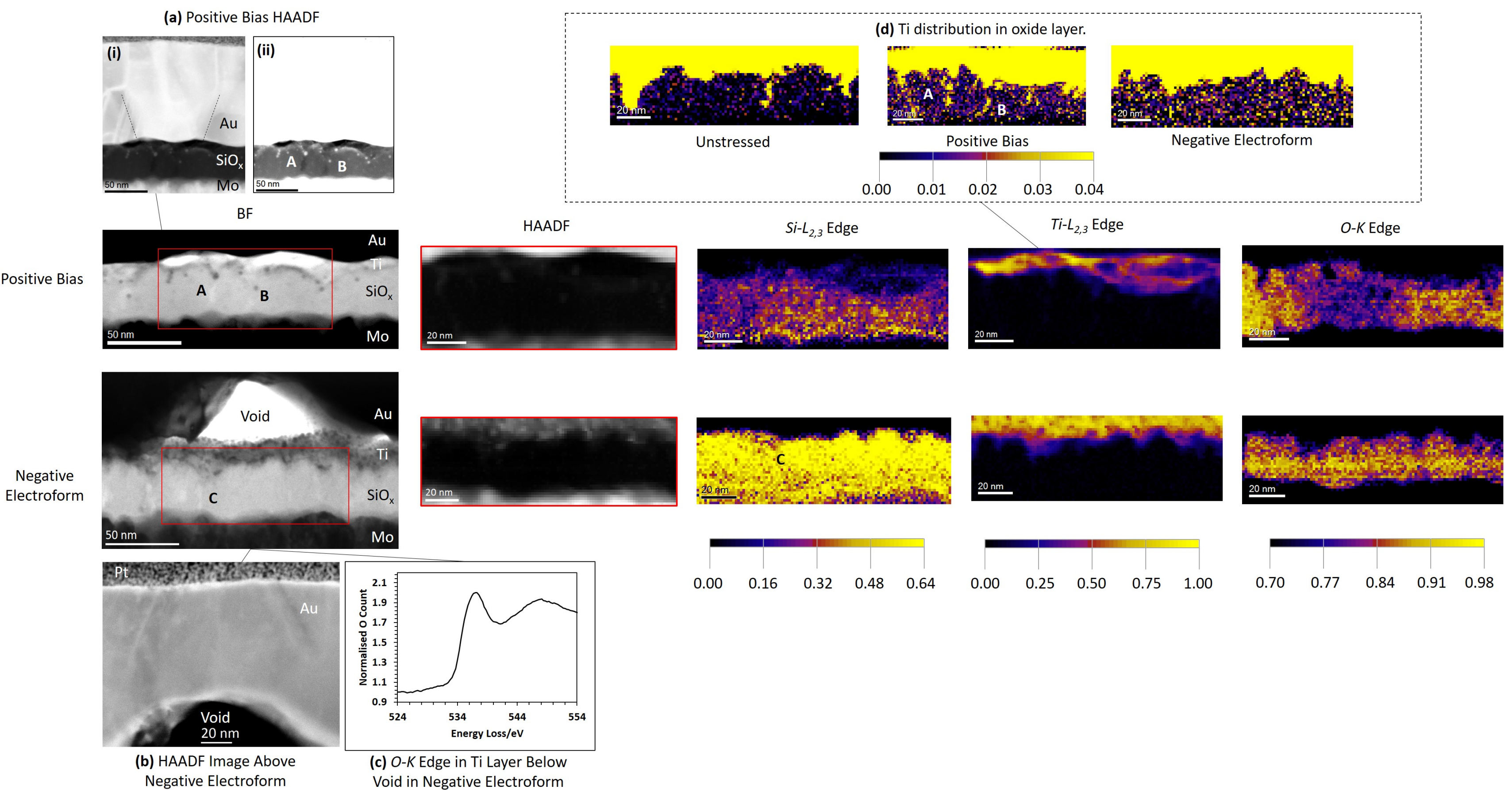


Figure 6.19: From device 3, EELS spectrum images have been taken within the red enclosed region shown in the BF STEM images. These regions were chosen deliberately below void structures observed at the top interface. **(a)** For the positively biased cross-section, features A and B in highlight relatively brighter vertical streaks across the thickness of the oxide layer in the BF image, with corresponding dark vertical streaks in the HAADF image in (a)(ii). (a)(ii) is a copy of (i) with enhanced contrast. **(b)** A HAADF image of the Au layer above the void for the negatively electroformed cross-section shows signs of physical stress. **(c)** A high-resolution EELS point scan taken at the edge of the Ti layer under the void in (b) shows a clear O signal at the *O-K* edge, whereas no Si signal was detected. **(d)** Ti elemental maps comparing the Ti signal in the oxide layer for the unstressed cross-section from Figure 6.14, and the stressed cross-sections shown in this Figure. A weak Ti signal is detected at features A and B in the positively biased cross-section.

## 6.4 Discussion and Summary

TEM characterisation of a series of electrically stressed *MIM* devices with an a-SiO$_x$ insulating layer has revealed change on an oxide-wide scale. Oxygen has been shown to be highly mobile during electrical stressing, with the presented data suggesting migration towards the positively biased electrode. Oxygen buildup at the electrode appears to result in its deformation and loss of O from the oxide layer. More direct evidence for this migration in device 1 was provided by Mehonic et al. [Mehonic 2016], where O emission was detected from the positively biased electrode as a result of electrical stressing. This loss of O may limit device lifetime and could suggest that a higher O content in the oxide layer is favourable as previously suggested by Chang et al. [Chang 2012]. This is supported by device 3's greater endurance of $\approx 10^7$ switching cycles as compared to $\approx 10^2$ cycles for device 1. In contrast to devices 1 and 3, no electrode deformation was observed in device 2. Device 2 has a comparatively thin top electrode layer ($\approx$10 nm). As a result, O could perhaps migrate along intercolumnar boundaries in the TiN layer before sufficient pressure is built up to cause deformation. This may also result in a more rapid loss of O and explain device 2's lack of switching behaviour. However, this is not clear due to the presence of the oxygen-rich interfacial later at the bottom electrode of device 2, which is also likely to contribute to hard breakdown. In device 3, two different electrode materials are used. Switching behaviour is only observed when the top Au electrode is negatively biased. In contrast to the bottom Mo electrode, Au does not form stable oxides under standard conditions. This may again result in more rapid O loss and poor device performance when the Au electrode is positively biased. However, Figure 6.19 also reveals the potential diffusion of Ti cations along intercolumnar boundaries, which could contribute to the formation of a metallic filament. Finally, removing intercolumnar boundary regions from the electrode layers may inhibit the loss of oxygen from the devices, and act to improve device endurance.

In chapter 5, the columnar microstructure of the a-SiO$_x$ layer was noted in Figure 5.6 for device 3, with an approximate column width of 20 nm. In the present chapter, similar structures were observed in device 3 as shown in Figure 6.14 and Figure 6.19. Furthermore, upon electrical stressing, the relative mass density maps in Figure 6.3 and Figure 6.10 for devices 1 and 2 suggested that periodic variations in density occur ap-

proximately every 10 nm along the oxide layer. Regions of low relative mass density were characterised by a relatively high O signal. Based on these observations, it was suggested that during electrical stressing, O may build-up at and migrate along intercolumnar boundaries. If a columnar width of 10 nm is assumed, this is shorter than an approximate 20 nm width for columns in device 3. Wider columns would more easily be observed within a TEM sample since information on thinner columns would be averaged out over the thickness of the sample. As previously suggested in chapter 5, the relatively rougher electrode surface of device 3 will enhance columnar growth [Thornton 1986]. This would result in more continuous intercolumnar boundaries. For devices 1 and 2, these structures may be more discontinuous, resulting in further difficulties in their observation. More continuous intercolumnar boundaries would provide a low resistance diffusion path for interstitial oxygen. This could in turn benefit device switching speeds, electroforming/switching voltages, and endurance. In the case of electroforming voltages and device endurance, this appears to be the case when comparing devices 1, 2, and 3, as discussed in chapter 5.

The EELS maps in this study revealed no signs of regions of pure silicon, with the resolution in the presented spectrum images reaching 0.7 nm per pixel. These measurements, in conjunction with previous studies on a-$SiO_x$ fabricated using sputtering methods [Zhang 2010][Sasaki 2003], suggest that the a-$SiO_x$ in the studied devices has a structure more consistent with the random bonding model (RBM) discussed in section 3.3 [Philipp 1972]. This implies an approximately homogenous distribution of O vacancies for the a-$SiO_x$ stoichiometries used in this investigation. As O outmigration has been detected [Mehonic 2016], the number of O vacancies in the oxide layer is likely to increase. One mechanism for the formation of a conductive path across the oxide layer is through the diffusion and aggregation of O vacancies. This will be explored in chapters 9 and 10. In section 3.5, the oxygen double bridge interstitial was suggested as a possible migratory species in a-$SiO_2$ as a result of its low barrier for diffusion ($\approx$0.20 eV) [Mehonic 2016]. This is a negatively charged defect, which would migrate towards the positively biased electrode and is consistent with many of the observations presented in this chapter. Mehonic et al. suggested that electron injection into the oxide layer during electrical stressing could allow the formation of such defects. The capture of electrons by O vacancy sites, a consequence of the RBM, may facilitate the formation of the oxygen double

bridge interstitial. As discussed in section 3.7, a similar mechanism was observed for O vacancies in crystalline $HfO_2$, whereby the trapping of electrons at O vacancy sites was found to strongly correlate with the formation of a nearby vacancy and interstitial O ion [Bradley 2015B]. This could provide an alternative mechanism to O vacancy aggregation for conductive path formation and is further discussed in chapter 10.

In summary, the presented data indicates structural reorganisation in the oxide matrix as a result of electrical stressing. This is an oxide-wide change and not confined to a conductive path region; however, such changes are likely to be precursors for conductive path formation. These results also indicate the loss of oxygen from the oxide layer during electrical stressing, which can result in deformation of the electrodes. Finally, oxygen could migrate towards and travel along intercolumnar boundaries observed in the a-$SiO_x$ layer as a result of the sputtering deposition method. These results suggest that the fabrication of the sputter-deposited a-$SiO_x$ layer greatly influences device performance.

# 7 Observation of Electrode Migration in *MIM* devices with Thin a-SiO$_x$ Insulating Layers

## 7.1 Introduction

As discussed in chapter 3, resistive switching behaviour in a-SiO$_x$ has been attributed to extrinsic [Wang 2014] or intrinsic processes [Yao 2010][Mehonic 2012][Chang 2012] [Wang 2013]. In the former case, electric field effects are believed to drive the formation of a metallic conductive filament formed from ions supplied by the anode [Wang 2014]. In the latter case, oxygen vacancy aggregation or additional vacancy production is thought to result in the formation of a silicon-rich conductive path. In such devices, in order to prevent the formation of a metallic filament, the choice of electrode material is very important. Metals which are relatively inert such as Pt [Wang 2013] or Au (device 3) are common choices. Alternatively, doped Si and C electrodes [Yao 2010][Yao 2012][Mehonic 2012] have also been used due to their desirable conductive properties. For similar reasons, TiN is a key electrode material in this investigation. The thickness of the a-SiO$_x$ layer has been relatively large in previous ReRAM studies where intrinsic switching was reported. Mehonic et al. used a-SiO$_x$ layers ranging from 15 to 120 nm in thickness [Mehonic 2012], whereas Yao et al. [Yao 2010] and Wang et al. [2013] used thicknesses of approximately 40 nm and 60 nm respectively. In contrast, technological advances have made possible the fabrication of ultra-thin oxide films, with the possibility of reaching thicknesses below 1 nm [Kim 2006]. For the two-terminal *MIM* structures used in ReRAM devices, this appears to be a great advantage, allowing a considerable increase in memory density. However, in the context of MOSFETs, this results in reliability issues as a result of current leakage. Furthermore, the electrical measurements performed by Chang et al. [Chang 2012] suggested that resistive switching in devices with thin oxide layers is less reliable. In this chapter, the following TEM investigation again suggests a limit to scaling, despite the choice of relatively inert TiN and Ru electrodes, and provides a physical explanation for this limit. It should be noted that for the samples in this chapter, FIB sample preparation was carried out by Hui Ru Tan and June Ong Lay Ting at IMRE.

## 7.2 Methodology

TEM sample cross-sections were prepared using an FEI Helios Nanolab 600 FIB. Lower resolution STEM imaging was carried out and EELS point spectra were acquired at 80 keV using an FEI Titan (S)TEM, as this high tension was found to produce minimal beam damage on the studied sample. Higher resolution, aberration-corrected images and an EELS spectrum image were acquired at 200 keV using a JEOL JEM-ARM200F TEM. A relatively short acquisition time of 30 ms was used with low-loss and core-loss maps being acquired simultaneously in order to minimise beam damage at this high tension. In both cases a GIF was used to record EELS spectra. For the FEI Titan (S)TEM, a 14.4 mrad convergence semi-angle and a 30 mrad collection semi-angle were recorded. Alternatively, for the JEOL JEM-ARM200F TEM, a 30 mrad convergence semi-angle and a 88 mrad collection semi-angle were recorded. All data processing was carried out using the Digital Micrograph© software. A first degree log polynomial background was found to best fit the EELS spectra. The Fourier-Log method was used to deconvolve the point spectra, whereas the Fourier-Ratio method was used for the core-loss spectrum image (see section 4.6). The displayed spectra have been normalised with respect to the highest recorded count in each individual spectrum.

## 7.3 Results

Figure 7.1 shows the structure of device 4. The reader is referred to Table 2 in section 4.4 for a more detailed summary of device 4.

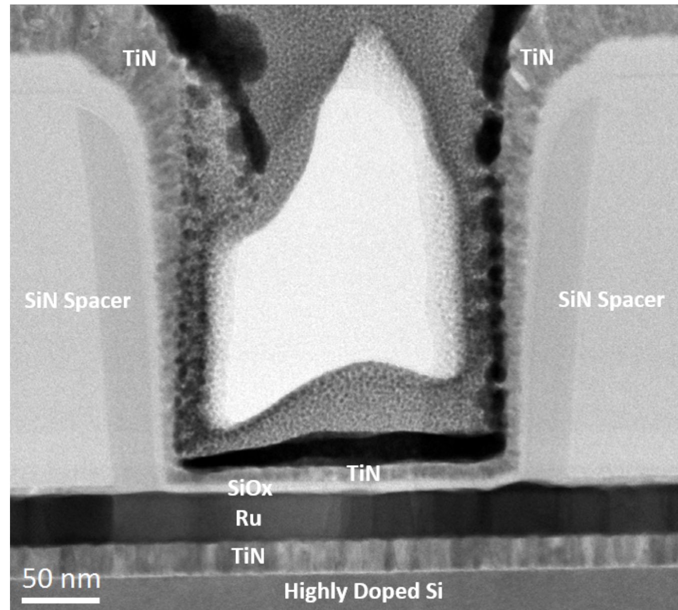


Figure 7.1: BF STEM image of an FIB-prepared cross-section of device 4. The top electrode consists of a TiN layer approximately 8 nm thick situated above an a-SiO$_x$ layer close to 5 nm in thickness. The bottom electrode consists of Ru and TiN electrodes approximately 30 nm and 20 nm in thickness. The *MIM* structure is located along the bottom of a trench structure with an area of approximately 200 nm$^2$. The top TiN layer can be observed to become thicker away from the bottom of the trench as a result of the preferred deposition of vapourised particles onto high points on the substrate surface during sputtering [Thornton 1986]. The Pt and Au layers are a result of FIB sample preparation.

Figure 7.2(Left) shows two HAADF images of unstressed and stressed cross-sections of device 4. Bumps are visible at the Ru interface near the edges of the TiN layer and at feature A in the unstressed cross-section. A similar feature is present in the stressed cross-section at feature B. Magnified BF STEM images are shown to the right with features A and B labelled accordingly. 3 to 4 nm of oxide is clearly visible between the TiN layer and the bump in the Ru layer at feature A. In contrast, at feature B, an oxide layer separating the electrode layers is not clearly visible. A low-angle annular dark field image (LAADF) of the same region on the stressed cross-section reveals that at feature B, a column of TiN approximately 10 nm in diameter appears to have shifted down, resulting in a filament-like structure bridging the oxide layer.

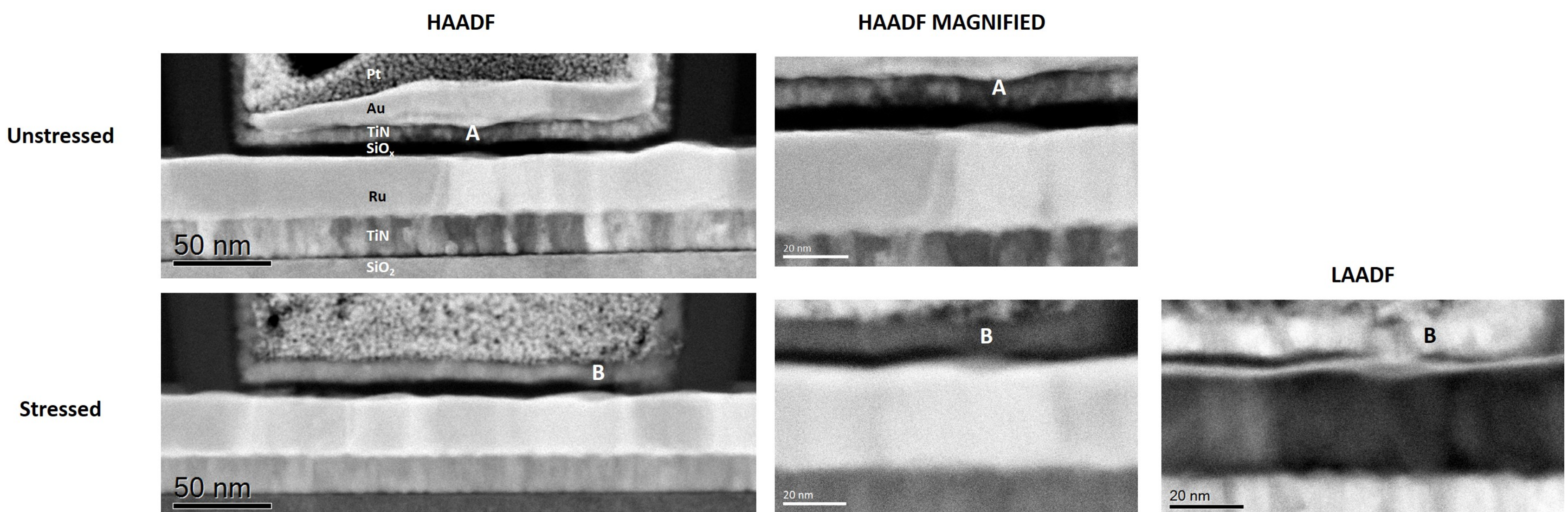


Figure 7.2: HAADF images of unstressed and stressed cross-sections from device 4 are shown on the left with the corresponding magnified images to the right. For the stressed cross-section, an additional low-angle annular dark field image (LAADF) is also shown. Features A and B highlight bumps on at the Ru interface, which protrude into the oxide layer. The Pt and Au layers are products of FIB fabrication and were not present when the device was subjected to electrical stressing. In comparison to the unstressed device, a column of TiN approximately 10 nm in diameter appears to have shifted downwards, resulting in the formation of a filament-like structure.

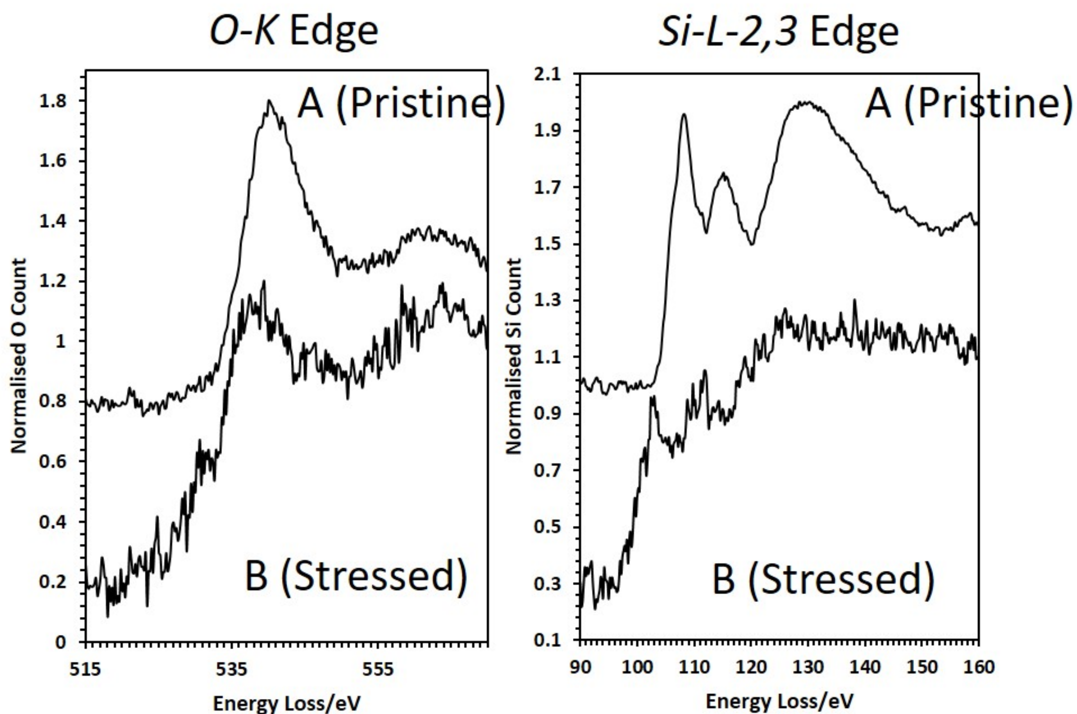


Figure 7.3: High resolution EELS point spectra taken in the oxide layer at features A and B from Figure 7.2. In the stressed cross-section, the *Si*-$L_{2,3}$ edge resembles that of pure silicon, suggesting a decrease in the number of Si-O bonds. This is consistent with the *O-K* edge [Muller 1999].

In order to initially understand the effect of this on the oxide layer, high-resolution EELS point spectra were acquired in the oxide layer at features A and B for comparison at the *Si*-$L_{2,3}$ and *O-K* edges. The resulting spectra are displayed in Figure 7.3. In the unstressed cross-section, the *Si*-$L_{2,3}$ edge ELNES resembles the spectrum of $SiO_2$ [Muller 1999], suggesting a relatively high concentration of Si-$O_4$ bonding environments. This is consistent with the signal at the *O-K* edge. In contrast, the corresponding signals in the stressed cross-section show significant changes. The *Si*-$L_{2,3}$ edge now strongly resembles that of pure Si [Muller 1999], suggesting that as a result of electrical stressing, a large number of Si-O bonds have been replaced with Si-Si bonds. This is in agreement with a much weaker signal at the *O-K* edge. The signal-to-noise ratio is weaker for the stressed cross-section and could be a result of the presence of TiN in the oxide layer as indicated by Figure 7.2.

To further understand the nature of the filamentary region, an aberration-corrected STEM was used to acquire an EELS spectrum image at feature B in Figure 7.2. The resulting

images and elemental maps are presented in Figure 7.4. From the HAADF image, the brighter intensity at the filament site cleary reveals the presence of heavier elements [Pennycook 1991]. An inspection of the magnified images of the breakdown site shown in Figure 7.5 shows crystallinity at the breakdown site. This appears to originate from the TiN layer and is consistent with the LAADF image in Figure 7.2. The elemental maps in Figure 7.4 correspond to the red enclosed region in the BF STEM image. The Ti and N elemental maps outline a similar bump feature along the top electrode, which overlaps with the bump observed at site B on the bottom Ru electrode. Regions of red intensity are seen to extend across into the TiN layer in the Ru map. However, this should be viewed with caution since carbon contamination was also observed to be present in the TiN layer in the EELS signal. The *C-K* edge and *Ru*-$M_{4,5}$ edge have onsets at 284 eV and 279 eV, leading to signal overlap, although an integration window between 320 eV to 335 eV was chosen in the Ru elemental map to minimise this effect. Regions of high Si intensity appear to overlap with the bump in the Ru map and suggest a bump structure protruding into the oxide layer surrounded by an Si-rich region. The corresponding ELNES at the *Si*-$L_{2,3}$ edge and the *O-K* edge are in agreement with the point scans in Figure 7.3. It should be noted that the highest O counts do not exactly correlate with the highest Si counts and are concentrated towards the top TiN electrode. This may indicate an upwards migration of O towards the positively biased electrode as suggested in chapter 6 [Mehonic 2016].

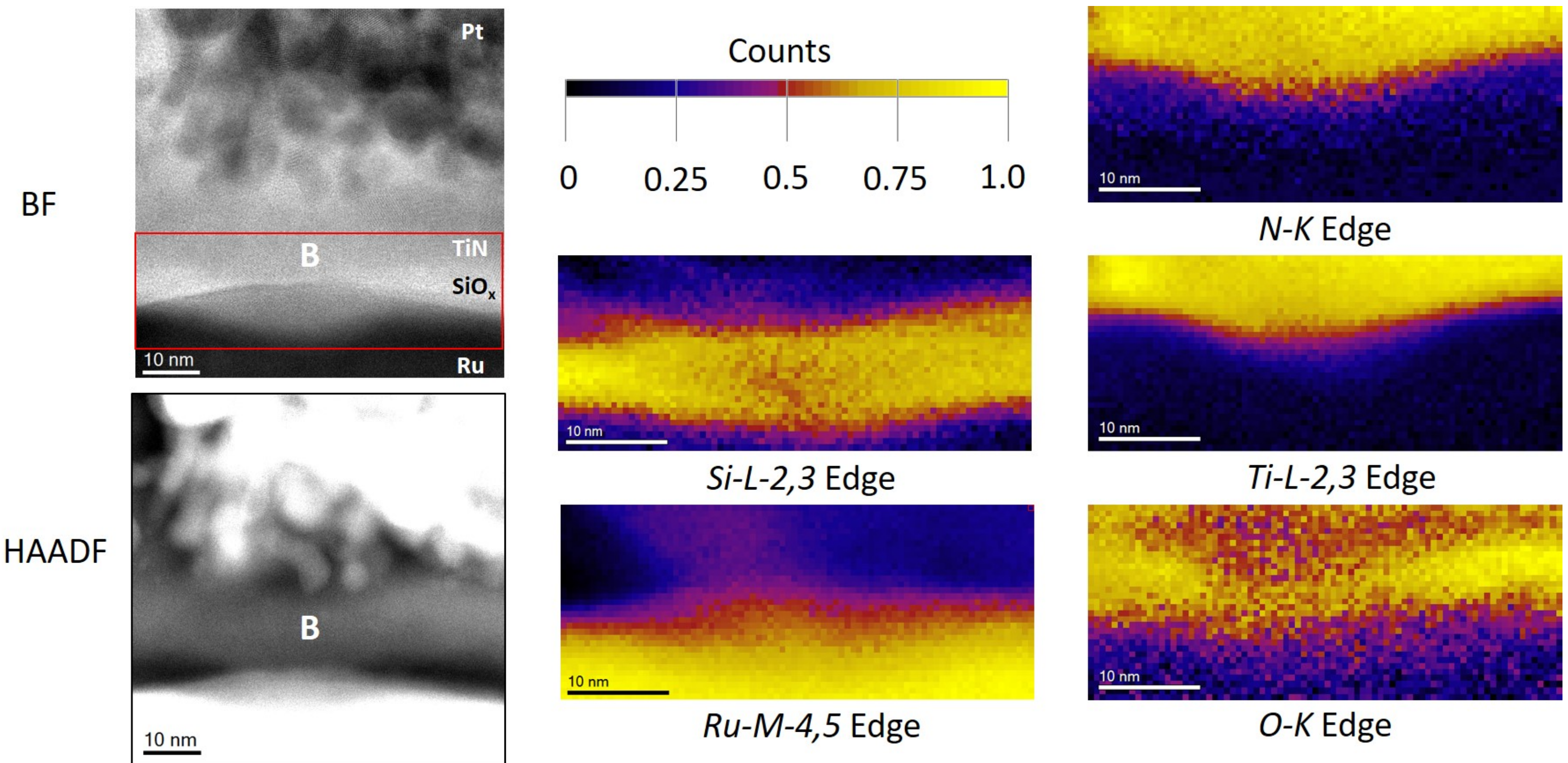


Figure 7.4: Elemental maps corresponding to the red enclosed region in the BF STEM image. The additional HAADF image highlights the presence of heavier elements at the filament site [Pennycook 1991]. Bumps can be observed in the TiN and Ru layers which overlap, indicating a filament structure where the electrodes have made electrical contact with one another. 'B' corresponds to feature B in Figure 7.2.

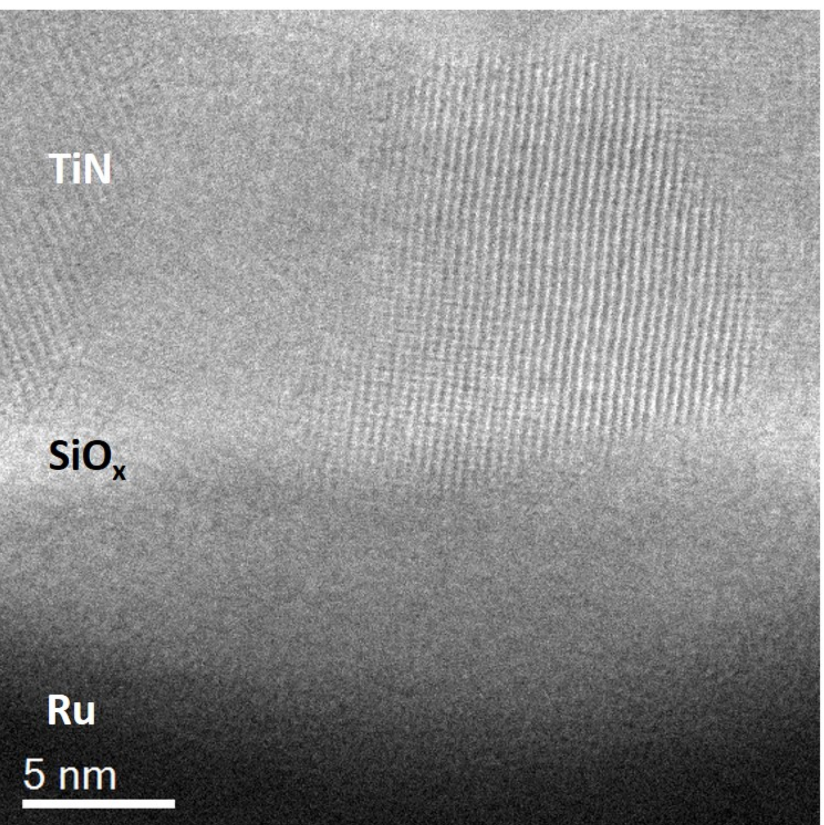


BF

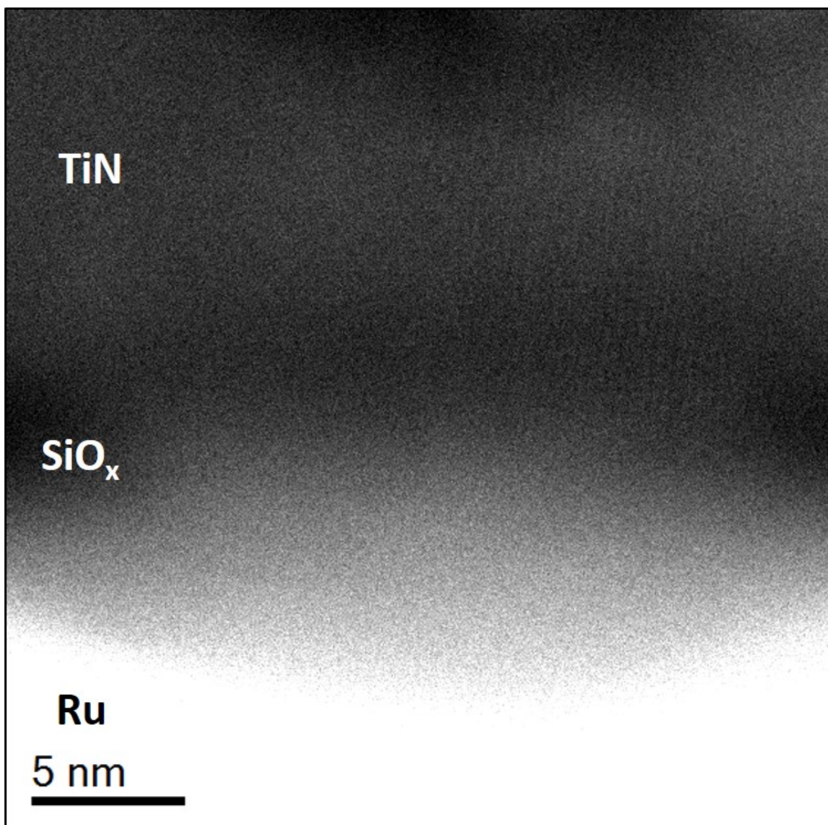


HAADF

Figure 7.5: Magnified BF STEM and HAADF images of the breakdown site in Figure 7.4. Crystallinity extends across the oxide layer and appears to originate from the TiN layer.

## 7.4 Discussion and Summary

In chapter 4 [Mehonic 2016], experimental evidence revealed global oxygen dynamics within the oxide layer, with the possibility of oxygen outmigration into the electrode layer. In the current chapter, a local breakdown site has been the focus of investigation. The O content at the breakdown site was observed to be relatively low, with EELS measurements suggesting the presence of regions of pure Si. This is consistent with the proposition of a silicon-rich conductive path forming during electroforming somewhere in the oxide layer.

However, an undesired effect of electrical stressing has also been observed whereby the TiN electrode appears to have locally migrated into the oxide layer, leading to the formation of a metallic filament. In chapter 5, as displayed in Table 2, breakdown occurred in device 4 at an approximate electric field strength of 14 MV $cm^{-1}$, assuming a 5 nm thickness for the oxide layer. This is far greater than the corresponding values in devices 1, 2, and 3. The bumps in the Ru interface will lead to further variations, with stronger local fields at thinner regions of the oxide. Such fields could be strong enough to cause migration of the relatively inert electrode material. No indication of a metallic filament was found in the switching oxide layers used in devices 1 and 3 (negative electroform).

A recent *in situ* TEM study by Yang et al. [Yang 2014B] revealed the possibilty of Pt migration in an a-$SiO_2$ insulating layer. Pt is a popular choice of material for an electrode and was not believed to promote metallic filamentation; however, Yang et al. showed that at high enough electric fields (> 4 MV $cm^{-1}$), Pt can be oxidised with resulting ion migration. Furthermore, Wang et al. [Wang 2016] recently observed the migration of Pd in sputtered a-$SiO_x$ films. Pd was also previously believed to be immobile during electrical stressing. These studies suggest that under the right conditions, even relatively inert electrode materials can be made to migrate through a dielectric layer. As shown in Table 2, devices 2 and 3 (positive bias) also supported electric fields strengths greater than 4 MV $cm^{-1}$. This may also indicate electrode migration in these devices and resulting hard breakdown as suggested in chapter 6 for device 3 (positive bias) in Figure 6.19(d). However, no evidence for this behaviour was found in device 2.

In summary, TEM analysis of an electrically stressed *MIM* structure with a comparatively

thin a-$SiO_x$ ($\approx$ 5 nm) layer has revealed the undesirable formation of a metallic filament resulting from TiN electrode migration. Although TiN is relatively , these results suggest that the strong electric field as a result of a thinner oxide layer will be sufficient to cause its migration into the oxide layer. This indicates that there are limitations to the thickness of an a-$SiO_x$ insulating layer needed for intrinsic switching behaviour, which will be important to consider in obtaining the optimal memory density for devices of this type.

# 8 Density Functional Theory

## 8.1 Introduction

In solid state physics, the many-body problem refers to the solution of the Schrödinger equation for a system of multiple nuclei and electrons. However, for systems with more than three of these particles, an analytical solution cannot be obtained and an approximate solution must be seeked. Given the large mass difference between atomic nuclei and electrons, in many cases nuclei can be treated as stationary on the timescale of electronic motion. This assumption, often referred to as the Born-Oppenheimer (BO) or adiabatic approximation [Born 1954], greatly simplifies the many-body problem. The solution of the Schrödinger equation then consists of solving for electronic and nuclear motion separately. Density functional theory (DFT) is a first principles method which is used to obtain an approximate solution to the Schrödinger equation of a many-electron system. In comparison to alternative first principles methods such as the Hartree-Fock method, DFT has a relatively low computational cost and can be used to study systems with hundreds to thousands of atoms. This made it ideal for the studies carried out on the aggregation and diffusion of oxygen vacancies in this thesis.

In DFT, the total energy $E$ of a many-electron system is expressed in terms of the single particle density, $n(\vec{r})$, so that $E = E[n(\vec{r})]$. $n(\vec{r})$ represents the probability of finding an electron at a particular location in space and has the advantage of being measured experimentally. This formalism is a result of the theorems of Hohenberg and Kohn [Hohenberg 1964]. Central to DFT is the solution of the Kohn-Sham equations [Kohn 1965], which will be introduced in the following section. This will be followed be description of the CP2K software used to carry out the calculations in this thesis. In chapters 9 and 10, adiabatic barriers for vacancy diffusion are calculated using the climbing-image nudged elastic band method (CI-NEB). This method will be discussed in the penultimate section [Henkelman 2000]. Finally, in chapter 10, negatively charged oxygen vacancies are considered. The treatment of charged defects requires correction schemes which will be described in the final section.

## 8.2 The Kohn-Sham Equations

The Kohn-Sham equations are a system of N equations for one-electron molecular orbitals, $\phi_i(\vec{r})$. $\phi_i(\vec{r})$ represent the molecular orbitals of a non-interacting system of electrons with an effective external potential described by the Kohn-Sham potential operator $\hat{V}_{KS}$, which as a conseqeuence of the theorems of Hohenberg and Kohn [Hohenberg 1964], is a functional of the single particle density $n(\vec{r})$, so that $\hat{V}_{KS} = \hat{V}_{KS}[n(\vec{r})]$. The Kohn-Sham equations are denoted

$$[-\frac{1}{2}\nabla_i{}^2 + \hat{V}_{KS}]\phi_i(\vec{r}) = \epsilon_i^{KS}\phi_i(\vec{r}), \tag{5}$$

where $-\frac{1}{2}\nabla_i{}^2 = \hat{T}$ represents the kinetic energy for the electron and $\epsilon_i^{KS}$ represents the Kohn-Sham energy of the electron [Kohn 1965]. For the system of non-interacting electrons described by the Kohn-Sham equations, $n(\vec{r})$ is simply expressed by

$$n(\vec{r}) = \sum_i^N \phi_i^* \phi_i \tag{6}$$

The Kohn-Sham equations are therefore coupled to one another via $\hat{V}_{KS}[n(\vec{r})]$, which can be decomposed into three components such that

$$\hat{V}_{KS} = \hat{V}_{ee} + \hat{V}_{ext} + \hat{V}_{xc}, \tag{7}$$

where $\hat{V}_{ee}$ accounts for the Coloumbic interactions between electrons in the system, $\hat{V}_{ext}$ accounts for the Coloumbic interactions between the electrons and the nuclei, and $\hat{V}_{xc}$ accounts for electron exchange and electron correlation effects. Electron exchange effects arise in the Hartree-Fock (HF) treatment of the many-body problem, resulting in contributions to the energy of the system through integrals $K_{ij}$ of the form

$$K_{ij} = -\frac{1}{2}\int\int_{AllSpace} \alpha_i^*(\vec{r}_1)\alpha_j^*(\vec{r}_2)\frac{1}{r_{12}}\alpha_j(\vec{r}_2)\alpha_i(\vec{r}_1)d\vec{r}_1 d\vec{r}_2, \tag{8}$$

where $\alpha_i$ and $\alpha_j$ represent the one-electron molecular orbitals in the HF approach, and $r_{12}$ is the interelectron distance. It should be noted that in HF theory, exchange effects are not included in Hamiltonian of the system, but are a result of using a Slater determinant to approximate the many-electron wavefunction. This represents an antisymmetrised product of one-electron molecular orbitals and takes into account the Pauli exclusion principle requirement for fermions. Electron correlation effects account for the deviation of the Hartree-Fock approximation from the real interacting system of electrons.

In order to solve the Kohn-Sham equations, an expression is required for $\hat{V}_{xc}$ .The most simple approximation for $\hat{V}_{xc}$ had already been suggested by Kohn and Sham in 1965 [Kohn 1965] and is referred to as the 'Local Density Approximation' (LDA). This term comes from the associated approximation of taking a system of constant density $\rho = constant$ and permitting density to vary on the incremental scale such that $\rho = \rho(\vec{r})$. An electron-nuclei system is modelled as a uniform distribution of negative electron charge density on a background of a uniform distribution of positive nuclear charge density, such that the system is electrically neutral. This system is termed a uniform electron gas. It is then assumed that the total exchange-correlation energy, $E_{xc}^{LDA}$, can be expressed in terms of single particle density, $n(\vec{r})$, so that

$$E_{xc}[n(\vec{r})] = \int_{AllSpace} n(\vec{r})\epsilon_{xc}[n(\vec{r})]d\vec{r}, \tag{9}$$

where $\epsilon_{xc}[n(\vec{r})]$ contains the exchange-correlation energy contribution per particle of the uniform electron gas expressed as a functional of $n(\vec{r})$. $\epsilon_{xc}[n(\vec{r})]$ is then split into exchange and correlation contributions:

$$\epsilon_{xc}[n(\vec{r})] = \epsilon_x[n(\vec{r})] + \epsilon_c[n(\vec{r})] \tag{10}$$

An expression for $\epsilon_x[n(\vec{r})]$ can be derived analytically and is often termed the 'Slater exchange'. This expression is, to within a prefactor, identical to an approximation to Hartree-Fock exchange energy suggested by Slater in 1951 [Slater 1951]. Various expressions for $\epsilon_c[n(\vec{r})]$ have been obtained [Koch 2001]. Although a crude approximation, the LDA is successful in determining molecular properties such as optimised geometries,

harmonic frequencies, and charge moments. However, examples of unsuccessful predictions include the overestimation of atomisation energies and the underestimation of semiconductor band gaps.

Improvements in energetic properties were achieved firstly by taking equation (9) to represent the first term in a Taylor expansion, so that $E_{xc} = [n(\vec{r}), \nabla n(\vec{r})]$. Such methods are termed generalised gradient approximations (GGA). Although these methods offer great improvements in the prediction of atomisation energies, the underestimation of semiconductor band gaps remains [Koch 2001]. 'Hybrid' functionals introduce a proportion of the exact exchange energy calculated using the HF method and deliver even greater improvements in the prediction of atomisation energies and the estimation of band gaps for semiconductors. These functionals are on the forefront of current DFT calculations and will be used in this investigation in order to accurately reproduce the band gap of a-$SiO_2$ (see section 8.5). However, the addition of HF calculations greatly increases the computational burden due to the presence of exchange integrals of the form shown in equation (8). The use of the 'Auxiliary Density Matrix Method' (ADMM) in the CP2K software (section 8.5) offers a novel solution to this problem.

## 8.3 Solving the Kohn-Sham Equations

In order to solve the Kohn-Sham equations, a self-consistent procedure must be used. A Slater determinant is used as an initial guess for the many-electron wavefunction $\Psi$, and is composed of the one-electron molecular orbitals, $\phi_i$. A common approach is to approximate $\phi_i$ as a linear combination of atomic orbitals (LCAO) so that

$$\phi_i = \sum_{\mu} c_{\mu i} \psi_{\mu}, \tag{11}$$

where $\psi_\mu$ represent the atomic orbitals and $c_{\mu i}$ are the relevant coefficients. The atomic orbitals are typically expanded using a basis set consisting of linear combinations of Gaussian functions (contracted Gaussian type orbitals (cGTO)) The LCAO approach provides an intuitive atom-centred picture where atomic orbitals can be expressed in a

relatively compact manner. In addition, the use of Gaussian basis sets is advantageous since analytical methods to deal with Gaussian integrals are well established; however, this results in errors due to the use of an incomplete basis set and does not satisfy the cusp condition for the electronic wavefunction near the nucleus. Alternatively, the molecular orbital $\phi_i$ can be expanded using a plane wave basis which has the advantage of providing a complete basis set in principle. Furthermore, plane waves are a natural choice for problems involving periodic boundary conditions. However, relative to cGTOs, a large quantity of plane waves is required to represent an electronic wavefunction. In addition, plane waves do not provide the intuitive physical picture provided by the LCAO. As will be described in the following section, in the CP2K software a dual representation of cGTOs and plane waves is used for computational efficiency.

The expansion of the molecular orbitals in equation (5) in terms of a chosen basis set $\{\beta_\mu\}$ results in the following eigenvalue problem [Vandevondele 2005]:

$$Kc = Sc\epsilon^{KS}, \tag{12}$$

where $K$ is the Kohn-Sham matrix consisting of integrals of the form

$$\int_{AllSpace} d\vec{r}\beta_\nu^*(\vec{r})[\frac{1}{2}\nabla_i{}^2 + \hat{V}_{KS}]\beta_\mu(\vec{r}), \tag{13}$$

and $S$ is the overlap matrix consisting of integrals of the form

$$\int_{AllSpace} d\vec{r}\beta_\nu^*(\vec{r})\beta_\mu(\vec{r}) \tag{14}$$

Finally, $c$ is a vector of the coefficients of the elements of $\{\beta_\mu\}$ and $\epsilon^{KS}$ is the vector of eigenvalues $\epsilon_i^{KS}$. By using an initial guess for $c$, the single particle density $n(\vec{r})$ can be calculated through equation (6) and $\hat{V}_{KS}$ can be constructed. Following this, the energy eigenvalues $\epsilon_i^{KS}$ can be obtained. If $S$ is a Hermitian matrix so that $S = (S^*)^T$, and positive definite so that $x^T Sx$ is positive for every non-zero column vector $x$ of real numbers, a Cholesky decomposition can be performed on $S$:

$$S = U^T U, \tag{15}$$

where $U$ is a lower triangular matrix of real, positive numbers. Equation (12) can hence be denoted

$$K' c' = c' \epsilon^{KS}, \tag{16}$$

where $K' = (U_T)^{-1} K U^{-1}$, and $c' = Uc$. New coefficients can then be obtained by the diagonalisation of $K'$ and a new single particle density can be calculated. The new and previous single particle densities are compared and the cycle is repeated until a self-consistent solution is obtained. The cost of such methods scales as $O(M^3)$, where $M$ is basis set size.

## 8.4 The CP2K Software for Density Functional Theory Calculations

The DFT calculations in this investigation were carried out using the Quickstep [Vandevondele 2005] package from the CP2K software. Quickstep can be described as a Gaussian and plane wave code (GPW) [Lippert 1997], employing a dual basis of cGTOs and plane waves in solving the Kohn-Sham equations. Wavefunctions are represented using cGTOs; however, the single-particle density is represented in terms of plane waves in order to calculate the energy of a system. This allows a number of improvements to the efficiency with which the Kohn-Sham equations can be solved. In solving the Kohn-Sham equations computationally, two processes dominate the calculation. Firstly, the calculation of the electron-electron Coulombic interaction energy, often referred to as 'Hartree' energy, and secondly, the solution of the eigenvalue problem in equation (12). By making use of a plane-wave representation of the system's single-particle density on a real space grid, Fast Fourier Transforms (FFTs) can be utilised to efficiently calculate the Hartree energy in a timeframe which scales linearly with system size. For resolving the eigenvalue problem, CP2K uses an alternative scheme to that used in section 8.3. The 'Orbital Transformation Method' (OT) paramatrises the vector of coefficients $c$ from

equation (12) by introducing the vector parameter $x$, such that

$$c(x) = c_0 cos(U) + xU^{-1} sin(U), \quad (17)$$

where $c_0$ is an initial vector which satisfies $c_0^T D c_0 = I$ (where $I$ is the idenity matrix), $x$ satifies the relation $x^T S c_0 = 0$, and $U = (x^T S x)^{\frac{1}{2}}$. This leads to a much improved cost for calculations scaling at $O(MN)$, where $M$ is basis set size and $N$ is the number of electrons in the system.

Due to the requirement of orthonormality of valence electron wavefunctions to core electron wavefunctions, valence electron wavefunctions oscillate rapidly near to atomic cores. The explicit treatment of core electrons therefore leads to an increased computational cost. In the pseudopotential approximation, the Coloumb potential due to the nucleus, and the effects of the core electrons, are approximated by an effective potential (termed a 'pseudopotential') which acts upon modified valence electron wavefunctions which have a smoother core component. A further improvement in the efficiency of the GPW method in CP2K is obtained through the use of the Goedecker, Teter, and Hutter pseudopotentials (GTH) [Goedecker 1996].

In this thesis, the bulk properties of oxygen vacancies and oxygen vacancy clusters in amorphous silicon dioxide are calculated. In principle this requires an infinitely large simulation cell; however, this is limited by computational resources. In practice this can be well approximated by using a sufficiently large cell in combination with periodic boundary conditions. The minimum bound for cell dimensions is perhaps 10 Å since the production of an oxygen vacancy has been calculated to produce network relaxation up to 10 Å from the vacancy site [Mukhopadhyay 2005]. In periodic systems, the wavefunction must satisfy Bloch's theorem. As a result, in order to obtain an accurate solution, ideally every wavevector $k$ in the system's first Brillouin zone should be accounted for in the calculation. However, Quickstep does not currently have this function implemented and only the $k = 0$ value is used, often termed the $\Gamma$ point. Improved $k$-space sampling can therefore only be achieved by using a sufficiently large simulation cell.

## 8.5 The PBE0-TC-LRC Hybrid Functional and The Auxiliary Density Matrix Method (ADMM)

The DFT calculations within this investigation make use of the PBE0-TC-LRC hybrid functional [Guidon 2009]. This functional originates from the earlier PBE0 hybrid functional [Adamo 1999]. For PBE0, the exchange-correlation energy, $E_{xc}^{PBE0}$, is derived according to

$$E_{xc}^{PBE0} = aE_x^{HF} + (1-a)E_x^{PBE} + (1-a)E_c^{PBE}, \tag{18}$$

where $E_x^{HF}$ is the exchange energy contribution from the HF Method, $E_x^{PBE}$ is the exchange energy contribution from the original GGA PBE functional [Perdew 1996], and $E_c^{PBE}$ is the correlation term for the PBE functional. $a$ is chosen to be 0.25, hence a combination of 25% HF exchange energy and 75% PBE exchange-correlation energy is utilised. The PBE0-TC-LRC functional offers great improvement in computational cost by calculating an accurate approximation for HF exchange energy. This is achieved by dividing the HF exchange term into short and long-range contributions. The short- range term consists of the same exchange operator from equation (8), with $r_{12}$ truncated at a distance of 2 Å. An additional long-range correction is then implemented for $r_{12}$ > 2 Å from $E_x^{PBE}$. The resulting exchange-correlation energy expression for PBE0-TC-LRC is then

$$E_{xc}^{PBE0-TC-LRC} = aE_x^{HF,TC} + aE_x^{PBE,LRC} + (1-a)E_x^{PBE} + (1-a)E_c^{PBE}, \tag{19}$$

where $E_x^{HF,TC}$ represents the Hartree-Fock exchange energy with a truncated Coloumb operator, and $E_x^{PBE,LRC}$ represents the long-range correction to the HF exchange energy using the PBE functional.

The implementation of the auxiliary density matrix method (ADMM) in CP2K further enhances the efficiency of hybrid functional calculations [Guidon 2010]. In order to calculate HF exchange energy, the one-electron wavefunctions $\alpha_k$ in equation (8) are expanded

using a basis set $\{\beta_\mu\}$ so that

$$K_{ij} = -\frac{1}{2}\int\int_{AllSpace}\sum_{\mu}\sum_{\nu}\sum_{\lambda}\sum_{\sigma} c_{\mu i}c_{\nu j}c_{\lambda j}c_{\sigma i}\beta^*_{\mu i}(\vec{r}_1)\beta^*_{\nu j}(\vec{r}_2)\frac{1}{r_{12}}\beta_{\lambda j}(\vec{r}_2)\beta_{\sigma i}(\vec{r}_1)d\vec{r}_1 d\vec{r}_2, \quad (20)$$

By summing over the indices $i$ and $j$, an element $P_{\mu\nu}$ of the density matrix $P$ is defined in

$$K[P] = -\frac{1}{2}\int\int_{AllSpace}\sum_{\mu\nu\lambda\sigma} P_{\mu\sigma}P_{\nu\lambda}\beta^*_{\mu}(\vec{r}_1)\beta_{\nu}(\vec{r}_2)\frac{1}{r_{12}}\beta_{\lambda}(\vec{r}_2)\beta_{\sigma}(\vec{r}_1)d\vec{r}_1 d\vec{r}_2, \quad (21)$$

where $P_{\mu\nu} = \sum_i c_{\mu i}c_{\nu i}$. $K$ represents the total HF exchange energy. However, the calculation of HF exchange energy scales very poorly at $O(M^4)$ where $M$ is basis set size. The auxiliary density matrix implemented for the PBE0-TC-LRC functional replaces $P$ with an auxiliary density matrix $\tilde{P} \approx P$ in which the electronic wavefunctions $\alpha_k$ are expanded in terms of an auxiliary basis set which is smaller in size or more rapidly decaying than $\{\beta_\mu\}$. A correction factor is then added to the approximate HF exchange which consists of the difference in DFT exchange energies between the original primary matrix and the auxiliary density matrix using the GGA PBE functional so that

$$K[P] \approx K[\tilde{P}] + (K^{GGA}[P] - K^{GGA}[\tilde{P}]) \quad (22)$$

## 8.6 The Calculation of Minimum Energy Paths (MEP) using the Nudged Elastic Band Method (NEB)

Since the migration of oxygen has been suggested for conductive path formation (see section 3.2), theoretical adiabatic barriers for oxygen vacancy diffusion will be calculated in chapters 9 and 10. The concept of activation energy is defined in Arrhenius' equation for the rate of a reaction, $k$, such that

$$k = Ae^{\frac{-E_{\alpha}}{k_B T}}, \tag{23}$$

where $A$ is the attempt frequency of the associated process, $E_{\alpha}$ is the activation energy per particle required for the process to occur, $k_B$ is the Boltzmann constant, and T is the system's temperature.

The nudged elastic band method (NEB) [Jónsson 1998] is a common approach to calculating minimum energy paths (MEPs) to estimate adiabatic reaction barriers. This method has been used successfully to obtain reaction barriers for the migration of oxygen vacancies and interstitials in a number of oxides including $\alpha$-quartz [Song 2001], $Ta_2O_5$ [Ramprasad 2003], $CeO_2$ [Nolan 2006], $HfO_2$ [Capron 2007] and ZnO [Huang 2009]. The NEB method is classed as a 'Chain of States' method. The initial and final configurations or 'frames' of the atomic coordinates for a reaction act as inputs for the algorithm. A chain of intermediate frames is then generated with the number of intermediate frames being arbitrary. These frames are often generated using simple linear interpolation. In the case of the NEB method, the frames are then constrained to one another by introducing a spring force between them analogous to Hooke's law $F = kX$, where $X$ is the displacement from a spring's relaxed position. The frames are then minimised with respect to energy taking into account not just interatomic forces in each frame, but also the spring forces acting upon each frame due to its adjacent frames. In this way an MEP can be traced out in configuration space. With all interatomic and spring forces present, the force $\mathbf{F_i}$ acting on the frame $i$ is given by

$$\mathbf{F_i} = -\nabla \mathbf{V}(\mathbf{R_i}) + \mathbf{F_i^s}, \tag{24}$$

where $\mathbf{V}(\mathbf{R_i})$ is the total potential energy of frame $i$, and $\mathbf{F_i^s}$ the spring force felt by frame $i$ due to frames $i-1$ and $i+1$ either side of it. However, the use of all of the components of interatomic and spring forces gives rise to two shortcomings. Firstly, the component of the spring force perpendicular to the reaction path tends to oppose the convergence of the frames onto the true MEP. This leads to an underestimation of MEP height and therefore reaction barrier height. Secondly, the component of the spring force parallel

to the reaction path will attempt to balance out the interatomic forces parallel to the reaction path. This leads to uneven frame spacing. In the NEB method, the spring force perpendicular to the reaction path and the interatomic forces parallel to the reaction path are projected out of equation (24). Consequently, during an NEB calculation, the force acting on each frame is given by

$$\mathbf{F_i^{NEB}} = -\nabla\mathbf{V}(\mathbf{R_i})_{\perp} + \mathbf{F^s_{i\|}}, \tag{25}$$

where $-\nabla\mathbf{V}(\mathbf{R_i})_{\perp}$ is the component of the interatomic forces perpendicular to the reaction path, and $\mathbf{F^s_{i\|}}$ is the spring force parallel to the reaction path. In this investigation, a variant of the NEB method known as the 'Climbing-Image' NEB method (CI-NEB) is used [Henkelman 2000]. Within this scheme, after a few energy minimisation steps, the spring forces on the highest energy image are removed and the perpendicular component of the interatomic forces is replaced with the inverted parallel component of the interatomic forces. This causes the image to rigorously converge to a saddle point, giving a more accurate estimation of a reaction barrier.

## 8.7 Corrections for Supercells with a Net Charge

Since the *MIM* devices to be studied are subjected to an electric field, the tunnelling of electrons between the oxide and electrodes could occur as discussed in section 3.5. The modelling of such a scenario will require the introduction of charge into a finite sized cell with periodic boundary conditions. This leads to two principle errors. Firstly, in a periodic calculation, the expectation values of the electrostatic potentials, $\langle\hat{V_{ee}}\rangle$ and $\langle\hat{V_{ext}}\rangle$, are set to 0 in order to prevent the divergence of the total energy of the system so that it is well-defined. The introduction of a defect into a pristine cell will change the expectation value to a non-zero value with respect to the pristine cell. In order ensure that the energy of the defected cell remains well defined, the expectation value of the electrostatic interactions must be reset to coincide with the pristine cell by applying a 'potential alignment' correction. Secondly, through the use of periodic boundary conditions, the introduction of a charge into a cell will also lead to the introduction of image charges in

neighbouring cells, and interactions between the charges in different cells. This unphysical interaction must be corrected for by applying an 'image charge' correction. In this thesis, Lany-Zunger charge corrections are used [Lany 2008][Lany 2009][Murphy 2013]. Within this formalism, charged defects are treated as classical multipoles up to and including a quadrupole. For a cell with defect $D$ and a charge $q$ present in the cell, the formation energy $\Delta H_{D,q}$ is obtained from the following expression:

$$\Delta H_{D,q}(E_f, \mu) = [E_{D,q} - E_P] + q(E_v + \Delta E_F) + \sum n_\alpha \mu_\alpha + E_{L-Z}, \tag{26}$$

where $E_{D,q}$ is the total energy of the supercell with the charged defect present, $E_P$ is the total energy of the pristine cell, and $\Delta E_F$ is Fermi energy with respect to the VBM. $E_v$ is equal to the energy difference between the cell with a hole introduced into the valence band in the dilute hole gas limit, and the corresponding pristine cell [Lany 2008][Lany 2009]. $n_\alpha$ represents the number of atoms of the species $\alpha$ added or removed from the cell ($n_\alpha$=+1 for removal and -1 for addition), with $\mu_\alpha$ being their chemical potential. $E_{L-Z}$ consists of the potential alignment ($\Delta E_{PA}$) and image charge correction ($E_{IC}$) terms. The former is denoted

$$\Delta E_{PA} = q(V_{D,q} - V_P), \tag{27}$$

where $V_{D,q}$ and $V_P$ represent atomic-sphere averaged electrostatic potentials at sites far away from the defect site in the defected and pristine cells. For the cubic cells used in this investigation, the latter is denoted

$$E_{IC} = (1 + f)\frac{q^2 \alpha_M}{2\epsilon L}, \tag{28}$$

where $f$=-0.35, $\alpha_M$ is the Madelung constant of the cell, $\epsilon$ is the dielectric constant, and $L$ is the cubed root of the cell volume.

# 9 The Diffusion and Aggregation of Neutral Oxygen Vacancies in Amorphous Silica

## 9.1 Introduction

As discussed in chapter 3, one suggestion for the formation of an Si-rich conductive path in a-SiO$_x$ during resistive switching is the diffusion and aggregation of oxygen vacancies. In section 3.7, a number of studies on crystalline oxides were discussed and revealed the material and morphology dependence of such processes. If oxygen vacancies are found to be sufficiently mobile, they could provide an important component to the large scale oxygen dynamics observed in chapter 6. This chapter firstly establishes that the aggregation of oxygen vacancies is energetically favourable for particular vacancy dimer and trimer configurations in a-SiO$_2$. An approximately homogenous distribution of oxygen vacancies is then assumed, since the results in chapter 6 and previous studies [Sasaki 2003][Zhang 2010] indicate that sputtered a-SiO$_x$ a structure resembling the random bonding model (RBM) for a-SiO$_x$ (see section 3.4). Barriers for vacancy diffusion are then calculated to understand whether vacancies could diffuse towards favourable sites in order to form aggregations. In addition, previously unreported trends between the structure of oxygen vacancies and the geometry of the pristine a-SiO$_2$ network are presented. It should be noted that since resistive switching has been observed in the studied devices at room temperature and pressure, the feasibility of oxygen vacancy diffusion is considered under these conditions.

## 9.2 Methodology

Five 216 atom a-SiO$_2$ geometries were selected from a series of structures produced using classical molecular dynamics and a melt and quench procedure using the LAMMPS code [Plimpton 1995] and the ReaxFF force field [Van Duin 2003]. These structures were produced prior to the current study courtesy of Al-Moatsem El-Sayed at UCL and are discussed in detail in previous publications [El-Sayed 2014][El-Sayed 2015A]. Starting from supercells with a $\beta$-cristobalite structure, the system was equilibrated at 300 K

and a pressure of 1 atm using a Berendsen thermostat and barostat [Berendsen 1984]. Maintaining the pressure at 1 atm, the temperature was linearly ramped to 5000 K. The temperature was maintained at 5000 K for 40 ps to ensure a complete melting of the initial structure and then brought down to 0 K at a rate of 8 K ps$^{-1}$. DFT was then used to optimise these starting geometries. One of the resulting a-$SiO_2$ structures is presented in Figure 9.1. Cell sizes ranged from 14.835 to 15.095 Å$^3$, with corresponding densities of 2.09 to 2.20 g cm$^{-3}$, which are also consistent with experiment (≈2.20 g cm). A range of densities was used since small variations in density can arise from differences in fabrication conditions [Mrstik 1999][Waseda 2007]. Additionally, in chapter 6, the a-$SiO_x$ layer was observed to exhibit variations in density within the oxide layer. Figure 9.2 shows the radial distribution functions derived from the studied geometries for Si-O, O-O, and Si-Si distances which first peak at 1.62 Å, 2.63 Å, and 3.13 Å, respectively. Furthermore, the histograms in Figure 9.3 show the distribution of (a) O-Si-O, and (b) Si-O-Si angles, taken from across all five geometries. The O-Si-O and Si-O-Si angles have mean values of 109.50$^\circ$ and 145.64$^\circ$, respectively, with angles distributed between 96$^\circ$ to 133$^\circ$, and 116$^\circ$ to 177$^\circ$. These values are in good agreement with previous experimental measurements [Mozzi 1969][Susman 1991]. Figure 9.3 shows the distribution of rings in the samples using King's criterion [King 1967]: 5-, 6-, and 7-member rings are the most common in agreement with previous theoretical studies [Rino 1993][Vollymayr 1996]. It should be noted that 8- and 9-member rings were only present in two of the five geometries and that these two geometries corresponded to the greatest cell sizes.

All DFT calculations were performed using the Gaussians and Plane Waves (GPW) [Lippert 1997] method as implemented in the CP2K code [VandeVondele 2005]. In attempt to more accurately reproduce the band gap of a-$SiO_2$, the PBE0-TC-LRC [Guidon 2009] non-local functional was used in conjunction with the auxiliary density matrix method (ADMM) [Guidon 2010] to reduce the computational expense. A long-range DZVP-MOLOPT basis set was used [VandeVondele 2007] along with the corresponding GTH pseudopotentials [Goedecker 1996] and a 400 Ry plane wave cutoff. This resulted in a mean one-electron band gap of 8.03 eV for the a-$SiO_2$ cells, which is the difference between the lowest unoccupied molecular orbital (LUMO) and highest occupied molecular orbital (HOMO) Kohn-Sham energies. This can be compared with approximately 9 eV from experimental measurements [DiStefano 1971]. Geometry optimisation was carried

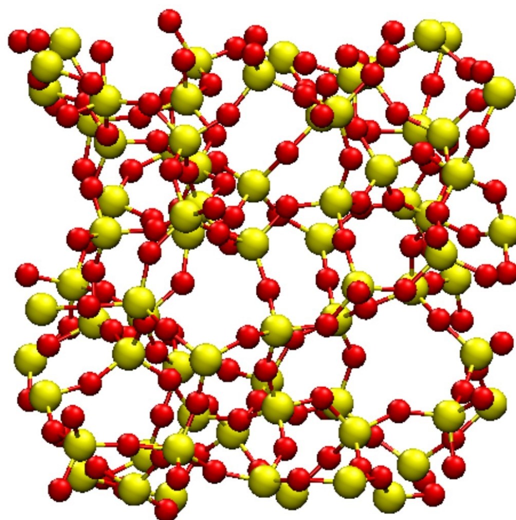

Figure 9.1: Example 216 atom a-$SiO_2$ structure produced using classical molecular dynamics. The yellow and red spheres represent Si and O atoms respectively.

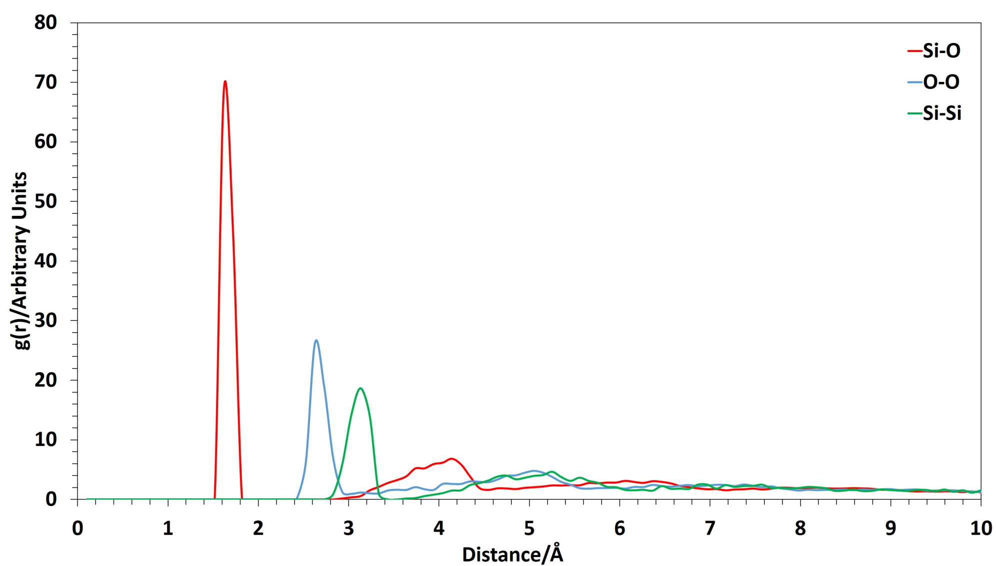


Figure 9.2: Radial distribution functions for Si-O, O-O, and Si-Si distances for the a-$SiO_2$ geometries used in this study. The first peaks of the S-O, O-O, and Si-Si distributions are at 1.62 Å, 2.63 Å, and 3.13 Å respectively.

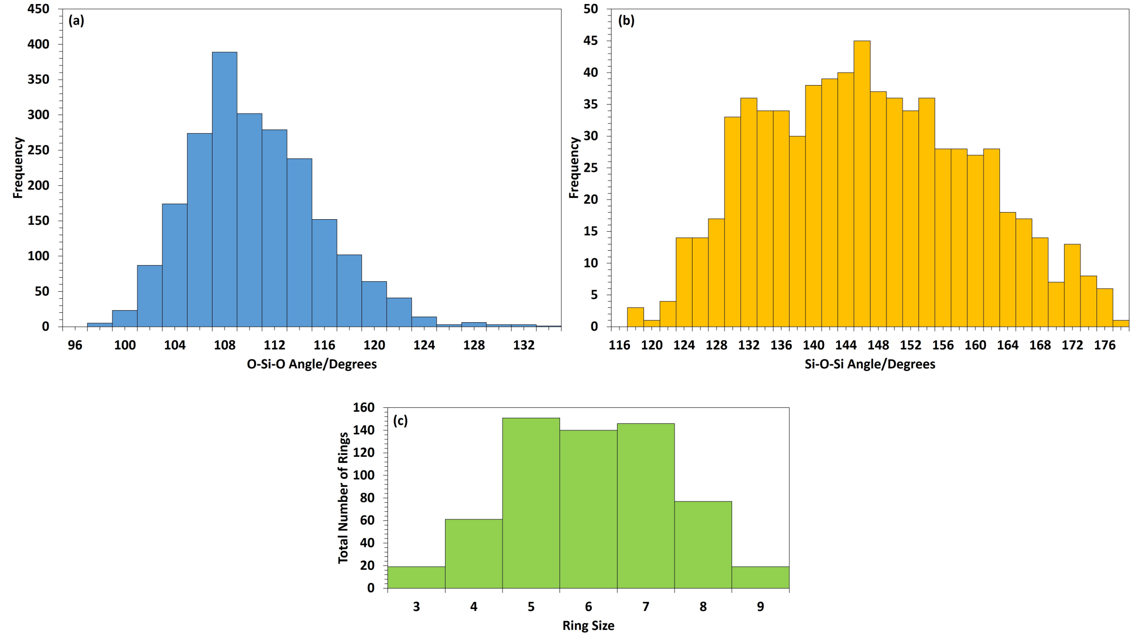


Figure 9.3: Distributions of **(a)** O-Si-O angles, **(b)** Si-O-Si angles, and **(c)** rings from across the studied a-$SiO_2$ geometries.

out using the Broyden-Fletcher-Goldfarb-Shanno (BFGS) scheme. In addition, Lany-Zunger charge corrections were used for calculations on charged cells with a dielectric constant of 3.9 [Lany 2009][Murphy2013]. Finally, adiabatic barriers for diffusion were calculated using the climbing image nudged elastic band (CI-NEB) method [Henkelman 2000] using 7 frames and a spring constant of -5.14 eV Å$^2$.

The calculation of formation energies of vacancies, aggregations of vacancies, and diffusion barriers required a selection of O vacancy sites which encompasses the range of local structural variations present in the amorphous material. In this study, pairs of nearest neighbour atom sites were selected so that they were situated within $N_{mr}$-member rings where $3 \leq N_{mr} \leq 7$, with equal weighting given to each value of $N_{mr}$. When the O atoms were removed, these sites would leave a di-vacancy pair within the corresponding ring. Ring sizes were classified according to King's criterion [King 1967] with Si atoms being used as nodes. Tri-vacancy sites were then formed from a subset of di-vacancy sites with all values of $N_{mr}$ represented. A total of 54 neutral O vacancies, 25 di-vacancy sites, and 12 tri-vacancy sites were obtained. As shown in previous studies, the removal of an O atoms leads to the formation of an Si-Si bond at the vacancy site with values ranging from 2.20 to 2.80 Å in literature [Martin-Samos 2004][Mukhopadhyay 2005][El-

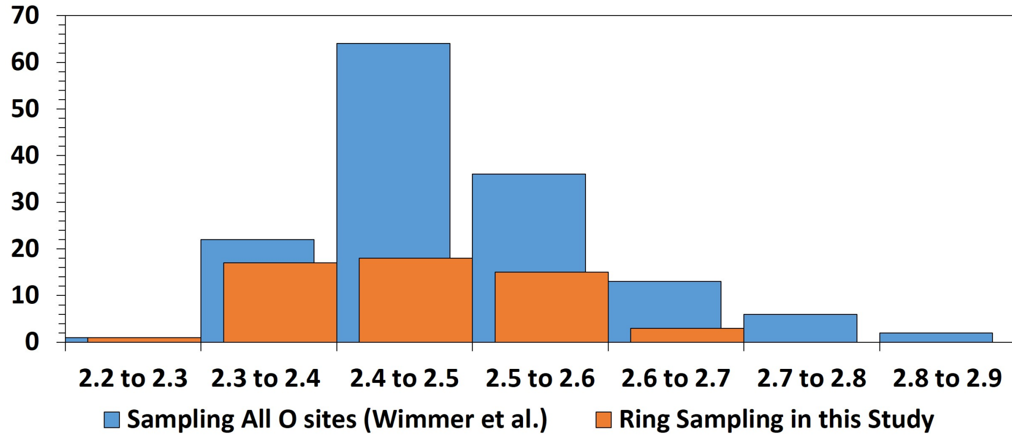


Figure 9.4: Histogram comparing the Si-Si bond lengths at O vacancies using the even ring sampling in this study, as compared to a previous study where all oxygen sites in a 216 atom a-$SiO_2$ cell were sampled [Wimmer 2016]. Both distributions peak at between 2.4 to 2.5 Å; however, this peaking is less prominent in the current study, which reflects the even ring sampling used. Sites between 2.7 to 2.9 Å were not encountered in this study, although they form 0.06% of the 144 oxygen sites sampled [Wimmer 2016].

Sayed 2015A]. The use of ring sampling was able to produce a comparable range from 2.25 to 2.70 Å. This study aimed to calculate 10 diffusion barriers for the migration of vacancies to a nearest neighbour site with two barriers obtained for every value of $N_{mr}$. The presented barrier heights describe the migration of the vacancy from the higher total energy configuration to the lower total energy configuration. It should be noted that due to the even sampling of vacancy sites from across ring structures, the presented results do not intend to account for a statistically weighted distribution of sites. Figure 9.4 shows a histogram of the Si-Si bond lengths obtained using this sampling method in comparison to a previous study [Wimmer 2016] with a-$SiO_2$ prepared using the same method [El-Sayed2014][El-Sayed 2015A]. Wimmer et al. sampled every O atom site in a 216 atom cell. Both distributions peak at between 2.4 to 2.5 Å; however, this peaking is less prominent in the current study, which reflects the use of even ring sampling. Sites between 2.7 to 2.9 Å were not encountered in the current study although they form 0.06% of the 144 O sites sampled by Wimmer et al. [Wimmer 2016].

For an O vacancy cluster composed of $n_{vac}$ vacancies, its corresponding formation energy, $E^{n_{vac}}_{form}$, was calculated using the following equation:

$$E^{n_{vac}}_{form} = E^{n_{vac}}_{defect} - E_{pristine} + n_{vac}\frac{1}{2}E_{O_2}, \quad (29)$$

where $E_{pristine}$ is the total energy of the pristine cell, $E^{n_{vac}}_{defect}$ is the total energy of the defected cell with $n_{vac}$ oxygen vacancies, and $E_{O_2}$ is the total energy of an $O_2$ molecule. In these calculations it is assumed that the Fermi level is suitably high that the neutral vacancies are stable. This is a reasonable assumption as, according to the study by Shen et al. [Shen 2015], the +/0 transition level for O vacancies in $SiO_2$ is around 2.5 eV above the top of the valence band, which is much lower than most relevant band offset energies of $SiO_2$ with Si or metallic electrodes [Afanas'ev 2014]. When an O vacancy is formed, before network relaxation, two Si atoms remain which are each bonded to three O atoms. Each Si atom forms the apex of a tetrahedron with the three O atoms (O1, O2, and O3) forming the vertices at the base as illustrated in Figure 9.5.

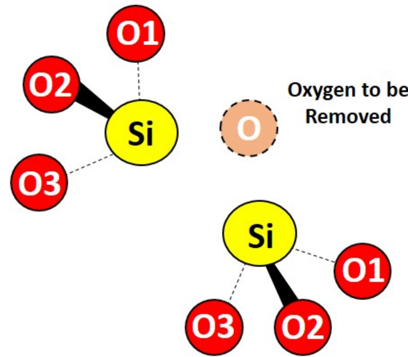


Figure 9.5: Illustration of an oxygen vacancy site. When the O atom is removed, each of the two remaining Si atoms form the apex of a tetrahedron with O1, O2, and O3 forming the vertices of its base.

The volume of the tetrahedron, $V_{tet}$, is given by

$$V_{tet} = \frac{1}{3!} \begin{vmatrix} x_{Si} & y_{Si} & z_{Si} & 1 \\ x_{O1} & y_{O1} & z_{O1} & 1 \\ x_{O2} & y_{O2} & z_{O2} & 1 \\ x_{O3} & y_{O3} & z_{O3} & 1 \end{vmatrix},$$

where $x_i$, $y_i$, and $z_i$ represent the coordinates of the corresponding atoms. For each vacancy site, the volumes corresponding to both Si atoms were summed to obtain total volume $V_{tot}$.

## 9.3 Results

### 9.3.1 Correlation Between Vacancy Formation Energy and Pristine Cell Geometry

As observed in previous studies [Mukhopadhyay 2005][El-Sayed 2015A], the formation of an Si-Si bond after the removal of an O atom resulted in a doubly occupied defect state located between 0.39 to 1.34 eV above the valence band maximum (VBM). In addition, the LUMO state was located between 7.04 and 8.20 eV above the VBM. Vacancy formation energies ranged between 6.02 to 7.64 eV. These values are 1 to 2 eV greater than those from prior studies [Martin-Samos 2004][Mukhopadhyay 2004][Anderson 2011]. In contrast to the current study in which the PBE0-TC-LRC functional was used to calculate the energy of a ground state oxygen molecule (triplet), Martin-Samos et al. used the LDA approach. Additionally, Anderson et al. used the GGA approach and also created oxygen vacancies prior to carrying out the melt and quench procedure, which more favourably accounts for network relaxation effects. Furthermore, Mukhopadhayay et al. used a HF implementation of the embedded cluster method, which again more favourably accounts for network relaxation, and used the energy of an individual O atom in the triplet state as opposed to an oxygen molecule. These differences in methodology could account for the variation in formation energy values between different studies. Previously, Mukhopadhyay et al. [Mukhopadhyay 2005] reported a strong positive correlation between vacancy formation energy and Si-Si bond length at the vacancy sites. This is also observed with the current data set as shown in Figure 9.6. In addition, a weakly negative correlation can be seen between Si-Si bond length and the LUMO as shown in Figure 9.7, where longer Si-Si bond lengths can be seen to correspond with lower energy LUMO states. This is in qualitative agreement with optical absorption spectra previously calculated by Mukhopadhyay et al. [Mukhopadhyay 2005], whereby longer Si-Si bond lengths corresponded to lower absorption energies. These trends are only observed after network relaxation.

Various criteria were tested at the vacancy sites in order to derive a relationship between the pristine cell and the resulting formation energies and Si-Si bond lengths after network relaxation. In addition to ring size, initial Si-Si distance and Si-O-Si bong angles were also examined at vacancy sites. No corresponding relationship was found in these cases

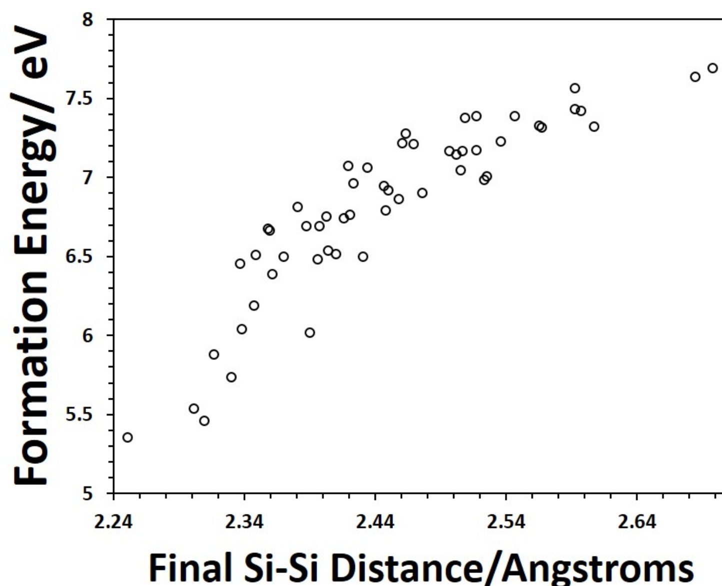


Figure 9.6: Vacancy formation energy plotted against Si-Si bond lengths at O vacancy sites after network relaxation. A positive correlation can be observed.

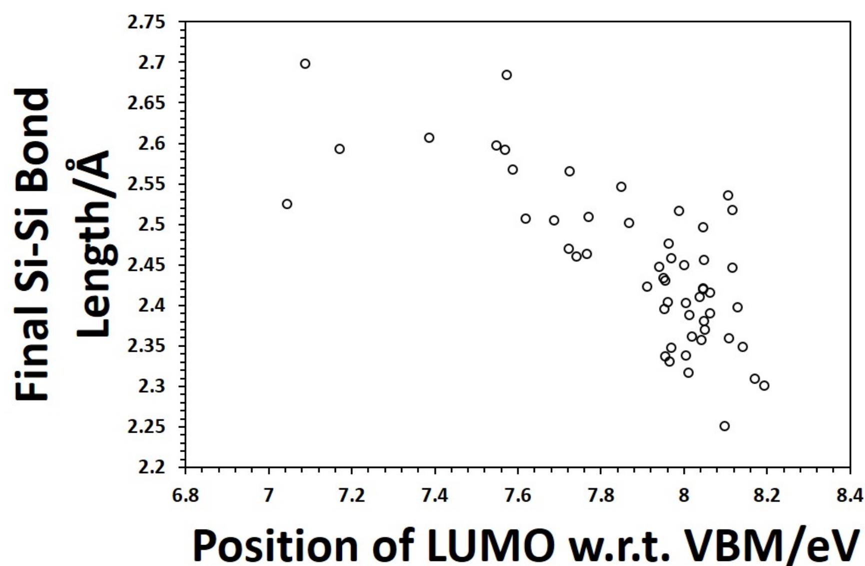


Figure 9.7: Si-Si bond lengths at neutral O vacancy sites after network relaxation plotted against the position of the LUMO with respect to the valence band maximum (VBM). A weakly negative correlation can be observed.

as reported in previous studies [Martin-Samos 2004][Mukhopadhyay 2005]. A notable positive correlation was finally observed between $V_{tot}$ and formation energy as shown in Figure 9.8(a). A linear fit of the form $y = Ax + B$ was was carried out using least squares regression and resulted in a correlation coefficient of 0.78. The corresponding residual plot is shown in Figure 9.8(b) and indicates a random distribution of data about the line of best fit. This suggests a good linear fit to the data. In order to test the predictibility indicated by this trend, an attempt was made to populate the lower end of the range of formation energies, which was more scarcely sampled. Five sites were identified using the linear relationship and their calculated values for formation energy are represented as the black filled circles on Figure 9.8(a). It should be noted that the lowest formation energy of the entire data set was identified in addition to successfully finding sites with relatively low formation energies. A similar linear relationship has been previously observed between vacancy formation energy and local atomic stress in a pristine cell calculated using a two-body potential [Martin-Samos 2004]. This could suggest that $V_{tot}$ varies approximately linearly with local atomic stress. An additional relationship between $V_{tot}$ and Si-Si bond length after network relaxation can also be observed in Figure 9.9. This is a result of the positive correlation between vacancy formation energy and Si-Si bond length [Mukhopadhyay 2005]. In this case, a quadratic polynomial fit of the form $Ax^2 + Bx + C$ was carried out using least squares regression and resulted in a correlation coefficient of 0.68. The corresponding residual plot is shown in Figure 9.9(b) and indicates a random distribution of data about the line of best fit. This suggests a reasonable quadratic fit to the data. The quadratic fit was then used to predict the distribution of Si-Si bond lengths at all O vacancy sites across the five 216 atoms cells (720 sites in total). This was compared to the distribution of Si-Si bond lengths in the study carried out by Wimmer et al. [Wimmer 2016], where all 144 O sites from a 216 atom cell were sampled. As shown in Figure 9.10, in both cases the majority of sites have a bond length between 2.3 and 2.6 Å with a most probable value between 2.40 and 2.5 Å. In contrast to the ring sampling used in this study (Figure 9.4), the predicted bond lengths are weighted more correctly in agreement with Wimmer et al. However, no bond lengths between 2.8 and 2.9 Å were predicted, although such sites form a negligible contribution to the study by Wimmer et al.

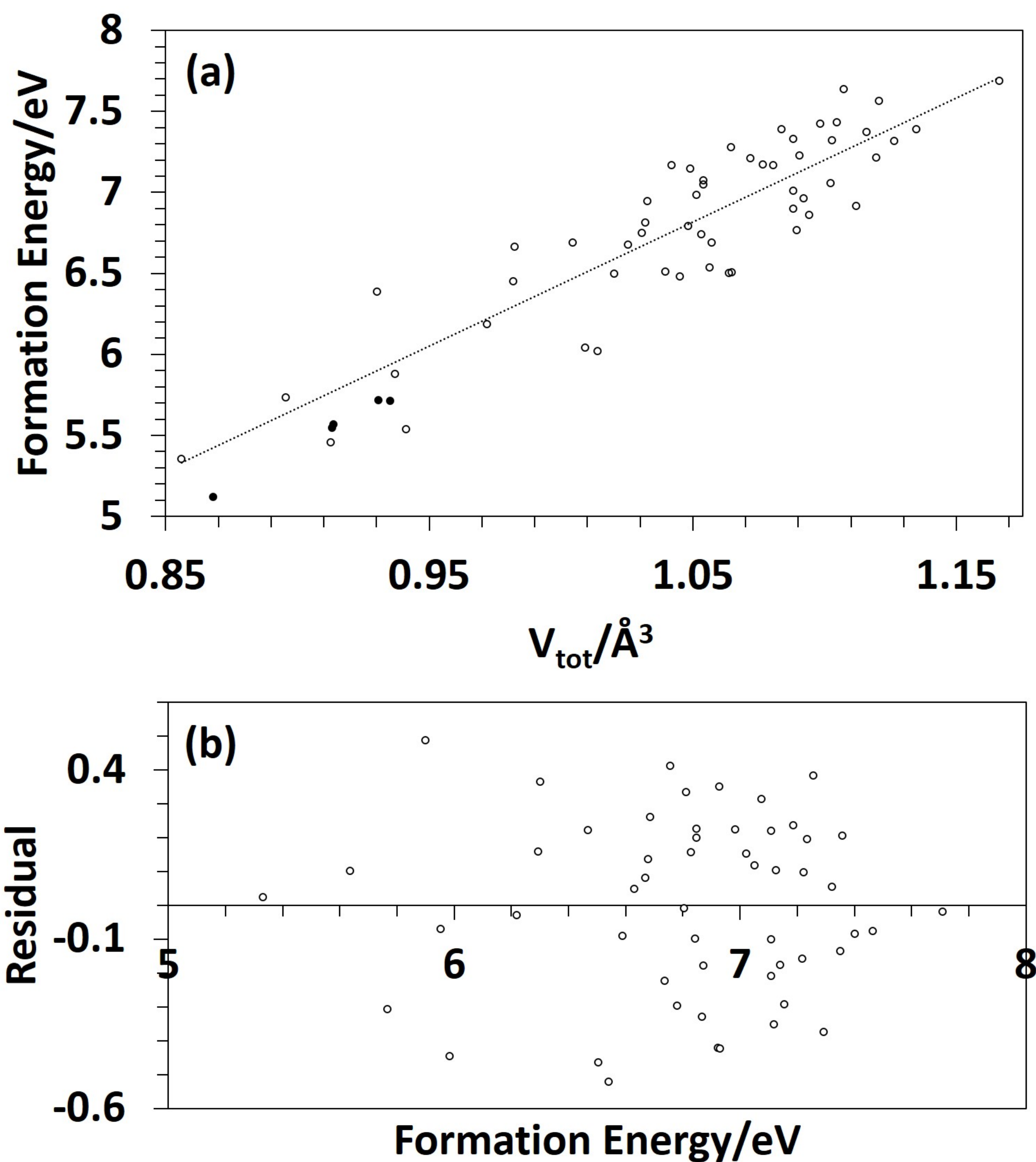


Figure 9.8: (**a**) Vacancy formation energy plotted against total tetrahedral volume $V_{tot}$. A linear fit of the form $Ax+B$ has been been carried out using least squares regression with a resulting correlation coefficient of 0.78. The black filled circles represent a successful attempt to populate the lower end of the range of formation energies using the linear fit, with the lowest value identified in the process. (**b**) Corresponding residual plot for (a). This indicates a random distribution of data points about the line of best fit, suggesting a good linear fit to the data.

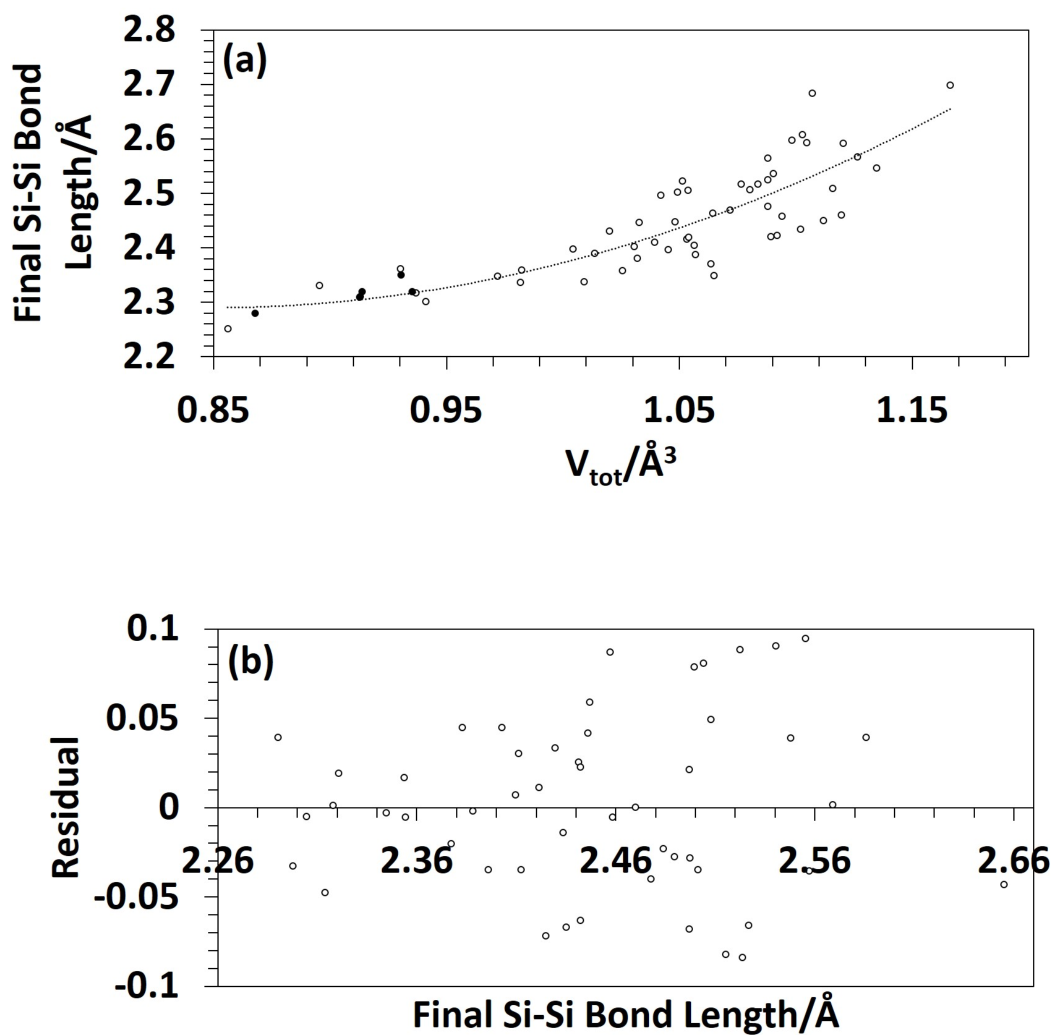


Figure 9.9: (**a**) Si-Si bond length after network relaxation plotted against total tetrahedral volume $V_{tot}$. A quadratic fit of the form $Ax^2 + Bx + C$ was carried out using least squares regression with a resulting correlation coefficient of 0.68. The black filled circles represent a successful attempt to populate the lower end of the range of Si-Si bond lengths using the linear fit from Figure 9.8. (**b**) Corresponding residual plot for (a). This indicates a random distribution of data points about the line of best fit, suggesting a reasonable quadratic fit to the data.

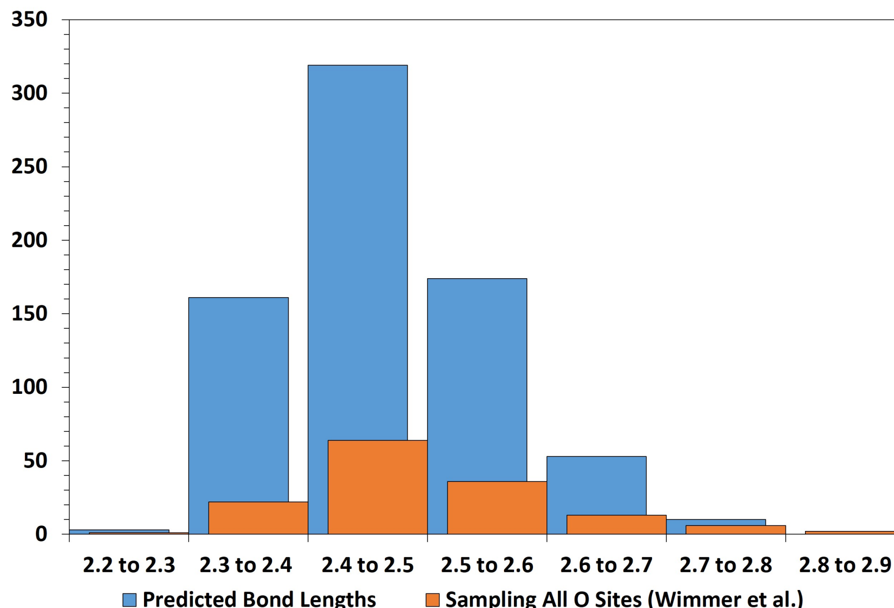


Figure 9.10: A histogram showing the predicted Si-Si bond lengths from all 720 O vacancies from the five studied 216 atom cells using the quadratic fit from Figure 9.9. The most probable bond length lies between 2.4 and 2.5 Å, with the majority of bond lengths falling between 2.3 and 2.5 Å. This is in agreement with the study carried out by Wimmer et al., where all oxygen sites in a 216 atom a-$SiO_2$ cell were sampled [Wimmer 2016].

### 9.3.2 Exploring the Aggregation of Oxygen Vacancies in Amorphous Silica

The removal of two nearest neighbour O atoms from the a-$SiO_2$ network resulted in the formation of two Si-Si bonds after network relaxation, ranging from 2.20 to 3.00 Å. This is an increase of 0.3 Å from the upper limit of the single vacancy case (2.70 Å). Similarly, after the removal of three nearest neighbour O atoms, three Si-Si bonds were formed, ranging from 2.40 to 3.00 Å. In this case there is an additional increase in the lower limit of the single vacancy case (2.25 Å) by 0.15 Å. These differences can be explained by the decrease in local density at the vacancy sites, resulting in the formation of longer bonds. In the di-vacancy case, the formation of the two Si-Si bonds most commonly resulted in the presence of two doubly occupied states in the band gap ranging from -0.06 to 0.40 eV, and 1.52 to 2.20 eV above the VBM, respectively. In comparison, the formation of three Si-Si bonds in the tri-vacancy case resulted in the presence of only two doubly occupied states in the band gap, ranging from 0.51 to 2.26 eV and 1.64 to 2.25 eV above the VBM, respectively. The mean position with respect to the VBM of the LUMO was observed to decrease with the removal of additional O atoms, as compared to 7.89 eV

in the single vacancy case. For di-vacancies, the LUMO was located 7.12 eV above the VBM on average, while for tri-vacancies this decreased to 6.73 eV. This may suggest optical absorption at lower energies with increasing vacancy cluster size as a result of the increase in Si-Si bond lengths in di- and tri-vacancy clusters [Mukhopadhyay 2005].

In order to gain an understanding of interactions between vacancies in aggregations, the formation energies of di- and tri-vacancy clusters per vacancy were compared with the mean formation energy of the vacancies when present at the very same locations individually. Figure 9.11 shows a scatter plot comparing these values for each vacancy cluster where (-) represent di-vacancy sites and (▲) represent tri-vacancy sites. A linear fit was performed using least squares regression and resulted in a correlation coefficient of 0.92 with a gradient of 1.00. These calculations suggest that, on average, there is no overwhelming trend for di- and tri-vacancies to cluster. The difference in energy between data points and the line of best fit can be interpreted as a measure of cluster binding energy for vacancies brought together from an initial infinite separation. 15 sites are positioned below the line of best fit, suggesting a gain in energy after vacancy aggregation relative to the sample average with maximum values of 0.13 eV and 0.18 eV for di- and tri-vacancies, respectively. 8 of the 15 favourable sites are vacancies situated within 3-member rings. A typical relaxed configuration of such a cluster is shown in Figure 9.12(a). The arrangement of Si atoms in a 3-member ring closely resembles that of the energetically favourable 'cyclic' geometry of an Si trimer [Raghavachari 1986][Tam 2015]. This may explain the favourable clustering of vacancies in 3-member rings. It should be emphasised, however, that 3-member rings represent a relatively small proportion of oxygen vacancy sites in the a-$SiO_2$ geometries (≈8%) as indicated in Figure 9.3(c). Furthermore, as shown in Figure 9.11(b), a tri-vacancy cluster can also be arranged in a 'Y' shape such that three Si atoms emerge outwards from a single Si atom. Alternatively, three vacancies may also be arranged in a chain consisting of four Si atoms as shown in Figure 9.11(c). Four out of the 15 favourable sites in Figure 9.11 correspond to a 'Y' arrangement, whereas tri-vacancy chains are all situated above the line of best fit. Previous studies on the optimum geometry of 4 Si atom clusters indicated that the 'Y' geometry is energetically favourable when compared to a chain of 3 vacancies [Raghavachari 1986], and could account for the favourable binding energies of the 'Y' geometry.

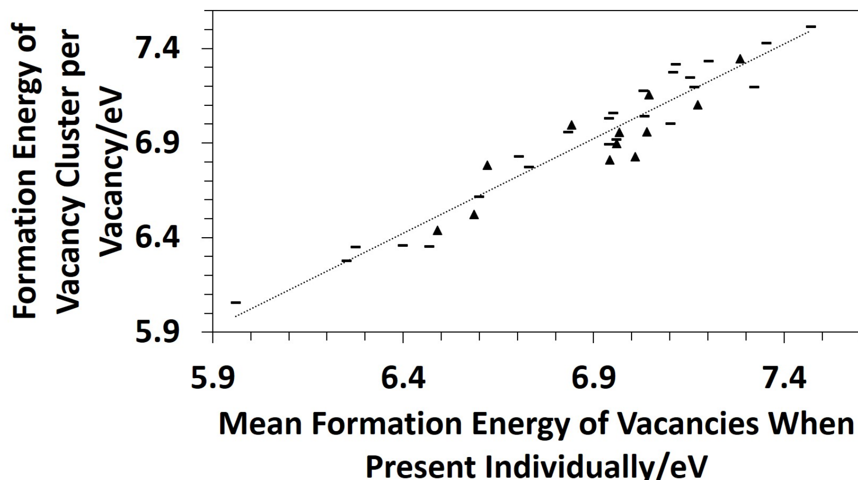


Figure 9.11: Scatter plot of formation energy of a di-vacancy or tri-vacancy cluster per vacancy plotted against the mean formation energy of the very same vacancies when present individually. (-) represent di-vacancy sites and (▲) represent tri-vacancy sites. A linear fit has been performed to the data points using least squares regression, resulting in a correlation coefficient of 0.92 and a gradient of 1.00.

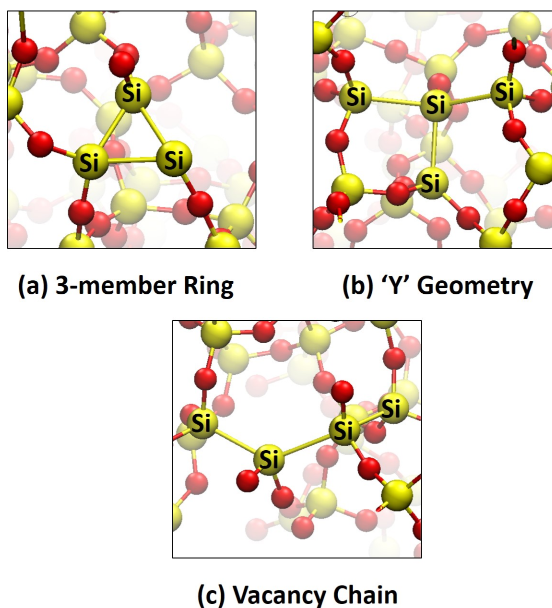


Figure 9.12: Final geometric configurations of tri-vacancy clusters. **(a)** Three O vacancies in a 3-member ring; **(b)** Y-type relaxed geometry of a tri-vacancy; **(c)** A tri-vacancy forming a chain.

### 9.3.3 Exploring the Migration of Neutral Oxygen Vacancies in Amorphous Silica

Assuming an approximately homogenous distribution of oxygen vacancies, energy barriers were calculated for the diffusion of neutral vacancies to study whether they are mobile enough to aggregate at energetically favourable sites. Two mechanisms were observed with resulting barrier heights between 3.2 and 5.6 eV, and a mean of 4.2 eV. A prototypical diffusion mechanism is illustrated in Figure 9.13(a) for $N_{mr} \geq 4$. The migrating O remains bonded to Si2 while diffusing towards the vacancy site, resulting in an increasingly stretched Si1-O bond (Figure 9.13(a)2) and the transfer of electron density from the vacancy to between Si1 and Si2 (Figure 9.13(a)4).

An alternative diffusion mechanism is illustrated in Figure 9.13(b) for $N_{mr}$=3. The diffusing O firstly bonds to Si3, with the electron density initially at the vacancy localising on the undercoordinated Si1 (Figure 9.13(b)2). The diffusing O then reforms its bond with Si1 and the electron density occupies an antibonding orbital between Si1 and Si2 (Figure 9.13(b)3). As the O settles into the vacancy position, the electron density finally occupies a bonding orbital between Si1 and Si2 (Figure 9.13(b)4). In addition to an alternative diffusion mechanism, O vacancies in a 3-member ring exhibited the lowest diffusion barrier of 3.2 eV. The calculated barrier heights suggest, however, that under room temperature operating conditions, the diffusion of neutral oxygen vacancies is not feasible.

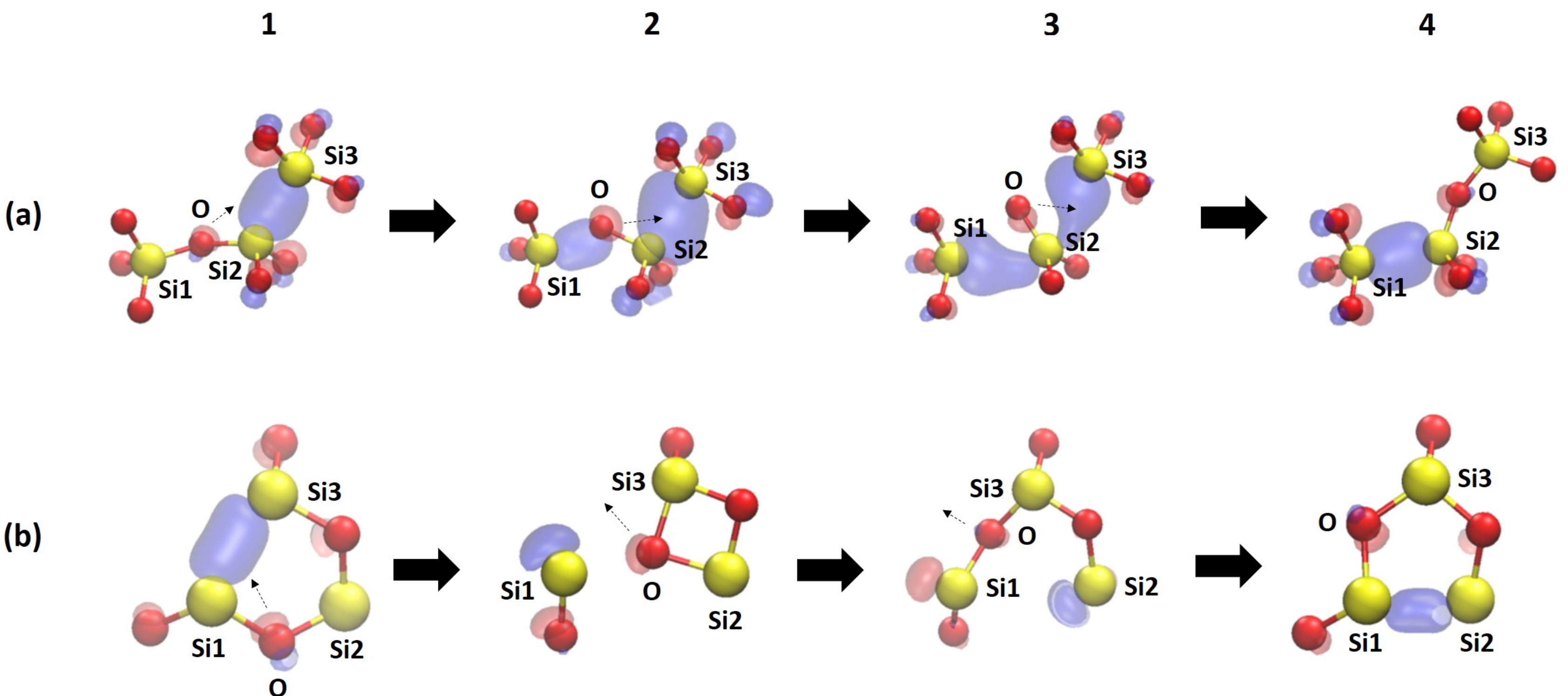


Figure 9.13: Schematic showing the HOMO during the diffusion of neutral oxygen vacancies to adjacent sites. Si atoms are represented as yellow spheres and O atoms as red spheres, and positive and negative isosurfaces are represented as blue and red, respectively, with approximate iso-values of $\pm 0.06$. The dotted arrows emphasize the motion of the associated atoms. **(a)** A prototypical mechanism for the migration of a neutral oxygen vacancy: **1.** O begins to migrate towards vacancy. **2,3,4.** As the Si1-O bond stretches, electron density from the vacancy site begins to localise between Si1 and Si2 resulting in the eventual transfer of the vacancy. **(b)** An alternative mechanism observed for 3-rings: **1.** O begins to migrate towards vacancy. **2.** Diffusing O forms bond with Si3, with electron density from the vacancy localising on the under-coordinated Si1. **3.** Diffusing O reforms bond with Si1 and the electron density occupies an antibonding orbital between Si1 and Si2. **4.** As the diffusing O settles into the vacancy, the electron density occupies a bonding orbital between Si1 and Si2.

## 9.4 Discussion and Summary

As suggested in section 8.3.1, $V_{tot}$ could be related to the local atomic stress at the vacancy site [Martin-Samos 2004]. From this perspective, a greater local volume corresponds to greater local stress at the vacancy site. Since the mass of the atoms in the tetrahedral units remains constant, this suggests that a lower local density at the vacancy site results in a higher local stress environment. The most common crystalline form of $SiO_2$, $\alpha$-quartz, has a greater density than its amorphous counterpart ($\approx$2.65 g cm$^{-3}$). Regions of relatively lower local density in a-$SiO_2$ may therefore correspond to regions of high local stress at which O vacancy formation is energetically more favourable. This provides one explanation for the relationship between vacancy formation energy and $V_{tot}$, and may suggest that atomic-level stress in a-$SiO_2$ can be characterised by short-range order involving just the first and second neighbour atoms with respect to the O vacancy. As demonstrated in section 8.3.1, such a relationship could useful in analysing the distribution of O vacancy sites in samples of a-$SiO_2$, or identifying particular sites of interest at a low compuational cost. A similar relationship may be applicable to other amorphous materials.

The calculations presented on di- and tri-vacancy clusters indicated that vacancies situated in a 3-member ring are energetically favourable environments. The diffusion of an oxygen vacancy along a 3-member ring also exhibited an alternative mechanism as described in Figure 9.13(b) and corresponded to the lowest diffusion barrier for diffusion of 3.2 eV. Previous studies have calculated relative strain energies of approximately 0.25 eV for 3-member rings [Hamann 1997][Uchino2000], which is notably higher than the corresponding 4-member ring value of 0.02 eV [Uchino 2000]. The behaviour of the 3-member ring during vacancy aggregation and diffusion could be a result of relatively high strain energy in Si-O bonds.

In summary, the presented calculations on di- and tri-vacancy clusters demonstrate that there are energetically favourable sites for the aggregation of oxygen vacancies in amorphous silica, with maximum binding energies of 0.13 eV and 0.18 eV, respectively. However, the average barrier for neutral vacancy diffusion was found to be 4.6 eV, rendering effective clustering of randomly distributed neutral vacancies unfeasible. Furthermore,

a useful criterion has been found, which allows the reasonable identification of oxygen vacancy sites with particular formation energies by analysing the pristine a-$SiO_2$ geometry. If oxygen vacancies do indeed aggregate, an alternative mechanism for diffusion may exist. In the following chapter, the effect of electron trapping on vacancy diffusion is explored.

# 10 Exploring Electron Trapping at Oxygen Vacancies

## 10.1 Introduction

In section 3.5, electron injection into a-$SiO_2$ during electrical stressing was discussed. In particular, Bersuker et al. proposed that electron trapping at oxygen vacancies contributes to additional trap generation [Bersuker 2008]. In this chapter, a first principles study of electron trapping at oxygen vacancies is carried out for a-$SiO_2$. Vacancies are shown to form stable electron traps, which are capable of trapping up to two electrons. The effect of electron trapping on vacancy diffusion is then studied. In addition, an insight into the overlap in trap level distributions of oxygen vacancies and intrinsic electron traps is gained.

## 10.2 Methodology

30 sites were chosen from across the range of Si-Si geometries from chapter 9 for studying electron trapping at oxygen vacancies. This included the very same sites used to calculate the barriers for diffusion for neutral oxygen vacancies. The parameters used for the following DFT and NEB calculations were identical to those used in chapter 10, and formation energies of charged vacancies were calculated using equation (26) from section 8.7. The reported defect state positions with respect to the conduction band minimum (CBM) refer to LUMO-HOMO values using the PBE0-TC-LRC functional. It should be noted that during the following NEB calculations, when two maxima were potentially present in the 7 frame calculation, the calculation was divided into two separate 7 frame calculations in order to accurately characterise the reaction path.

As will be shown below, at higher Fermi level positions, extra electrons can be trapped by neutral O vacancies and change their mobility. However, the vacancy diffusion process competes with thermal ionisation of trapped electrons into the conduction band of a-$SiO_2$. Thermal ionisation energies were calculated for single electrons trapped at vacancy sites using DFT total energy values. The difference between optical ($E_{opt}$) and thermal ($E_{therm}$) ionisation energies of electrons trapped at oxygen vacancies can be ex-

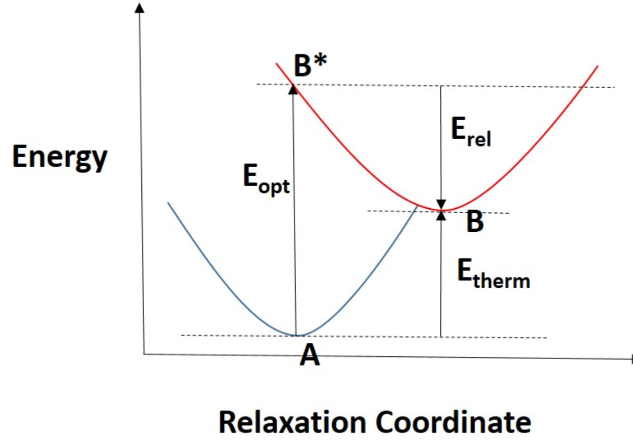


Figure 10.1: Schematic illustrating the difference between optical ($E_{opt}$) and thermal ($E_{therm}$) ionisation energies using potential energy surfaces. Optical ionisation corresponds to a Frank-Condon type transition of the electron from trap state $A$ to the conduction band state $B^*$ with no associated network relaxation. In contrast, thermal ionisation is a phonon assisted process whereby full network relaxation ($E_{rel}$) takes place in the transition of the electron from trap state A to conduction band state B.

plained by using the potential energy surface schematic in Figure 10.1 [Gavartin 2006]. Optical ionisation corresponds to a rapid Frank-Condon type transition of the electron from the trap state $A$ into to the conduction band state $B^*$ with no associated network relaxation. In contrast, thermal ionisation is a slower phonon assisted process with sufficient time for full network relaxation ($E_{rel}$) to take place while the electron transitions from trap state A to conduction band state B. This is illustrated by the change in relaxation coordinate between states A and B in Figure 10.1 [Gavartin 2006]. In order to obtain the thermal ionisation energy, firstly optical ionisation energies, $E_{opt}$, and network relaxation energies, $E_{rel}$, were calculated as defined below [Foster 2002][Gavartin 2006]:

$$E_{opt} = E^{0}_{q=-1} - E^{-1}_{q=-1} + E^{-1}_{pristine} - E^{0}_{pristine} + E_{corr}, \tag{30}$$

where $E^{0}_{q=-1}$ is the energy of the $q = -1$ geometry with charge 0, $E^{-1}_{q=-1}$ is the energy of the $q = -1$ geometry with charge -1, $E^{-1}_{pristine}$ is the energy of the pristine cell with a delocalised electron in the conduction band, and $E_{pristine}$ is the energy of the pristine cell. $E_{corr}$ is a Lany-Zunger charge correction term included due to the presence of localised charge in $E^{-1}_{q=-1}$. Additionally,

$$E_{rel} = E^0_{q=-1} - E^0_{q=0}, \tag{31}$$

where $E^0_{q=0}$ is the energy of the $q = 0$ geometry with charge 0, and $E^0_{q=-1}$ is the energy of the $q = -1$ geometry with charge 0. Thermal ionisation energy, $E_{therm}$, is then approximately given by

$$E_{therm} = E_{opt} - E_{rel} \tag{32}$$

## 10.3 Results

### 10.3.1 Competition for Electrons between O Vacancies and Intrinsic Traps

In 10 of the 30 sites chosen for the study, the injected electrons localised onto intrinsic trap sites present in the cell before the formation of the vacancy. However, for the 20 remaining sites, the electron trapping occurred at the vacancies, despite the presence of intrinsic electron trapping precursor sites. In Figure 10.2, the injected electron is trapped at an intrinsic site on Si3, despite the presence of the vacancy between Si1 and Si2. This effect is correlated with the geometry of vacancy sites. Figure 10.3 shows a scatter plot with the Si-Si bond length of the studied vacancies plotted against the position of the lowest unoccupied molecular orbital (LUMO) of the 215 atom cell in which the vacancy was situated. The position of the LUMO is measured with respect to the valence band maximum (VBM). The white circles indicate cells where electron injection resulted in localisation at the O vacancy, whereas the black filled circles indicate cells where the electron localised onto an intrinsic trap. Trapping at intrinsic sites appears to frequently occur for short Si-Si bond lengths with no trapping observed above bond lengths of 2.48 Å. This suggests that O vacancies with longer Si-Si distances form deeper electron traps below the distribution of intrinsic traps.

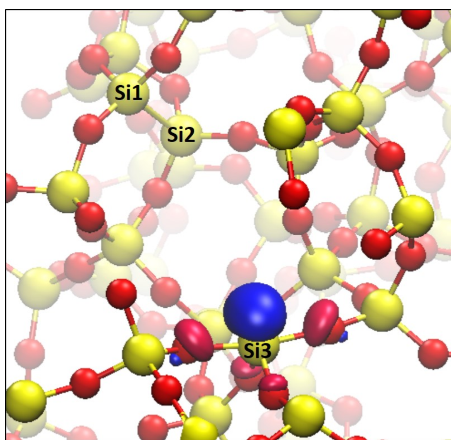


Figure 10.2: HOMO in a-$SiO_2$ cell showing injected electron trapped at an intrinsic site on Si3, despite the presence of the vacancy between Si1 and Si2. Positive and negative isosurfaces are shown as blue and red, respectively, with approximate iso-values of $\pm 0.06$.

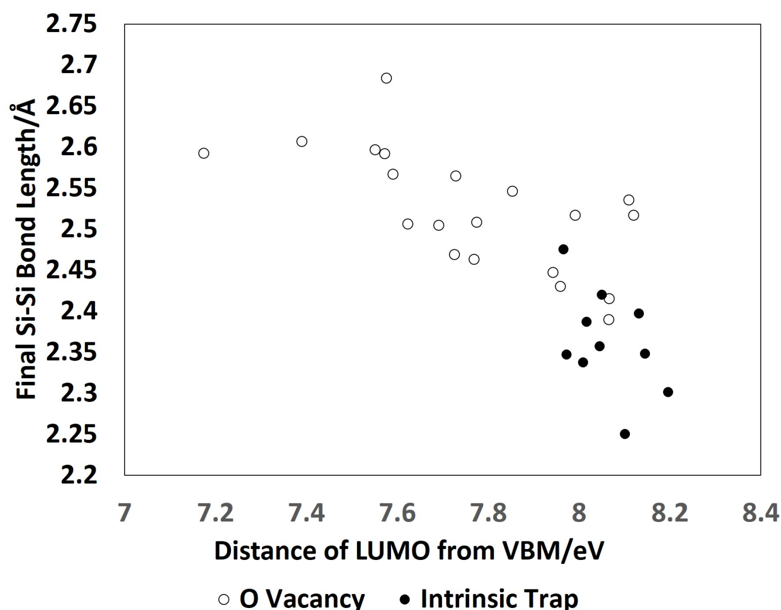


Figure 10.3: Scatter plot with the Si-Si bond length of the studied vacancies plotted against the position of the lowest unoccupied molecular orbital (LUMO) of the 215 atom cell in which the vacancy was situated. The position of the LUMO is measured with respect to the valence band maximum (VBM). The white circles indicate cells where electron injection resulted in localisation at the O vacancy, whereas the black filled circles indicate cells where the electron localised onto an intrinsic trap.

### 10.3.2 Electron Trapping at O Vacancies

For the 20 vacancies at which the injected electron had localised, Si-Si bond lengths at neutral vacancies ranged from 2.39 to 2.68 Å, with a corresponding doubly occupied defect state located between 0.39 and 1.34 eV above the VBM. The localisation of the electron resulted in local geometry distortion around the vacancy site with an increase in Si-Si bond length ranging from 2.34 to 3.01 Å. The electron occupied a defect state situated between 1.61 and 3.08 eV below the CBM. Finally, the injection of a second electron led to pairing with the first electron in the antibonding orbital and an additional increase in Si-Si bond length to between 2.47 and 3.43 Å. In this case, the defect state occupied by the electron pair was located between 0.84 and 2.79 eV below the CBM.

Formation energies for O vacancies in $q$=0,-1, and -2 charge states as a function of Fermi level position are shown in Figure 10.4. The dashed lines show the extremes of the range of formation energies obtained for each charge state. The distributions of charge transition levels for $q$=1 and -2 are shown in Figures 10.5(a) and (b), respec-

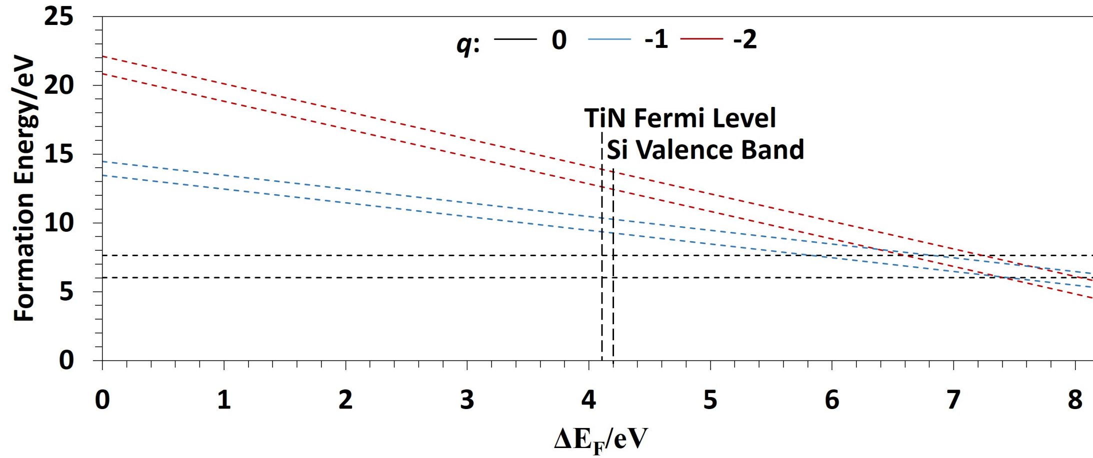


Figure 10.4: Formation energies of neutral, single negative, and double negatively charged oxygen vacancies as a function of Fermi energy, $\Delta E_F$, where $\Delta E_F$=0 at the VBM. The dashed lines represent maxima and minima in the data distribution. Also shown are the positions of the valence bands of Si [Afanas'ev 2014] and TiN [Afanas'ev 2005] in the band gap.

tively. It can be seen that at approximately 6.2 eV, single electron trapping becomes energetically favourable, while at 6.4 eV double electron trapping can become favourable at some vacancies. Furthermore, Figure 10.6 shows a negative correlation between the charge transition level for $q$=-1 and Si-Si bond length. This indicates that O vacancies with shorter Si-Si bond lengths tend to be the least favourable sites for electron trapping. In contrast, Figure 10.7(a) and (b) suggest a positive correlation between the optical and thermal ionisation energies of a trapped electron and Si-Si bond length. The optical ionisations energies in Figure 10.7(a) range from 2.49 to 3.57 eV, with a mean value of 3.07 eV. This is consistent with previous calculations of optical absorption bands at approximately 3.0 eV for a-$SiO_2$ [Kimmel 2009] and 3.3 eV for $\alpha$-quartz [Sushko 2005] using the time-dependent DFT method. The thermal ionisation energies in Figure 10.7(b) range from 0.95 eV to 2.23 eV with a mean of 1.58 eV. The positive correlations suggest that electrons trapped at O vacancies with short Si-Si bond lengths would tend to ionise the most effectively. It should be emphasised that the distribution of vacancy sites shown in the scatter plots are a product of sampling method used in this study, and a more accurate distribution would require a weighted sampling method.

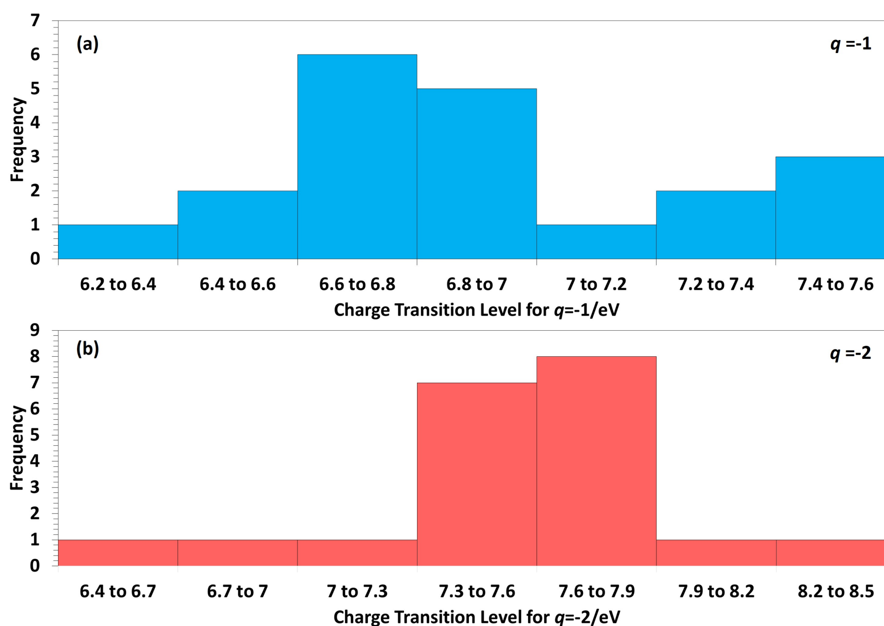


Figure 10.5: **(a)** Histogram summarising charge transition levels for $q$=-1 from Figure 10.4, which represent the values of $\Delta E_F$ for which the $q$=-1 vacancy is energetically more favourable than the neutral vacancy. This suggests that single electron trapping becomes energetically favourable at approximately 6.2 eV. **(b)** Histogram summarizing charge transition levels for $q$=-2 from Figure 10.4, which represent the value of $\Delta E_F$ for which the $q$=-2 vacancy is energetically more favourable than the $q$=-1 vacancy. This suggests that double electron trapping becomes energetically favourable at approximately 6.4 eV.

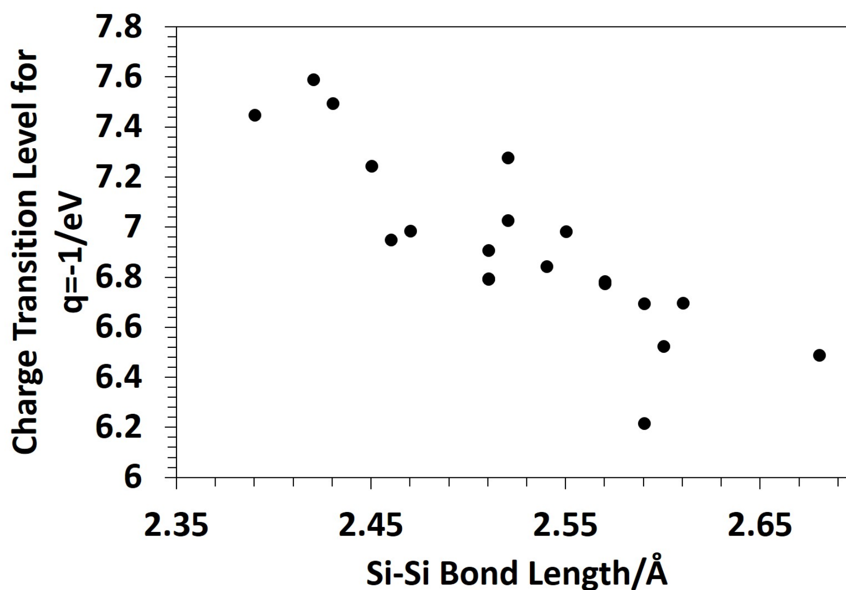


Figure 10.6: Charge transition levels for $q$=-1 from Figure 10.4 as a function of Si-Si bond length for the neutral vacancy. A negative correlation can be observed, which indicates that electron trapping is least favourable at short Si-Si bond lengths.

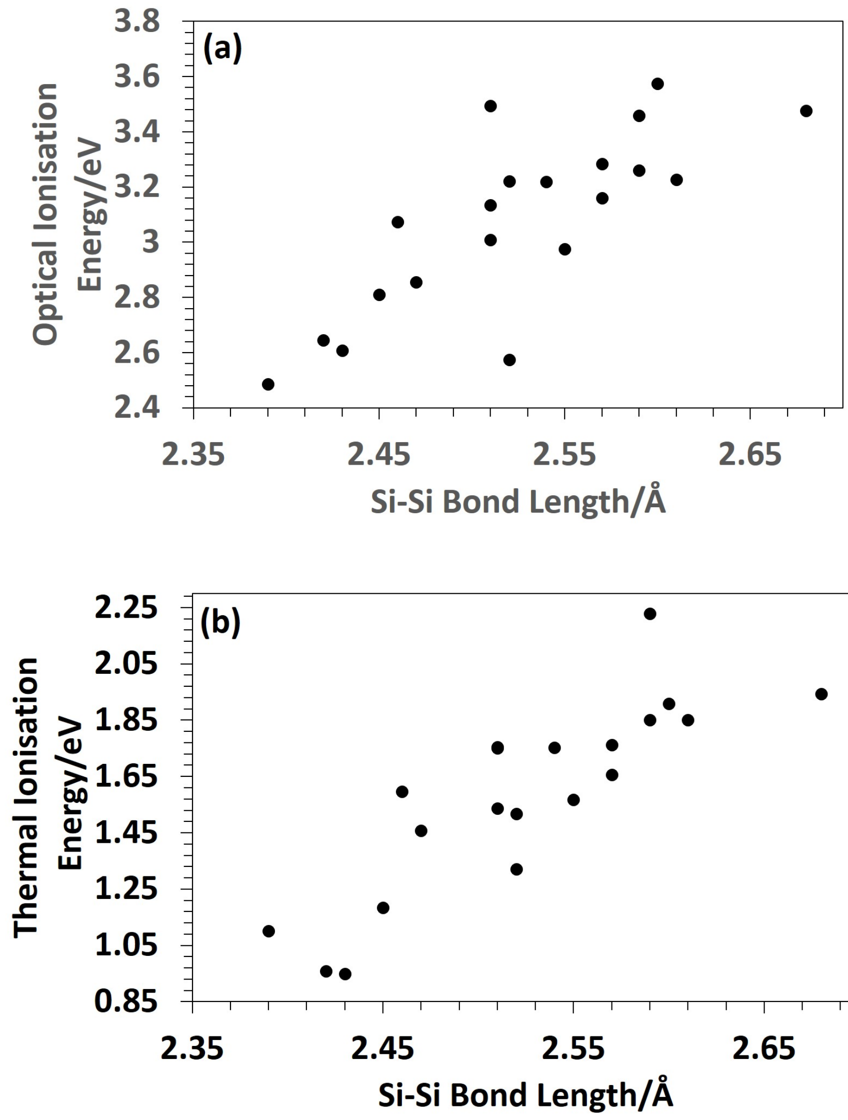


Figure 10.7: **(a)** Optical, and **(b)** Thermal ionisation energy as a function of Si-Si bond length for the neutral vacancy. A positive correlation can be observed, which suggests that electrons trapped at vacancies with shorter Si-Si bonds ionise more rapidly.

In CMOS devices, silicon oxides are typically interfaced with Si, with a resulting valence band offset of approximately 4.4 eV [Afanas'ev2014]. Additionally, in the present ReRAM study, for many devices silicon oxide is interfaced with TiN [Mehonic 2015][Mehonic 2016], with an offset of 4.2 eV [Afanas'ev 2005] between the Fermi level of TiN and the $SiO_2$ CBM. A MOSFET with a Si gate typically operates at voltages close to 1 V, while the ReRAM devices with TiN electrode layers have been observed to switch at approximately 3 V [Mehonic 2015]. Moreover, the initial electroforming step required a greater voltage of approximately 6 V. For Si and TiN electrodes, the presented results indicate that electron trapping at oxygen vacancies may be become an energetically feasible process for voltages distributed around 2 V.

### 10.3.3 The Migration of Negatively Charged Oxygen Vacancies

In order to understand the effect of electron trapping on vacancy diffusion, adiabatic barriers for the diffusion of negatively charged vacancies with $q$=-1 and -2 were calculated. Extra electrons were added to the cells used to calculate diffusion barriers for neutral vacancies in chapter 9. A total of 8 adiabatic barriers were obtained from the 10 initial pairs of vacancy sites. This was a result of the injected electrons localising onto intrinsic electron traps in the remaining 2 cases. The barrier calculations indicated that the mean barrier height is reduced by 1.9 eV with respect to the neutral vacancy (4.6 eV) case for $q$=-1. Barrier heights ranged from 1.8 eV to 3.3 eV, with a mean value of 2.7 eV. An analysis of the HOMO state occupied by the additional electron revealed that the migration of an O atom towards the vacancy site results in an intermediate state, which resembles an intrinsic electron trap [Figure 10.8(c)]. As the O atom diffuses, the O-Si1-O angle becomes greater, resulting in electron localisation at the widened angle and increased repulsion between Si1 and the diffusing O. This lowers the total energy of the intermediate state during diffusion [Figure 10.8(b),(c),(d)]. As in the case of neutral vacancies, migration within a 3-member ring resulted in the lowest barrier of 1.8 eV. However, an alternative mechanism for diffusion was not observed.

Diffusion barrier calculations for $q$=-2 resulted in multiple possibilities with a mean decrease in barrier height of 0.6 eV. The corresponding barrier heights ranged from 1.5 to

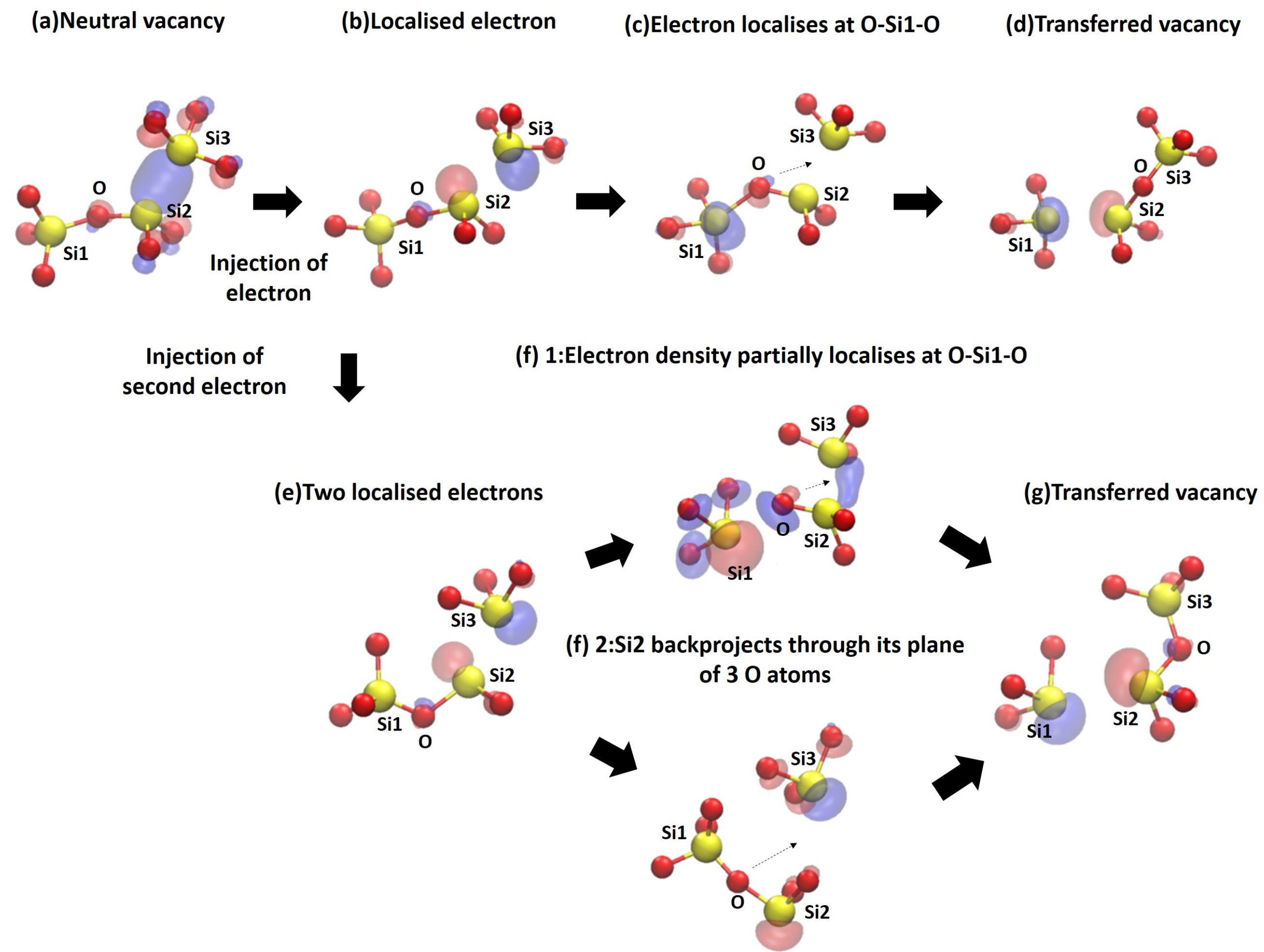


Figure 10.8: Schematic showing the HOMO during the diffusion of negatively charged oxygen vacancies to adjacent sites. Si atoms are represented as yellow spheres and O atoms as red spheres, and positive and negative isosurfaces are represented as blue and red, respectively, with approximate iso-values of $\pm 0.06$. The dotted arrows emphasize the motion of the associated atoms. **(a),(b),(c),(d)** Diffusion of single negatively charged oxygen vacancy. **(a),(b),(e),(f),(g)** Diffusion of double negatively charged oxygen vacancy.

2.8 eV, with a mean height of 2.0 eV. In five cases, the extra electron pair was observed to partially localise at the O-Si1-O wide angle as seen for $q$=-1 [Figure 10.8(f)1], resulting in increased repulsion between Si3 and the diffusing O. In the three remaining cases, Si2 was observed to back-project [Mukhopadhyay 2004][Sushko 2005] through its plane of O atoms [Figure 10.8(f)2]. The back-projected configuration formed an intermediate energy minimum between the initial and final configurations, with 2 electrons localised on Si2 and Si3 respectively. This suggests a two-step diffusion process, which requires the initial backprojection of Si1 followed by the diffusion of O. The barriers corresponding to this reaction pathway formed the upper limit of the calculated values. For the 3-member ring, the back-projected state was found to be the lowest energy configuration, suggesting that the diffusion of the vacancy would not be an energetically favourable process. Therefore the average barrier height of 2.0 eV does not account for the 3-member ring. This barrier height is greater than a mean value of 1.6 eV for thermal ionisation energy. Furthermore, in several cases thermal ionisation energies into the conduction band for the vacancies used in the barrier calculations are lower in energy than the diffusion barrier heights. These results suggest that thermal ionisation of O vacancies with trapped electrons can compete with the diffusion process. Ionisation would result in neutral vacancies which are immobile.

## 10.4 Discussion and Summary

The data presented in chapter 9 indicated the existence of favourable configurations of vacancy dimers and trimers. In the current chapter, it has been shown that electron trapping at vacancy sites facilitates diffusion. However, the presented calculations indicate this would be an inefficient process due to relatively high barriers for diffusion, which are in competition with the ionisation of the electrons. This suggests an alternative mechanism for the accumulation of oxygen vacancies under electrical bias. A recent study has shown that double electron trapping at intrinsic electron traps facilitates the formation of a Frenkel pair consisting of an oxygen vacancy and oxygen double bridge interstitial [Gao 2016]. This occurs with a favourable energy barrier of approximately 0.7 eV. Furthermore, the results presented in chapter 6 suggest the loss of oxygen during electrical stressing [Mehonic 2016]. This indicates additional oxygen vacancy production during electrical stressing. The mechanism described by Gao et al. [Gao 2016] may play an important role in this process.

As discussed in section 3.7, Bradley et al. [Bradley 2015B] showed the possibility of Frenkel pair formation through double electron trapping at oxygen vacancies $HfO_2$. The trapped electrons facilitated the formation of a nearby oxygen vacancy and an $O^{2-}$ ion. In two of the 20 studied sites in this chapter, an Si-O bond at the vacancy site stretched to beyond 2.0 Å when two electrons localised at the vacancy. In Figure 10.9(a), two electrons have localised on the vacancy between Si3 and Si4 and resulted in the stretching of the Si3-O bond to 2.03 Å from an initial value of 1.68 Å for the neutral vacancy. The associated O was found to be capable of forming a lower energy oxygen double bridge interstitial with a nearby Si. In Figure 10.9(b), the O atom forms a double bridge interstitial between Si1 and Si2. The configuration in (b) was lower in total energy and NEB calculations suggested a barrierless transition. However, this process was observed under very rare cases in comparison to the Frenkel pair generation mechanism discussed by Gao et al. [Gao 2016]. In contrast to $HfO_2$, this could indicate that electron trapping at vacancies may not play such a direct role during breakdown as suggested by Bersuker et al. [2008].

In several cases, electron trapping was observed to occur at intrinsic electron traps

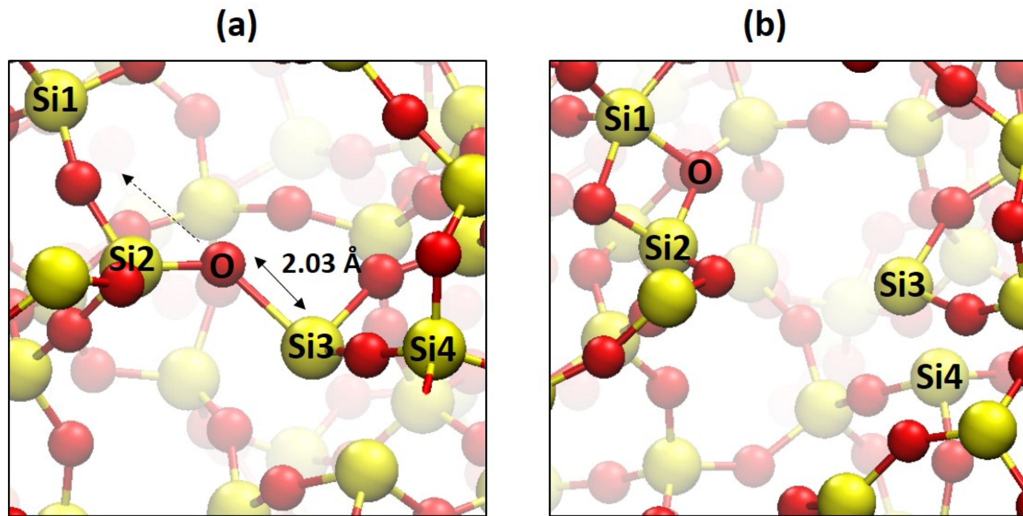


Figure 10.9: **(a)** Two electrons localised on the vacancy between Si3 and Si4 and resulted in the stretching of the Si3-O bond to 2.03 Å from an inital value of 1.68 Å for the neutral vacancy. **(b)** The weakened Si3-O bond allows the O atom to form a double bridge interstitial between Si1 and Si2 in a barrierless transition.

present nearby the oxygen vacancy, both of which have close charge transition levels [El-Sayed 2015A]. These traps can interact with electrons injected into the system in two ways: i) as stepping stones for electron tunnelling under bias; ii) if two electrons meet at an intrinsic site, new neutral oxygen vacancy can be created, again contributing to an electron current through the oxide [Gao 2016]. The presented calculations suggest that longer Si-Si bonds form trap states below the distribution of intrinsic traps. Electrical measurements made by Mehonic et al. [Mehonic 2012A] indicated that trap-assisted tunnelling is the major process responsible for conduction in the low resistance state during resistive switching in a-$SiO_x$. Depending on their respective concentrations, since the distributions in the trap levels of oxygen vacancies and intrinsic sites overlap, both can contribute to an electron percolation path through the oxide. Further experimental studies of a-$SiO_x$ films with different concentrations of oxygen vacancies could shed further light on the mechanisms of these processes.

In summary, the presented calculations suggest that it is energetically favourable for oxygen vacancies to trap one or two electrons at Fermi energies above 6.2 eV and 6.4 eV, respectively. This improves vacancy mobility; however, electrons trapped at vacancies would compete with the thermal ionisation of the electrons into the conduction band and with intrinsic electron traps, preventing effective diffusion from taking place.

# 11 Conclusion and Further Work

This thesis aimed to improve our understanding of resistive switching behaviour intrinsic to a sputter-deposited a-SiO$_x$ layer in a series of *MIM* stacks. The presented studies addressed the structural changes associated with resistive switching, and how the structure of the *MIM* stacks could affect device performance. The main new results can be summarised as follows:

- In sputter-deposited silicon suboxides, oxide-wide structural reorganisation occurs during electrical stressing. This is a result of large-scale oxygen dynamics, which can result in oxygen outmigration from the oxide and electrode deformation. This is contrary to the relatively inert behaviour expected from insulating materials.
- The fabrication of sputter-deposited silicon suboxides greatly influences device performance. Firstly, growing the oxide layer on a rougher substrate surface promotes lower electroforming voltages and greater device endurance. This is consistent with enhanced columnar microstructure in the oxide, and EELS data indicates that inter-columnar boundaries could play an important role in oxygen transport. Secondly, thin oxide layers ($< 5$ nm) will lead to electrode migration into the oxide layer as a result of high electric fields. This will limit the thickness of the oxide layer needed for intrinsic switching behaviour.
- The formation of oxygen vacancy dimers and trimers is energetically favourable at some sites in amorphous silicon dioxide, with maximum binding energies of 0.13 eV and 0.18 eV, respectively. However, neutral oxygen vacancies are immobile under room temperature operating conditions and diffuse with a mean adiabatic barrier height of 4.6 eV.
- In amorphous silicon dioxide, single and double electron trapping is energetically feasible at oxygen vacancies at Fermi energies above 6.2 and 6.4 eV, respectively. This greatly improves vacancy mobility, with average adiabatic barrier heights of 2.7 eV and 2.0 eV, respectively. However, vacancy diffusion competes with thermal ionisation of the electrons into the conduction band. Oxygen vacancies also compete with intrinsic sites for electron trapping. This results in an inefficient diffusion

process, which cannot explain the formation of a silicon-rich conductive path and suggests an alternative mechanism for oxygen vacancy accumulation.

These results will help guide the optimisation of future silicon suboxide-based ReRAM devices and provide new insights into the role of oxygen vacancies during the electrical stressing of silicon oxides. Of the devices studied in this thesis, device 3 provides a good starting point for further optimisation, with Au/Ti and Mo top and bottom electrodes, an oxide layer width of approximately 35 nm, an RMS surface roughness of 1.10 nm at the oxide-electrode interface, and a resulting enhanced columnar microstructure with an approximate column width of 20 nm. Device 3 typically electroforms at 4 V with an endurance on the order of $10^7$ cycles as described in chapter 5. Additional electrical characterisation experiments revealed set and reset voltages of approximately -1 and 1.5 V, respectively, and resistance state retention exceeding $10^4$ s [Mehonic 2017]. For the low deposition temperatures studied here, the columnar microstructure of the oxide is a product of the surface roughness of the electrode onto which the oxide is deposited through atomic shadowing effects [Thornton 1986]. Since a notable columnar microstructure is only observed in device 3, the use of Mo is a good starting point for a bottom electrode material: the roughness of the deposited electrode can be changed by referring to the zone model [Thornton 1974] in order to systemically study how roughness affects device performance in future work, and find an optimum roughness value for a particular choice of oxide thickness (e.g. 35 nm) and top electrode (e.g. Au/Ti as in the case for device 3). Given that the loss of oxygen from the oxide layer was observed during electrical stressing, the higher oxygen content in device 3 (x$\approx$2) may also play a role in the greater device endurance when compared to device 2 (x$\approx$1.3). Increased reliability has also been suggested previously for higher oxygen content [Chang 2012]. This indicates a stoichiometry with x$\approx$2 as an appropriate choice for further device optimisation.

At the time of writing, commercial dynamic RAM (DRAM) and Flash technologies scale as low as 16 nm. An a-$SiO_x$-based ReRAM device must therefore be capable of competing with and surpassing such length scales. A columnar width of 20 nm in device 3 would suggest memory density is currently not capable of competing with DRAM and Flash. Further work should aim to minimise the width of oxide columns while still allowing for the formation of continuous intercolumnar boundaries. This would involve tayloring

the bottom electrode surface, so that highpoints on the surface are closer to one another, while still providing a relatively rough surface (e.g RMS roughness of 1.10 nm and above). One approach could be the testing of different choices of electrode materials, although materials such as Ag or Cu, which have previously been shown to exhibit ECM behaviour, should be avoided. Possible choices may include other relatively inert materials such as TiN, Rh, or Ru. Additionally, fine-tuning could be achieved by making use of advances in nanopatterning techniques [Lei 2007].

Once electroformed, device 3 already outcompetes the most advanced commercial Flash technologies, which require maximum voltages of $\approx$ 3 V. However, the most advanced commercial DRAM cells require a maximum voltage of $\approx$1 V. Although device 3 currently requires voltages as high as 1.5 V to function (assuming electroforming is carried out during device fabrication), it has the advantage of non-volatility. Lower operating voltages could perhaps be achieved by reducing the thickness of the oxide layer due to an increased electric field in the layer, although the results in chapter 7 indicate a limit to its thickness in order to maintain the intrinsic nature of the switching. After optimising the roughness of the bottom electrode, a systematic study of how the thickness of the oxide layer affects switching behaviour can be carried out for a particular choice of top electrode. Finally, due to differences in work functions, operating voltages and currents will be impacted by the choice of electrode materials. In the case of device 3, an arrangement of a Au/Ti top electrode and a Mo bottom electrode resulted in comparatively small operating voltages; however, a current compliance of 1 mA was used. Typically, currents on the order of 100 $\mu$A are employed in current CMOS technology. Once the bottom electrode roughness and oxide layer thickness are optimised, future work may aim to then find an optimum choice of top electrode to minimise operation voltages and currents. After settling on a choice of top electrode materials, further current reduction can be achieved by adjusting the current compliance of the device from 1 mA for device 3, as discussed in chapter 5, to a value around 100 $\mu$A. However, this will reduce the difference in resistance between high and low resistance states, and a compromise may have to be reached.

A deeper experimental analysis of columnar boundaries will be challenging and could be facilitated through fabrication. With respect to TEM analysis, care would be needed to

minimise sample thickness during FIB preparation and analysis would be greatly facilitated with a high-resolution aberration-corrected STEM. Furthermore, the use of *in situ* TEM studies would not only allow the observation of conductive path formation, but could also reveal the behaviour of intercolumnar boundaries during electrical stressing. Future computational work could focus on the modelling of columnar microstructure. Strain at column boundaries may result in an abundance of electron traps, which are required for the mechanism for oxygen vacancy generation in a-$SiO_2$ suggested by Gao et al. [Gao 2016]. Such structures maybe comparable to silica surfaces [Ceresoli 2000][Rimola 2013]. Analogies with this model can be drawn with resistive switching in $HfO_2$ layers, where conductive paths have been shown to preferentially form at grain boundaries [Bersuker 2008][Lanza 2012A][Lanza 2012B]. Furthermore, the observed oxidation and deformation of the negatively biased electrode in device 3 is not clearly understood and has also been reported previously for $TiO_2$ [Jeong 2008]. Prior theoretical [Gao 2016] and experimental studies [Mehonic 2016], including results in this thesis, have suggested oxygen migration towards the positively biased electrode during electrical stressing. As reported for positively biased electrodes by Mehonic et al., it would be inciteful to carry out *in situ* electrical stressing combined with RGA analysis for a negatively electroformed electrode in order to detect the emission of any oxygen gas. Finally, previous studies have shown that dopants such as Ge or Li can form electron traps in $\alpha$-quartz [El-Sayed 2014]. Electron trapping at such defects may facilitate the formation of interstitial oxygen [Gao 2016]. The effects of doping in the oxide layer could have scope for further experimental and computational studies.

# 12 Bibliography

[Adamo 1999]Adamo, Carlo, and Vincenzo Barone. "Toward reliable density functional methods without adjustable parameters: The PBE0 model." The Journal of Chemical Physics 110, no. 13 (1999): 6158-6170.

[Afanas'ev 1997]Afanas'ev, Valerie V., and Andre Stesmans. "Analysis of near-interfacial $SiO_2$ traps using photon stimulated electron tunneling." Microelectronic Engineering 36, no. 1 (1997): 149-152.

[Afanas'ev 2005]Afanas'ev, Valerie V., Andre Stesmans, L. Pantisano, and T. Schram. "Electron photoemission from conducting nitrides ($TiN_x$, $TaN_x$) into $SiO_2$ and $HfO_2$." Applied Physics Letters 86, no. 23 (2005): 2902.

[Afanas'ev 2014]Afanas'ev, Valeri V. "Electron band alignment at interfaces of semiconductors with insulating oxides: an internal photoemission study." Advances in Condensed Matter Physics 2014 (2014): 301302

[Akiyama 2005]Akiyama, Toru, Hiroyuki Kageshima, Masashi Uematsu, and Tomonori Ito. "Theoretical investigation of oxygen diffusion in compressively strained high-density $\alpha$-quartz." Japanese Journal of Applied Physics 44, no. 10R (2005): 7427.

[Alay-e-Abbas 2016]Alay-e-Abbas, Syed Muhammad, Safdar Nazir, and Ali Shaukat. "Formation energies and electronic structure of intrinsic vacancy defects and oxygen vacancy clustering in $BaZrO_3$." Physical Chemistry Chemical Physics 18, no. 34 (2016): 23737-23745.

[Anderson 2011]Anderson, Nathan L., Ravi Pramod Vedula, Peter A. Schultz, Renee M. Van Ginhoven, and Alejandro Strachan. "First-principles investigation of low energy E' center precursors in amorphous silica." Physical Review Letters 106, no. 20 (2011): 206402.

[Anderson 2012]Anderson, Nathan L., Ravi Pramod Vedula, Peter A. Schultz, Renee M. Van Ginhoven, and Alejandro Strachan. "Defect level distributions and atomic relaxations induced by charge trapping in amorphous silica." Applied Physics Letters 100, no. 17

(2012): 172908.

[Bakos 2002]Bakos, T., S. N. Rashkeev, and S. T. Pantelides. "Reactions and diffusion of water and oxygen molecules in amorphous $SiO_2$." Physical Review Letters 88, no. 5 (2002): 055508.

[Batson 1993]Batson, P. E. "Simultaneous STEM imaging and electron energy-loss spectroscopy with atomic-column sensitivity." Nature 366, no. 6457 (1993): 727-728.

[Becke 1993]Becke, Axel D. "Density functional thermochemistry. III. The role of exact exchange." The Journal of Chemical Physics 98, no. 7 (1993): 5648-5652.

[Berendsen 1984]Berendsen, Herman JC, JPM van Postma, Wilfred F. van Gunsteren, A. R. H. J. DiNola, and J. R. Haak. "Molecular dynamics with coupling to an external bath." The Journal of Chemical Physics 81, no. 8 (1984): 3684-3690.

[Bersuker 2008]Bersuker, G., D. Heh, C. Young, H. Park, P. Khanal, L. Larcher, A. Padovani et al. "Breakdown in the metal/high-k gate stack: Identifying the "weak link" in the multilayer dielectric." Paper presented at IEEE International Electron Devices Meeting, San Francisco, CA, December 15-17, 2008.

[Bersuker 2011]Bersuker, G., D. C. Gilmer, D. Veksler, P. Kirsch, L. Vandelli, A. Padovani, L. Larcher et al. "Metal oxide resistive memory switching mechanism based on conductive filament properties." Journal of Applied Physics 110, no. 12 (2011): 124518.

[Boero 1997]Boero, Mauro, Alfredo Pasquarello, Johannes Sarnthein, and Roberto Car. "Structure and hyperfine parameters of $E_1$' centers in $\alpha$-quartz and in vitreous $SiO_2$." Physical Review Letters 78, no. 5 (1997): 887.

[Bongiorno 2002]Bongiorno, Angelo, and Alfredo Pasquarello. "Oxygen diffusion through the disordered oxide network during silicon oxidation." Physical Review Letters 88, no. 12 (2002): 125901.

[Born 1954]Born, Max, and R. Oppenheimer. "On the quantum theory of molecules." Annalen Der Physik 84, no. 4 (1927): 457-484.

[Bracewell 1956]Bracewell, Ronald N. "Strip integration in radio astronomy." Australian

Journal of Physics 9, no. 2 (1956): 198-217.

[Bradley 2015A]Bradley, Samuel R., Gennadi Bersuker, and Alexander L. Shluger. "Modelling of oxygen vacancy aggregates in monoclinic $HfO_2$: can they contribute to conductive filament formation?." Journal of Physics: Condensed Matter 27, no. 41 (2015): 415401.

[Bradley 2015B]Bradley, Samuel R., Alexander L. Shluger, and Gennadi Bersuker. "Electron-Injection-Assisted Generation of Oxygen Vacancies in Monoclinic $HfO_2$." Physical Review Applied 4, no. 6 (2015): 064008.

[Brady 1959]Brady, George W. "A study of amorphous SiO." The Journal of Physical Chemistry 63, no. 7 (1959): 1119-1120.

[Buckwell 2015]Buckwell, Mark, Luca Montesi, Stephen Hudziak, Adnan Mehonic, and Anthony J. Kenyon. "Conductance tomography of conductive filaments in intrinsic silicon-rich silica RRAM." Nanoscale 7, no. 43 (2015): 18030-18035.

[Capron 2007]Capron, Nathalie, Peter Broqvist, and Alfredo Pasquarello. "Migration of oxygen vacancy in $HfO_2$ and across the $HfO_2$/$SiO_2$ interface: A first-principles investigation." Applied Physics Letters 91, no. 19 (2007): 2905.

[Carrasco 2004]Carrasco, J., N. Lopez, and F. Illas. "First principles analysis of the stability and diffusion of oxygen vacancies in metal oxides." Physical Review Letters 93, no. 22 (2004): 225502.

[Carrasco 2006]Carrasco, Javier, Nuria Lopez, Francesc Illas, and H-J. Freund. "Bulk and surface oxygen vacancy formation and diffusion in single crystals, ultrathin films, and metal grown oxide structures." The Journal of Chemical Physics 125, no. 7 (2006): 074711.

[Celano 2015]Celano, Umberto, Ludovic Goux, Robin Degraeve, Andrea Fantini, Olivier Richard, Hugo Bender, Malgorzata Jurczak, and Wilfried Vandervorst. "Imaging the Three-Dimensional Conductive Channel in Filamentary-Based Oxide Resistive Switching Memory." Nano Letters 15, no. 12 (2015): 7970-7975.

[Ceresoli 2000]Ceresoli, Davide, Marco Bernasconi, Simonetta Iarlori, Michele Parrinello, and Erio Tosatti. "Two-membered silicon rings on the dehydroxylated surface of silica." Physical Review Letters 84, no. 17 (2000): 3887.

[Chang 2012]Chang, Yao-Feng, Pai-Yu Chen, Burt Fowler, Yen-Ting Chen, Fei Xue, Yanzhen Wang, Fei Zhou, and Jack C. Lee. "Understanding the resistive switching characteristics and mechanism in active $SiO_x$-based resistive switching memory." Journal of Applied Physics 112, no. 12 (2012): 123702.

[Chen 2013]Chen, Jui-Yuan, Cheng-Lun Hsin, Chun-Wei Huang, Chung-Hua Chiu, Yu-Ting Huang, Su-Jien Lin, Wen-Wei Wu, and Lih-Juann Chen. "Dynamic Evolution of Conducting Nanofilament in Resistive Switching Memories." Nano Letters 13, no. 8 (2013): 3671-3677.

[Coleman 1967]Coleman, M. V., and D. J. D. Thomas. "The Structure of Silicon Oxide Films." physica status solidi (b) 22, no. 2 (1967): 593-602.

[Conibeer 2008]Conibeer, Gavin, Martin Green, Eun-Chel Cho, Dirk König, Young-Hyun Cho, Thipwan Fangsuwannarak, Giuseppe Scardera et al. "Silicon quantum dot nanostructures for tandem photovoltaic cells." Thin Solid Films 516, no. 20 (2008): 6748-6756.

[Crowther 1970]Crowther, R. A., D. J. DeRosier, and A. Klug. "The reconstruction of a three-dimensional structure from projections and its application to electron microscopy." Proceedings of the Royal Society of London A: Mathematical, Physical and Engineering Sciences 317, no. 1530 (1970): 319-340.

[Cuong 2007]Cuong, Do Duc, Bora Lee, Kyeong Mi Choi, Hyo-Shin Ahn, Seungwu Han, and Jaichan Lee. "Oxygen vacancy clustering and electron localization in oxygen-deficient SrTiO 3: LDA+ U study." Physical Review Letters 98, no. 11 (2007): 115503.

[Degraeve 1999]Degraeve, Robin, Ben Kaczer, and Guido Groeseneken. "Degradation and breakdown in thin oxide layers: mechanisms, models and reliability prediction." Microelectronics Reliability 39, no. 10 (1999): 1445-1460.

[DiMaria 1989]DiMaria, D. J., and J. W. Stasiak. "Trap creation in silicon dioxide produced by hot electrons." Journal of Applied Physics 65, no. 6 (1989): 2342-2356.

[DiMaria 1993]DiMaria, D. J., E. Cartier, and D. Arnold. "Impact ionization, trap creation, degradation, and breakdown in silicon dioxide films on silicon." Journal of Applied Physics 73, no. 7 (1993): 3367-3384.

[DiMaria 1994]DiMaria, Donelli J., J. R. Kirtley, E. J. Pakulis, D. W. Dong, T. S. Kuan, F. L. Pesavento, T. N. Theis, J. A. Cutro, and S. D. Brorson. "Electroluminescence studies in silicon dioxide films containing tiny silicon islands." Journal of Applied Physics 56, no. 2 (1984): 401-416.

[DiStefano 1971]DiStefano, T. H., and D. E. Eastman. "The band edge of amorphous $SiO_2$ by photoinjection and photoconductivity measurements." Solid State Communications 9, no. 24 (1971): 2259-2261.

[Donadio 2001]Donadio, Davide, Marco Bernasconi, and Mauro Boero. "Ab initio simulations of photoinduced interconversions of oxygen deficient centers in amorphous silica." Physical Review letters 87, no. 19 (2001): 195504.

[Dumin 1995]Dumin, D. J., J. R. Maddux, R. Subramoniam, R. S. Scott, S. Vanchinathan, N. A. Dumin, K. J. Dickerson, S. Mopuri, S. M. Gladstone, and T. W. Hughes. "Characterizing wearout, breakdown, and trap generation in thin silicon oxide." Journal of Vacuum Science & Technology B 13, no. 4 (1995): 1780-1787.

[Egerton 1996A]Egerton, R. "Applications of Energy-Loss Spectroscopy". In *Electron Energy-Loss Spectroscopy in the Electron Microscope*, 312-321. 2nd ed. New York: Springer, 1996.

[Egerton 1996B]Egerton, R. "Applications of Energy-Loss Spectroscopy". In *Electron Energy-Loss Spectroscopy in the Electron Microscope*, 334-345. 2nd ed. New York: Springer, 1996.

[Egerton 1996C]Egerton, R. "Applications of Energy-Loss Spectroscopy". In *Electron Energy-Loss Spectroscopy in the Electron Microscope*, 374-378. 2nd ed. New York: Springer, 1996.

[Egerton 1996D]Egerton, R. "Quantitative Analysis of the Energy-Loss Spectrum". In *Electron Energy-Loss Spectroscopy in the Electron Microscope*, 262-269. 2nd ed. New

York: Springer, 1996.

[Egerton 1996E]Egerton, R. "Quantitative Analysis of the Energy-Loss Spectrum". In *Electron Energy-Loss Spectroscopy in the Electron Microscope*, 245-249. 2nd ed. New York: Springer, 1996.

[Egerton 1996F]Egerton, R. "Quantitative Analysis of the Energy-Loss Spectrum". In *Electron Energy-Loss Spectroscopy in the Electron Microscope*, 277-283. 2nd ed. New York: Springer, 1996.

[Egerton 1996G]Egerton, R. "Applications of Energy-Loss Spectroscopy". In *Electron Energy-Loss Spectroscopy in the Electron Microscope*, 301-307. 2nd ed. New York: Springer, 1996.

[El-Sayed 2013]El-Sayed, Al-Moatasem, Matthew B. Watkins, Alexander L. Shluger, and Valeri V. Afanas'ev. "Identification of intrinsic electron trapping sites in bulk amorphous silica from ab initio calculations." Microelectronic Engineering 109 (2013): 68-71.

[El-Sayed 2014]El-Sayed, Al-Moatasem, Matthew B. Watkins, Valery V. Afanas'ev, and Alexander L. Shluger. "Nature of intrinsic and extrinsic electron trapping in $SiO_2$." Physical Review B 89, no. 12 (2014): 125201.

[El-Sayed 2015A]El-Sayed, Al-Moatsem, "Atomistic Modelling of Charge Trapping Defects in Silicon Dioxide." Ph.D. Dissertation, University College London, 2015.

[El-Sayed 2015B]El-Sayed, Al-Moatsem, K. Tanimura, and A. L. Shluger. "Optical signatures of intrinsic electron localization in amorphous $SiO_2$." Journal of Physics: Condensed Matter 27, no. 26 (2015): 265501.

[Fogarty 2010]Fogarty, Joseph C., Hasan Metin Aktulga, Ananth Y. Grama, Adri C.T. Van Duin, and Sagar A. Pandit. "A reactive molecular dynamics simulation of the silica-water interface." The Journal of Chemical physics 132, no. 17 (2010): 174704.

[Forty 1986]Forty, A. J., M. Kerkar, J. Robinson, S. M. El-Mashri, and E. N. Farrabaugh. "A STRUCTURAL INVESTIGATION OF SOME EVAPORATED SiOx FILMS." Le Journal de Physique Colloques 47, no. C8 (1986): 857.

[Foster 2002]Foster, Adam S., F. Lopez Gejo, A. L. Shluger, and Risto M. Nieminen. "Vacancy and interstitial defects in hafnia." Physical Review B 65, no. 17 (2002): 174117.

[Fujii 2014]Fujii, Takashi, Masashi Arita, Yasuo Takahashi, and Ichiro Fujiwara. "In situ transmission electron microscopy analysis of conductive filament during solid electrolyte resistance switching." Applied Physics Letters 98, no. 21 (2011): 212104.

[Ganduglia-Pirovano 2015]Ganduglia-Pirovano, M. V. "Oxygen Defects at Reducible Oxide Surfaces: The Example of Ceria and Vanadia." In *Defects at Oxide Surfaces*, 149-184. 1st ed. Switzerland: Springer, 2015.

[Gao 2016]Gao, David Z., Al-Moatasem El-Sayed, and Alexander L. Shluger. "A mechanism for Frenkel defect creation in amorphous $SiO_2$ facilitated by electron injection." Nanotechnology 27, no. 50 (2016): 505207.

[Gavartin 2006]Gavartin, J. L., D. Muñoz Ramo, A. L. Shluger, G. Bersuker, and B. H. Lee. "Negative oxygen vacancies in $HfO_2$ as charge traps in high-k stacks." Applied Physics Letters 89, no. 8 (2006): 082908

[Gilbert 1972]Gilbert, Peter. "Iterative methods for the three-dimensional reconstruction of an object from projections." Journal of Theoretical Biology 36, no. 1 (1972): 105-117.

[Goedecker 1996]Goedecker, S., M. Teter, and Jürg Hutter. "Separable dual-space Gaussian pseudopotentials." Physical Review B 54, no. 3 (1996): 1703.

[Grau-Crespo 2009]Grau-Crespo, R., K. C. Smith, T. S. Fisher, N. H. De Leeuw, and U. V. Waghmare. "Thermodynamics of hydrogen vacancies in $MgH_2$ from first-principles calculations and grand-canonical statistical mechanics." Physical Review B 80, no. 17 (2009): 174117.

[Greaves 1986]Greaves, G. N., X. L. Jiang, R. N. Jenkins, E. Holzenkampfer, and S. Kalbitzer. "The Local Structure of A-SiOx: H Films." Le Journal de Physique Colloques 47, no. C8 (1986): C8-853.

[Guidon 2009]Guidon, Manuel, Jürg Hutter, and Joost VandeVondele. "Robust Periodic Hartree-Fock Exchange for Large-Scale Simulations Using Gaussian Basis Sets." Jour-

nal of Chemical Theory and Computation 5, no. 11 (2009): 3010-3021.

[Guidon 2010]Guidon, Manuel, Jürg Hutter, and Joost VandeVondele. "Auxiliary density matrix methods for hartree-fock exchange calculations." Journal of Chemical Theory and Computation 6, no. 8 (2010): 2348-2364.

[Hamann 1997]Hamann, D. R. "Energies of strained silica rings." Physical Review B 55, no. 22 (1997): 14784.

[Hamann 1998]Hamann, D. R. "Diffusion of atomic oxygen in $SiO_2$." Physical Review Letters 81, no. 16 (1998): 3447.

[Hartwigsen 1998]Hartwigsen, C., Sephen Goedecker, and Jürg Hutter. "Relativistic separable dual-space Gaussian pseudopotentials from H to Rn." Physical Review B 58, no. 7 (1998): 3641.

[Henkelman 2000]Henkelman, Graeme, Blas P. Uberuaga, and Hannes Jónsson. "A climbing image nudged elastic band method for finding saddle points and minimum energy paths." The Journal of Chemical Physics 113, no. 22 (2000): 9901-9904.

[Heyd 2003]Heyd, Jochen, Gustavo E. Scuseria, and Matthias Ernzerhof. "Hybrid functionals based on a screened Coulomb potential." The Journal of Chemical Physics 118, no. 18 (2003): 8207-8215.

[Hohenberg 1964]Hohenberg, Pierre, and Walter Kohn. "Inhomogeneous electron gas." Physical review 136, no. 3B (1964): B864.

[Hohl 2003]Hohl, Achim, Thomas Wieder, P. A. Van Aken, T. E. Weirich, G. Denninger, M. Vidal, S. Oswald, C. Deneke, J. Mayer, and H. Fuess. "An interface clusters mixture model for the structure of amorphous silicon monoxide (SiO)." Journal of Non-Crystalline Solids 320, no. 1 (2003): 255-280.

[Hoshino 2003]Hoshino, Tadatsugu, Masayuki Hata, Saburo Neya, Yasushiro Nishioka, Takanobu Watanabe, Kosuke Tatsumura, and Iwao Ohdomari. "Diffusion of molecular and atomic oxygen in silicon oxide." Japanese Journal of Applied Physics 42, no. 6R (2003): 3560.

[Hosono 2001]Hosono, Hideo, Yoshiaki Ikuta, Takeru Kinoshita, Kouichi Kajihara, and Masahiro Hirano. "Physical disorder and optical properties in the vacuum ultraviolet region of amorphous $SiO_2$." Physical Review Letters 87, no. 17 (2001): 175501.

[Huang 2009]Huang, Gui-Yang, Chong-Yu Wang, and Jian-Tao Wang. "First-principles study of diffusion of oxygen vacancies and interstitials in ZnO." Journal of Physics: Condensed Matter 21, no. 19 (2009): 195403.

[Huang 2012]Huang, Pinshane Y., Simon Kurasch, Anchal Srivastava, Viera Skakalova, Jani Kotakoski, Arkady V. Krasheninnikov, Robert Hovden et al. "Direct imaging of a two-dimensional silica glass on graphene." Nano Letters 12, no. 2 (2012): 1081-1086.

[Ielmini 2009]Ielmini, Daniele. "Reliability issues and modeling of flash and post-flash memory." Microelectronic Engineering 86, no. 7 (2009): 1870-1875.

[Jeong 2008]Jeong, Doo Seok, Herbert Schroeder, Uwe Breuer, and Rainer Waser. "Characteristic electroforming behavior in Pt/$TiO_2$/Pt resistive switching cells depending on atmosphere." Journal of Applied Physics 104, no. 12 (2008): 3716.

[Jin 2001]Jin, Young-Gu, and K. J. Chang. "Mechanism for the enhanced diffusion of charged oxygen ions in $SiO_2$." Physical Review Letters 86, no. 9 (2001): 1793.

[Johanessen 1975]Johannessen, J. S., W. E. Spicer, and Y. E. Strausser. "Phase separation in silicon oxides as seen by Auger electron spectroscopy." Applied Physics Letters 27, no. 8 (1975): 452-454.

[Jónsson 1998]Jónsson, Hannes, Greg Mills, and Karsten W. Jacobsen. "Nudged elastic band method for finding minimum energy paths of transitions." In *Classical and Quantum Dynamics in Condensed Phase Simulations*, 385-404. 1st ed. Singapore: World Scientific, 1998.

[Kawase 2007]Kawase, Noboru, Mitsuro Kato, Hideo Nishioka, and Hiroshi Jinnai. "Transmission electron microtomography without the "missing wedge" for quantitative structural analysis." Ultramicroscopy 107, no. 1 (2007): 8-15.

[Kenyon 1994]Kenyon, A. J., P. F. Trwoga, M. Federighi, and C. W. Pitt. "Optical prop-

erties of PECVD erbium-doped silicon-rich silica: evidence for energy transfer between silicon microclusters and erbium ions." Journal of Physics: Condensed Matter 6, no. 21 (1994): L319.

[Khriachtchev 2012]Khriachtchev, Leonid, Stefano Ossicini, Fabio Iacona, and Fabrice Gourbilleau. "Silicon nanoscale materials: From theoretical simulations to photonic applications." International Journal of Photoenergy 2012 (2012): 872576.

[Kim 2006]Kim, Kyung Joong, Ki Tae Park, and Jong Wan Lee. "Thickness measurement of $SiO_2$ films thinner than 1 nm by X-ray photoelectron spectroscopy." Thin Solid Films 500, no. 1 (2006): 356-359.

[Kimmel 2009]Kimmel, Anna, Peter Sushko, Alexander Shluger, and Gennadi Bersuker. "Positive and negative oxygen vacancies in amorphous silica." ECS Transactions 19, no. 2 (2009): 3-17.

[King 1967]King, Shirley V. "Ring configurations in a random network model of vitreous silica." Nature 213, no. 5081 (1967): 1112-1113.

[Knoll 1932]Knoll, Max, and Ernst Ruska. "Beitrag zur geometrischen Elektronenoptik. I." Annalen der Physik 404, no. 5 (1932): 607-640.

[Kohn 1965]Kohn, Walter, and Lu Jeu Sham. "Self-consistent equations including exchange and correlation effects." Physical Review 140, no. 4A (1965): A1133.

[Koch 2001]Koch, Wolfram, and Max C. Holthausen. "The Quest for Approximate Exchange-Correlation Functionals". In *A Chemist's Guide to Density Functional Theory*, 69-85. 2nd ed. Weinheim: Wiley-VCH, 2001.

[Kuzovkov 2001]Kuzovkov, V. N., A. I. Popov, E. A. Kotomin, M. A. Monge, R. Gonzalez, and Y. Chen. "Kinetics of nanocavity formation based on F-center aggregation in thermochemically reduced MgO single crystals." Physical Review B 64, no. 6 (2001): 064102.

[Lakoubovskii 2008]Lakoubovskii, K., K. Mitsuishi, Y. Nakayama, and K. Furuya. "Thickness measurements with electron energy loss spectroscopy." Microscopy Research and

Technique 71, no. 8 (2008): 626-631.

[Lamb 1967]Lamb, D. R., and P. C. Rundle. "A non-filamentary switching action in thermally grown silicon dioxide films." British Journal of Applied Physics 18, no. 1 (1967): 29.

[Lamkin 1992]Lamkin, M. A., F. L. Riley, and R. J. Fordham. "Oxygen mobility in silicon dioxide and silicate glasses: a review." Journal of the European Ceramic Society 10, no. 5 (1992): 347-367.

[Lany 2008]Lany, Stephan, and Alex Zunger. "Assessment of correction methods for the band-gap problem and for finite-size effects in supercell defect calculations: Case studies for ZnO and GaAs." Physical Review B 78, no. 23 (2008): 235104.

[Lany 2009]Lany, Stephan, and Alex Zunger. "Accurate prediction of defect properties in density functional supercell calculations." Modelling and Simulation in Materials Science and Engineering 17, no. 8 (2009): 084002.

[Lanza 2012A]Lanza, M., K. Zhang, M. Porti, M. Nafria, Z. Y. Shen, L. F. Liu, J. F. Kang, D. Gilmer, and G. Bersuker. "Grain boundaries as preferential sites for resistive switching in the $HfO_2$ resistive random access memory structures." Applied Physics Letters 100, no. 12 (2012): 123508.

[Lanza 2012B]Lanza, M., G. Bersuker, M. Porti, E. Miranda, M. Nafria, and X. Aymerich. "Resistive switching in hafnium dioxide layers: local phenomenon at grain boundaries." Applied Physics Letters 101, no. 19 (2012): 193502.

[Lee 2007]Lee, Bora, Kyeong Mi Choi, Hyo-Shin Ahn, Seungwu Han, and Jaichan Lee. "Oxygen vacancy clustering and electron localization in oxygen-deficient $SrTiO_3$: LDA+ U study." Physical Review Letters 98, no. 11 (2007): 115503.

[Lee 2011]Lee, Myoung-Jae, Chang Bum Lee, Dongsoo Lee, Seung Ryul Lee, Man Chang, Ji Hyun Hur, Young-Bae Kim et al. "A fast, high-endurance and scalable non-volatile memory device made from asymmetric $Ta_2O_{5-x}$/$TaO_{2-x}$ bilayer structures." Nature Materials 10, no. 8 (2011): 625-630.

[Lei 2007]Lei, Yong, Weiping Cai, and Gerhard Wilde. "Highly ordered nanostructures with tunable size, shape and properties: a new way to surface nano-patterning using ultra-thin alumina masks." Progress in Materials Science 52, no. 4 (2007): 465-539.

[Li 2008]Li, X., C. H. Tung, and K. L. Pey. "The nature of dielectric breakdown." Applied Physics Letters 93, no. 7 (2008): 072903.

[Lim 2015]Lim, Ee Wah, and Razali Ismail. "Conduction Mechanism of Valence Change Resistive Switching Memory: A Survey." Electronics 4, no. 3 (2015): 586-613.

[Lippert 1997]Lippert, Gerald, and J. Hutter and M. Parinello. "A hybrid Gaussian and plane wave density functional scheme." Molecular Physics 92, no. 3 (1997): 477-488.

[Magyari-Köpe 2012]Magyari-Köpe, Blanka, Seong Geon Park, Hyung-Dong Lee, and Yoshio Nishi. "First principles calculations of oxygen vacancy-ordering effects in resistance change memory materials incorporating binary transition metal oxides." Journal of Materials Science 47, no. 21 (2012): 7498-7514.

[Martin-Samos 2004]Martin-Samos, L., Y. Limoge, N. Richard, J. P. Crocombette, G. Roma, E. Anglada, and E. Artacho. "Oxygen neutral defects in silica: Origin of the distribution of the formation energies." Europhysics Letters 66, no. 5 (2004): 680.

[McCann 2011]McCann, Michael T.P., Damian A. Mooney, Mahfujur Rahman, Denis P. Dowling, and J.M. Don MacElroy. "Novel, nanoporous silica and titania layers fabricated by magnetron sputtering." ACS Applied Materials Interfaces 3, no. 2 (2011): 252-260.

[Mehonic 2012A]Mehonic, Adnan, Sébastien Cueff, Maciej Wojdak, Stephen Hudziak, Olivier Jambois, Christophe Labbé, Blas Garrido, Richard Rizk, and Anthony J. Kenyon. "Resistive switching in silicon suboxide films." Journal of Applied Physics 111, no. 7 (2012): 074507.

[Mehonic 2012B]Mehonic, Adnan, Maciej Wojdak, Stephen Hudziak, Richard Rizk, and Anthony J. Kenyon. "Electrically tailored resistance switching in silicon oxide." Nanotechnology 23, no. 45 (2012): 455201.

[Mehonic 2015]Mehonic, Adnan, Mark Buckwell, Luca Montesi, Leon Garnett, Stephen

Hudziak, Sarah Fearn, Richard Chater, David McPhail, and Anthony J. Kenyon. "Structural changes and conductance thresholds in metal-free intrinsic SiOx resistive random access memory." Journal of Applied Physics 117, no. 12 (2015): 124505.

[Mehonic 2016]Mehonic, Adnan, Mark Buckwell, Luca Montesi, Manveer Singh Munde, David Gao, Stephen Hudziak, Richard J. Chater et al. "Silica: Nanoscale Transformations in Metastable, Amorphous, Silicon-Rich Silica." Advanced Materials 28, no. 34 (2016): 7549.

[Mehonic 2017]Mehonic, Adnan, Manveer S. Munde, Wing H. Ng, Mark Buckwell, Luca Montesi, Michel Bosman, and Anthony J. Kenyon (2017). "Intrinsic resistance switching in amorphous silicon oxide for high performance $SiO_x$ ReRAM devices." Microelectronic Engineering 178 (2017): 98-103.

[Midgley 2003]Midgley, P. A., and Matthew Weyland. "3D electron microscopy in the physical sciences: the development of Z-contrast and EFTEM tomography." Ultramicroscopy 96, no. 3 (2003): 413-431.

[Midgley 2009]Midgley, Paul A., and Rafal E. Dunin-Borkowski. "Electron tomography and holography in materials science." Nature Materials 8, no. 4 (2009): 271-280.

[Modlin 1985]Modlin, Douglas N., and William A. Tiller. "Effects of Coronal Discharge Induced Oxygen Ion Beams and Electric Fields on Silicon Oxidation Kinetics II. Electric Field Effects." Journal of The Electrochemical Society 132, no. 7 (1985): 1659-1663.

[Montesi 2016]Montesi, Luca, Mark Buckwell, Konstantin Zarudnyi, Leon Garnett, Steven Hudziak, Adnan Mehonic, and Anthony J. Kenyon. "Nanosecond Analog Programming of Substoichiometric Silicon Oxide Resistive RAM." IEEE Transactions on Nanotechnology 15, no. 3 (2016): 428-434.

[Movchan 1969]Movchan, B. A., and A. V. Demchishin. "STRUCTURE AND PROPERTIES OF THICK CONDENSATES OF NICKEL, TITANIUM, TUNGSTEN, ALUMINUM OXIDES, AND ZIRCONIUM DIOXIDE IN VACUUM." Fiz. Metal. Metalloved. 28 (1969): 653-660.

[Mozzi 1969]Mozzi, R. L., and B. E. Warren. "The structure of vitreous silica." Journal of

Applied Crystallography 2, no. 4 (1969): 164-172.

[Mrstik 1999]Mrstik, B. J., V. V. Afanas'ev, Andre Stesmans, P. J. McMarr, and R. K. Lawrence. "Relationship between oxide density and charge trapping in $SiO_2$ films." Journal of Applied Physics 85, no. 9 (1999): 6577-6588.

[Mukhopadhyay 2004]Mukhopadhyay, Sanghamitra, Peter V. Sushko, A. Marshall Stoneham, and Alexander L. Shluger. "Modeling of the structure and properties of oxygen vacancies in amorphous silica." Physical Review B 70, no. 19 (2004): 195203.

[Mukhopadhyay 2005]Mukhopadhyay, Sanghamitra, Peter V. Sushko, A. Marshall Stoneham, and Alexander L. Shluger. "Correlation between the atomic structure, formation energies, and optical absorption of neutral oxygen vacancies in amorphous silica." Physical Review B 71, no. 23 (2005): 235204.

[Muller 1999]Muller, David A., T. Sorsch, S. Moccio, F. H. Baumann, K. Evans-Lutterodt, and G. Timp. "The electronic structure at the atomic scale of ultrathin gate oxides." Nature 399, no. 6738 (1999): 758-761.

[Murphy 2013]Murphy, Samuel T., and Nicholas DM Hine. "Anisotropic charge screening and supercell size convergence of defect formation energies." Physical Review B 87, no. 9 (2013): 094111.

[Nolan 2006]Nolan, Michael, Joanne E. Fearon, and Graeme W. Watson. "Oxygen vacancy formation and migration in ceria." Solid State Ionics 177, no. 35 (2006): 3069-3074.

[Onfrio 2015]Onofrio, Nicolas, David Guzman, and Alejandro Strachan. "Atomic origin of ultrafast resistance switching in nanoscale electrometallization cells." Nature Materials 14, no. 4 (2015): 440-446.

[Orellana 2001]Orellana, W., Antônio JR da Silva, and A. Fazzio. "$O_2$ Diffusion in $SiO_2$: Triplet versus Singlet." Physical review letters 87, no. 15 (2001): 155901.

[Osburn 1972]Osburn, C. M., and E. J. Weitzman. "Electrical conduction and dielectric breakdown in silicon dioxide films on silicon." Journal of The Electrochemical Society

119, no. 5 (1972): 603-609.

[Pacchioni 1997]Pacchioni, Gianfranco, and Gianluigi Ieranò. "On the origin of the 5.0 and 7.6 eV absorption bands in oxygen deficient $\alpha$-quartz and amorphous silica. A first principles quantum-chemical study." Journal of Non-Crystalline Solids 216 (1997): 1-9.

[Pantelides 2008]Pantelides, S. T., Z-Y. Lu, C. Nicklaw, T. Bakos, S. N. Rashkeev, D. M. Fleetwood, and R. D. Schrimpf. "The E' center and oxygen vacancies in $SiO_2$." Journal of Non-Crystalline Solids 354, no. 2 (2008): 217-223.

[Park 2013]Park, Gyeong-Su, Young Bae Kim, Seong Yong Park, Xiang Shu Li, Sung Heo, Myoung-Jae Lee, Man Chang et al. "In situ observation of filamentary conducting channels in an asymmetric $Ta2O_{5-x}/TaO_{2-x}$ bilayer structure." Nature Communications 4 (2013): 2382

[Pasquarello 1998]Pasquarello, Alfredo, and Roberto Car. "Identification of Raman defect lines as signatures of ring structures in vitreous silica." Physical Review Letters 80, no. 23 (1998): 5145.

[Pennycook 1991]Pennycook, S. J., and D. E. Jesson. "High-resolution Z-contrast imaging of crystals." Ultramicroscopy 37, no. 1 (1991): 14-38.

[Perdew 1992]Perdew, John P., and Yue Wang. "Accurate and simple analytic representation of the electron-gas correlation energy." Physical Review B 45, no. 23 (1992): 13244.

[Perdew 1996]Perdew, John P., Kieron Burke, and Matthias Ernzerhof. "Generalized gradient approximation made simple." Physical review letters 77, no. 18 (1996): 3865.

[Pey 2012]Pey, K. L., C. H. Tung, M. K. Radhakrishnan, L. J. Tang, and W. H. Lin. "Dielectric breakdown induced epitaxy in ultrathin gate oxide-a reliability concern." Paper presented at IEEE International Electron Devices Meeting, San Francisco, CA, December 8-11, 2002.

[Philipp 1972]Philipp, Herbert R. "Optical and bonding model for non-crystalline SiOx and SiOxNy materials." Journal of Non-Crystalline Solids 8 (1972): 627-632.

[Pintilie 2010]Pintilie, I., C. M. Teodorescu, F. Moscatelli, R. Nipoti, A. Poggi, S. Solmi, L. S. Lovlie, and B. G. Svensson. "Analysis of electron traps at the 4H-SiC/$SiO_2$ interface; influence by nitrogen implantation prior to wet oxidation." Journal of Applied Physics 108, no. 2 (2010): 024503.

[Plimpton 1995]Plimpton, Steve. "Fast parallel algorithms for short-range molecular dynamics." Journal of Computational Physics 117, no. 1 (1995): 1-19

[Radon 1986]Radon, Johann. "On the determination of functions from their integral values along certain manifolds." IEEE Transactions on Medical Imaging 5, no. 4 (1986): 170-176.

[Raghavachari 1986]Raghavachari, Krishnan. "Theoretical study of small silicon clusters: equilibrium geometries and electronic structures of $Si_n$ (n= 2-7, 10)." The Journal of Chemical Physics 84, no. 10 (1986): 5672-5686.

[Ramprasad 2003]Ramprasad, R. "First principles study of oxygen vacancy migration in tantalum pentoxide." Journal of Applied Physics 95, no. 3 (2004): 954-957.

[Rimola 2013]Rimola, Albert, Dominique Costa, Mariona Sodupe, Jean-François Lambert, and Piero Ugliengo. "Silica surface features and their role in the adsorption of biomolecules: computational modeling and experiments." Chemical Reviews 113, no. 6 (2013): 4216-4313.

[Rino 1993]Rino, José P., Ingvar Ebbsjö, Rajiv K. Kalia, Aiichiro Nakano, and Priya Vashishta. "Structure of rings in vitreous $SiO_2$." Physical Review B 47, no. 6 (1993): 3053.

[Rudra 1987]Rudra, Jayanta K., and W. Beall Fowler. "Oxygen vacancy and the $E_1$' center in crystalline $SiO_2$." Physical Review B 35, no. 15 (1987): 8223.

[Russo 2007]Russo, U., Daniele Ielmini, C. Cagli, A. L. Lacaita, Silvia Spiga, C. Wiemer, M. Perego, and M. Fanciulli. "Conductive-filament switching analysis and self-accelerated thermal dissolution model for reset in NiO-based RRAM." Paper presented at IEEE International Electron Devices Meeting, Washington, DC, December 10-12, 2007.

[Sarnthein 1995]Sarnthein, Johannes, Alfredo Pasquarello, and Roberto Car. "Structural and Electronic Properties of Liquid and Amorphous $SiO_2$: An Ab Initio Molecular Dynamics Study." Physical Review letters 74, no. 23 (1995): 4682.

[Sasaki 2013]Sasaki, M., and T. Ehara. "Silicon oxide thin films prepared by vacuum evaporation and sputtering using silicon monoxide." Journal of Physics: Conference Series 417, no. 1 (2017), 012028.

[Schindler]Schindler, Christina, S.C. Puthen Thermadam, Rainer Waser, and Michael N. Kozicki. "Bipolar and Unipolar Resistive Switching in Cu-Doped $SiO_2$." IEEE Transactions on Electron Devices 54, no. 10 (2007): 2762-2768.

[Schulmeister 2003]Schulmeister, Klaus, and Werner Mader. "TEM investigation on the structure of amorphous silicon monoxide." Journal of Non-Crystalline Solids 320, no. 1 (2003): 143-150.

[Shen 2015]Shen, Xiao, Sarit Dhar, and Sokrates T. Pantelides. "Atomic origin of high-temperature electron trapping in metal-oxide-semiconductor devices." Applied Physics Letters 106, no. 14 (2015): 143504.

[Slater 1951]Slater, John C. "A simplification of the Hartree-Fock method." Physical Review 81, no. 3 (1951): 385.

[Skuja 1998]Skuja, Linards. "Optically active oxygen-deficiency-related centers in amorphous silicon dioxide." Journal of Non-Crystalline Solids 239, no. 1 (1998): 16-48.

[Song 2001]Song, Jakyoung, L. René Corrales, Georg Kresse, and Hannes Jónsson. "Migration of O vacancies in $\alpha$-quartz: The effect of excitons and electron holes." Physical Review B 64, no. 13 (2001): 134102.

[Stoneham 2001]Stoneham, A. Marshall, Marek A. Szymanski, and Alexander L. Shluger. "Atomic and ionic processes of silicon oxidation." Physical Review B 63, no. 24 (2001): 241304.

[Stoyanov 2007]Stoyanov, E., F. Langenhorst, and G. Steinle-Neumann. "The effect of valence state and site geometry on Ti L3, 2 and OK electron energy-loss spectra of $Ti_xO_y$

phases." American Mineralogist 92, no. 4 (2007): 577-586.

[Suele 1997]Suehle, John S., and Prasad Chaparala. "Low electric field breakdown of thin $SiO_2$ films under static and dynamic stress." IEEE Transactions on Electron Devices 44, no. 5 (1997): 801-808.

[Sulimov 2002]Sulimov, Vladimir B., Peter V. Sushko, Arthur H. Edwards, Alexander L. Shluger, and A. Marshall Stoneham. "Asymmetry and long-range character of lattice deformation by neutral oxygen vacancy in $\alpha$-quartz." Physical Review B 66, no. 2 (2002): 024108.

[Sushko 2005]Sushko, P. V., S. Mukhopadhyay, A. M. Stoneham, and A. L. Shluger. "Oxygen vacancies in amorphous silica: structure and distribution of properties."Microelectronic Engineering 80 (2005): 292-295.

[Susman 1991]Susman, S., K. J. Volin, D. L. Price, M. Grimsditch, J. P. Rino, R. K. Kalia, P. Vashishta, G. Gwanmesia, Y. Wang, and R. C. Liebermann. "Intermediate-range order in permanently densified vitreous $SiO_2$: A neutron-diffraction and molecular-dynamics study." Physical Review B 43, no. 1 (1991): 1194.

[Syzmanski 2001]Szymanski, M. A., A. M. Stoneham, and A. Shluger. "The different roles of charged and neutral atomic and molecular oxidising species in silicon oxidation from ab initio calculations." Solid-State Electronics 45, no. 8 (2001): 1233-1240.

[Tam 2015]Tam, Nguyen Minh, Tran Dieu Hang, Hung Tan Pham, Huyen Thi Nguyen, My Phuong Pham Ho, Pablo A. Denis, and Minh Tho Nguyen. "Bonding and singlet-triplet gap of silicon trimer: Effects of protonation and attachment of alkali metal cations." Journal of Computational Chemistry 36, no. 11 (2015): 805-815.

[Tamura 2004]Tamura, Tomoyuki, Guang-Hong Lu, Ryoichi Yamamoto, and Masanori Kohyama. "First-principles study of neutral oxygen vacancies in amorphous silica and germania." Physical Review B 69, no. 19 (2004): 195204.

[Temkin 1975]Temkin, R. J. "An analysis of the radial distribution function of $SiO_x$." Journal of Non-Crystalline Solids 17, no. 2 (1975): 215-230.

[Thomas 2013]Thomas, Jürgen, Jürgen Ramm, and Thomas Gemming. "Density measurement of thin layers by electron energy loss spectroscopy (EELS)." Micron 50 (2013): 57-61.

[Thornton 1974]Thornton, John A. "Influence of apparatus geometry and deposition conditions on the structure and topography of thick sputtered coatings." Journal of Vacuum Science & Technology 11, no. 4 (1974): 666-670.

[Thornton 1986]Thornton, John A. "The microstructure of sputter-deposited coatings." Journal of Vacuum Science & Technology A 4, no. 6 (1986): 3059-3065.

[Uchino 2000]Uchino, Takashi, Yukio Kitagawa, and Toshinobu Yoko. "Structure, energies, and vibrational properties of silica rings in $SiO_2$ glass." Physical Review B 61, no. 1 (2000): 234.

[VandeVondele 2005]VandeVondele, Joost, Matthias Krack, Fawzi Mohamed, Michele Parrinello, Thomas Chassaing, and Jürg Hutter. "Quickstep: Fast and accurate density functional calculations using a mixed Gaussian and plane waves approach." Computer Physics Communications 167, no. 2 (2005): 103-128.

[VandeVondele 2007]VandeVondele, Joost, and Juerg Hutter. "Gaussian basis sets for accurate calculations on molecular systems in gas and condensed phases." The Journal of Chemical Physics 127, no. 11 (2007): 114105.

[Van Duin 2003]Van Duin, Adri C.T., Alejandro Strachan, Shannon Stewman, Qingsong Zhang, Xin Xu, and William A. Goddard. "ReaxFFSiO reactive force field for silicon and silicon oxide systems." The Journal of Physical Chemistry A 107, no. 19 (2003): 3803-3811.

[Vollmayr 1996]Vollmayr, Katharina, Walter Kob, and Kurt Binder. "Cooling-rate effects in amorphous silica: A computer-simulation study." Physical Review B 54, no. 22 (1996): 15808.

[Wallis 1995]Wallis, D. J., P. H. Gaskell, and R. Brydson. "Oxygen K near l-edge spectra of amorphous silicon suboxides." Journal of Microscopy 180, no. 3 (1995): 307-312.

[Wang 2013]Wang, Yuefei, Xinye Qian, Kunji Chen, Zhonghui Fang, Wei Li, and Jun Xu. "Resistive switching mechanism in silicon highly rich $SiO_x$ (x< 0.75) films based on silicon dangling bonds percolation model." Applied Physics Letters 102, no. 4 (2013): 042103.

[Wang 2014]Wang, Gunuk, Yang Yang, Jae-Hwang Lee, Vera Abramova, Huilong Fei, Gedeng Ruan, Edwin L. Thomas, and James M. Tour. "Nanoporous Silicon Oxide Memory." Nano Letters 14, no. 8 (2014): 4694-4699.

[Wang 2016]Wang, Zhongrui, Hao Jiang, Moon Hyung Jang, Peng Lin, Alexander Ribbe, Qiangfei Xia, and J. Joshua Yang. "Electrochemical metallization switching with a platinum group metal in different oxides." Nanoscale (2016).

[Warren 1992]Warren, B. E. "X-RAY DETERMINATION OF THE STRUCTURE OF GLASS*." Journal of the American Ceramic Society 75, no. 1 (1992): 5-10.

[Waseda 2007]Waseda, Atsushi, and Kenichi Fujii. "Density evaluation of silicon thermal-oxide layers on silicon crystals by the pressure-of-flotation method." IEEE Transactions on Instrumentation and Measurement 56, no. 2 (2007): 628-631.

[Waser 2012]Waser, Rainer, "Redox-based Resistive Switching Memories". In *Nanoelectronics and Information Technology*, 685-708. 3rd ed. Weinheim: Wiley-VCH, 2012.

[Williams 2009A]Williams, David.B., and C.Barry Carter. "The Instrument." In *Transmission Electron Microscopy: A Textbook for Materials Science*, 141-169. 2nd ed. New York: Springer, 2009.

[Williams 2009B]Williams, David.B., and C.Barry Carter. "Electron Sources." In *Transmission Electron Microscopy: A Textbook for Materials Science*, 73-87. 2nd ed. New York: Springer, 2009.

[Williams 2009C]Williams, David.B., and C.Barry Carter. "Lenses, Apertures, and Resolution." In *Transmission Electron Microscopy: A Textbook for Materials Science*, 91-114. 2nd ed. New York: Springer, 2009.

[Williams 2009D]Williams, David.B., and C.Barry Carter. "How to 'See' Electrons." In *Transmission Electron Microscopy: A Textbook for Materials Science*, 115-125. 2nd ed.

New York: Springer, 2009.

[Williams 2009E] Williams, David.B., and C.Barry Carter. "Specimen Preparation." In *Transmission Electron Microscopy: A Textbook for Materials Science*, 173-203. 2nd ed. New York: Springer, 2009.

[Williams 2009F]Williams, David.B., and C.Barry Carter. "Scattering and Diffraction." In *Transmission Electron Microscopy: A Textbook for Materials Science*, 23-36. 2nd ed. New York: Springer, 2009.

[Williams 2009G]Williams, David.B., and C.Barry Carter. "X-ray Spectrometry." In *Transmission Electron Microscopy: A Textbook for Materials Science*, 581-601. 2nd ed. New York: Springer, 2009.

[Williams 2009H] Williams, David.B., and C.Barry Carter. "Electron Energy-Loss Spectrometers and Filters." In *Transmission Electron Microscopy: A Textbook for Materials Science*, 679-698. 2nd ed. New York: Springer, 2009.

[Wimmer 2016]Wimmer, Yannick, Al-Moatasem El-Sayed, Wolfgang Gös, Tibor Grasser, and Alexander L. Shluger. "Role of hydrogen in volatile behaviour of defects in $SiO_2$-based electronic devices." Proceedings of Royal Society A 472, no. 2190 (2016), 20160009.

[Wyckoff 1963]Wyckoff, W. G. *Crystal Structures Vol. 1*, 312. 2nd ed. New York: Interscience.

[Xu 2010]Xu, Zhi, Yoshio Bando, Wenlong Wang, Xuedong Bai, and Dmitri Golberg. "Real-time in situ HRTEM-resolved resistance switching of $Ag_2S$ nanoscale ionic conductor." ACS Nano 4, no. 5 (2010): 2515-2522.

[Yang 2012]Yang, Yuchao, Peng Gao, Siddharth Gaba, Ting Chang, Xiaoqing Pan, and Wei Lu. "Observation of conducting filament growth in nanoscale resistive memories." Nature Communications 3 (2012): 732.

[Yang 2014A]Yang, Yang, Weiming Lü, Yuan Yao, Jirong Sun, Changzhi Gu, Lin Gu, Yanguo Wang, Xiaofeng Duan, and Richeng Yu. "In situ TEM observation of resistance

switching in titanate based device." Scientific Reports 4 (2014):3890.

[Yang 2014B]Yang, Yuchao, Peng Gao, Linze Li, Xiaoqing Pan, Stefan Tappertzhofen, ShinHyun Choi, Rainer Waser, Ilia Valov, and Wei D. Lu. "Electrochemical dynamics of nanoscale metallic inclusions in dielectrics." Nature Communications 5 (2014):4232.

[Yao 2010]Yao, Jun, Zhengzong Sun, Lin Zhong, Douglas Natelson, and James M. Tour. "Resistive switches and memories from silicon oxide." Nano Letters 10, no. 10 (2010): 4105-4110.

[Yao 2012]Yao, Jun, Lin Zhong, Douglas Natelson, and James M. Tour. "In situ imaging of the conducting filament in a silicon oxide resistive switch." Scientific Reports 2 (2012):242.

[Yasaitis 1972]Yasaitis, John A., and Roy Kaplow. "Structure of amorphous silicon monoxide." Journal of Applied Physics 43, no. 3 (1972): 995-1000.

[Yassine 2000]Yassine, Abdullah M., H. E. Nariman, Michael McBride, Mirac Uzer, and Kola R. Olasupo. "Time dependent breakdown of ultrathin gate oxide." IEEE Transactions on Electron Devices 47, no. 7 (2000): 1416-1420.

[Yurtsever 2006]Yurtsever, Aycan, Matthew Weyland, and David A. Muller. "Three-dimensional imaging of nonspherical silicon nanoparticles embedded in silicon oxide by plasmon tomography." Applied Physics Letters 89, no. 15 (2006): 151920.

[Zachariasen 1932]Zachariasen, William H. "The atomic arrangement in glass." Journal of the American Chemical Society 54, no. 10 (1932): 3841-3851.

[Zamoryanskaya 2007]Zamoryanskaya, M. V., and V. I. Sokolov. "Cathodoluminescence study of silicon oxide-silicon interface." Semiconductors 41, no. 4 (2007): 462-468.

[Zhang 2010]Zhang, Wa Li, Sam Zhang, Ming Yang, Zhen Liu, ZhanHong Cen, Tupei Chen, and Dongping Liu. "Electroluminescence of as-sputtered silicon-rich $SiO_x$ films." Vacuum 84, no. 8 (2010): 1043-1048.